

How declining ocean oxygen
threatens marine life p. 429

Extreme wildfires can help create
their own weather p. 457

Daily patterns of human gene
expression measured p. 478

Science

\$15
3 FEBRUARY 2023
science.org

AAAS

A MAGMATIC WEB

Seismology maps
connections among
Hawaiian volcanoes

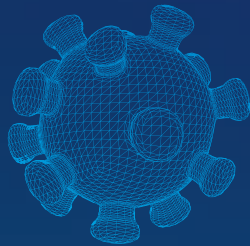
pp. 434 & 462



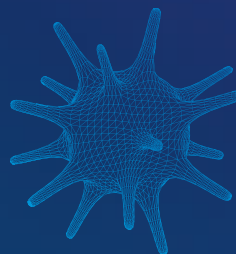
ONE TEST. THREE ANSWERS.

A new tool for differential diagnosis
of COVID-19 and flu

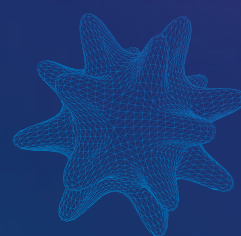
✓ COVID-19



✓ FLU A



✓ FLU B



COVID-19 and flu have similar symptoms, which is why the ease and efficiency of testing with the Panbio™ COVID-19/Flu A&B Rapid Panel is a great choice for differential diagnosis.

One test provides three results in just 15 minutes — speeding your ability to diagnose and make treatment decisions at the point of care.

One test means less demand on physicians, staff and lab workers. One swab means less discomfort for patients. One set of answers for COVID-19 and flu empowers timely decision-making to effectively treat patients, help prevent further transmission and avoid unnecessary antibiotic use.

LEARN MORE AT [GLOBALPOINTOFCARE.ABBOTT](https://globalpointofcare.abbott)

© 2023 Abbott. All rights reserved. All trademarks referenced are trademarks of either the Abbott group of companies or their respective owners. Any photos displayed are for illustrative purposes only. COL-17861-01 01/23

16th Edition BBVA Foundation Frontiers of Knowledge Awards

With the collaboration of



The **BBVA Foundation Frontiers of Knowledge Awards** recognize and reward world-class research and artistic creation, prizing contributions of singular impact for their originality and significance. The name of the scheme is intended to denote not only research work that substantially enlarges the scope of our current knowledge – pushing forward the frontiers of the known world – but also the meeting and overlap of different disciplinary areas and the emergence of new fields.

The Frontiers of Knowledge Awards honor fundamental disciplinary or interdisciplinary advances across a broad expanse of the knowledge map of the 21st century.

The BBVA Foundation is assisted in the award process by the **Spanish National Research Council (CSIC)**.

Categories

- 1/ **Basic Sciences (Physics, Chemistry, Mathematics)**
- 2/ **Biology and Biomedicine**
- 3/ **Information and Communication Technologies**
- 4/ **Ecology and Conservation Biology**
- 5/ **Climate Change**
- 6/ **Economics, Finance and Management**
- 7/ **Humanities and Social Sciences**
- 8/ **Music and Opera**

In Humanities and Social Sciences, the award will alternate annually between these two disciplinary domains, with this sixteenth edition dedicated to the Social Sciences.

Nomination

Nominations are invited from scientific or artistic societies and organizations, public or private R&D centers, university and hospital departments, schools of music, orchestras, and organizations working on or around the issue of climate change, as well as other institutions specified in the call conditions.

Entry submission

The nomination period concludes at **16:00 GMT on June 30, 2023**.

www.frontiersofknowledgeawards-fbbva.es

Fundación BBVA
Plaza de San Nicolás, 4 · 48005 Bilbao
Paseo de Recoletos, 10 · 28001 Madrid
awards-info@fbbva.es



(From left) Fabio Segura (co-CEO, Jacobs Foundation), Lavinia Jacobs (President, Jacobs Foundation), Daniel Schwartz (2021 prize recipient), Charles Nelson (2021 prize recipient), Terrie Moffitt (2010 prize recipient and chair of the KJJ Research Prize jury), and Simon Sommer (co-CEO, Jacobs Foundation).

The Klaus J. Jacobs Research Prize: A force for good

The field of child and youth development is a complex one that, like many other areas of research, requires collaborations that transcend individual disciplines and bring together diverse experiences and research modalities. The Jacobs Foundation, based in Switzerland, understands this concept. In an effort to support science that enables sound solutions to challenging research problems, the foundation inaugurated the Klaus J. Jacobs (KJJ) Research Prize in 2009. The prize celebrates unique perspectives in child and youth development and learning, and is consequently not limited to specific fields, with past prizes having been awarded to researchers in psychology, economics, neuroscience, and education.

"The KJJ Research Prize is focused on multidisciplinary because you get the biggest ideas and the most exciting discoveries when you bring together different parts of developmental and learning science," says Terrie Moffitt, one of the early recipients of the KJJ Research Prize, who shared the award with her husband, Avshalom Caspi. Moffitt is the Nannerl O. Keohane University Professor of Psychology at Duke University and professor of Social Development at King's College London, and chair of the jury of the KJJ Research Prize. Caspi is professor of Psychology & Neuroscience at Duke University, and professor of Personality Development at the Institute of Psychiatry, Psychology, & Neuroscience at King's College London. Together, they codirect the Dunedin Study, a longitudinal analysis of all the babies born in 1972 in Dunedin, in New Zealand. Considered one of the most relevant longitudinal investigations in the field, Moffitt and Caspi engage specialists in

psychology, economics, public health, genetics, dentistry, ophthalmology, and more. "As a collaborative team, we can inform each other and make cross-discipline leaps," she says. "That's what leads to unexpected, new discoveries."

At the time they won the prize in 2010, the two scientists had launched another major longitudinal project, the Environmental Risk (E-Risk) Longitudinal Twin Study, with a new cohort of kids—this time looking at all the twins born in the United Kingdom in 1994 and 1995 who were growing up in disadvantaged or adverse circumstances, particularly those born to teenage mothers. Long-term, longitudinal projects like this require significant financial resources, says Moffitt. The support from the KJJ Research Prize allowed the team to be creative and expand the type of data they collected, often in real time. For example, Moffitt and Caspi realized the value of taking and scrutinizing blood samples from the twins, to ascertain the presence of stress biomarkers in the children. With the KJJ Research Prize funding, they could seize the opportunity to immediately augment their study to achieve new goals. "There were rapid response things we could do with the money," she says. "We were able to be nimble."

"The kind of support that this field needs most is for longitudinal research," says Ulman Lindenberger, director at the Max Planck Institute for Human Development, codirector of the Max Planck UCL Centre for Computational Psychiatry and Ageing Research, and a member of the Jacobs Foundation Board of Trustees. "In order to start a project where you know you can follow kids for multiple years—from infancy to age 8, for example—you need this financial stability."

Making a positive difference

The Jacobs Foundation serves as a model of a new way of advancing science through strategic philanthropy. The prize is eclectic and about inclusiveness, says Moffitt. "We are open to considering anybody whose work directly leads to science that makes children's lives better," she adds.

A call for nominations is announced in mid-January of every other year and global and disciplinary diversity of nominations is encouraged. The prize jury looks for researchers with a record of groundbreaking work at an international level and whose research will continue to make a fundamental and positive difference in the lives of children and youth. "It is an acceleration prize," says Moffitt, "to give people the freedom provided by a major injection of cash so that they can take their science in exciting directions and improve its reach."

Prize recipients are expected and encouraged to stay engaged with the Jacobs Foundation and contribute to an enriching and forward-thinking network that fosters growth of the field of child development and learning. "Especially during

the time of COVID when everyone was downtrodden and stressed, the Jacobs Foundation was a place where you got the feeling that things are moving, things can happen, and they will find a way," says Moffitt. "There's such positivity—the whole foundation just radiates optimism."

Since receiving the prize, Moffitt has continued to serve the Jacobs Foundation and KJJ Research Prize because she wants to be a part of this force for premier science. "It's a great organization and it makes you feel like you are part of something that is bigger and more important than just yourself and your own laboratory," she says. "I love being chair of the jury. And I do think the prize makes a difference for the field."

Sponsored by



The Klaus J. Jacobs Research Prize is awarded every other year by the Jacobs Foundation to researchers who have made pioneering scientific contributions in any scholarly discipline aiming at improving learning, development, and living conditions of children and youth. It is endowed with 1 million Swiss Francs, and prize recipients can use CHF 900,000 for the project itself and CHF 100,000 for additional support such as travel and professional development.

"It's a prize that was needed because it provides visibility to the field of child and youth development and it gives the top scientists in the field the extra boost and research money to realize an ambitious project that might be beyond reach without the prize," says Ulman Lindenberg, member of the Jacobs Foundation Board of Trustees.

The prize is inclusive of all areas of scholarship, and welcomes nominations from experts in educational sciences, psychology, economics,

sociology, family studies, media studies, political sciences, linguistics, neurosciences, computer sciences, medical sciences, and many others. "There is a good alignment between the prize and what the foundation is known for—namely to fund research that is based on good scholarship and has been shown to work," says Lindenberg.

And while it is still in its adolescence, the prize has already transformed lives and opportunities to serve children through ambitious science. "This award, which is a tribute to Klaus [J. Jacobs]'s humanitarian vision, I think over time will be regarded as a Nobel Prize of research in youth development," said Albert Bandura, late professor of social science in psychology, Stanford University, and previous member of the KJJ Research Prize jury.

Nominations for 2023 are now open and should be submitted by March 15, 2023. For more information, please visit bit.ly/KJJprize2023 or contact award@jacobsfoundation.org.





NGS library prep? We've got you covered.

For 13 years, NEB[®] has addressed library prep challenges by offering solutions that streamline workflows, minimize inputs, and improve library yield and quality. In fact, use of NEBNext[®] reagents has been cited in >20,000 publications.

With over 90 products in the NEBNext portfolio and direct access to experts in NGS and enzymology, NEB can support library preparation for all of your sample types, for a wide range of sequencing platforms and throughputs.

The NEBNext Ultra[™] II workflow, which lies at the heart of the NEBNext library prep solution, is available in a variety of streamlined and convenient kit formats. For added flexibility, NEBNext kits are easily scalable for automation on liquid

handling instrumentation. As a reagent manufacturer, NEB is ideally positioned to support your large volume and custom needs through our OEM & Customized Solutions group.

Our expertise, proven track record and depth of portfolio make NEBNext a preferred choice for high-quality sample preparation. We're ready to show you why it should be yours.



Interested in giving NEBNext a try? Learn more and request a sample at [NEBNext.com](https://www.neb.com).

Products and content are covered by one or more patents, trademarks and/or copyrights owned or controlled by New England Biolabs, Inc (NEB). The use of trademark symbols does not necessarily indicate that the name is trademarked in the country where it is being read; it indicates where the content was originally developed. The use of these products may require you to obtain additional third-party intellectual property rights for certain applications. For more information, please email busdev@neb.com.

© Copyright 2022, New England Biolabs, Inc.; all rights reserved.



be INSPIRED
drive DISCOVERY
stay GENUINE

CONTENTS

3 FEBRUARY 2023 • VOLUME 379 • ISSUE 6631



429

Low oxygen is shaping the hunting behavior of sharks such as this shortfin mako.

NEWS

IN BRIEF

420 News at a glance

IN DEPTH

422 U.S. scientists brace for greater scrutiny of risky research

Expert panel recommends broader reviews of research involving pathogens or toxins that could have “dual use” *By J. Kaiser*

423 As some postdocs’ pay rises, funding fears grow

Salary mandates in California and Washington leave many lab heads scrambling *By K. Langin*

424 Pot residues show how ancient Egyptians made a mummy

Analysis reveals the chemicals applied to corpses in a 2700-year-old mummification workshop *By A. Curry*

PODCAST

425 New COVID-19 vaccine strategy would mimic flu’s annual shots

Scientists and regulators seek new course amid uncertainty *By J. Couzin-Frankel*

427 Protein decoys may battle COVID-19 and more

Drugs designed to resemble viruses’ cellular targets move into clinical trials *By R. F. Service*

428 Neanderthals lived in groups big enough to eat giant elephants

Meat from the butchered beasts would have fed hundreds *By A. Curry*

SCI. ADV. RESEARCH ARTICLE BY S. GAUDZINSKI-WINDHEUSER ET AL. 10.1126/SCIADV.ADG6072

FEATURES

429 Breathless oceans

Warming oceans are running short of oxygen, and the fiercest marine predators are already feeling the effects *By W. Cornwall*

INSIGHTS

PERSPECTIVES

434 The Pāhala swarm of earthquakes in Hawai’i

A magma network may feed into different volcanoes, including Mauna Loa and Kilauea *By A. F. Flinders*

RESEARCH ARTICLE p. 462

436 Working at room temperature

A solid-state electrolyte enables a lithium-air battery to operate at 25°C *By D. Dong and Y.-C. Lu*

REPORT p. 499

437 Managing sources of error during pandemics

The COVID-19 pandemic has highlighted important considerations for modeling future pandemics *By S. Cauchemez et al.*

439 One carbon—four new bonds

Stable carbenes deliver a carbon atom to simple amides, producing a range of cyclic compounds *By Y. Nakano and D. W. Lupton* REPORT p. 484

POLICY FORUM

441 The NIH-led research response to COVID-19

Investment, collaboration, and coordination have been key *By F. Collins et al.*

BOOKS ET AL.

445 Arid lands, imperial ambitions

Desert knowledge exchange cloaked imperial goals, argues a political geographer *By P. Karimi*

446 Seller’s market

A pair of historians explain how market fundamentalism leads to science denial *By H. H. Thorp*

445



PHOTOS: (TOP TO BOTTOM) DAVID SALVADORI/WIPIC/ALAMY STOCK PHOTO; JOHNNYREIG/GETTY IMAGES

YOUR RESEARCH HAS ITS REWARDS.



Submit an essay by 3/15/23 to enter to win \$25K.

The prestigious international *Science* & PINS Prize is awarded annually to outstanding early-career researchers in the emerging field of neuromodulation. Findings already show improved outcomes in several neurological disorders. To enter, just write a 1000-word essay about your research performed in the last three years. The Grand Prize winner will be presented a US\$25,000 award, as well as have their essay published in *Science* magazine and on *Science* Online. A runner-up will have their essay published online. For additional inquiries, email SciencePINSPrize@aaas.org.



[SCIENCE.ORG/PINS](https://www.science.org/pins)

LETTERS

447 Protect seagrass meadows in China's waters

By J. Du et al.

447 Risks of China's increased forest area

By Y. Niu et al.

448 Invest in early-career researchers in Brazil

By T. B. Guedes et al.

RESEARCH

IN BRIEF

449 From *Science* and other journals

REVIEW

452 Plant science

The mechanics of plant morphogenesis

*E. Coen and D. J. Cosgrove*REVIEW SUMMARY; FOR FULL TEXT:
DOI.ORG/10.1126/SCIENCE.ADE8055

RESEARCH ARTICLES

453 Organic chemistryComputer-aided key step generation in alkaloid total synthesis *Y. Lin et al.***457 Wildfires**

Smoke-weather interaction affects extreme wildfires in diverse coastal regions

*X. Huang et al.***462 Volcanology**

The magmatic web beneath Hawai'i

J. D. Wilding et al.

PERSPECTIVE p. 434

468 Neuroscience

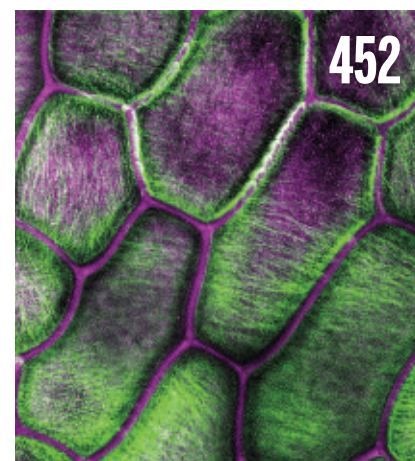
Suppressing feedback signals to visual cortex abolishes attentional modulation

*S. R. Debes and V. Dragoi***474 Ice structure**

Medium-density amorphous ice

*A. Rosu-Finsen et al.***478 Circadian rhythms**Sex-dimorphic and age-dependent organization of 24-hour gene expression rhythms in human *L. Talamanca et al.***484 Organic chemistry**Single-carbon atom transfer to α,β -unsaturated amides from N-heterocyclic carbenes *M. Kamitani et al.*

PERSPECTIVE p. 439

488 Flexible devicesLiquid metal-based soft, hermetic, and wireless-communicable seals for stretchable systems *Q. Shen et al.*

Distinctive cellulose fiber alignment (green) in the most recently deposited surface of multilayered cell walls (purple) in an epidermal peel of onion scale

494 Organic chemistryAsymmetric counteranion-directed photoredox catalysis *S. Das et al.***499 Batteries**A room temperature rechargeable Li_2O -based lithium-air battery enabled by a solid electrolyte *A. Kondori et al.*

PERSPECTIVE p. 436

DEPARTMENTS

419 Editorial

Revolt against educational rankings

By H. H. Thorp

510 Working Life

Losing, and finding, a home

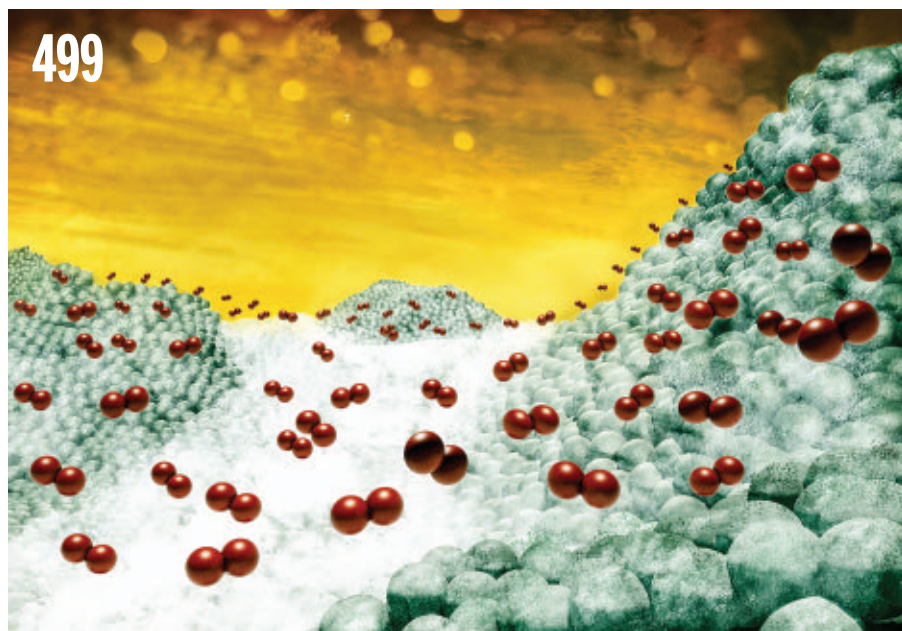
By B. A. Wanchisen and H. A. Schweingruber

ON THE COVER

Streams of lava erupted by Mauna Loa in December 2022 flow toward Mauna Kea on the horizon. As this photograph was taken, Mauna Loa's neighboring volcano Kilauea was experiencing an eruption of its own. Analysis

of small earthquakes detected deep beneath the surface revealed the details of Kilauea's and Mauna Loa's intertwined magma plumbing systems. See pages 434 and 462.

Photo: Mike Mezeul II

New Products.....506
Science Careers.....507

The illustration shows a solid electrolyte-cathode-air interface in a solid-state lithium-air battery, with the deposition of lithium oxide on the cathode surface.

SCIENCE (ISSN 0036-8075) is published weekly on Friday, except last week in December, by the American Association for the Advancement of Science, 1200 New York Avenue, NW, Washington, DC 20005. Periodicals mail postage (publication No. 484460) paid at Washington, DC, and additional mailing offices. Copyright © 2023 by the American Association for the Advancement of Science. The title SCIENCE is a registered trademark of the AAAS. Domestic individual membership, including subscription (12 months): \$165 (\$74 allocated to subscription). Domestic institutional subscription (51 issues): \$2411; Foreign postage extra: \$107. First class, airmail, student, and emeritus rates on request. Canadian rates with GST available upon request. GST #125488122. Publications Mail Agreement Number 1069624. Printed in the U.S.A.

Change of address: Allow 4 weeks, giving old and new addresses and 8-digit account number. **Postmaster:** Send change of address to AAAS, P.O. Box 96178, Washington, DC 20009-6178. **Single-copy sales:** \$15 each plus shipping and handling available from backissues.science.org; bulk rate on request. **Authorization to reproduce** material for internal or personal use under circumstances not falling within the fair use provisions of the Copyright Act can be obtained through the Copyright Clearance Center (CCC), www.copyright.com. The identification code for Science is 0036-8075. Science is indexed in the Reader's Guide to Periodical Literature and in several specialized indexes.

ANNOUNCING THE 2022 Swanson & META award winners



Lynwood W. Swanson Scientific Research Award

Dr. Kate Jackson
*Professor of Biology,
Whitman College*

Lynwood W. Swanson Scientific Research Award

Dr. Cara Wall-Scheffler
*Professor and Chair
of Biology, Seattle
Pacific University*

Lynwood W. Swanson Promise for Scientific Research Award

Dr. Margaret Metz
*Associate Professor of
Biology, Lewis and
Clark College*



Murdock Exemplary Teacher-Researcher Award

Ms. Elizabeth Beks
*Science Teacher,
North Pole High School*

We are honored to recognize the scientific accomplishments of these esteemed researchers.

Visit the page below
to read about each winner's
contributions to their fields:



murdocktrust.org/swanson-meta-2022



College Science Research
A MURDOCK TRUST PROGRAM



Partners in Science
A MURDOCK TRUST PROGRAM



M.J. Murdock
CHARITABLE TRUST

Where Science Gets Social.

AAAS.ORG/COMMUNITY



**Member
COMMUNITY**
AAAS

AMERICAN ASSOCIATION FOR THE ADVANCEMENT OF SCIENCE

Revolt against educational rankings

The ranking of universities and colleges at the national and global level is a well-known dubious practice. Flawed methodologies generate distorted and inaccurate profiles of these institutions. Yet, rankings have remained a popular and trusted measure of “the best” by the public. *U.S. News & World Report* has long had a stranglehold on US higher education. Using algorithms that process various measurements such as standardized test scores, alumni giving, and opinion surveys, it publishes annual ranked lists of undergraduate colleges as well as graduate, business, law, and medical schools. For too long, parents, politicians, and trustees have treated these lists with more importance than they deserve. That may be ending, as prestigious law and medical schools have started to walk away from this “evaluation.”

I spent 15 years in academic administration working under this tyranny. In a choice I later regretted, I voluntarily filled out meaningless surveys from *U.S. News* about the “reputation” of other institutions (questions like “Give every university a 1-5 ranking” or “Name the five most innovative universities”). I also endured meeting after meeting of trustees talking about how important it was for our university to “get ahead” of certain other universities (mostly the ones their friends went to). And I watched as Washington University in St. Louis School of Law sold its soul by trying to attract students with high entrance exam test scores through offers of financial aid, whether they needed it or not. It was an unsuccessful effort to get into *U.S. News*’s “T-14”—the top 14 law schools in the nation.

There are two obvious methodological problems with all of this. One is that the numerical rankings suffer from false precision. Is there really a difference between #10 and #11 in the undergraduate school rankings? Johns Hopkins University famously had a plan called “10 by 20” with the goal of getting to #10 by 2020. Hopkins is a great undergraduate institution—whether it’s #10 or #11 is meaningless, but it did indeed make it into the top 10 ahead of schedule, which no doubt delighted its trustees and students.

The other methodological problem is that rankings reward those schools that boost measurements by ad-

mitting students who have had the advantages of better pre-college education and test preparation coaching, and whose wealth will make them likely future donors. Equally worthy applicants without such resources lose out. Other aspects used in the measurements such as size of individual classes, faculty salaries, faculty-to-student ratio, and the amount of available financial aid also favor universities with vast financial endowments and income.

The good news is that in recent months, a reckoning has begun. Last September, Columbia University chose not to participate in the undergraduate rankings after an enterprising professor discovered that the school was fudging its own numbers. When Columbia’s data were corrected, it dropped from #2 to #18, allowing other colleges to inch up the list.

Two months later, law schools began pushing back. Yale and Harvard Law Schools announced that they would refuse to provide data to *U.S. News*, and several outstanding law schools followed suit. There are some excellent law schools, such as University of Chicago, Vanderbilt, and Washington University in St. Louis, that have stuck to participating in the rankings, no doubt because of pressure from their alumni, students, and trustees. When these schools inevi-

tably move up in rank because higher-ranked schools have dropped out, they will send out gleeful press releases about their new status.

This revolt against rankings has now begun in the world of science as the University of Pennsylvania, Harvard, Stanford, Columbia, and Washington University in St. Louis also recently moved against the medical school rankings. This is a great sign. Faculty at medical schools that haven’t dropped out yet should pressure their deans to follow suit. In announcing its decision, the dean of Washington University’s medical school said, “...it is time to stop participating in a system that does not serve our students or their future patients.”

There are many theories about how higher education in the United States lost its way. A reasonable hypothesis is that it started in 1983 when *U.S. News* published its first list. It’s been downhill ever since. Time to turn it around.

—H. Holden Thorp



H. Holden Thorp is Editor-in-Chief of the *Science* journals and is also a faculty member in the Department of Chemistry and in the School of Medicine at Washington University in St. Louis, St. Louis, MO, USA. hthorp@aaas.org; [@hholdenthorp](https://twitter.com/hholdenthorp)

“Is there really a difference between #10 and #11 in the undergraduate school rankings?”

IN BRIEF

Edited by Jeffrey Brainard

COVID-19

NIH oversight of EcoHealth grant rapped

A federal watchdog has found the U.S. National Institutes of Health (NIH) did not properly oversee a grant to the EcoHealth Alliance, a New York City-based nonprofit that funded work at the Wuhan Institute of Virology (WIV) in China. In 2020, then-President Donald Trump claimed SARS-CoV-2 could have come from the WIV lab, an idea that many scientists continue to say lacks evidence. Soon after, NIH terminated the EcoHealth grant, which had provided \$600,000 to WIV. The 18-month-long audit by the Office of Inspector General of the Department of Health and Human Services says NIH did not provide a valid reason for the termination or provide EcoHealth with required information for appealing the decision. The report also finds that "NIH did not effectively monitor or take timely action to address" problems with the project's compliance, such as a 2-year delay in a progress report from EcoHealth that described potentially risky virus experiments. And auditors concluded that EcoHealth's monitoring of WIV eroded once the pandemic started and that EcoHealth had overbilled \$90,000 in expenses on NIH grants totaling \$8 million from 2014 to 2021. EcoHealth responded that the audit "did not find significant issues" in its performance. NIH said it is improving its oversight.

Pandemic declaration extended

INFECTIOUS DISEASES | Three years after it started, the COVID-19 pandemic continues to be a Public Health Emergency of International Concern (PHEIC), the World Health Organization (WHO) declared this week. But a special emergency committee for the disease hinted that the designation—which gives WHO recommendations more heft and can influence travel and quarantine policies—might end later this year. Since WHO first declared COVID-19 a PHEIC on 30 January 2020, the panel has recommended 11 times to keep the designation in place. Although COVID-19 is causing fewer deaths now than 1 year ago, it "remains a dangerous infectious disease," the panel said, with more than 170,000 COVID-19-related deaths reported within the past

8 weeks, about 80,000 of them in China. The committee encouraged WHO to integrate SARS-CoV-2 surveillance into monitoring of influenza viruses. It asked the agency to assess how ending the PHEIC would affect the development and authorization of COVID-19 diagnostics, therapeutics, and vaccines. Separately, the administration of President Joe Biden said this week it will end the U.S. declaration of a national public health emergency in May. That policy has, for example, paid for COVID-19 testing and treatment for people lacking health insurance.

New official worries Iran scientists

LEADERSHIP | Many Iranian scientists are dismayed about the 17 January appointment of Abdolhossein Khosropanah, a

hardline conservative cleric, as the new secretary of the Supreme Council of the Cultural Revolution (SCCR). Among other responsibilities, SCCR elects university deans and the presidents of the Academy of Sciences and the Academy of Medical Sciences. As its secretary, Khosropanah, who succeeded a more moderate cleric, will not formally participate in decisions but can wield considerable informal power. Khosropanah has promoted unproven Islamic medicine against COVID-19—claiming it cured him three times—and has been accused of plagiarism.

China's R&D outlay surges again

FUNDING | China's expenditures on R&D rose 10.4% in 2022, to 3.09 trillion yuan (\$457 billion), the country's National Bureau of Statistics says. It was the seventh year in a row spending rose by 10% or more. In 2020, China's R&D spending was about 15% less than that of the United States.

Dolphins boost fishers' haul

ANIMAL BEHAVIOR | For more than a century, artisanal fishers in southern Brazil have worked alongside wild bottlenose dolphins in an unusual example of cooperative hunting. The dolphins chase a 40-centimeter-long fish called the Lebranche mullet (*Mugil liza*) toward shore, where fishers standing in shallow water toss their nets. Now, researchers



Fishers and dolphins work together to catch mullet at Praia da Tesoura in Laguna, Brazil.

PHOTO: FÁBIO DAURA-JORGE/FEDERAL UNIVERSITY OF SANTA CATARINA

SPACE FLIGHT

Nuclear rocket eyed for Mars trips

NASA and the Defense Advanced Research Projects Agency (DARPA) plan to launch and test a nuclear-powered rocket engine in space as soon as 2027, the agencies announced last week. Such engines promise higher thrust and efficiency than conventional ones, enabling faster travel times and bigger payloads for human missions to Mars, the agencies say. Although NASA has experimented with nuclear engines since the 1960s, none has been demonstrated in space. Powered by low-enriched uranium, the engine's fission reactor will heat and vaporize liquid propellants, shooting the gases out of a nozzle to provide thrust. NASA will provide the engine and DARPA the experimental spacecraft that will carry it. The design plans include a safety review.



A nuclear rocket engine could be two to five times more efficient than one using chemical propellants, supporters say.

have quantified the benefits for the fishers: They increase the odds of catching mullet 17-fold when they throw their nets in sync with the dolphins' predatory dives. These mammals use rapid-fire echolocation, a sign of hunting, when the fishers are casting. But this teamwork has become less common during the past 16 years as overfishing by artisanal and commercial fishers has reduced mullet populations, the scientists report this week in the *Proceedings of the National Academy of Sciences*.

Scientists' job joy stays strong

WORKPLACE | Job satisfaction in 2021 among U.S. scientists and engineers holding Ph.D.s matched the high levels recorded prepandemic, according to survey findings reported last week by the U.S. National Science Foundation. Across academe, government, and industry, between 89% and 95% of respondents said they were very or somewhat satisfied with their principal job, about the same levels as in 2019. Employment also stayed high, at about 85%. In 2021, 3% reported that COVID-19 influenced them to work only part time or not at all, for example because of pandemic-related family responsibilities, reduced hours, or layoffs, the Survey of Doctorate Recipients found.

Reports of Long Covid wane

PUBLIC HEALTH | Long Covid's prevalence among Americans who've had the virus is declining, a survey indicates. The new data come from the Household Pulse Survey, run by the U.S. Census Bureau; during the pandemic, it has added questions about COVID-19. The most recent results, analyzed last week by the Kaiser Family Foundation, showed that in June 2022, 19% of people who reported having had a bout of COVID-19 said they had Long Covid when they took the survey. By January, that number had dropped to 11%. The decline suggests at least some people are recovering from the chronic, disabling symptoms, such as fatigue and breathlessness, associated with Long Covid. It also suggests the risk of developing Long Covid may have dropped over time. Still, the U.S. prevalence is about 6%, as researchers study how to treat it.

Lander returns to research jobs

WORKPLACE | Eric Lander, who resigned in February 2022 as President Joe Biden's top science adviser after an investigation found he bullied subordinates, will resume academic research positions he held before starting that position. He had taken leave from the Broad Institute and faculty positions at Harvard University and

the Massachusetts Institute of Technology to work for the White House. The institute's director, Todd Golub, wrote Broad researchers last week that "we have high expectations for all Broadies to foster an inclusive culture of respect. ... Eric also deeply values this culture and is committed to upholding it."

Hallucinogen tackles depression

CLINICAL RESEARCH | The psychedelic compound dimethyltryptamine (DMT) has shown promise in treating major depressive disorder in an early stage trial, a drugmaker said last week in a press release. It is one of several hallucinogens medical researchers have been testing for mental disorders such as anxiety and post-traumatic stress disorder. The short duration of DMT-induced trips, lasting 20 minutes to 1 hour, may offer an alternative to longer treatment sessions needed with other psychedelics, such as psilocybin and LSD. In the DMT trial, half of the 34 participants received an active dose, the other half only a placebo; all also received supportive therapy. Using a standardized rating scale for major depression, researchers found those who received DMT showed a significant reduction in their symptoms at the end of 2 weeks compared with placebo, according to the firm Small Pharma, which made the test compound.



Biohazard suits protect scientists working with pathogens. New U.S. rules aim to protect the public.

IN DEPTH

SCIENCE & SECURITY

U.S. scientists brace for greater scrutiny of risky research

Expert panel recommends broader reviews of research involving pathogens or toxins that could have “dual use”

By Jocelyn Kaiser

Federally funded scientists who work with potentially harmful bacteria, viruses, and other agents could soon face a major expansion of U.S. government oversight. An expert group last week recommended broadening rules that require universities and funding agencies to determine whether proposed studies count as dual-use research—work that carries the risk of intentionally or accidentally creating a bioweapon. Currently, such reviews are only required for experiments involving 15 dangerous agents. But the panel argues the reviews should now extend to work with all human, plant, and animal pathogens, even those causing only mild disease.

Coming from the National Science Advisory Board for Biosecurity (NSABB), the recommendation reflects the heightened concern about biosafety and biosecurity catalyzed by the COVID-19 pandemic, which some allege originated from a laboratory in Wuhan, China. But the proposal has drawn fierce pushback from many researchers and even one NSABB member. Extending dual-use reviews to all disease-causing viruses, bacteria, and fungi is “a potential for disas-

ter” because it could hamstring even routine studies, warned NSABB panelist Mark Denison, a virologist at Vanderbilt University, at a 27 January meeting. The move and other policy changes could even hinder crucial work to fight pandemics, critics say.

NSABB’s chair, however, downplayed such concerns. “We ... suspect this will be a very small subset of research that would ultimately require a full [dual-use] review,” said Gerald Parker, a biosecurity expert at Texas A&M University, College Station. If funding agencies adopt the policy, he said, they will need to clarify how they plan to prevent it from hampering research.

The rules for managing “dual-use research of concern” (DURC) emerged after letters holding anthrax killed five people in the United States in 2001. Under 2012 and 2014 federal policies, researchers working with any of 15 “select agents,” including anthrax and Ebola virus, must decide whether a planned study falls into any of seven problematic categories. For example, if they plan to modify an agent to make it drug-resistant or more transmissible, institutional biosafety committees (IBCs) must report it to federal officials and include a risk management plan. (In rare cases, institutions have

decided the work won’t move forward.)

Such studies continued to stir concerns, however. In 2017, the Department of Health and Human Services (HHS) added review rules for a subset of DURC: “gain-of-function” studies that modify viruses such as severe acute respiratory syndrome and H5N1 avian influenza in ways that could make them more dangerous to humans. But HHS has only reviewed three experiments under this policy, known as Potential Pandemic Pathogen Care and Oversight (P3CO). Some scientists say these policies are too lax, and that the National Institutes of Health (NIH) has improperly exempted problematic studies, including some involving mpox and bat coronaviruses. In February 2022, NIH and the White House asked NSABB to revisit and harmonize the DURC and P3CO policies.

NSABB’s recommendation reflects longstanding concerns that limiting DURC reviews to a list of specific agents could miss high-risk studies. For example, the current policy does not cover reconstructing an extinct virus such as horsepox, a relative of smallpox. Some institutions already extend DURC reviews to all pathogen work.

Under the new proposal, local IBCs would review studies with any pathogen that fit the DURC criteria. They would also look for studies that fall under an expanded P3CO definition: any work that is “reasonably anticipated” to generate a pathogen that is likely to pose a “severe threat to public health,” even if it is only moderately transmissible or virulent. The P3CO policy would no longer exempt studies done for disease surveillance or vaccine development, but promises expedited review of such studies.

Many virologists worry the new reviews could delay work with relatively benign agents such as cold viruses, herpesviruses, and viruses modified to treat cancer. They fear the rules also could complicate basic studies that manipulate viruses to understand protein function. Denison and others note that deliberately creating viruses resistant to drugs is essential to developing antiviral treatments. “At the moment it looks like this would significantly slow down science,” says influenza virologist Seema Lakdawala of Emory University.

If NIH and other agencies adopt the rules—and it’s not clear when that might happen—NSABB recommends the government create a special office to help researchers comply. The panel also wants the policy to apply to privately funded research, but that could require a lengthy regulatory process or Congress to pass new laws. ■

PHOTO: CYDNEY SCOTT FOR BOSTON UNIVERSITY PHOTOGRAPHY

WORKFORCE

As some postdocs' pay rises, funding fears grow

Salary mandates in California and Washington leave many lab heads scrambling

By Katie Langin

Postdocs—the Ph.D.s who do much of the labor of science—are notoriously underpaid. But the problem has intensified over the past year as postdocs struggle to get by amid soaring inflation and professors report problems recruiting Ph.D. graduates to fill positions. Several institutions and states have recently implemented policies to increase their pay. But these policies haven't always come with an increase in funding, leaving lab leaders wondering how to cover rising staff costs and what the downstream effects will be. “I think a lot of faculty feel extremely trapped,” one professor says.

“This is much needed change; postdocs are simply not paid enough,” says Kelly Stevens, an associate professor of bio-engineering at the University of Washington, Seattle. In that state, a law went into effect in January stipulating that organizations with 51 or more employees must pay salaried employees at least \$65,478 per year; the National Institutes of Health (NIH) starting postdoc salary, which many institutions use as a baseline to set their postdoc pay, is \$54,840. But the new mandate puts lab leaders in a tough position, Stevens adds, because federal research grants haven't kept up with inflation and necessities such as lab supplies are also becoming pricier. “The money has to come from somewhere,” she says.

The push to raise pay is especially strong in high cost of living areas. In November 2022, the Massachusetts Institute of Technology (MIT) announced that, starting this year, the minimum postdoc salary will be \$65,000. In December, University of California (UC) postdocs won a new contract that will bring their minimum salary to \$71,490 by October 2026. And last week, Princeton University announced it will raise its minimum postdoc salary to \$65,000 in March.

These increased salaries are still a far cry from what Ph.D. graduates can make in many industry positions. But for those who want to stick with academia, the raises may help relieve some financial stress. “A postdoc has to earn a living wage,” says Benedict Borer, an environmental microbiologist and president of the MIT Postdoctoral Association. Before the recent raise at MIT, he adds, it had “become difficult for ... postdocs, especially postdocs with fam-

ily, to actually just get through the year.”

Professors contacted by *Science* agree. “The whole profession has to face up to, ‘Yeah, OK, we have all been collectively underpaying the postdocs,’” one says. “We have a selfish reason to want to pay them better,” another adds: “We want to be able to attract ... the best talent.”

But many of those faculty members are also left worrying who will foot the bill. MIT and Princeton have allocated temporary supplementary funding to cover the salary increases. UC, however, hasn't as of now provided additional funding. “Funding [for

to better support and retain postdocs, which it will issue later this year. At a December Advisory Committee to the Director meeting, acting NIH director Lawrence Tabak expressed optimism that the working group would come up with tangible solutions. “The current system ... is no longer sustainable,” he said. “It's very, very important that we lay out what the potential options are.” But solutions will not come easy, he added. “It is a zero-sum game ... so spending our way out of this, I think, is going to be complicated.”

Many of the professors *Science* spoke with hope Congress or state governments will



postdocs] is primarily provided by external grants from the federal government or private fellowships,” a university spokesperson wrote in an email to *Science*.

“Most people’s analysis is that we will just have to have smaller labs,” says Bassem Al-Sady, an associate professor of epigenetics at UC San Francisco. That’s fine for him personally—he likes the feel of a smaller lab and wants to pay his postdocs a wage that makes their lives “stress-free.” But he worries about what will happen down the line when faculty members in high cost of living areas go to renew their federal grant support and their application is compared with those from researchers who could afford to hire more lab members. “I wonder if it causes a disparity in competitiveness.”

NIH established a working group in November to come up with recommendations

commit additional funds to help address the problem. “To me, the answer is invest more money in [academic science], not shrink it,” a research institute executive and scientist told *Science* on the condition that she remain anonymous. She’s currently looking at her institution’s finances to determine how much it can afford to raise its postdoc salaries—and she hopes government agencies are doing the same. “What I would hope is that the government is feeling the urgency as much as we feel ... to find money somewhere.”

“There’s only so much funding you can ask individual faculty to obtain given scarce federal support,” Al-Sady adds. In December, he wrote to his state representatives to ask that more funding be set aside for California’s universities. “Please, please help us!” he wrote. “There is no place I would rather be, but I cannot do it without some support.” ■



ARCHAEOLOGY

Pot residues show how ancient Egyptians made a mummy

Analysis reveals the chemicals applied to corpses in a 2700-year-old mummification workshop

By **Andrew Curry**

For the ancient Egyptians, mummification was a spiritual process imbued with deep meaning. Ancient texts show it took 70 days, with carefully defined rituals and invocations, to prepare the deceased for an eternal afterlife. It also required specialized skills, long lists of ingredients, and a professional class of embalmers steeped in religious and chemical knowledge.

But what went into—or was smeared on, brushed over, and wrapped around—the mummified bodies themselves has been mostly guesswork on the part of modern scholars. “There’s almost no textual evidence,” says Philipp Stockhammer, an archaeologist at the Ludwig Maximilian University of Munich. “How this worked, how the substances were mixed, how they were named—this wasn’t known.”

That changes with a study Stockhammer and his colleagues published this week in *Nature*. By identifying residues from labeled jars

found in an ancient Egyptian mummification workshop, the researchers were able to show the process involved complex chemistry and exotic ingredients, including resins sourced from a continent away. “You can actually look into the vessels and see what’s still inside,” says Barbara Huber, an archaeological scientist at the Max Planck Institute for Geoanthropology who was not involved with the research.

The new evidence emerged from a 2700-year-old (664 B.C.E.–525 B.C.E.) burial complex south of Cairo called Saqqara. In 2016, University of Tübingen archaeologist Ramadan Hussein, who died in the spring of 2022, identified shallow aboveground

pits where the dead would have been covered in natron, a salt mixture used to dry out the body after death. Partway down a nearby shaft was an underground chamber outfitted with flat stone niches for corpses—a workshop for mummifiers. “It’s the first physical evidence for the places where they worked,” says University of York archaeochemist Stephen Buckley. At the very



The label on a jar from a mummification workshop read “to be put upon his head.”

Embalming a body in ancient Egypt combined ritual, chemistry, and ingredients from distant sources.

bottom of the shaft, 30 meters down, were burial chambers.

A body that began the mummification process at the top of the “funeral home” could have been buried directly below, presumably after spending a few weeks being prepared in the underground chamber. “It was a protoindustrial mummification workshop for the upper class,” Stockhammer says.

The shaft had been carefully filled with sand, rocks—and dozens of embalming vessels that seemed to have been ritually disposed of after workers had used them. “They turned it into a hiding place for the tools,” Hussein said in an interview before his death. “We found cups, bowls, plates, and incense burners inscribed with the names of oils and substances used for embalming.”

The researchers used a dentist’s drill to remove coin-size fragments a few millimeters thick from the inside of the containers, then analyzed their chemical makeup using gas chromatography-mass spectrometry. Earlier studies had analyzed mummies from museum collections and identified embalming chemicals including tree resins and bitumen. But this is the first to examine vessels found in the context of a mummification workshop.

The analysis revealed traces of animal fats, beeswax, vegetable oils, and bitumen along with multiple plant resins—ingredients that were probably mixed and heated to form ointments. Their properties made them particularly easy to recover from pottery vessels, even after thousands of years. “The more fatty and sticky a residue is, the better results you get,” Stockhammer says. “We had good organic preservation, and we had residues that preserve well.”

After being immersed in natron, corpses were treated with the sticky mixtures to seal the skin, blocking decay and decomposition by bacteria. “The materials we found have an antibacterial function,” Stockhammer says. “It’s the most complicated part of the process, where the chemistry really starts.” Some ointments may have been smeared directly on the corpses; others were probably applied to the linen bandages, which may have been dipped directly into wide-mouthed “goldfish bowl” vessels.

Some of the bowls still had stains on the outside from spills and dripping mummy wrappings. Many also bore labels naming specific ingredients—*antiu* or *sefet*—or giving more general descriptions, like “to make his odor pleasant” and “treatment of the head.” “For the first time, you have a direct correlation between text and a spe-

cific residue,” Huber says. “I don’t know if there’s a better case study than having them all together.”

The finds may require reassessment of ancient Egyptian texts. The word *antiu*, for example, appears thousands of times in Egyptian sources, and for more than a century Egyptologists have thought it referred to myrrh, the resin of a particular thorn tree. But vessels labeled *antiu* at the mummification workshop contained other substances—most notably cedar, sourced at the time from the mountains of Lebanon. “Possibly *antiu* is just a generic word for resin,” Hussein said before his death. *Sefet*, described as one of the “seven sacred oils” in many ancient texts, turned out to be a mixture of cypress or juniper resin and animal fat.

The researchers also identified more exotic ingredients, including dammar and elemi, resins extracted from hardwoods native to Southeast Asian rainforests thousands of kilometers from ancient Egypt. Cedar and pistachio, meanwhile, were sourced from around the Mediterranean, and pitch from the Dead Sea. “Almost all the things embalmers needed came from outside Egypt,” Stockhamer says. “And you need a lot of this to mummify and embalm, not just a few grams. Even if it’s just a few thousand individuals a year who are high-status enough to be mummified, it’s still a lot of material. Mummification drove globalization.”

The substances themselves may have been selected precisely because they were hard to get. “Some of the materials may have been used not because they were more effective, but because they were exotic—‘Look at the size of my world, that I can get something from so far away,’” Buckley says.

Some scientists caution that the mummification compounds could have degraded and changed over time, throwing off the analysis. “They may have gone a little too far in the interpretation,” says Kate Fulcher, a heritage scientist at the British Museum. “No one’s done a controlled experiment where we’ve aged resin for 3000 years and seen how it’s deteriorated—we don’t know how these [chemical compounds] look after all this time.”

But the chemical artistry behind the pot residues is unmistakable, reflecting precise knowledge of ingredients, temperatures, and cooking times won over hundreds, if not thousands, of years. Ancient Egyptians “spent more than 2000 years trying to perfect the preservation of the human body—that’s 2000 years trying to perfect their workflow,” Stockhamer says. “The chemical knowledge they must have had in this workshop was amazing.” ■

COVID-19

New COVID-19 vaccine strategy would mimic flu’s annual shots

Scientists and regulators seek new course amid uncertainty

By Jennifer Couzin-Frankel

COVERID-19 vaccination in the United States is set to change this year. The Food and Drug Administration (FDA) is planning a shift toward a single booster shot, administered in the fall, like the strategy used for influenza. Members of an FDA vaccine advisory panel meeting last week generally endorsed the idea and also said all COVID-19 vaccines should have the same composition going forward. Today, the initial shots are based on the virus that emerged in Wuhan, China, in 2019, whereas most boosters also target the Omicron variant.

Yet many important questions remain. It’s not clear whether a COVID-19 booster can protect for a full year, whether some vaccinated people who have also been infected with COVID-19 could wait longer, or which variants the annual shot should target. Nor is it clear how many people would embrace another booster. “Where are we headed?” Jerry Weir of FDA’s Office of Vaccines Research and Review asked at the 26 January meeting. “I don’t know, but we just follow the data we have.”

Science asked researchers to weigh in on some of the most urgent questions.

Q: What are the pros and cons of an annual booster—the influenza strategy?

A: The influenza vaccine consists of an annual dose tailored to flu strains expected to circulate next winter. FDA officials say they anticipate something similar for COVID-19: assessing strains “at least annually” and conferring with advisers in early June to settle on the makeup of a fall vaccine. (Executives at vaccinemakers Pfizer and Moderna said that schedule would pose no problem; Novavax would want to know the strain around March, a company official said.) Many researchers agree the regimen is less cumbersome and confusing than multiple boosters per year, and it makes sense to “vaccinate with the circulating variants,” says immunologist Rafi Ahmed, director of the Emory Vaccine Center.

But flu is seasonal, Ahmed and others note, whereas the coronavirus circulates year-round. People who contract COVID-19 in August—which is vanishingly rare for flu—would have to decide whether to also take a shot in the fall, when their immunity may still be robust. It’s also unclear whether an annual booster offers everyone enough protection for a whole year. The durability question “is a big one,” says immunologist Jennifer Gommerman of the University of Toronto. FDA indicated it might recommend two doses for the elderly, the immunocompromised, and children who’ve had fewer than two doses.

More data could help bolster—or weaken—the case for a once-a-year vaccine.

Because the current vaccines are especially protective against severe disease, it’s crucial for the U.S. Centers for Disease Control and Prevention (CDC) “to tell us exactly who’s getting hospitalized and dying from the virus,” panel member Paul Offit, an infectious disease specialist at the Children’s Hospital of Philadelphia, said at the meeting. Offit craves details on patients’ ages, whether and how their immune system is compromised, and whether they received antiviral medications. “Only then can we make the decision about who gets vaccinated, with what, and when.” Bruce Gellin, a global public health specialist at the Rockefeller Foundation, added a caveat as well: “This is not influenza, and we need to keep paying attention to that to make sure we don’t just follow that dogma.”

Q: How should the annual vaccine recipe be picked?

A: The FDA panel voted to give all of the vaccines the same composition, which for now means the current boosters’ “bivalent” formulation, evenly split between vaccine targeting the Wuhan strain and Omicron subvariants BA.4 and BA.5.

When the plan for a bivalent booster was agreed on in June 2022, it was something of a hedge: Although the original Wuhan variant was long gone, FDA advisers worried an Omicron-only vaccine would be less effective against an entirely new SARS-CoV-2 variant that might emerge. The advisers also hesitated then

to modify the primary two-dose series.

Because there were no human studies of the BA.4/BA.5 bivalent vaccine at the time, FDA relied on limited human data on vaccines containing an earlier version of Omicron, BA.1, and mouse data on a BA.4/BA.5 bivalent. There were “theoretical reasons why it was a good reason to switch the variant, without a lot of solid science, in my view,” says Philip Krause, who recently stepped down as FDA’s deputy chief of vaccines. The “bivalent was authorized awfully quickly,” says Columbia University virologist David Ho.

By now, some studies, including one last week from CDC, have shown the bivalent vaccine generates somewhat higher antibody levels and disease protection than the original shot. Other groups, including Ho’s team, have reported no difference. Ho speculates that including the ancestral strain makes it more difficult for the immune system to ramp up against Omicron. He hopes any new switch will be based on more solid data.

At the meeting, advisers also said they would like more data about the vaccines in babies and young toddlers. Pfizer presented bivalent vaccine data that included just 24 children under the age of 2; the company said more is on the way. Moderna is beginning a study of its bivalent shot in 3- to 5-month-olds. Advisers wondered whether the companies should test different doses and different intervals between doses in young children, especially because those under age 1 are at a higher risk of severe COVID-19 than older kids.

Q: By now, most people have had COVID-19 at least once, in addition to vaccine doses. Does this enhance protection?

A: Multiple studies suggest “hybrid immunity”—from both vaccines and infec-

tions—is a sturdier shield against infection, and especially against severe disease, than infection or vaccination alone. In January, a meta-analysis of 26 studies, published in *The Lancet Infectious Diseases*, found that 1 year after vaccination, hybrid immunity conferred about 42% protection from infection in adult populations and a whopping 97% protection from hospital admission or severe illness. (The study reported that this was better protection than from infection or vaccination alone.) People with hybrid immunity, the authors noted, “might be able to extend the period before booster vaccinations are needed compared to individuals who have never been infected.” But how hybrid immunity should play into vaccine recommendations remains uncertain.

Q: Will people take more boosters?

A: Maybe, maybe not. Vaccine uptake has slid with each successive booster offering. Currently, only 15% of the U.S. population—and 40% of those 65 and older—has received the bivalent shot. By comparison, about half the population gets a flu vaccine annually, including about three-quarters of those 65 and up. People eschewing boosters aren’t just “the antivaxxers, it’s a whole portion of the population,” many of whom got the primary vaccine series, says Mark Slifka, an immunologist at Oregon Health and Science University.

The immediate side effects of the messenger RNA (mRNA) vaccines—which can cause flulike illness for a day or two—may deter people, he says. Public confusion over how well boosters work or how necessary they are is also fueling hesitancy, a CDC survey reported last month. FDA and CDC officials hope simplifying the regimen by offering just a single annual shot will attract more takers.

Q: Might non-mRNA vaccines improve uptake or offer other benefits?

A: Several advisers to FDA worried last week’s meeting focused too heavily on the mRNA shots—today’s dominant technology. “I don’t want this meeting to be hijacked by mRNA vaccines,” said Pamela McInnes, a retired deputy director of the National Center for Advancing Translational Sciences.

Alternatives to mRNA technology might appeal to some people, especially if they have fewer side effects or offer better protection. Novavax’s vaccine uses a combination of viral proteins and an adjuvant that boosts the immune response—a classic combination also used in other vaccines that often yields durable protection. But real-world studies of Novavax’s vaccine have been limited, and its uptake has been disappointing in European countries. In the United States, the vaccine is only authorized for the unvaccinated and those who haven’t gotten any boosters. Its limited availability is unfortunate, says Stanford University immunologist Bali Pulendran: “I would have liked to have had that choice myself.”

Q: COVID-19 vaccines offer limited protection against infection. Could nasal vaccines be a solution?

A: A vaccine highly protective against infection would be ideal. Even mild COVID-19 still carries a risk of Long Covid, infections remain disruptive, and rampant transmission risks creating new and more hazardous variants. “It’s the infections right now that are important,” says Charlotte Thålin, a physician and immunology researcher at the Karolinska Institute. “That’s what causes the virus to mutate.”

Some researchers believe nasal vaccines, which aim to induce immunity at mucous membranes, might fit the bill. Thålin has found intriguing clues in a study that has documented vaccinations and infections in 2000 health care workers in Sweden since April 2020. In September 2022, she and her colleagues reported that people who were infected early in the pandemic, before they were vaccinated, had detectable levels of SARS-CoV-2-specific antibodies of a type named IgA in their noses; those in the vaccine-only group did not. Thålin thinks nasal vaccines would be more effective than current shots at stimulating such antibodies, which might block COVID-19 infections right where they start, in the respiratory tract.

“There’s a public health need for next-generation vaccines,” John Beigel of the National Institute of Allergy and Infectious Diseases told meeting attendees. Infection and transmission, he said, “are the outcomes that are increasingly important.” ■



U.S. officials hope simplifying the COVID-19 vaccine strategy will help persuade more people to take the shots.

PHOTO: HANS GUTKNECHT/MEDIA NEWS GROUP/LOS ANGELES DAILY NEWS VIA GETTY IMAGES

Protein decoys may battle COVID-19 and more

Drugs designed to resemble viruses' cellular targets move into clinical trials

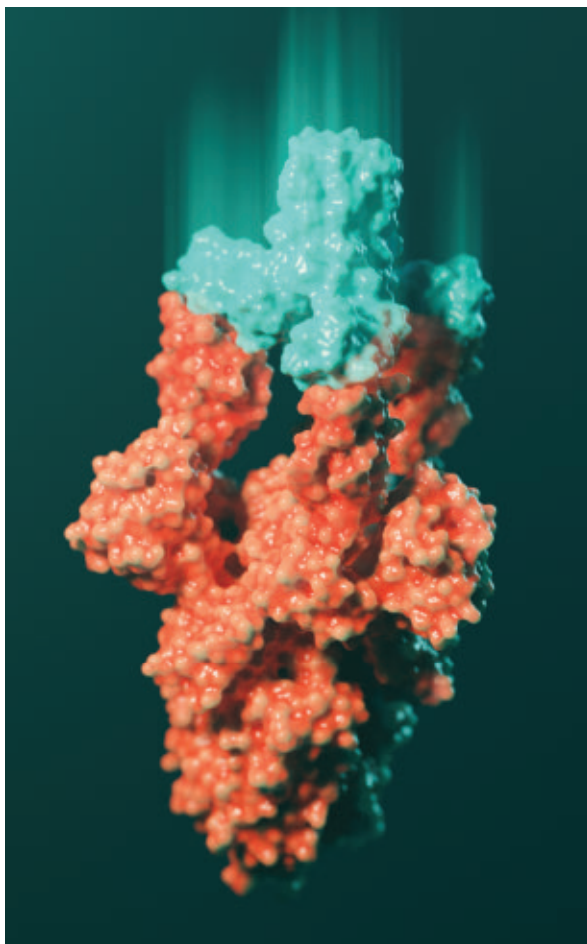
By Robert F. Service

As the fight against COVID-19 wears on and the virus continues to mutate, vaccines and monoclonal antibody drugs are losing some of their punch. That's added urgency to a strategy for preventing and treating the disease that, in theory, could stop all variants of SARS-CoV-2. The idea is to flood the body with proteins that mimic the angiotensin-converting enzyme 2 (ACE2) receptor, the cell-surface protein that coronavirus uses to gain entry into cells. These decoys would bind to SARS-CoV-2's spike protein, disarming it. The molecules might both protect people from getting infected and help COVID-19 patients clear the virus from the body.

One ACE2 decoy recently completed initial safety trials in humans, and trials of other decoy designs are expected to launch soon. A new preprint also shows that giving mice a gene coding for a decoy can provide long-term protection, a strategy that might help millions of immune-compromised people who are unable to mount a robust immune response to vaccines. Success against COVID-19 might also boost efforts to develop decoys against other infectious diseases ranging from influenza to Ebola.

"These [compounds] could be a game changer," says Erik Procko, a biochemist at Cyrus Biotechnology, a Seattle-based biotech company working to commercialize decoys to fight SARS-CoV-2 and human cytomegalovirus.

The decoy strategy was investigated during the outbreak of severe acute respiratory syndrome (SARS) 2 decades ago. In 2005, Josef Penninger, a molecular biologist then at the Institute of Molecular Biology in Vienna, and his colleagues discovered that the SARS coronavirus, a SARS-CoV-2 relative, binds to ACE2 in mice. The receptor protein normally helps regulate blood pressure and other metabolic processes, but it can also contribute to conditions such as lung failure.



A compact protein (blue) that binds all three receptor-binding domains on SARS-CoV-2's spike (red) may stymie the virus from entering cells.

Penninger's team synthesized just the part of ACE2 that protrudes above the cell surface and is exposed to the virus. They showed that the decoy partially protected mice from lung failure and other symptoms driven by ACE2 dysfunction. But they didn't have time to test their decoy on animals with SARS before the original outbreak fizzled out.

When SARS-CoV-2 made its appearance in late 2019, Penninger, now at the University of British Columbia, Vancouver, and his colleagues jumped back in. After his team and others showed that ACE2 was the target for SARS-CoV-2 as well, they pulled their decoys off the shelf. The molecules proved effective against SARS-CoV-2 infection in cell cultures and in mice, and Penninger licensed the strategy to APEIRON Biolog-

ics, an Austrian company he had previously founded.

It organized small human trials of an injected form of the ACE2 decoy. The protein was shown to be safe—notably it did not trigger blood pressure anomalies or other metabolic issues—but it had little effect in reducing the severity of COVID-19. Penninger argues this was likely because it was given to patients relatively late in their disease. The company is now pursuing a version that can be inhaled and last year concluded an initial safety study in humans. Though the company has yet to publish the results, Penninger, who has seen the data, says, "There's no reason not to move [the compound] forward," as either a treatment if given early enough, or as a preventive.

Other groups also jumped on the decoy idea, creating novel versions designed to last longer in the body and bind more tightly to the virus' spike protein, reducing the needed dose. In 2020, for example, researchers led by David Baker, a protein designer at the University of Washington (UW), Seattle, engineered a decoy made up of three copies of the ACE2-binding region, matching the three-part symmetry of ACE2 on cell membranes (*Science*, 9 September 2020, p. 426).

Tests on cells and mice challenged with SARS-CoV-2 showed the decoys were highly effective at blocking infection. Baker's team has since partnered with a South Korean startup called SK Bioscience, which says it plans to begin human safety tests later this year.

Procko, a former postdoc in Baker's lab who moved to the University of Illinois (UI), Urbana-Champaign, in 2014, took a different tack. Following a long-used strategy for increasing the potency of antibody-based drugs, Procko and his colleagues linked the so-called Fc region from a human antibody to an ACE2 decoy. The Fc region caused it to form pairs, which bind more tightly to the spike protein (*Science*, 4 August 2020, p. 1261). Procko and his colleagues also mutated their decoys to further increase their binding strength

and prevent them from cutting other proteins, part of ACE2's natural function. The changes proved so effective at protecting mice from SARS-CoV-2, Procko says, that he left UI and joined Cyrus, which plans to launch a clinical trial of the compound.

Now, Nathaniel Landau, a microbiologist at New York University (NYU), and his colleagues have posted results showing a decoy similar to Procko's protected mice against infection by many of the latest Omicron variants of SARS-CoV-2, which have evolved to evade antibody drugs that work against the original virus. Researchers think the decoys, in contrast, are unlikely to lose their potency. If SARS-CoV-2 does evolve to prevent decoys from binding, the virus' own ability to bind to and infect cells will probably suffer as well. "It puts the viruses in checkmate," says Landau, who published the findings in a 2 January preprint on bioRxiv.

The NYU team also went a step further. The body would quickly break down a dose of inhaled or injected decoys. But in a second preprint posted on 12 January on bioRxiv the researchers reported they'd packaged a gene for the decoy into viruses commonly used as "vectors" to deliver disease-treating genes. Injecting a small dose into mice, they showed the vectors infected muscle cells, causing them to churn out the decoy, which then protected the animals from infection for up to 2 months.

Landau acknowledges that regulators aren't likely to approve gene therapy targeting SARS-CoV-2 in otherwise healthy people. However, he adds, "It could be extremely useful for immunocompromised people who can't generate an effective immune response" to either a natural infection or a vaccine. Guangping Gao, a gene therapy expert at the University of Massachusetts Chan Medical School, agrees, saying, "This project has great potential." Others note, however, that the immune system often fights off viral vectors, which could limit the effectiveness of the approach for preventing COVID-19.

However they're delivered, using decoys to stymie SARS-CoV-2 could be just the beginning. Baker's UW colleague Lauren Carter, a pharmaceutical bioengineer at the university's Institute for Protein Design, notes that Baker's group and others are already designing decoys to fight mpox, influenza, Ebola and even HIV—previous efforts to deceive the AIDS virus this way failed in clinical trials but there is new optimism about improved decoys for it.

"This could be the avant-garde of pandemic prevention," she says. "All we need is the structure [of a viral target] to design against." ■

PALEOANTHROPOLOGY

Neanderthals lived in groups big enough to eat giant elephants

Meat from the butchered beasts would have fed hundreds

By Andrew Curry

On the muddy shores of a lake in east-central Germany, Neanderthals gathered some 125,000 years ago to butcher massive elephants. With sharp stone tools, they harvested up to 4 tons of flesh from each animal, according to a study that is casting these ancient human relatives in a new light. The degree of organization required to carry out the butchery—and the sheer quantity of food it provided—suggests Neanderthals could form much larger social groups than previously thought.

The find comes from a trove of animal bones and stone tools uncovered in the 1980s by coal miners near the town of Neumark-Nord. The finds date to a relatively warm period in Europe known as the Eemian interglacial, 75,000 years before modern humans arrived in Western Europe. They include the bones and tusks of more than 70 mostly adult male straight-tusked elephants (*Palaeoloxodon antiquus*), an extinct species almost twice the size of modern African elephants that stood nearly 4 meters tall at the shoulder. Most had been left in dozens of piles along the ancient lakeshore over the course of about 300 years.

"We wondered, 'What the hell are 70 elephants doing there?'" says Lutz Kindler, an archaeozoologist at the MONREPOS Archaeological Research Center.

To find out, he and his colleague Sabine Gaudzinski-Windheuser, also an archaeozoologist at MONREPOS, spent months examining the 3400 elephant bones, which are now stored in a warehouse. Some weighed dozens of kilograms and required a forklift to move. Under a microscope, Gaudzinski-Windheuser says, nearly every bone showed signs of butchery.

Although Neanderthals were known to be capable hunters, these cutmarks "seem to be the first evidence of large-scale elephant hunting," says April Nowell, an archaeologist at the University of Victoria who was not involved with the research.

Gouges and scratches on nearly every bone show the butchers were thorough in their slaughter. "They really went for every scrap of meat and fat," says University of Leiden archaeologist and study co-author Wil Roebroeks. The bones hadn't been gnawed by scavengers like wolves or hyenas, suggesting nothing was left for them.

The meat from a single elephant would have been enough to feed 350 people for a week, or 100 people for a month, the researchers calculate. In the past, Neanderthals were thought to live in small, highly mobile groups of about 20 individuals at most, but the elephant bounty suggests far bigger groups—big enough to slaughter and process an entire elephant and big enough to consume it—once lived near the

site, the researchers report this week in *Science Advances*. "This is really hard and time-consuming work," Kindler says. "Why would you slaughter the whole elephant if you're going to waste half the portions?"

The researchers "make a good case these huge food packages mean much larger groups," says University of Reading archaeologist Annemieke Milks, who was not involved in the research. "Maybe it's a large, seasonal gathering, or they're

storing food—or both."

Nowell agrees, adding that felling an elephant must have required careful orchestration. The hunters likely singled out adult males, which roam alone without the protection of a female-led herd. "It would necessitate a high level of competence in sequencing and planning out the hunt and coordinating everybody."

That doesn't mean Neanderthals always lived and worked in large groups. But the results, like other recent findings, show these archaic humans were more sophisticated than once assumed. "If one regional group of Neanderthals was capable of such behavior, other groups elsewhere surely would have been capable, too," says retired University of Nevada, Reno, archaeologist Gary Haynes. "This lets us imagine Neanderthals as more like modern humans rather than as humanoid brutes, as they once were interpreted." ■

"Why would you slaughter the whole elephant if you're going to waste half the portions?"

Lutz Kindler,

MONREPOS Archaeological Research Center

BREATHLESS OCEANS

Warming oceans are running short of oxygen, and the fiercest marine predators are already feeling the effects

By **Warren Cornwall**, off the Canary Islands in Spain



Sometimes salvation arrives in the darkest hours. After nearly 4 days and nights of futility, the cry came from the back of the small fishing boat 3 hours after sunset. “Azul! Azul! Azul!”

Rayco Garcia Habas stood at the railing near the stern, straining against the fishing rod as a mas-

sive fish—a blue (*azul*) shark, he was sure—tugged it toward the dark Atlantic waters. He looked over his shoulder at a watching team of biologists, grinned, and called out “*Cervezas! Cervezas!*”

The beers (*cervezas*) would have to wait. First, this champion spearfisher-turned-fishing guide for scientists would need to reel in whatever was at the other end of the

A captured blue shark will be fitted with sensors to study how low ocean oxygen affects its behavior.

line. Then, the scientists would have to drag the shark—if it was a shark—to the boat’s side, drill two holes in its dorsal fin, and attach a device resembling an oversize neon orange lightbulb.

If all went well, within minutes the shark



Off Gran Canaria, one of the Canary Islands, a small fishing boat carried a team of scientists hoping to tag sharks swimming toward an expanding low-oxygen zone.

would return to the waters off the southern tip of Gran Canaria, an island 210 kilometers west of the Moroccan coast. The device it now carried would record every twitch of its scythe-shaped tail, every dive into the twilight depths, every current through which it swam. Its journey would offer a window into an unsettling environmental trend, called ocean deoxygenation, that is affecting marine life, including some of the sea's most potent predators.

Climate change is leaching oxygen from the ocean by warming surface waters. Two other climate-related threats to the seas—ocean acidification and marine heat waves—get more attention from scientists and the public. But some researchers believe deoxygenation could ultimately pose a more significant threat, making vast swaths of ocean less hospitable to sea life, altering ecosystems, and pushing valuable fisheries into unfamiliar waters. As global warming continues, the problem is sure to get worse, with disturbing forecasts that by 2100 ocean oxygen could decline by as much as 20%. Sharks—fast-moving fish that burn lots of oxygen, sit at the top of food chains and crisscross huge ocean expanses—should be sensitive indicators of the effects.

This is why a group of U.K. and Portuguese scientists took to the sea aboard Garcia Habas's boat in November 2022. His announcement of a shark on the line jolted them into action. Knee pads were tightened. Hands slid back inside gloves removed after

a false alarm an hour earlier. "Finally!" said David Sims, the bearded marine biologist heading the expedition.

SIMS, FROM THE U.K. Marine Biological Association and the University of Southampton, has experienced his share of drama, disappointment, and occasional comedy over 3 decades of studying sharks. He's donned a chainmail suit to swim with 3-meter bull sharks. He once led a boat in hot pursuit of what he thought was a school bus-size basking shark—only to find the wake he was following came from a lone salmon. He tangled with a feisty catshark that sprang from the water and latched onto his flashlight. The lanky 53-year-old recounts these tales with a delight seemingly undiminished since, as a young child, he was enchanted by sharks that washed up on the beaches near his home on England's southeast coast.

Sims first noticed a link between shark behavior and oxygen levels in the early 2000s. He and several friends had spent years deciphering the feeding and mating habits of small-spotted catsharks, meter-long, cream-colored fish with cartoonishly large eyes. They worked in an inlet on the southwest Irish coast, where the deeper waters grew stagnant over the summer. When Sims looked at data from tracking tags attached to the sharks, he saw the fish swam closer to the surface in summer, skirting a pocket of low oxygen. "It was really a classic case of decreasing oxygen clearly displacing

the sharks from where they wanted to be," Sims says.

The discovery was just a footnote in his catshark work. But the observation came back to him around 2011, when he was tracking blue and shortfin mako sharks traversing the eastern side of the Atlantic Ocean. After affixing satellite-connected tags to a handful of the fish, he was mystified when the sharks seemed drawn to a large patch of water where northwest Africa bulges into the Atlantic, a region known to be low in oxygen. These open-ocean sharks are the Olympic sprinters of the marine world—makos are capable of bursts of up to 35 kilometers per hour. Why would they head toward places with less oxygen? And what could it mean for the future of marine life as vast stretches of low-oxygen water grow bigger around the world?

SCIENTISTS FOR YEARS have documented oxygen-starved dead zones in places like the Gulf of Mexico and the Baltic Sea. There, pollution from nutrients running off the land, such as synthetic fertilizer, sparks algae blooms. Microbes feast on the rotting vegetation, consuming oxygen. A surge of low-oxygen water can flood an area so quickly that crabs, sea stars, and even fish suffocate before they escape. Low-oxygen zones also form naturally along the western edges of the Americas and Africa, where oxygen-depleted water that hasn't seen daylight for decades wells up.

In the open ocean, currents and storms churn the water, keeping oxygen levels higher. Yet since the 1990s climate models have foretold that a warming climate would deplete oxygen there, too. Surface water warmed by rising air temperatures holds less oxygen, and the growing temperature contrast between surface layers and colder, deeper water slows the mixing that transports oxygen into the depths. At higher latitudes, melting ice can flood surface layers with fresh, low-density meltwater, strengthening the layering and reducing mixing.

In 2008, a paper in *Science* sounded the alarm. German and U.S. scientists found that the low-oxygen zones off Africa and the Americas were growing deeper and losing still more oxygen. Since the 1960s these areas had expanded by about 4.5 million square kilometers, close to the area of the European Union. In the waters frequented by Sims's sharks off Africa's northwest coast, the low-oxygen layer had nearly doubled in thickness over 5 decades, from 370 meters to 690 meters. By 2008 its top had risen to less than 150 meters below the surface. The global trend, the scientists warned, "may have dramatic consequences for ecosystems and coastal economies."

In 2017, scientists delivered more troubling news in *Nature*. Overall, the world's oceans had already lost some 2% of their oxygen since 1960, roughly double what climate models predicted.

For Andreas Oschlies, a biogeochemist at the GEOMAR Helmholtz Centre for Ocean Research Kiel and a leading expert on modeling oxygen in the ocean, the implications were staggering. If the trend continues, it could mean a potential loss of 20% by 2100, he says. That's equal to going from sea level to more than 2000 meters elevation on land. "I thought 'Wow!'" Oschlies recalls. "That's the biggest change and maybe the most worrying change that we see in the ocean. Immediately I thought of (past) major extinction events." For example, at the end of the Permian period 256 million years ago, rising ocean temperatures and an 80% plunge in oxygen levels helped drive the largest extinction in Earth's history. Up to 96% of all marine species disappeared.

By comparison, the 2% drop in oxygen levels seen so far might not sound like much. But global averages can be misleading, warns Lisa Levin, a biological

oceanographer at the Scripps Institution of Oceanography who has studied the effects of low oxygen on ocean ecosystems for more than 30 years. "There are places in the ocean where there's been much bigger declines," Levin says. "These changes are probably very important."

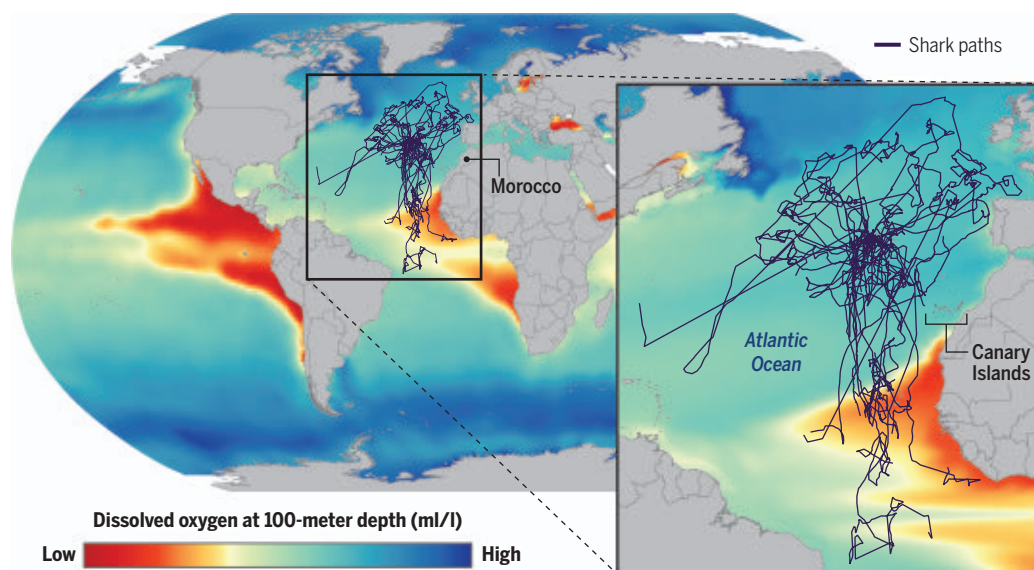
OFF THE COAST OF OREGON, fishers in 2002 began pulling up traps full of suffocated crabs. Low oxygen levels are routine in those waters, which are fed by a deep, oxygen-depleted current from the North Pacific Ocean that wells up near the coast. Nutrients in the upwelling make the area a fertile fishing ground. They also nourish algae that deplete oxygen even further as they decay.

rarily deplete oxygen in a patch of ocean. But this decline looks unlikely to relent. Oxygen levels have dropped steadily, by 30% over the past half-century, in the current that washes the Oregon coast. At the same time, coastal winds that drive the upwelling have strengthened, possibly because of rising land temperatures. Jack Barth, an OSU oceanographer, wonders whether oxygen in the region will drop by another one-third in the next 50 years. "That's what's a little scary," he says.

Even if falling oxygen doesn't kill marine animals, it can affect them in myriad ways. It can interfere with fish hormones crucial to reproduction, stunt growth in young fish, weaken immune systems, and even strike animals blind. "We have species off of southern California that are fairly sus-

Sea changes

Low-oxygen zones that form where currents concentrate depleted water along the western edges of continents have grown over the past half-century. Migratory blue and shortfin mako sharks tagged with tracking devices showed a preference for a large patch of low-oxygen water off the northwest coast of Africa, perhaps because it confines their prey in shallower waters.



But 2002 was extreme. Scientists found oxygen levels had fallen by 65%, compared with historical averages, in more than 800 square kilometers of coastal waters. "I thought it was just a one-off. This is the Pacific Ocean with waves and winds. We're not supposed to run out of oxygen," says Francis Chan, a marine ecologist at Oregon State University (OSU), Corvallis, who studied the event. "Then it happened again the next year, and then the year after, and the year after, and the year after."

Today, scientists in Oregon talk of a "hypoxia season." Some summers, low-oxygen waters off the coast cover as much as 15,000 square kilometers, equal to the Gulf of Mexico's dead zone. It's not unusual for shifting currents or a flush of pollution to tempo-

ceptible to oxygen loss, and they are going to be affected," says Lillian McCormick, a postdoctoral researcher at the University of California, San Diego.

Working as a Ph.D. student in Levin's lab, McCormick found that larvae of two species common in southern California waters—the market squid and graceful rock crab—start to lose their eyesight when oxygen drops by less than 10%. At lower levels, the animals are nearly blind. Vision problems could make it harder for them to hunt—or avoid becoming something else's meal, she says.

On a larger scale, some organisms could be pushed out of their habitats. As water warms, ocean dwellers consume oxygen more quickly, putting them on a collision course with falling oxygen supplies. Based on metabolic

limits and changing ocean conditions, scientists in 2015 calculated that the amount of habitable space in shallow ocean waters for common species such as Atlantic cod, rock crab, and tropical sea bream could shrink as much as 26% by the end of the century.

In 2018, the scientific arm of the United Nations, UNESCO, issued a report titled *The Ocean is Losing its Breath*. A year later, the International Union for Conservation of Nature (IUCN) published a 588-page tome detailing the threat to ocean ecosystems and the people who rely on them. In a 2020 paper, scientists concluded that in this century, declining oxygen would likely have a bigger impact on the ocean than underwater heat waves and ocean acidification. Those threats are familiar, but “oxy-

gen still isn’t on most people’s radars,” says Levin, who worked on the study.

That’s why it’s important to watch the sharks, Levin says. Not only are they potentially vulnerable to oxygen loss, but sharks also capture headlines. “If [Sims] wrote the exact same paper and it was about some fish that nobody had heard of with an obscure name that’s 6 inches long, it wouldn’t have the same impact,” Levin says. “Observations on species that people care about will really help.”

SINCE FIRST NOTICING that sharks were drawn toward the African coast, Sims has pieced together an explanation for their behavior. He suspects the low-oxygen zone acts like a fence, confining mackerel, saury,

and other prey into a smaller, oxygen-rich pool of water near the surface. That creates rich hunting grounds for the sharks.

Tags that he and collaborators have placed on more than 100 blue and mako sharks support the idea. Normally, both shark species dive to 1000 meters or more in search of food. But when tagged makos arrived in the zone, they stayed above 200 meters. The blue sharks, which have a bigger appetite for hypoxia-tolerant squid and octopuses, still swam into places with lower oxygen. But their average diving depth of 750 meters was 40% shallower than usual. That scenario mirrors decade-old observations that other large predatory ocean fish—marlin and sailfish—also keep near the surface in areas where deeper water is depleted of oxygen.

The sharks aren’t the only predators in those waters. Fishing fleets spooling out longlines—kilometers-long floating lines festooned with hooks—zero in on these same spots in pursuit of blue sharks. Worldwide, as many as 20 million blue sharks are caught each year for their fins and meat, and IUCN now labels the species as “near threatened.” Although trade in shortfin makos is restricted, these endangered sharks also die when they are accidentally hooked.

The sharks’ habits could increase their peril. Sims’s research showed that fishing ships congregating above the low-oxygen hot spots off the African coast catch more sharks in less time than in more oxygenated waters just to the north. Spanish fishing boat captains have told him they “know they are able to go there and catch them [blue sharks] in higher rates,” he says.

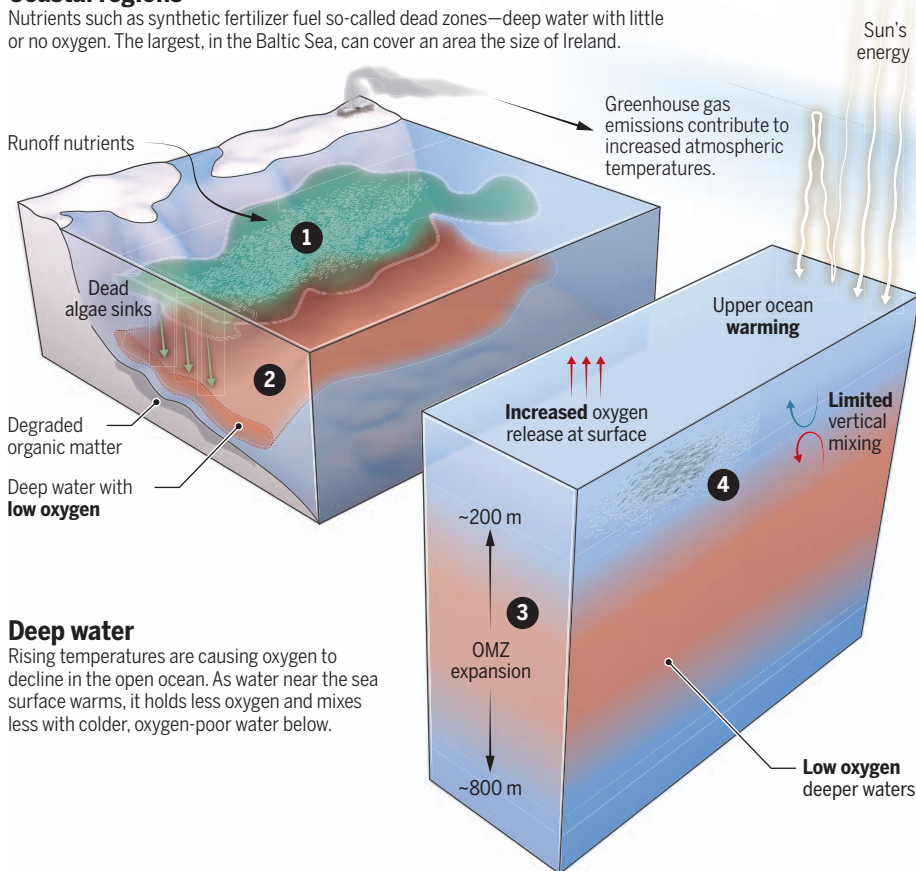
Sims’s initial work couldn’t prove low oxygen was driving the sharks to shallower depths, however, nor explain what metabolic trade-offs the sharks were making as they dove into oxygen-poor waters. All he had was a relatively coarse picture of shark movements, and his estimates of oxygen levels were based on models rather than direct measurements. So Sims teamed up with Nuno Queiroz, a former Ph.D. student now at the University of Porto, to build fish tags that could directly trace water conditions and capture more detail about the sharks’ behavior. The November expedition to the Canary Islands was part of what could be called Shark Tracking, Version 2.0.

Troubled waters

Average oxygen levels in the ocean have fallen by 2% over the past 50 years, and could fall 20% by the end of this century, making some parts of the ocean less habitable to sea life.

Coastal regions

Nutrients such as synthetic fertilizer fuel so-called dead zones—deep water with little or no oxygen. The largest, in the Baltic Sea, can cover an area the size of Ireland.



Deep water

Rising temperatures are causing oxygen to decline in the open ocean. As water near the sea surface warms, it holds less oxygen and mixes less with colder, oxygen-poor water below.

1 Biomass production

Nutrients such as nitrogen and phosphorus are flushed into coastal waters, sparking algae blooms.

2 Dead zone

The algae dies and sinks to the bottom, where microbes feast on it and consume oxygen.

3 Expanding oxygen minimum zones (OMZs)

As oxygen levels fall in the open ocean, regions that are naturally low in oxygen because of current patterns are expanding vertically. Their area also grew by some 4.5 million square kilometers over the past half-century.

4 Compressed habitat

As these OMZs grow, they threaten to displace fish that seek more oxygen-rich water near the surface. There are concerns this could make them more vulnerable to overfishing.

ABOARD THE ADONEY, Sims pulled one of the newest tags from a backpack. Hefting the orange device in one hand, he explained that it had sensors to measure oxygen in seawater, as well as temperature and pressure. An accelerometer can track subtle changes in the shark’s position, even counting tailbeats to gauge when it sprints to



Marine biologist David Sims shows how to fasten a tracker to a shark's fin (left). Sharks also carry a larger tag (right) that can monitor ocean oxygen and shark behavior.

catch prey. Another, similar-looking model attached to some sharks contains a tiny video camera offering a shark's-eye view of its travels, a small propeller to measure swimming speed, and a sensor for muscle temperatures, a clue to how hard the shark is working. Either tag pops off after 2 days and floats to the surface to be retrieved. Tagged sharks also often carry smaller, longer lived sensors, to track their movements.

Members of Sims's team had already tested the devices on sharks swimming near the Azores, 1300 kilometers northwest of the Canary Islands. Now, Sims had come to the southern tip of Gran Canaria, one of the only land bases for tagging sharks near the low-oxygen zone. So far, though, he had seen little more than gulls.

Team members had spent the previous week trolling off nearby Tenerife island and tagged just a single blue shark. By day four on this foray, the odds of using up Sims's stash of five of the fanciest sensors seemed extremely low. Yet he showed few chinks in his upbeat demeanor. "Raring to go," he announced in the hotel lobby early one morning, after several fruitless trips to sea.

As the team motored toward new fishing grounds farther west on the fourth day, sightings of other sea life raised hopes. A pilot whale spouted in the distance. In the afternoon, Garcia Habas landed several skipjack tuna. Shortly after nightfall, a fierce tussle ended when he reeled in a silver, goggle-eyed swordfish. It was hoisted

briefly for a photo, then heaved overboard. Finally, the drought seemed to end when Garcia Habas announced he had a shark on the line. After 10 minutes of tug-of-war, the sleek, ghostly form of a 2.4-meter blue shark suddenly materialized, illuminated by the green glow of a light lowered into the water. Garcia Habas eased the fish toward the boat and into the hands of the waiting scientists.

Like a pit crew at a Formula One race, they worked in a controlled frenzy. Ph.D. student Ivo Costa looped a rope over the shark's tail to hold it tight, then reached over the railing and grasped its two pectoral fins. He wrestled it onto its back to calm it, then flipped it onto its belly. Sims leaned far overboard and with both hands held a piece of plastic tight against the shark's dorsal fin to guide where the holes would be drilled. Matt Waller, another Ph.D. student, crowded in, drill in hand. The boat rocked, periodically lowering the entire melee into the waves, making the procedure akin to doing surgery while riding a bucking horse.

After 11 long minutes, Garcia Habas pulled the hook from the corner of the shark's mouth. It lazily descended out of sight, seemingly dazed by the ordeal, its fin adorned with the orange sensor. Costa gave Garcia Habas a high-five. Giddy laughter rose into the darkness. "It's like scoring a goal," Sims said with a grin.

It proved to be the only goal for the week. The following day, the last chance to catch a shark, the team fished the same area un-

til 10:30 p.m. and saw little but swarms of mackerel. As they cruised back toward the hotel lights lining the hillsides, Sims stood quietly on the deck gazing to sea, thinking, he said, about "what might have been."

There will be more chances. In April, a Ph.D. student is scheduled to board a Spanish commercial fishing boat for a 3-month stint tagging sharks directly inside the low-oxygen area. In November, Sims is traveling to Mexico's Sea of Cortez to tag whale sharks. He wonders whether the low-oxygen zone there might be causing them to swim closer to the surface, making them vulnerable to boat strikes. He and others are developing a new oxygen sensor that could stay on a fish for months, and he is finalizing plans to build a \$2.2 million shark "treadmill." Hung from the side of a ship, it would enable him to gather a detailed picture of how much oxygen a shark actually needs.

As Sims's team returned to the harbor empty-handed on that final night, the blue shark they had caught—which he dubbed "Warren Jr." (I'm honored)—swam steadily south. When the large sensor popped off after 2 days, the fish had already traveled 47 kilometers. Twenty-five days later, when a second, smaller sensor surfaced, the shark was 413 kilometers southwest of Gran Canaria, closing in on the low-oxygen zone and the waiting fishing boats. ■

This story was supported by a grant from the Vapnek Family Fund.

INSIGHTS

PERSPECTIVES



GEOPHYSICS

The Pāhala swarm of earthquakes in Hawai‘i

A magma network may feed into different volcanoes, including Mauna Loa and Kīlauea

By **Ashton F. Flinders**

On 27 November 2022, a short-lived hour of increased seismicity heralded the awakening of Mauna Loa Volcano in Hawai‘i after 38 years without eruption. The eruption began in the summit caldera before quickly transitioning into the Northeast Rift Zone, feeding lava flows for about 2 weeks before flows stalled less than 3 km from the island’s main

east-west highway. A primary goal of volcano monitoring is to provide early and accurate warnings of impending eruptions. But even for volcanoes as robustly monitored as Mauna Loa and its neighbor, Kīlauea, both short-term (hours to days) and long-term (months to years) forecasting is challenging. On page 462 of this issue, Wilding *et al.* (1) present a catalog of relocated earthquake hypocenters (points of origin) for Hawai‘i, providing unprecedented detail on the possible pathways for magma (molten rock beneath Earth’s surface) from the mantle to Kīlauea and Mauna Loa.

Three questions limit long-term forecasting ability: where magma is stored, the time scale of magma storage and ascent, and the pathways from magma source to the surface. Of these, two can be addressed through geophysical and geochemical techniques. Zones of magma storage can be inferred through seismic and/or geodetic modeling (2, 3), whereas petrological methods can estimate pre-eruptive depths (4) and time scales of magma storage (5). Tracking earthquakes associated with dike emplacement (which form when magma vertically intrudes into the surrounding rock) enables estimates

US Geological Survey, Hawaiian Volcano Observatory, Hilo, HI, USA. Email: aflinders@usgs.gov



Mauna Loa on the Island of Hawai'i started erupting in November 2022 after almost 40 years of silence. Its magma supply may come from a widespread network connecting volcanic hotspots.

cations that were detected with amplitude-based algorithms and/or humans manually picking earthquake arrival times. These methods are inherently limited in their ability to detect earthquakes below the algorithms' signal-to-noise thresholds and beyond the capacity of interactive identification. For example, a recent study of 32 years of seismicity for the island of Hawai'i included 275,000 relocated earthquakes between 1986 and 2018 (8). Wilding *et al.* present a machine learning-based earthquake detection and relocation catalog of 387,000 earthquakes for the island of Hawai'i, between January 2018 and May 2022.

The new catalog of Wilding *et al.* notably includes the continuing swarm of mantle earthquakes east of the town of Pāhala, situated on the southeastern flank of Mauna Loa. The authors detected a remarkable ~192,000 earthquakes from this region. Over the period of their catalog, this region has been the source of 18 magnitude 4.0 to 5.0 earthquakes, and the US Geological Survey's Hawaiian Volcano Observatory (HVO) has issued 19 public information statements detailing the ongoing activity. Prior to 2015, fewer than five deep (>25 km) earthquakes per week were detected by HVO in this region. By the end of 2015, the number had quadrupled. By August 2019, HVO was detecting, in real time, up to 600 earthquakes every week, a 120-fold increase relative to pre-2015 rates.

This persistent source of seismicity, the "Pāhala swarm," was identified by HVO in the 1960s, and it was suggested to be attributed to deep upwelling magma (9). Given Pāhala's location, 40 and 50 km from the summits of Kilauea and Mauna Loa, respectively, it was unclear how magma in this region might relate to surface volcanism, if at all (10). It was proposed that the Pāhala swarm might represent a magma pathway from the Hawaiian hot spot plume to Mauna Loa and Kilauea (10). However, other processes have been proposed to explain Hawaiian mantle seismicity, including tectonic faulting in the brittle lithosphere (11), and crustal loading and lithospheric flexure (bending of Earth's outer rigid layer) (12).

Wilding *et al.* relocated the Pāhala swarm into two vertically offset clusters. The lower cluster (45- to 51-km depth) consists almost exclusively of long-period earthquakes, typically indicative of magma and/or hydrothermal fluid transport, and/or exsolution of gas dissolved in magma, and oscillations in fluid pressure. This cluster is coincident with a

region previously interpreted as a possible magma-rich volume (13). The upper cluster (36- to 43-km depth) is composed primarily of volcano-tectonic earthquakes, which relocate into vertical stacks of inclined planes of seismicity. Wilding *et al.* interpret the upper cluster as a mantle sill complex. Equally striking are two inferred magma and/or hydrothermal fluid pathways from this upper cluster. One pathway connects to the crustal reservoir complex of Kilauea, and another connects to beneath the décollement on the eastern flank of Mauna Loa. Although relocations of hypocenters do not allow direct quantification of the physical process of seismogenesis (processes that cause earthquakes), the method of Wilding *et al.* enables mapping of potential pathways much more rapidly than traditional approaches. However, continued effort to transition these research methods into real-time relocations for volcano monitoring and long-term forecasting is required.

The Pāhala swarm may be the longest and most intense noneruptive volcano-related earthquake swarm ever observed by a seismic network (14). It is unclear whether the processes involved represent an archetype of hot spot island volcanism and/or hydrothermal fluid transport—unobserved elsewhere because of less comprehensive seismic networks and observing time frames—or whether these processes are specific to Hawai'i.

The recent eruption of Mauna Loa was preceded by months to years of heightened levels of seismicity and summit deformation. Whether the Pāhala swarm was unrelated to this unrest or was an indication of increased deep-magma supply to Mauna Loa and Kilauea is unclear (1, 15). Greater understanding of the Pāhala swarm and possible magma pathways could have a profound impact on long-term volcano hazard assessments. ■

REFERENCES AND NOTES

1. J. D. Wilding, W. Zhu, Z. E. Ross, J. M. Jackson, *Science* **379**, 462 (2023).
2. A. F. Flinders *et al.*, *Geology* **46**, 799 (2018).
3. D. Dzurisin, M. Lisowski, C. W. Wicks, M. P. Poland, E. T. Endo, *J. Volcanol. Geotherm. Res.* **150**, 35 (2006).
4. K. D. Putirka, *Rev. Mineral. Geochem.* **69**, 61 (2008).
5. A. E. Rubin *et al.*, *Science* **356**, 1154 (2017).
6. A. M. Rubin, D. Gillard, J.-L. Got, *J. Geophys. Res.* **103**, 10003 (1998).
7. P. G. Okubo *et al.*, *U.S. Geol. Surv. Prof. Pap.* **1801**, 67 (2014).
8. R. S. Matoza *et al.*, *Earth Space Sci.* **8**, 1 (2020).
9. K. Aki, R. Y. Koyanagi, *J. Geophys. Res.* **86**, 7095 (1981).
10. T. L. Wright, F. W. Klein, *Lithos* **87**, 50 (2006).
11. C. J. Wolfe, P. G. Okubo, P. M. Shearer, *Science* **300**, 478 (2003).
12. M. E. Pritchard, A. M. Rubin, C. J. Wolfe, *Geophys. J. Int.* **168**, 419 (2007).
13. A. G. Wech, W. A. Thelen, *Geophys. Res. Lett.* **42**, 7090 (2015).
14. J. P. Benoit, S. R. McNutt, *U.S. Geol. Surv. Open-File Rep.* **96-69**, 96 (1996).
15. M. K. Burgess, D. C. Roman, *J. Geophys. Res.* **48**, e2020GL01096 (2021).

Published online 22 December 2022

10.1126/science.adf2993

of magma ascent rates (6). However, only high-precision relocation of earthquake hypocenters provides the means to constrain the magmatic web of sills (horizontal intrusions of magma between layers of rock) and dikes connecting deep magma sources to the surface. The initial location of earthquakes is typically based on triangulation using earthquake arrival times. Relocating improves those initial locations, producing more accurate information about an earthquake's point of origin.

The Island of Hawai'i is one of the most well-monitored active volcanic regions on Earth, and earthquake relocations have been published semi-regularly since 1994 (7). These studies have provided insights into crustal and mantle fault structures, locations of magma reservoirs and rift zones, and planes of slip between the volcanic pile and the oceanic crust (décollements) (8). Previous studies started with earthquake lo-

BATTERIES

Working at room temperature

A solid-state electrolyte enables a lithium-air battery to operate at 25°C

By **Dejian Dong** and **Yi-Chun Lu**

Energy storage in the form of rechargeable batteries is becoming increasingly important for a range of applications, including transportation and grid reserves. Lithium-air (Li-air or Li-O₂) batteries offer great promise because of their low cost and high energy density (1). On page 499 of this issue, Kondori *et al.* (2) describe a Li-air battery that leverages the advantages of both organic and inorganic electrolytes in a composite solid-state matrix at room temperature (25°C). The discovery provides new design opportunities to achieve Li-based chemistry at room temperature, and energy density in batteries that is much higher than afforded by current Li-ion technology.

The main reaction product in a Li-air/O₂ battery can be one of three compounds: lithium superoxide (LiO₂, which requires one electron input per oxygen input) (3), lithium peroxide (Li₂O₂, requiring two electrons per oxygen) (4), and lithium oxide (Li₂O, requiring four electrons per oxygen) (5). The highest energy capacity (amount of stored energy) is gained from the four-electron reaction that generates Li₂O. However, at room temperature and in an air-rich environment, oxygen (O₂) prefers receiving two electrons to form Li₂O₂ rather than four electrons to generate Li₂O because Li₂O₂ is thermodynamically more stable than Li₂O. Also, a Li-air/O₂ battery based on O₂/Li₂O₂ chemistry suffers from side reactions involving an LiO₂ intermediate that is reactive and could degrade electrodes and electrolytes (6). Alternatively, a two-electron Li₂O₂/Li₂O reaction that is not under an air/O₂ atmosphere is more stable because of the absence of LiO₂ intermediates. But a Li₂O₂/Li₂O reaction is unlikely to proceed in the presence of an air/O₂-rich environment because the O₂/Li₂O₂ reaction would prevail. This makes it difficult to achieve a high-energy capacity, four-electron reaction by combining two two-electron reactions (O₂/Li₂O₂ and Li₂O₂/Li₂O).

Although a four-electron Li-air/O₂ reac-

tion has been achieved at high temperature (~150°C) using a molten salt electrolyte and a high-selectivity catalyst (5), the temperature requirement increases operation cost. Kondori *et al.* discovered that the reaction is attainable at room temperature using a stable solid-state electrolyte with a high ionic conductivity and a catalyzed gas diffusion layer (see the figure). Solid-state electrolytes are attracting attention because they are safer to use compared with liquid electrolytes (7). Solid-state Li super-ionic conductor materials include organic polymer-based electrolytes and inorganic (oxide, sulfide, halide)-based electrolytes (8). Among inorganic-based solid-state electrolytes, those that are sulfide based can achieve ionic conductivities close to or higher than those of conventional liquid electrolytes (7). However, the electrochemical and chemical stability of sulfide-based electrolytes toward O₂ and water is a concern (9). Polymer-based electrolytes are flexible, resulting in lower contact resistance (10). A polymer electrolyte based on polyethylene oxide (PEO) has been extensively studied since the 1970s. Its ionic conductivity can be tailored by modulating the molecular weight of PEO and Li salt concentration (source of Li ions), as well as by the addition of nanoparticles, cross-linkers, and plasticizers (promotes plasticity). It can

also be modified if it is hybridized with an inorganic solid-state electrolyte (10).

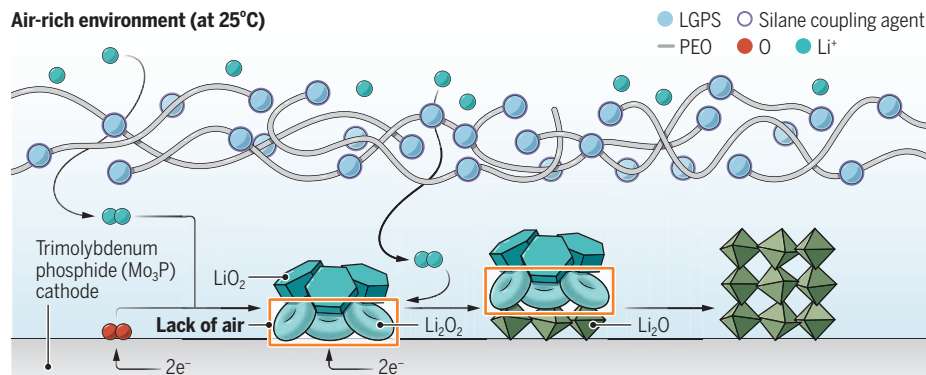
Kondori *et al.* synthesized a solid-state electrolyte by using a silane coupling agent, mPEO-TMS {3-[methoxy(polyethyleneoxy)₆₋₉ propyl]trimethoxysilane} to chemically bond with nanoparticles containing the Li super-ionic conductor Li₁₀GeP₂S₁₂ (LGPS) in a matrix of lithium bis(trifluoromethanesulfonyl) imide (LiTFSI) solubilized in PEO. This composite electrolyte combines several advantages of organic and inorganic solid-state electrolytes. It displays conductivity (0.52 mS cm⁻¹) that is 10 times greater than that of the solid electrolyte without the nanoparticles. Higher Li transference is attributed not only to Li transport pathways in LGPS, PEO, and mPEO-TMS but also to the absence of a phase boundary between PEO and LGPS. Electrochemical stability of the nanoparticles with a Li metal anode and the active cathode interfaces was enhanced through the formation of strong chemical bonds between S atoms in Li₂S clusters (within the nanoparticles) and the Si atoms (in the mPEO-TMS matrix).

Kondori *et al.* used this well-designed solid-state electrolyte together with a previously reported catalyst, trimolybdenum phosphide (Mo₃P) (11), to achieve a reversible four-electron Li₂O reaction at 25°C for 1000 cycles. The formation of Li₂O₂ and Li₂O was initially observed for the first 15 min, after which Li₂O became the dominant discharge product. The authors speculate that the initial formation of a LiO₂/Li₂O₂ interphase was uniform on the walls of the valley of the cathode. This could provide the needed mixed electronic/ionic conduction properties for further electrochemical reduction. After reaching a steady state,

Good for a thousand cycles

A Li-air/O₂ battery is designed to favor the formation of Li₂O as the dominant discharge product rather than Li₂O₂ and LiO₂ at room temperature. A polymer electrolyte based on polyethylene oxide (PEO) that is embedded with Li₁₀GeP₂S₁₂ (LGPS) nanoparticles displays high ionic conductivity and high cycle stability through a reversible four-electron transfer process. Further characterization of this system includes determining how to create a local air-deficient environment by design.

Air-rich environment (at 25°C)



Electrochemical Energy and Interfaces Laboratory,
Department of Mechanical and Automation Engineering,
The Chinese University of Hong Kong, Hong Kong SAR,
China. Email: yichunlu@mae.cuhk.edu.hk

Li_2O_2 becomes isolated beneath the LiO_2 where no O_2 gas is present, and Li_2O_2 comes in direct contact with the cathode where electronic conduction is the most favorable. These conditions allow the two-electron reduction of Li_2O_2 to Li_2O . Combining two two-electron reactions ($\text{O}_2/\text{Li}_2\text{O}_2$ and $\text{Li}_2\text{O}_2/\text{Li}_2\text{O}$) thus yields the highly desirable four-electron Li-air/ O_2 chemistry. The formation of Li_2O was verified by in situ Raman spectroscopy, differential electrochemical mass spectrometry, and x-ray diffraction.

Although the proposed mechanism of Li_2O generation is plausible (the cathode valley wall scenario), it is not clear what specific criteria for the solid-state electrolyte (ionic conductivity, Li transference), microstructure of the cathode-electrolyte interface, and selectivity of catalyst are needed to ensure the production of Li_2O . The proposed mechanism of Kondori *et al.* necessitates that the entire conductive cathode surface is covered with $\text{LiO}_2/\text{Li}_2\text{O}_2$ to allow the sequential formation of Li_2O from Li_2O_2 (otherwise O_2 reduction to Li_2O_2 will still prevail). It is not clear how to design such a local air/ O_2 -deficient environment. Deeper understanding of this mechanism will enable rational designs for integrated electrode-electrolyte assemblies for four-electron Li-air/ O_2 batteries that operate at room temperature. In addition, to make full use of the high energy density based on four-electron Li-air/ O_2 chemistry, it is critical to develop lightweight, electronically and ionically conducting porous structures to host Li_2O . Notably, the long-term cycling test in the study of Kondori *et al.* was conducted at a low areal capacity (capacity per unit of geometric area) (0.1 mAh cm^{-2}), and the verification of O_2 evolution was only available for one cycle. Characterizing cycling stability at a higher areal capacity and verifying O_2 evolution efficiency at later cycling stages (e.g., 100th, 500th cycles) (12) are critical to better understand the system. ■

REFERENCES AND NOTES

1. T. Liu *et al.*, *Chem. Rev.* **120**, 6558 (2020).
2. A. Kondori *et al.*, *Science* **379**, 499 (2023).
3. J. Lu *et al.*, *Nature* **529**, 377 (2016).
4. Z. Peng, S. A. Freunberger, Y. Chen, P. G. Bruce, *Science* **337**, 563 (2012).
5. C. Xia, C. Y. Kwok, L. F. Nazar, *Science* **361**, 777 (2018).
6. Y. Qiao, K. Jiang, H. Deng, H. Zhou, *Nat. Catal.* **2**, 1035 (2019).
7. A. Banerjee, X. Wang, C. Fang, E. A. Wu, Y. S. Meng, *Chem. Rev.* **120**, 6878 (2020).
8. A. Manthiram, X. Yu, S. Wang, *Nat. Rev. Mater.* **2**, 16103 (2017).
9. N. Kamaya *et al.*, *Nat. Mater.* **10**, 682 (2011).
10. M. Armand, *Solid State Ion.* **69**, 309 (1994).
11. A. Kondori *et al.*, *Adv. Mater.* **32**, 2004028 (2020).
12. G. Cong, W. Wang, N.-C. Lai, Z. Liang, Y.-C. Lu, *Nat. Mater.* **18**, 390 (2019).

VIEWPOINT: COVID-19

Managing sources of error during pandemics

The COVID-19 pandemic has highlighted important considerations for modeling future pandemics

By Simon Cauchemez¹, Paolo Bosetti¹, Benjamin J. Cowling^{2,3}

The COVID-19 pandemic has shown the critical role that quick and robust risk assessment can play during epidemics of emerging pathogens to guide evidence-based policy-making. Generating such assessments, however, is a challenging task because the estimation of key quantities such as the incidence and severity of infection, the transmission potential, the impact of nonpharmaceutical interventions (NPIs), and vaccine effectiveness is affected by multiple sources of error. Complex epidemic dynamics further blur assessments. Modeling has proved critical to help tackle these issues in the context of COVID-19, through the detailed analysis of surveillance data and epidemiological investigations. However, additional challenges are emerging now that the most acute phase of the pandemic is over, and it is important to learn from this experience to improve the response to future pandemics.

During epidemics, monitoring the incidence of infection is crucial to characterize the extent of viral circulation and the build-up of population immunity and to estimate key parameters such as the severity of infection. Over the past 3 years, it has been difficult to estimate the incidence of severe acute respiratory syndrome coronavirus 2 (SARS-CoV-2) infections over time because a substantial fraction of infections are not detected and enumerated in population-level case counts. In this context, modelers quickly proposed methods to estimate the true levels of infection from incomplete data. For example, in January 2020, when only 41 cases were confirmed in Wuhan, the analysis of data on international cases (three confirmed cases out of 3300 international passengers leaving

Wuhan per day) suggested that 1700 (95% confidence interval, 400 to 4500) COVID-19 infections had already occurred in Wuhan (1). Later on, total numbers of infections were reconstructed from counts of severe cases combined with COVID-19 severity estimates (2). Uncertainty around these estimates was reduced once serology became available, even though interpretation can sometimes be challenging given antibody decay and assays with imperfect sensitivity and specificity.

Estimating the “true” number of infections from data on severe cases is more challenging now that the proportion of infections that lead to severe disease is influenced by many different factors (such as SARS-CoV-2 variant, vaccination status, past infections, and age). Routine COVID-19 testing among new nonrespiratory hospital admissions is carried out in some locations and could provide an indicator of the prevalence of asymptomatic and very mild infections in the community, but corrections (for example, for the population age structure) would likely be needed. Studies in which a large number of individuals are randomly tested each month for SARS-CoV-2 infection, such as the REACT-1 study that was carried out in the UK between May 2020 and March 2022 (3), are costly but constitute the most reliable way to monitor infections in the community. Because estimating the incidence of infection is an essential but complex task for the study of many infectious diseases, there would be value in implementing REACT-1-like studies beyond the first few waves of a pandemic. Cost is an important barrier but might be partly alleviated by using the same platform to study multiple pathogens.

To generate a pandemic with large population impact, an emerging or reemerging infectious agent needs both the capacity to spread widely in human populations (transmission potential) and also to cause disease in infected individuals (severity of infection). Characterizing these two dimensions is necessary to anticipate the overall impact of a pandemic. The most familiar metric to characterize the severity of COVID-19 is the “case fatality risk” (CFR; sometimes called the case fatality rate), which reflects the risk of mortality among COVID-19 cases detected

¹Mathematical Modelling of Infectious Diseases Unit, Institut Pasteur, Université Paris Cité, CNRS UMR2000, Paris, France. ²World Health Organization Collaborating Centre for Infectious Disease Epidemiology and Control, School of Public Health, Li Ka Shing Faculty of Medicine, The University of Hong Kong, Hong Kong Special Administrative Region, China. ³Laboratory of Data Discovery for Health, Hong Kong Science and Technology Park, New Territories, Hong Kong Special Administrative Region, China. Email: simon.cauchemez@pasteur.fr

Identifying COVID-19 cases through testing, as shown here in Shanghai in December 2022, is important to enable accurate modeling.



with surveillance. However, because case ascertainment can vary from one location to another, CFR estimates are typically affected by the quality of surveillance. A more standard metric, the infection fatality risk (IFR), should have more stable properties but can still be influenced by sources of error that affect estimates of the number of infections and the number of deaths.

Concerning the number of deaths, excess mortality data indicate that in some locations, official statistics largely underestimated the death toll because individuals dying of COVID-19 were rarely confirmed in a laboratory (4). In addition, some confirmed COVID-19 deaths may have occurred with COVID-19 coincidentally rather than being caused by COVID-19. Despite these challenges, early IFR estimates on the order of 0.5 to 1% for COVID-19 (2) were roughly consistent with those obtained later on, when availability of serology reduced the uncertainty about the number of infections. The COVID-19 pandemic also highlighted the importance of characterizing severity by age, which requires good demographic data. In future epidemics, substantial risk remains that poor estimates of the number of infections early on lead to important errors in severity estimates, affecting the evaluation of population impact and consequent decision-making. The implementation of REACT-1-like studies to estimate incidence could provide more accurate denominators for severity assessments and should be considered in future pandemic plans.

The transmission potential of a pathogen, which is necessary to anticipate its epidemic dynamics, is typically measured by the reproduction number, R (mean number of persons infected by a case). R can be estimated directly by analyzing chains of transmis-

sion, but this information is rarely available. Fortunately, R can also be estimated by other means—for example, from the rate at which cases increase in a population (5). However, such an approach may overestimate R in the common situation when there is a surge in reporting after an infectious disease alert, and estimates are sensitive to assumptions about the generation time (average time lag between infection of a primary case and of their secondary cases). Before the SARS-CoV-2 pandemic, it was considered that the generation time would remain stable during an epidemic, and so it was thought to be sufficient to estimate generation time once from the first few hundred cases. However, the SARS-CoV-2 pandemic has shown that control measures or new variants can modify this quantity (6). Moving forward, it seems important to develop data collection protocols (beyond the first few hundred cases) and statistical methods to monitor changes in the generation time and to correct R estimates accordingly. Similar efforts should be made to monitor overdispersion in transmission [that some cases infect many other people (also known as superspreading), whereas other cases do not transmit onward] because failing to do so may lead to inaccurate predictions of epidemic dynamics, particularly at the start of an epidemic (7).

Early in the COVID-19 pandemic, NPIs were the only tool available to mitigate infections (2, 8, 9). Although policy-makers would prefer to implement the least disruptive but most effective measures to control COVID-19 transmission, identifying this set of measures has proved challenging. This is because estimating the individual effects of various NPIs is affected by multiple sources of error: endogeneity, in which NPIs are implemented when transmission is high so that naïve correlation

studies may wrongly conclude that effective NPIs are associated with fast epidemic growth; multicollinearity, in which NPIs are often implemented simultaneously, making it impossible to disentangle individual effects; and heterogeneity and data quality, in which in an attempt to increase statistical power, meta-analyses have combined data from multiple countries, but such comparisons may be affected by differences in local settings, data quality, NPI definitions, and population adherence to NPIs. Identifying the impact of specific interventions mostly from aggregated population-level data such as epidemic curves therefore requires great care, with an important role for statistical and mathematical modeling (8).

Behavioral changes constitute another important source of error, and it remains difficult to anticipate how individuals will respond to governmental measures and how this response may change over time, impeding epidemic forecasting (10). More research is needed to precisely quantify behavioral changes over time and space, to ascertain the determinants of these changes, and to determine how to optimally integrate them into mathematical models, with key input expected from social scientists. Jointly analyzing the mass of data collected about behaviors, perceptions, NPIs, and epidemic dynamics over the past 3 years across multiple continents could provide insights on the interplay between behaviors and epidemics. This should be complemented with qualitative research to further understand these complex interactions.

Once vaccines became available, the benefits of vaccination were assessed by estimating vaccine effectiveness, which compares the risks of infection, severe COVID-19, and death in individuals that have and have not been

vaccinated, with major impact on expected population-level dynamics (11). Although the first vaccine trials and then observational studies of vaccine effectiveness were carried out in largely infection-naïve populations (12), the proportion of unvaccinated individuals gaining some degree of protection through natural infection increased over time. This phenomenon is expected to increasingly bias vaccine effectiveness estimates downward. Now that most individuals have been infected with SARS-CoV-2 at least once and are vaccinated, it becomes impossible to consider naïve unvaccinated individuals as the reference group, and waning of immunity has become the central issue. For these reasons, vaccine effectiveness estimates should now be based on time since the last dose to monitor the continued value and impact of booster doses and estimate waning of immunity. Similar problems occur with the estimation of the intrinsic severity (such as risk of severe COVID-19, given infection

in a naïve individual) of new variants. For example, the impression in populations with high levels of vaccination and past infections that Omicron variants led to much milder infections than past variants was somewhat contradicted by studies that estimated that intrinsic severity was quite similar to that of the ancestral strain (13).

Throughout the COVID-19 pandemic, mathematical models have played an essential role in estimating key parameters, monitoring population immunity, building short-term forecasts and medium-term intervention scenarios, and anticipating the impact of variants and of vaccination (2, 8, 9, 11, 14). The simple model structures that described the early spread of SARS-CoV-2 were revised incrementally to capture important changes in SARS-CoV-2 epidemiology, such as the emergence of new variants or the impact of immunity not only from infections but also from vaccinations. These revisions were supported by COVID-19 data analyses that provided estimates for key parameters (2, 8, 12–14). After a large number of increments (such as for variants Alpha, Delta, and Omicron; vaccinations with two, three, and four doses; and decay of immunity), SARS-CoV-2 models now often comprise thousands of equations. This large number of parameters, and the difficulty to estimate these parameters and track infections and population immunity, all contribute to making current model outputs unstable and sensitive to modeling assumptions. After 3 years of tracking successive pandemic waves with

these models, the transition to endemicity is an opportunity to develop models that can describe the epidemic process in a simpler way, similar to what is done for other infectious diseases such as influenza. Key for success will be to identify a more parsimonious description of population immunity against infection and severe disease without having to calibrate models to years of epidemic time series. More research is therefore needed to determine whether population immunity could be summarized with a few biomarkers, such as neutralizing antibody titers (14) or other immune markers. The development of mathematical models that robustly integrate data from SARS-CoV-2 antigenic maps could

also improve risk assessment in the context of emerging variants (15).

Decades of research on epidemics in epidemiology, mathematical modeling, and public health have generated a range of surveillance systems, study designs, and methods with which to allow more accurate situational

awareness and address common sources of error during epidemic risk assessments. These approaches proved critical during the COVID-19 pandemic. Now that the most acute phase of the COVID-19 pandemic is over, improving this toolbox, through the development and deployment of new data collection protocols and methods, must remain a priority to effectively manage COVID-19 as the virus moves to endemicity and surveillance approaches change. This will also be important to strengthen preparations for future emerging pathogens. ■

REFERENCES AND NOTES

1. WHO Collaborating Centre for Infectious Disease Modelling, MRC Centre for Global Infectious Disease Analysis; Abdul Latif Jameel Institute for Disease and Emergency Analytics; Imperial College London, UK, "Report 1 - Estimating the potential total number of novel Coronavirus (2019-nCoV) cases in Wuhan City, China" (Imperial College London, 2020); <https://bit.ly/3lCu69W>.
2. H. Salje *et al.*, *Science* **369**, 208 (2020).
3. P. Elliott *et al.*, *Science* **376**, eabq4411 (2022).
4. J. A. Lewnard *et al.*, *Lancet Infect. Dis.* **22**, 463 (2022).
5. A. Cori, N. M. Ferguson, C. Fraser, S. Cauchemez, *Am. J. Epidemiol.* **178**, 1505 (2013).
6. S. T. Ali *et al.*, *Science* **369**, 1106 (2020).
7. J. O. Lloyd-Smith, S. J. Schreiber, P. E. Kopp, W. M. Getz, *Nature* **438**, 355 (2005).
8. Y. Li *et al.*, *Lancet Infect. Dis.* **21**, 193 (2021).
9. R. Sonabend *et al.*, *Lancet* **398**, 1825 (2021).
10. S. Funk *et al.*, *Epidemics* **10**, 21 (2015).
11. C. M. Saad-Roy *et al.*, *Science* **370**, 811 (2020).
12. N. Dagan *et al.*, *N. Engl. J. Med.* **384**, 1412 (2021).
13. Y. M. Mefsin *et al.*, *Emerg. Infect. Dis.* **28**, 1856 (2022).
14. A. B. Hogan *et al.*, SSRN 10.2139/ssrn.4135323 (2022).
15. A. Z. Mykytyn *et al.*, *Sci. Immunol.* **7**, eabq4450 (2022).

ACKNOWLEDGMENTS

B.J.C. consults for AstraZeneca, Fosun Pharma, GSK, Moderna, Pfizer, Roche, and Sanofi Pasteur.

10.1126/science.add3173

CHEMISTRY

One carbon—four new bonds

Stable carbenes deliver a carbon atom to simple amides, producing a range of cyclic compounds

By Yuji Nakano and David W. Lupton

The naturally high abundance of carbon and its prevalence in all known organisms makes it one of the most important elements in chemistry. Consequently, synthetic manipulation of carbon-containing molecules has broad effects on science and society. Although chemical reactions that construct one or two new bonds to a single carbon are common, those that construct three or more are less developed, despite the potential to allow for the rapid assembly of complex materials that could have applications in medicine and materials science. On page 484 of this issue, Kamitani *et al.* (1) report a reagent that allows the insertion of a single carbon atom into common unsaturated amides to give a range of cyclic amide products.

Chemical reactions that construct more than one bond in a single process most commonly involve initiating bond-forming events across different carbon atoms in a molecule (2), as exemplified by the landmark synthesis of progesterone (3). Reactions that lead to the construction of multiple bonds at a single carbon are more specialized and often involve the reactions of carbenes (species with a pair of non-bonding electrons and two other groups). For example, diazomethane, a common precursor to a carbene, allows insertion reactions to be achieved with ketones, providing two new carbon-carbon bonds in the process (4). Other carbene precursors have also been developed whereby in a single-step or multistep sequence, up to four new bonds can be constructed. These types of reactions are important for chemical synthesis and continue to be applied in the preparation of important molecules in medicine.

The work of Kamitani *et al.* exploits N-heterocyclic carbenes (NHCs) (5) as reagents that are capable of allowing single-carbon atom insertion with the construction of four new bonds. The process

constructs one new carbon-carbon bond, one new carbon-nitrogen bond, and two new carbon-hydrogen bonds. NHCs are some of the earliest carbenes to be isolated (6), although before isolation, they had been predicted on the basis of chemical reaction outcomes in studies dating from the 1950s. NHCs have a rich involvement in organic synthesis, serving as stabilizing components in metal complexes (7), cofactors in biocatalytic processes (8), or catalysts in their own right (9). To allow the reported chemistry, the authors use NHCs with enhanced reactivity (10) compared with more common versions that were unable to accomplish the reaction effectively.

The chemical steps associated with the discovery were examined by monitoring the transfer of protons and carbons. This allowed the authors to propose a process in which the NHC serves as a two-electron donor adding into the acrylamides to construct the first new bond. In the simplest version of the reaction, proton transfers followed by amine addition then construct the carbon-nitrogen bond. Most examples in the study of Kamitani *et al.* involve a slightly more complex bond-forming sequence in which aryl migration occurs before carbon-nitrogen bond formation. The carbon-carbon and carbon-nitrogen bond formation has some analogy in NHC-catalyzed processes (11) with similar intermediates postulated in computational studies (12) and nonproductive catalytic reactions (13). Finally, the product is formed through a series of proton transfers that construct two carbon-hydrogen bonds and dissociate a diimine, thereby completing the reaction (see the figure).

The early steps in this synthesis have some precedent (11), but the overall process allows a highly distinct reaction pathway that enables the conversion of common unsaturated amides into cyclized materials. Kamitani *et al.* explored the utility of the reaction across a range of starting materials, including those bearing potentially sensitive functional groups. In addition, the conversion of the resul-

tant products to more advanced materials was also considered. The application of this reaction with more complex starting materials makes a two-stage introduction of cyclic amides from common aryl amines possible. Notably, such cyclic amides have long-established antibacterial activity; thus, new approaches to their preparation have the potential to support the discovery of new antibiotics.

The reaction reported by Kamitani *et al.* is highly original and gives rise to exciting opportunities that extend this single-carbon atom insertion. In its current form, two carbon-hydrogen bonds are constructed. If one of these hydrogens was replaced by any other element, then the products would bring up to three non-hydrogen components together. This would greatly

increase the complexity of the products formed and could allow for the realization of complicated target syntheses. Moreover, the delivery of a single carbon atom in the form of a stabilized NHC, with loss of a diimine, introduces substantial waste with an atomically large reagent delivering just a single atom. Methods that enable the recapture of this by-product and recycling into the NHC reagent could allow for important advances toward realizing a circular chemical economy.

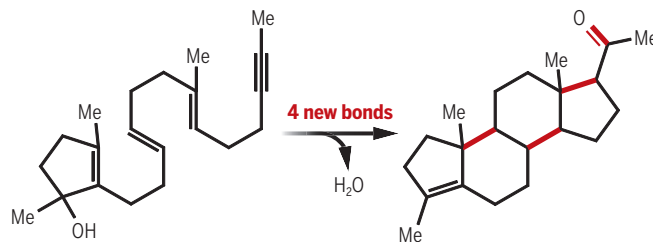
Although efficiency is a central tenet of many new reactions, this is largely defined by minimizing expenditure—whether it be material, thermal, or temporal—but not necessarily by maximizing utility arising from the complexity of the product (14). The chemistry introduced by Kamitani *et al.* delivers the maximum number of new bonds about a single carbon. The development of approaches whereby four distinct bonds are assembled at a single carbon has great potential utility. Though the work of Kamitani *et al.* introduces an exciting approach to such chemistry, two of the new bonds are to hydrogen. Future directions are likely to address this, ultimately allowing a single carbon atom to undergo bond formation with four distinct fragments. ■

Constructing new bonds

To assemble complex molecules, the ability to install more than one new bond in a single operation is often advantageous and allows more rapid access to the desired target.

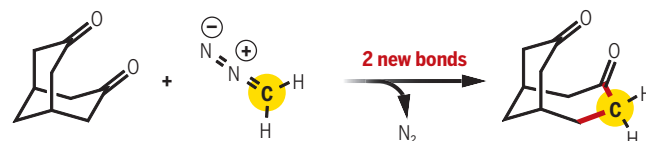
Building multiple bonds in one operation

New bonds are constructed at a number of distinct positions within the molecule to enable a synthesis of progesterone.



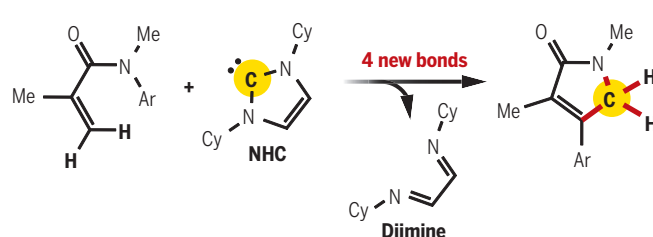
Insertion of a carbene with diazomethane

Two new bonds are constructed to a single carbon atom (highlighted), which is inserted into the starting material to give a ring-expanded product.



Insertion of a carbon with N-heterocyclic carbenes (NHCs)

Four bonds are constructed to a single carbon atom (highlighted), which is inserted into the starting material to give a cyclic amide product.



Ar, aryl; Cy, cyclohexyl; Me, methyl.

REFERENCES AND NOTES

1. M. Kamitani *et al.*, *Science* **379**, 484 (2023).
2. L. F. Fieser, *J. Am. Chem. Soc.* **79**, 115 (1957).
3. W. S. Johnson, M. B. Gravestock, B. E. McCarry, *J. Am. Chem. Soc.* **93**, 4332 (1971).
4. G. R. Krow, *Tetrahedron* **43**, 3 (1987).
5. P. Bellotti, M. Koy, M. N. Hopkinson, F. Glorius, *Nat. Rev. Chem.* **5**, 711 (2021).
6. A. J. Arduengo III, R. L. Harlow, M. Kline, *J. Am. Chem. Soc.* **113**, 361 (1991).
7. H.-W. Wanzlick, H.-J. Schönherr, *Angew. Chem. Int. Ed.* **7**, 141 (1968).
8. R. Breslow, *J. Am. Chem. Soc.* **80**, 3719 (1958).
9. T. Ukai, R. Tanaka, T. Dokawa, *Yakugaku Zasshi* **63**, 296 (1943).
10. B. Maji, M. Breugst, H. Mayr, *Angew. Chem. Int. Ed.* **50**, 6915 (2011).
11. X. B. Nguyen, Y. Nakano, D. W. Lupton, *Aust. J. Chem.* **73**, 1 (2020).
12. R. C. Johnston, D. T. Cohen, C. C. Eichman, K. A. Scheidt, P. Ha-Yeon Cheong, *Chem. Sci.* **5**, 1974 (2014).
13. X. B. Nguyen *et al.*, *Angew. Chem. Int. Ed.* **58**, 11483 (2019).
14. P. A. Wender, B. L. Miller, *Nature* **460**, 197 (2009).

ACKNOWLEDGMENTS

D.W.L. is supported by the Australian Research Council (DP200101448 and DP210103053).

The NIH-led research response to COVID-19

Investment, collaboration, and coordination have been key

By Francis Collins¹, Stacey Adam², Christine Colvis³, Elizabeth Desrosiers⁴, Ruxandra Draghia-Akli⁵, Anthony Fauci⁶, Maria Freire², Gary Gibbons⁷, Matthew Hall³, Eric Hughes⁸, Kathrin Jansen⁹, Michael Kurilla³, H. Clifford Lane⁶, Douglas Lowy¹⁰, Peter Marks¹¹, Joseph Menetski², William Pao⁹, Eliseo Pérez-Stable¹², Lisa Purcell¹³, Sarah Read⁶, Joni Rutter³, Michael Santos², Tara Schwetz¹⁴, Jeffrey Shuren¹¹, Timothy Stenzel¹¹, Paul Stoffels¹⁵, Lawrence Tabak¹⁴, Karen Tountas², Bruce Tromberg¹⁶, David Wholley², Janet Woodcock¹¹, John Young¹⁷

Though the COVID-19 pandemic, which has claimed the lives of at least 6.5 million individuals worldwide, is not yet over, it is not too soon to consider the strengths and weaknesses of the research response and some of the lessons that can be learned. Much important research has investigated key public health and clinical issues such as masking, indoor air ventilation, and prone ventilation. But, arguably, no research has been more innovative and impactful than that of the biomedical community around vaccines, therapeutics, and diagnostics. Drawing on our experience leading US-driven elements of this global biomedical research effort, we review here major cross-sector initiatives led by the National Institutes of Health (NIH) and its partners. We outline key milestones (see the figure) and crucial lessons learned, with the goal of informing and guiding the research community's response to future pandemics (see the box).

As emphasized by the Lancet Commission (1) and many others, COVID-19 has reaffirmed the importance of international coordination in addressing public health challenges. The US biomedical research community has learned much from—and shared much with—their international partners. Yet it is also essential to recognize the value of sustained learning and constant preparation because, in the past, many aspirational goals have failed to be fully realized (2).

INVESTING IN VACCINE DEVELOPMENT AND EVALUATION

The research response to severe acute respiratory syndrome coronavirus 2 (SARS-CoV-2), the novel coronavirus that causes

COVID-19, was not invented from scratch. Decades of basic research in virology, molecular biology, genomics, immunology, structural biology, epidemiology, and multiple other scientific fields made it possible to mount therapeutic and vaccine efforts within days of the public release of the sequence of the viral genome (3). Before the COVID-19 pandemic, mRNA vaccines had not yet been proven safe and effective for any infectious disease. However, data that had been gathered over the past two decades, including codon optimization and refinement of delivery systems, provided confidence that this approach could work—and ultimately saved months in the face of a rapidly spreading pandemic. Only the nucleotide sequence of SARS-CoV-2 posted on the internet on 10 January 2020 was needed to start the design. In an effort that has been well described elsewhere (3, 4), the first injections in research volunteers were initiated in a phase 1 NIH-Moderna clinical trial just 65 days after the posting of the viral genome sequence. A parallel effort by Pfizer-BioNTech proceeded at the same fast pace, and Janssen, AstraZeneca, and Novavax followed closely behind. Of critical importance was the initiation of a US government program, Operation Warp Speed (OWS), to provide financial support for large-scale vaccine and therapeutic trials and support for the manufacturing of millions of doses of vaccines at financial risk to the US government even before their safety and efficacy had been shown (4). Clinical trial endpoints were harmonized, and five of the six pivotal studies were overseen by a single NIH-convened Data and Safety Monitoring Board. As part of this, NIH HIV vaccine evaluation networks were partnered with units based

in contract research organizations (CROs).

When unblinded in November 2020, the results of the randomized phase 3 clinical trials of the mRNA vaccines outperformed all but the most optimistic expectations—more than 90% efficacy in preventing symptomatic disease and an excellent safety record. In just 11 months from identification of the pathogen, two vaccines received emergency use authorization (EUA) from the US Food and Drug Administration (FDA). Most other vaccines have taken at least a decade to develop.

BUILDING DIVERSITY IN CLINICAL TRIALS

One hallmark of the pandemic is that the burden of COVID-19 has not been evenly distributed across populations. In the United States, the burden has fallen heavily on older individuals and Black, Hispanic, and American Indian people, particularly those in underserved communities—hospitalizations and deaths were significantly higher among these groups. For scientific credibility and public acceptance, it was critical to include volunteers in vaccine and therapeutic clinical trials who represented the diversity of the US population. At the start of the phase 3 vaccine trials, the individuals most likely to participate were white, and thus diversity was expected to be limited. Leadership from NIH, the Surgeon General's office, participating companies, and trial recruitment centers convened weekly to identify ways to ensure diversity. The NIH Community Engagement Alliance (CEAL) Against COVID-19 Disparities (<https://covid19community.nih.gov/>) was formed and expedited efforts to work directly with disproportionately affected communities in multiple states (5). This initiative was

¹National Human Genome Research Institute, Bethesda, MD, USA. ²The Foundation for the National Institutes of Health, North Bethesda, MD, USA. ³National Center for Advancing Translational Sciences, Bethesda, MD, USA. ⁴Merck, Rahway, NJ, USA. ⁵The Janssen Pharmaceutical Companies of Johnson & Johnson, Titusville, NJ, USA. ⁶National Institute of Allergy and Infectious Diseases, Bethesda, MD, USA. ⁷National Heart, Lung, and Blood Institute, Bethesda, MD, USA. ⁸Teva Pharmaceuticals, Tel Aviv, Israel. ⁹Pfizer, New York, NY, USA. ¹⁰National Cancer Institute, Bethesda, MD, USA. ¹¹US Food and Drug Administration, Silver Spring, MD, USA. ¹²National Institute on Minority Health and Health Disparities, Bethesda, MD, USA. ¹³Vir Biotechnology, San Francisco, CA, USA. ¹⁴Office of the Director, National Institutes of Health, Bethesda, MD, USA. ¹⁵Galapagos, Mechelen, Belgium. ¹⁶National Institute of Biomedical Imaging and Bioengineering, Bethesda, MD, USA. ¹⁷Roche, Basel, Switzerland. Email: francis.collins@nih.gov

informed by NIH's 30-year history of supporting community-engaged research, which encourages researchers to embrace principles of full partnership to build sustainable mutual trust with community organizations. CEAL's efforts were also guided by the epidemiology of the pandemic in the summer of 2020 and focused on areas in which disadvantaged communities were experiencing the greatest burden of illness. Recruitment sites with a track record of effectively engaging underserved communities were given enhanced support. An innovative partnership with CVS Health Corporation provided vaccine trial information to individuals who had just tested negative for COVID-19. With a shared commitment to the tenet that diversity is an essential feature for an effective roll-out of a vaccine, the groups developed and implemented new approaches for promoting inclusive participation in research in communities of color, and at least 30% of enrollees in most of the vaccine trials were from racial or ethnic minority groups.

PRIORITIZING THERAPEUTIC TRIALS

By March 2020, it became clear that COVID-19 was spreading rapidly and that finding effective therapeutics for both outpatients and inpatients would be critical. The timetable for developing a new small-molecule antiviral was likely to be much longer than a year. Thus, the focus in 2020 was the testing of therapeutic agents developed for other diseases (so-called "repurposing") and the development and testing of monoclonal antibodies directed at the spike protein of the virus. Initial clinical trial efforts were well intentioned but mostly small and underpowered (many directed at hydroxychloroquine or convalescent plasma)

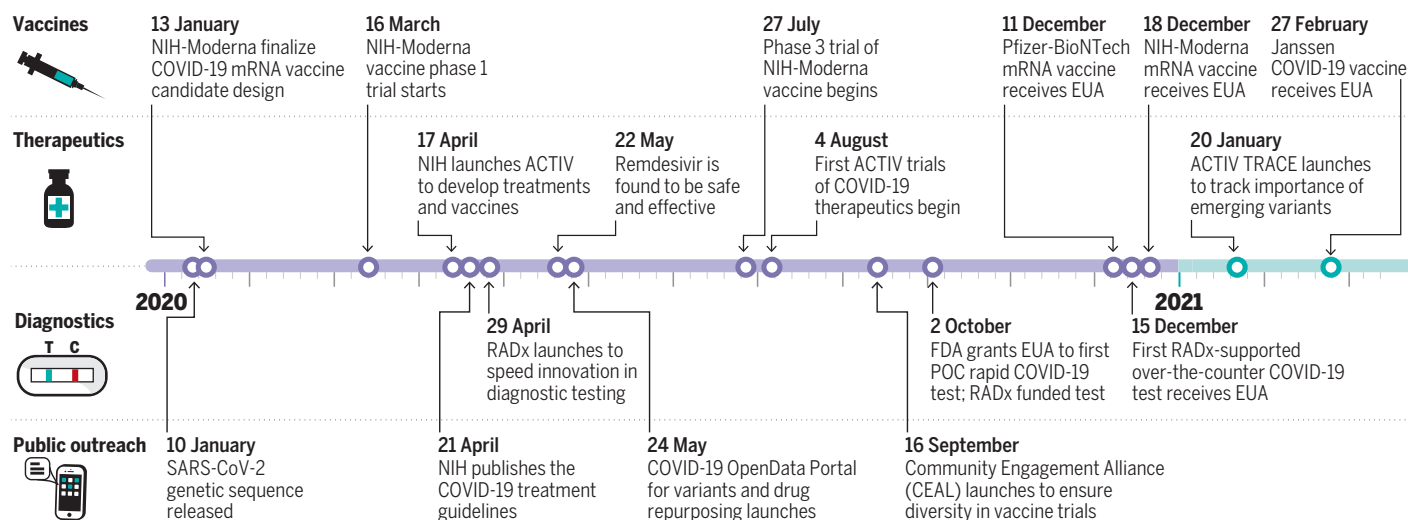
and/or failed to include an appropriate control group (6).

The United States and United Kingdom mobilized in different ways but in close communication. In the United Kingdom, the RECOVERY trial worked through the National Health System to rapidly randomize tens of thousands of hospitalized patients starting in March 2020 with a low-touch approach that featured direct patient recruitment with no need for clinician involvement. An important result was the demonstration in June 2020 that the anti-inflammatory dexamethasone reduced 28-day mortality in patients with severe respiratory complications. Because such a national health care system was lacking in the United States, NIH first tapped into trial networks and contract mechanisms already in place for other infectious and noninfectious diseases. An early result was the launch in February 2020 of the Adaptive COVID-19 Treatment Trial, a randomized, placebo-controlled study of remdesivir, an antiviral that was originally considered for use against other RNA viruses like hepatitis C, Ebola, and Middle East respiratory syndrome coronavirus (MERS-CoV). On the basis of those results, remdesivir received an FDA EUA for COVID-19 in May 2020.

To speed evaluation of other FDA-approved drugs, as well as monoclonal antibodies, NIH launched a public-private partnership called Accelerating COVID-19 Therapeutic Interventions and Vaccines (ACTIV) (<https://fnih.org/our-programs/ACTIV>) in April 2020 (7). This partnership with other federal agencies, 20 companies, and several nonprofit organizations involved more than 100 scientists from all sectors in a team-science approach to achieve rapid testing of potential treatments and mount the largest, most compre-

hensive drug repurposing effort to date. This included a highly efficient, rigorous process for soliciting candidate compounds; assembling uniform dossiers of relevant data and conducting a systematic evaluation of more than 800 agents with various mechanisms of action; and selecting 34 agents for inclusion in ACTIV master protocols. ACTIV incorporated pharmaceutical company, academic, and government statisticians into integrated teams that worked closely with the FDA to build 11 master protocol designs aimed at testing different classes of drugs in multiple patient settings. Many of these used innovative statistical designs and, as understanding of COVID-19 evolved, sought to validate new composite symptomatic endpoints for accelerated regulatory approvals. Using online surveys, ACTIV also developed a targeted inventory of NIH- and CRO-sponsored clinical sites and combined it with geographic mapping, disease incidence data, and visualization capabilities to generate a geotracking tool that enabled researchers to create a hybrid, COVID-19-ready site infrastructure. All of these represent innovations that should enable NIH and its partners to pivot more rapidly to address future pandemics. Managed by a mix of academic experts and the staff at the Foundation for the NIH (FNIH), and funded in part through OWS, ACTIV has so far completed testing of 29 candidates, enrolling more than 22,000 participants in more than 40 substudies. Six of those candidates have shown compelling evidence of benefit and are now approved for clinical use. Nineteen (including ivermectin) have been shown definitively to be ineffective, which is valuable knowledge to reduce misinformation and focus on providing effective treatments to appropriate patients.

Key milestones in developing COVID-19 vaccines, therapeutics, diagnostics, and public outreach



To help guide decisions by health care workers, NIH also convened a panel of medical and regulatory experts early in the pandemic to review and synthesize available data from clinical trials and other study reports. Although not a typical role for NIH, the first NIH COVID-19 treatment guidelines (<https://www.covid19treatmentguidelines.nih.gov/>) were published in April 2020 at the request of US Department of Health and Human Services (HHS) Secretary Alex Azar, which provided health care workers with guidance on how to use therapeutics (8). Since then, the panel has issued more than 60 updated editions, and the guidelines have been visited more than 45 million times.

The repurposing of existing approved compounds for any disease, particularly a new infectious disease threat, is worth a major investment because, if successful, this approach can save time and potentially many lives. Yet given the high chance of trial failure for repurposed drugs, development of therapeutics based on intimate knowledge of the specific pathogen remains important. Following the examples set by herpesvirus and HIV research and with prior investments in the molecular biology of coronaviruses, the experience with COVID-19 has again underscored the importance of empowering programs to identify specific targeted small molecules against an emerging pandemic pathogen (9). Monoclonal antibodies and small-molecule oral antiviral drugs [nirmatrelvir and ritonavir (Paxlovid) and molnupiravir (Lagevrio)] that target SARS-CoV-2 and were initially authorized for emergency use by the FDA have provided substantial benefit in limiting the severity of disease in high-risk individuals. Still, more work on antivirals, especially those with different mechanisms of

action, is needed and is now being pursued for SARS-CoV-2 by NIH's Antiviral Program for Pandemics (<https://www.niaid.nih.gov/research/antivirals>) and other academic and industry efforts.

STREAMLINING DEVELOPMENT OF DIAGNOSTIC TESTS

Testing for SARS-CoV-2 got off to a slow and frustrating start in the United States. Even after reliable assays based on polymerase chain reaction (PCR) had been developed, testing had to be carried out in central laboratories, and the return of results often took several days. By the time someone received a positive result, they had often already exposed others if they had not self-quarantined. What was needed was a way to support innovative product development by businesses and academic centers that had new ideas about diagnostics and a promise to reach the market in a matter of weeks, rather than years. In April 2020, just 5 days after receiving funding through a special appropriation from Congress, NIH launched the Rapid Acceleration of Diagnostics (RADx) initiative (<https://www.nih.gov/research-training/medical-research-initiatives/radx>) and set up a system for inventors to pitch their diagnostic platforms to a group of experts in engineering, technology, manufacturing, and business development (10). These experts evaluated the most promising technologies through a rigorous, multi-step process known as an innovation funnel (11). Those that achieved specific milestones received ongoing regulatory advice from the FDA; additional funding for development, optimization, and validation; and ultimately EUA by the FDA. NIH, the FDA, and their RADx partners also established the capability to accelerate EUAs for home rapid antigen

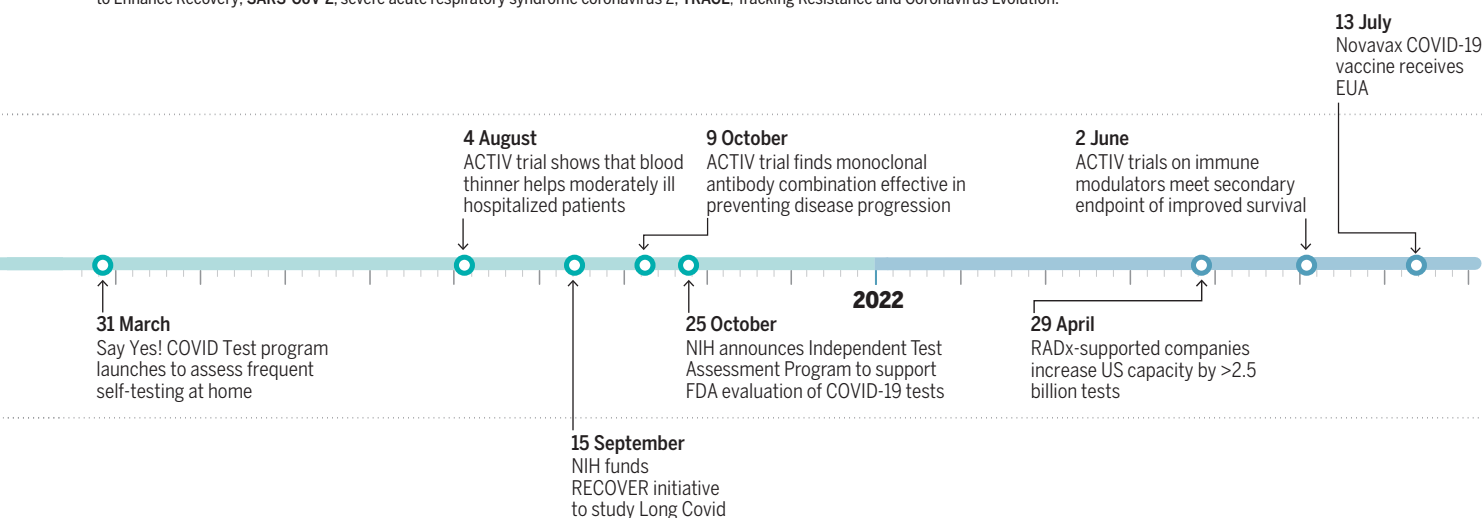
tests and, through the RADx Independent Test Assessment Program (ITAP), evaluate tests at risk for reduced accuracy because of new variants (12). Through this approach, new and well-validated tests were broadly reaching the market in just a few months. At the time of this writing, 49 tests have been granted EUA—16 that are lab-based, 20 that are point-of-care, and 13 that are home tests. About 3 billion tests were added to US capacity from RADx, which helped drive a national paradigm shift in which rapid home and point-of-care tests have become the dominant form of testing (13).

An additional component of this effort that focused on underserved populations, RADx-UP (<https://radx-up.org/>), worked with community partners to identify effective strategies for reducing disparities in COVID-19 testing and addressing other health needs in these communities.

LOOKING TO THE FUTURE

Although the worst days of the pandemic may be behind us, the timeline of the biomedical research community's response to COVID-19 is still being written. The novel coronavirus and its variants will likely continue to present considerable public health challenges around the globe for years or even decades, requiring continued vigilance and sustained support for development of updated vaccines, tests, and therapies. Among the most frustrating challenges is the syndrome of post-acute sequelae of SARS-CoV-2 (PASC), often referred to as Long Covid. The heterogeneity of symptoms; differences in severity; unknown incidence, prevalence, and duration; and sometimes delayed onset of new and varied symptoms all contribute to difficulty in recognizing the

ACTIV, Accelerating COVID-19 Therapeutic Interventions and Vaccines; EUA, emergency use authorization; FDA, US Food and Drug Administration; NIH, National Institutes of Health; POC, point of care; RADx, Rapid Acceleration of Diagnostics; RECOVER, Researching COVID to Enhance Recovery; SARS-CoV-2, severe acute respiratory syndrome coronavirus 2; TRACE, Tracking Resistance and Coronavirus Evolution.



potential important health impact of PASC. Early reports in the literature and discussions within the medical community were largely anecdotal. Recognizing the potential substantial health impact of PASC, NIH and HHS sought funding in the fourth quarter of 2020, which enabled the 2021 launch of a comprehensive program, called the NIH Researching COVID to Enhance Recovery (RECOVER) initiative (<https://recover-covid.org/>), which is already yielding data and results.

Among the efforts underway are those to understand why many individuals who recover from an initial infection later go on to develop new and potentially debilitating symptoms (14). Is this persistence of the virus? A consequence of the microvascular thromboses that can be part of the acute illness? An immune system on high alert that is unable to reset? To explore hypotheses such as these, RECOVER has funded more than 40 research projects that aim to advance knowledge about how COVID-19 affects different

body tissues and organs. Many of these investigator-initiated pathobiology studies are using RECOVER clinical data and specimens and involve teams working collaboratively in multiple cross-cutting areas, for example, immunology, to accelerate the breadth, depth, and pace of knowledge acquisition, particularly for clinical phenotypes and subphenotypes. Clinical trials to prevent and treat these lingering effects of COVID-19 are being initiated.

An overarching theme among lessons learned from this experience (see the box) is the need for ongoing global surveillance and advanced readiness to deal with emerging pathogens. We must sustain our current focus on pandemic preparedness and resist the temptation to slip back into complacency. Substantial resources will be needed to improve and streamline disease surveillance and reporting systems in the United States and around the world. Likewise, the research and policy communities must invest in steps now to encourage development

of candidate vaccines, targeted therapeutics, and point-of-care diagnostics for future predictable pathogens. The G7's 100 Days Mission (<https://www.gov.uk/government/publications/100-days-mission-to-respond-to-future-pandemic-threats>) aims to formalize this goal by supporting the kind of advanced preparation that will make diagnostics, therapeutics, and vaccines available within 100 days of the emergence of a pandemic pathogen.

The COVID-19 pandemic has also shone a bright light on the limitations of our current science communications systems to convey accurate information to the public, especially when faced with an avalanche of misinformation and disinformation coming from social media. Serious consideration of how better to empower trusted sources of information at the local level is needed, as is additional behavioral research on how to motivate rational decision-making about personal health care in the face of the current divisiveness of societies and an erosion of trust in science.

Perhaps the most valuable lesson that COVID-19 has taught the research community—and hopefully society more broadly—is the importance of collective effort and continuous investment in basic and applied research. It takes more than individual ingenuity and hard work for biomedical research to respond swiftly and effectively to a rapidly emerging public health challenge. For this pandemic, it required the coordinated efforts of thousands of creative researchers, administrators, and community partners who were supported by much needed resources and provided with rapid, free access to decades of discoveries made by their scientific forebears. ■

Lessons from COVID-19 for biomedical research

Supporting science

- Invest broadly in basic, undirected virology, structural biology, genomics, molecular biology, immunology, epidemiology, and other key disciplines to build fundamental knowledge.
- Support local and global surveillance to achieve the earliest possible detection of an emerging pathogen.
- Begin now to develop vaccines (to phase 1), targeted therapeutics, and point-of-care diagnostics for the most likely future pathogens.
- Stabilize and sustain large-scale global clinical trial networks to further enhance engagement with community hospitals and international partners. Keep these “warm” and ready for action when needed.
- Ensure immediate public release of research results.
- Build trust through ongoing support of community-engaged networks that are based on partnerships between community organizations and scientists.
- Make a major investment in behavioral and social science research to develop more effective ways of addressing vaccine hesitancy, crisis management, and other responses to public health messages.

Responding when a pandemic pathogen emerges

- Engage partners from all research and development sectors from the start as a critical enabler to bring vaccines, drugs, and diagnostics on a large scale to people worldwide.

- Prioritize shared agreement among research partners about openness of data and lack of concern about who gets credit.
- Encourage upfront development of master protocols for clinical trials, with details on design, scale, and endpoints agreed to by all parties (15).
- Obtain substantial resources quickly to support the development and optimization of vaccines, therapeutics, diagnostics, independent diagnostic validation, and advanced clinical trials.
- Ensure that prepurchase agreements derisk the major push needed from industry and provide researchers with downstream access to data, specimens, and products.
- Require diversity of trial participants for equity and scientific credibility.
- Shorten timetables for clinical trials. Use simultaneous adaptive phase 2 and 3 approaches, rather than sequential phases with down time between.

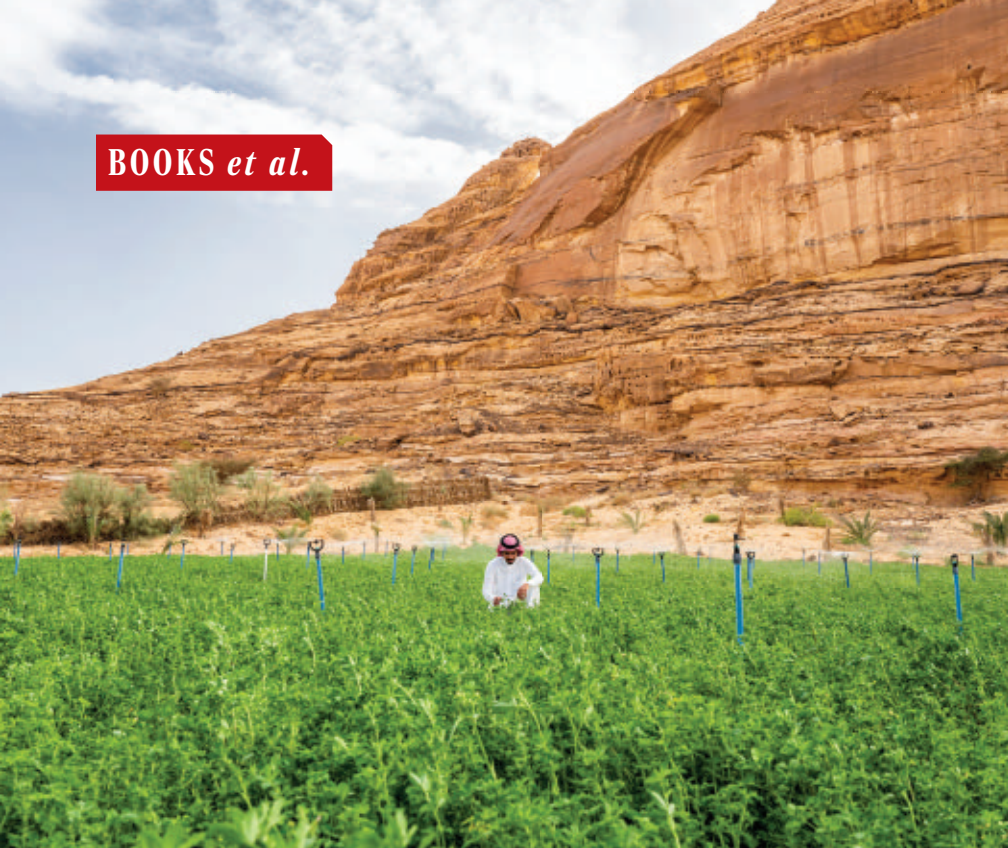
Moving research findings into the clinic

- Closely involve regulators to avoid missteps that can cost months.
- Establish a rigorous, trustworthy clinical guidelines system to translate research findings into clinical practice in real time.
- Develop and deploy a creative and rapid-fire communications network that clarifies the provisional nature of scientific conclusions but uses all forms of media to provide accessible and accurate information to the public, especially to underserved communities.

REFERENCES AND NOTES

1. J. D. Sachs *et al.*, *Lancet* **400**, 1224 (2022).
2. N. Lurie, T. Manolio, A. P. Patterson, F. Collins, T. Frieden, *N. Engl. J. Med.* **368**, 1251 (2013).
3. A. S. Fauci, *Science* **372**, 109 (2021).
4. M. Slaoui, M. Hepburn, *N. Engl. J. Med.* **383**, 1701 (2020).
5. M. P. Andrasik *et al.*, *PLOS ONE* **16**, e0258858 (2021).
6. H. C. Lane, A. S. Fauci, *N. Engl. J. Med.* **384**, 755 (2021).
7. F. S. Collins, P. Stoffels, *JAMA* **323**, 2455 (2020).
8. F. S. Collins, *Science* **371**, 1081 (2021).
9. B. J. Tromberg *et al.*, *N. Engl. J. Med.* **383**, 1071 (2020).
10. NIH, RADx Tech/ATP/ITAP dashboard; <https://www.nibib.nih.gov/covid-19/radx-tech-program/radx-tech-dashboard>.
11. S. C. Schachter, J. A. Parrish, *IEEE Open J. Eng. Med. Biol.* **2**, 118 (2021).
12. HHS Press Office, “New HHS actions add to Biden administration efforts to increase access to easy-to-use over-the-counter COVID-19 tests” (HHS, 2021); <https://www.nibib.nih.gov/news-events/newsroom/new-hhs-actions-add-biden-administration-efforts-increase-access-easy-use-over-counter-covid-19-tests>.
13. NIH, Authorized tests for COVID-19 diagnostics; <https://www.nibib.nih.gov/covid-19/radx-tech-program/authorized-tests>.
14. E. R. Pfaff *et al.*, *Lancet Digit. Health* **4**, e532 (2022).
15. L. LaVange *et al.*, *Ann. Intern. Med.* **174**, 1293 (2021).

10.1126/science.adf5167



A farmer tends an alfalfa crop in Al-'Ula, Saudia Arabia.

GEOGRAPHY

Arid lands, imperial ambitions

Desert knowledge exchange cloaked imperial goals, argues a political geographer

By **Pamela Karimi**

Whether in search of information on oil excavation, water management, or agricultural infrastructure in the Middle East, many scholars often inevitably end up not in the Arabian peninsula but in the American archives, where there is an abundance of records of US experts and politicians who exported technical assistance to the region. In *Arid Empire*, Natalie Koch reveals a more complex account of the reciprocal relationships between Arabia and the drylands of the American Southwest from their origins in the mid-19th century through today. These narratives are informed by archival documents, newspaper clips, governmental reports, university records, and visual materials.

Divided into six chapters, the narrative begins with the true tale of a caravan of camels led by a Syrian cameleer that were enlisted to help the US Army take control of the southwest terrains and its Native

American populations in 1856. Although the camel corps was unsuccessful, and ultimately overshadowed by the ensuing Civil War, the country's interest in expertise, knowledge, and experiments in the deserts of the Middle East endured, and an exchange of agricultural practices flourished.

By the mid-20th century, however, an imbalanced relationship between the two arid regions had begun to emerge. In 1942, the Roosevelt administration embarked on a mission that aimed to transfer agricultural practices from Arizona to Saudi Arabia and the Trucial States under the pretense of improving the lives of the Arab people. However, the initiative brought with it a lucrative business, selling machinery, storage and processing resources, and trade materials. This hidden supply chain was an indication, argues Koch, of the imperialistic ambitions of the US in the Middle East. This and other examples reveal how the US strategy in the Middle East was not dissimilar from those employed by white

European settlers to secure resources on Native American lands and gain revenue from them.

In addition to these ulterior motives, Koch maintains that the aid offered by the US was often not sustainable. The agricultural solutions the country helped put in place to mitigate food shortages in Arabia during the 1970s oil crisis, for example, worked briefly, but a lack of water resources rendered this program wide of the mark over the long term. Meanwhile, desalination techniques, an export from the University of Arizona solar and environmental research laboratories, had also failed to deliver meaningful change to the Middle East by the end of the 1970s and remain unrealized to this day.

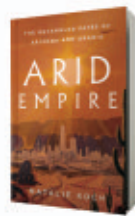
Lest we assume that desert politics are remnants of a bygone era, Koch argues that they also play a vital role in how we think about the future. Deserts frequently serve as platforms for oft-untenable apocalyptic visions of a warming planet and imminent challenges of securing food, energy, and water. Focusing on Biosphere 2—formerly an analog for human settlements on lunar surfaces and currently an Earth system science research facility in Oracle, Arizona—Koch shows how imperialism similarly pervaded this project, drawing on the trope of environmental salvation to ultimately build settler colonial structures of exclusion and Indigenous dispossession.

In the book's final pages, readers learn that a science-based knowledge economy has also come to shape the development agendas of today's Arab ruling elites. Regrettably, ambitious projects such as the Masdar eco-city—a sustainable urban community in Abu Dhabi that took inspiration from Biosphere 2—did not fully deliver their promises of overcoming climate change and reaching net-zero emissions.

Without falling into the traps and tropes of orientalist discourse and postcolonial theory, Koch successfully capitalizes on a series of carefully documented case studies to unpack the United States' often elusive and indirect pseudocolonial ambitions. In doing so, she reveals

how, in the name of scientific progress and technological advancement, US policymakers and private companies—with close ties to institutions of higher education—gained access to desert resources and profited from them, all while claiming to reject old-world colonial attitudes. The outcomes were nonetheless similar. ■

10.1126/science.adf4887



Arid Empire:
The Entangled Fates
of Arizona and Arabia
Natalie Koch
Verso, 2023. 208 pp.

The reviewer is at the Department of Art Education, Art History, and Media Studies, University of Massachusetts, Dartmouth, Dartmouth, MA 02747, USA. Email: pamela.karimi@umassd.edu

ECONOMICS

Seller's market

A pair of historians explain how market fundamentalism leads to science denial

By H. Holden Thorp

The landmark book *Merchants of Doubt*, by Naomi Oreskes and Erik Conway, meticulously documented how prominent scientists lacking relevant expertise used their credentials and influence to enhance conservative opposition to government regulation on matters ranging from tobacco and secondhand smoke to climate change (1). As Oreskes and Conway explain in their outstanding new book, *The Big Myth*, the pair were challenged by Senator Tim Wirth to produce a companion book that explained what to do about the findings presented in *Merchants*. That is not precisely where they ended up—it is probably more accurate to say that *Merchants* gave us the “how” of science denial, and *The Big Myth* gives us the “why”—but the new book is no less important.

The “why” of science denial, the authors argue, is market fundamentalism—the belief that free markets unencumbered by government regulation can solve any problem through what Ronald Reagan repeatedly called the “magic of the marketplace.” Although popularized in the 1980s, this philosophy was the result of 100 years of

methodical efforts to build the political case—and resulting political coalition—for doubting evidence that favored government regulation. The authors weave an engaging tale with compelling underlying research that shows why scientific research on topics ranging from climate change to COVID-19 is so effortlessly dismissed.

Many of the seeds of market fundamentalism were planted in the 1920s, when struggles ensued over how to provide electricity to rural America. Specifically, great debates occurred over whether rural electrification was best provided by private entities or by regulated public-private partnerships. To fight government involvement, power companies formed a trade association, the National Electric Light Association (NELA), that instigated a pro-business propaganda campaign that included introducing materials into grade-school textbooks. NELA established a framework that many future anti-regulation campaigns would follow.

The next big move by market fundamentalists occurred in the late 1930s, when an industry group called the National Association of Manufacturers (NAM) cultivated what they called the “tripod of freedom.” This concept held that three aspects of American life were inseparable: civil and religious liberty, representative democracy, and free private enterprise. NAM propagated this idea through a radio program called *The American Family*

The Big Myth: How American Business Taught Us to Loathe Government and Love the Free Market

Naomi Oreskes and Erik M. Conway
Bloomsbury, 2023. 576 pp.



Robinson, which reenvisioned the 1812 novel *The Swiss Family Robinson* through a lens of free enterprise in an effort to convince Americans that free markets were coequal with democracy and personal liberty. With that idea in place, it was easy to argue that impediments to free enterprise through government regulation were tantamount to the dismantling of the democratic system and encroachment on individual freedom.

In subsequent sections, eye-opening episodes abound. In chapter 6 (“The Big Myth Goes West”), the authors expose how Rose Wilder Lane, a founder of American libertarianism and the daughter of *Little House on the Prairie* author Laura Ingalls Wilder, shaped her mother’s children’s novels to serve as instruments of market fundamentalism. In chapter 7 (“A Questionable Gospel”), they explain how Christianity was reframed in the mid-20th century by leaders such as Norman Vincent Peale from a pursuit focused on compassion and collective welfare to one of personal liberty. And in chapter 9 (“Steering the Chicago School”), they explain how the “Chicago school” of free-market economics—a philosophical framework that emerged at the University of Chicago during the 1930s and was exemplified by the work of economist Milton Friedman—provided an intellectual basis for laissez-faire economics that was validated by numerous Nobel Prizes. Astoundingly, although Friedman’s ideas have never been rigorously verified by experiment, they remain prominent in the field of economics.

The COVID-19 pandemic, which emerged as Oreskes and Conway were writing *The Big Myth*, provides a perfect endpiece for the book. Here, the authors show how 100 years of anti-regulation propaganda enabled vaccine hesitancy and pushback over mask mandates.

For scientists who are dumbfounded by anti-science attitudes, understanding this history is vital. Only by understanding the forces that cause science denial can anything be done about it. Like *Merchants of Doubt* before it, *The Big Myth* offers crucial insight into this phenomenon. ■

REFERENCES AND NOTES

1. N. Oreskes, E. M. Conway, *Merchants of Doubt* (Bloomsbury, 2010).



One hundred years of anti-regulation propaganda preceded mask pushback during the COVID-19 pandemic.

10.1126/science.adf5459

China's marine and coastline conservation efforts have not reversed the decline of seagrass meadows.

Edited by Jennifer Sills

Protect seagrass meadows in China's waters

Seagrass meadows are crucial habitats that contribute to biodiversity, food security, and climate mitigation (1). China harbors 22 seagrass species, accounting for about 30% of global seagrass plant diversity (2). Seagrasses were once common across China's coastlines, but since the 1970s, six seagrass species and more than 80% of the seagrass meadows in China's coastal waters have disappeared (2, 3), compared with a global decline of 29% of known seagrass meadows since 1879 (4). The remaining seagrass meadows suffer from sparse coverage and habitat fragmentation (5), with negative cascading effects on the species that rely on them. In August 2022, the seagrass mega-herbivore *Dugong dugon* became functionally extinct in Chinese marine waters (6), highlighting the urgency of seagrass conservation.

China has taken steps to protect and restore marine and coastal ecosystems, including seagrasses. A seagrass survey from 2015 to 2020 identified about 26,000 ha of remaining seagrasses in China (3, 7). Three protected areas (about 40,953 ha in total) that include seagrasses have been established (8), and some seagrasses have been protected through China's recent ecological redline policy (9). Seagrass meadows were also listed in the National Plan for Major Conservation and Restoration Projects of Important Ecosystems (2021–2035) (10), and some restoration projects of seagrass meadows have been implemented. However, these efforts have not yet been able to effectively reverse the degradation of China's seagrass meadows.

Urgent action is needed to maintain and protect the remaining seagrass meadows in China. Due to incomplete spatial and seasonal coverage of previous surveys, the exact spatial distribution of China's seagrass meadows is still unknown. Hence, long-term and large-scale monitoring of seagrass meadows should be conducted to discover unknown seagrass habitats; otherwise, they could disappear before they have been discovered. In addition, China must improve seagrass protection. The existing protected areas for seagrasses are all located in southern China, and there are no seagrass reserves at all in the temperate waters of northern China (8). Finally, human activities such as land reclamation, harbor construction, eutrophication, aquaculture, and overfishing, which pose substantial threats to seagrass meadows in China, should be regulated (2, 8).

The Wuhan Declaration of the Convention on Wetlands, adopted in November 2022, calls for priority conservation and management of vulnerable ecosystems, including seagrass meadows (11). The UN Decade on Ecosystem Restoration also encourages the active restoration of billions of hectares of ecosystems worldwide, including seagrasses (12). China should respond to these calls by establishing a seagrass conservation and restoration plan with goals and actions at both national and local scales.

Jianguo Du^{1,2}, Bin Chen^{1,2}, Ivan Nagelkerken³, Shiquan Chen⁴, Wenjia Hu^{1,2*}

¹Third Institute of Oceanography, Ministry of Natural Resources, Xiamen 361005, China. ²Key Laboratory of Marine Ecological Conservation and Restoration, Ministry of Natural Resources, Xiamen 361005, China. ³School of Biological Sciences and the Environment Institute, The University of Adelaide, Adelaide, Australia. ⁴Hainan Academy of Ocean and Fisheries Sciences, Haikou 570125, China.

*Corresponding author. Email: huwenjia@tio.org.cn

REFERENCES AND NOTES

1. R. Unsworth *et al.*, *Science* **377**, 609 (2022).
2. F. Y. Zhen *et al.*, *Biodivers. Sci.* **21**, 517 (2013) [in Chinese].
3. Y. Zhou, "The 'Lung of the Sea' in China must be taken care of," *China Science Daily* (2022); <https://news.sciencenet.cn/sbhtmlnews/2022/9/371226.shtml> [in Chinese].
4. M. Waycott *et al.*, *Proc. Natl. Acad. U.S.A.* **106**, 12377 (2009).
5. Z. J. Wu *et al.*, *Mar. Environ. Sci.* **40**, 542 (2021) [in Chinese].
6. M. L. Lin *et al.*, *R. Soc. Open. Sci.* **9**, 211994 (2022).
7. S. Yu *et al.*, *Atlas of Seagrass in China* (China Ocean Press, Beijing, 2022) [in Chinese].
8. W. J. Hu *et al.*, *Ecol. Indic.* **129**, 107960 (2021).
9. Y. Bai *et al.*, *Nat. Commun.* **9**, 1 (2018).
10. National Development and Reform Commission and Ministry of Natural Resources, "National Plan for Major Conservation and Restoration Projects of Important Ecosystems (2021–2035)" (2020); <https://www.ndrc.gov.cn/xxgk/zcfb/tz/202006/P020200611354032680531.pdf> [in Chinese].
11. Ramsar, "Wuhan Declaration" (2022); <https://www.ramsar.org/document/wuhan-declaration>.
12. UN Decade on Ecosystem Restoration, "Oceans and Coasts" (2021); <https://www.decadeonrestoration.org/types-ecosystem-restoration/oceans-and-coasts>.

10.1126/science.adg2926

Risks of China's increased forest area

Between 2010 and 2020, China increased its forest area by 193,680 km² (1). The country plans to plant 70 billion more trees before 2030 (2). Although the UN's Global Forest Goals regard the increase of forest cover as a primary goal (3), the types of trees and locations selected for planting can determine whether increased cover constitutes a conservation success or an environmental threat.

Based on the UN's definition of "forest" (1), all types of tree plantations can be classified as forest. Thus, gains in forest cover will not necessarily offset losses of ecosystem services—such as

carbon storage, biodiversity, and water resources—that resulted from native forest loss (4). In China, the increase in forest cover primarily took place in the sensitive dryland areas in the north and west (5). Future efforts are planned in regions even farther north (6), where tree planting can exacerbate water shortages and destroy locally adapted shrubs and grasses (7). These harms are not balanced out by benefits; forestation has limited climate change mitigation potential in dryland regions given their reduced ability to reflect sunlight (known as the albedo effect) (8).

The absolute power of China's central government makes implementing "land greening" programs at the national scale easier but allows local governments little flexibility, regardless of the suitability of their region. The central government's focus on forest cover (9) overlooks key issues such as tree species, forest diversity, bioclimatic location, and planting density. Widespread mortality has been reported in the monocultural forests of world's largest afforestation project, the "Green Great Wall" in northern China (10), which is not surprising given that artificial monocultural forests with fast-growing trees and even-aged stands are highly vulnerable to drought, pest, fire, and emerging disturbance interactions. Before proceeding with China's tree planting goals, carbon fixation efficiency, which varies among tree species, needs to be further evaluated in combination with water cycling and tree longevity (11).

Relying on forest cover as an evaluation measure may backfire on China's forest biodiversity conservation and natural resource protection. Intact primary forests in the south have been deforested and replaced with plantations that produce rubber, timber, fruits, and other non-wood forest products (12). Plantations boost forest cover, but the loss of intact forests, their ecosystem function, and the services they provide cannot be compensated with reforestation activities alone (4).

Halting the destruction of native vegetation is far more critical than increasing forest cover. By adhering to a national tree-planting plan without taking proper precautions for the protection of biodiversity, China is increasing ecological and social risks. Policymakers should give more consideration to site-specific, natural reforestation with appropriate tree species. Focusing on reducing industrial emissions will meet environmental goals more effectively than simplistically increasing forest cover.

Yujie Niu^{1,2*}, Victor Squires³, Anke Jentsch¹

¹Disturbance Ecology and Vegetation Dynamics, Bayreuth Center of Ecology and Environmental

Research, University of Bayreuth, Bayreuth, Bavaria Germany. ²College of Grassland Science, Gansu Agricultural University, Lanzhou, Gansu, China. ³University of Adelaide, Adelaide, SA, Australia.

*Corresponding author.

Email: yujie.niu@uni-bayreuth.de

REFERENCES AND NOTES

1. Food and Agriculture Organization of the United Nations, "Global forest resources assessment 2020: Main report" (2020).
2. The World Economic Forum, "China will aim to plant and conserve 70 billion trees by 2030 as part of the global tree movement" (2022).
3. United Nations, "Global forest goals and targets of the UN strategic plan for forests 2030" (2019).
4. P. Curtis, *et al.*, *Science* **361**, 1108 (2018).
5. C. Gerlein-Safdi *et al.*, *One Earth* **2**, 98 (2020).
6. National Forestry and Grassland Administration, "Timely start to the sixth phase of the 'Great Green Wall'" (2022); www.forestry.gov.cn/sbj/5342/20220801/101831516654000.html [in Chinese].
7. S. Cao, L. Chen, X. Yu, *J. Appl. Ecol.* **46**, 3 (2009).
8. S. Rohatyn *et al.*, *Science* **377**, 1436 (2022).
9. National Forestry and Grassland Administration, "'Forest Chief System Supervision and Assessment Measures' was released" (2022); www.forestry.gov.cn/main/58/20220309/095312966770391.html [in Chinese].
10. Y. Ji *et al.*, *J. Arid Environ.* **174**, 104076 (2020).
11. C. Körner, *Science* **355**, 130 (2017).
12. N. Hoang, K. Kanemoto, *Nat. Ecol. Evol.* **5**, 845 (2021).

10.1126/science.adg0210

Invest in early-career researchers in Brazil

Luiz Inácio Lula da Silva started his third term as president of Brazil in January. In his November 2022 speech at the United Nations Climate Change Conference (COP27), Lula committed to halt deforestation, stop illegal mining and other environmentally damaging activities, and make the country a global leader in addressing climate change (1). He has also declared that Brazil's path to becoming a developed and self-sufficient country depends on science, technology, and innovation (1, 2). His position on these matters has already unlocked international investments for the country, which will likely increase (3). To make good on his promises, Lula should invest in Brazil's early-career scientists.

In the past two decades, the number of students graduating with PhDs in Brazil more than doubled, and Brazil's scientific output grew substantially (4–6). Between 1991 and 1995, Brazil's scientists published 24,039 papers, earning Brazil a world ranking of 23rd based on numbers of papers published; between 2007 and 2011, Brazil's scientists published 147,503 papers, increasing its global ranking to 13th (5). In 2011, during Lula's second term, Brazil continued its trend of investing in science by starting the Science without Borders government postgraduate scholarship

program, which supported study abroad for science, technology, engineering, and mathematics students (7).

Since 2015, however, repeated budget cuts have damaged the country's educational and academic systems (8, 9). As a result, many of Brazil's 100,000 highly trained early-career scientists, including graduates of the Science without Borders program, are currently unemployed or working in jobs outside of science (7, 10). In 2019, they faced unemployment rates 12 times higher than the global average (6).

Investing in the expertise of young scientists will help Brazil pursue the environmental goals set by the Paris Accord and the Kunming-Montreal Global Biodiversity Framework (both ratified by Brazil) (11). Early-career scientists can devote their skills to helping Brazil accomplish the 2030 Agenda for Sustainable Development, adopted by the UN General Assembly in 2015 (12), and they can contribute to building a green economy based on human capital, technology, and innovations rather than natural resources exploitation. We urge the new government to develop programs to attract and retain researchers who earned their qualifications over the past decade and can now focus on Brazil's development and economic growth.

Thais B. Guedes^{1,2*}, José Alexandre F. Diniz-Filho³, Luisa Maria Diele-Viegas⁴, João Filipe R. Tonini⁵, Alexandre Antonelli^{2,6,7}

¹Instituto de Biologia, Universidade Estadual de Campinas, Campinas, São Paulo, Brazil.

²Gothenburg Global Biodiversity Centre, University of Gothenburg, Göteborg, Sweden. ³Departamento de Ecologia, Universidade Federal de Goiás, Goiânia, Goiás, Brazil. ⁴Instituto de Biologia, Universidade Federal da Bahia, Salvador, Bahia, Brazil. ⁵Department of Biology, University of Richmond, Richmond, VA, USA. ⁶Royal Botanic Gardens, Kew, Richmond, Surrey, UK. ⁷Department of Biology, University of Oxford, Oxford, UK.

*Corresponding author.

Email: thaisbguedes@yahoo.com.br

REFERENCES AND NOTES

1. J. Spring, W. James, "COP 27: Greeted like a rock star Brazil's Lula promise to protect Amazon," *Reuters* (2022).
2. H. B. Nader, *Science* **378**, 931 (2022).
3. M. Murray, R. More, "Germany willing in principle to revive Amazon Fund—development ministry," *Reuters* (2022).
4. C. A. Nobre, *Nature* **574**, 455 (2019).
5. J. Leta, B. Thijs, W. Glänzel, *Encontros Bibli Rev. Eletrôn. Bibliotec. Ciênc. Inform.* **18**, 51 (2013).
6. B. Roscoe, I. Soares, "Desemprego entre mestres e doutores no Brasil chega a 25%," *Correio Braziliense* (2019) [in Portuguese].
7. F. Marques, *Pesquisa FAPESP* **256**, 27 (2017) [in Portuguese].
8. H. Escobar, "Orçamento 2021 condena ciência brasileira a 'estado vegetativo,'" *Jornal da USP* (2020) [in Portuguese].
9. R. O. Andrade, *Nature* **572**, 575 (2019).
10. C. H. L. Silva Júnior *et al.*, *Science* **374**, 948 (2021).
11. S. G. Latoya Abulu, "Nations adopt Kunming-Montreal Global Biodiversity Framework," *Mongabay* (2022).
12. United Nations, "Transforming our world: The 2030 Agenda for Sustainable Development" (2015).

10.1126/science.adg4131

RESEARCH

IN SCIENCE JOURNALS

Edited by
Michael Funk

WILDFIRES

Feedback promotes fire

How much might interactions between wildfires and local meteorology affect short-term wildfire variability? Huang *et al.* show that large-scale feedbacks are an important driving force on extreme fires in the Mediterranean, the West Coast of the United States, and Southeastern Asia. Smoke

aerosols trap and absorb solar energy, changing local wind and rainfall patterns and ultimately enhancing fire emissions. These interactions constitute a positive feedback that increases air pollution exposure and accelerates wildfire expansion.

—HJS *Science*, add9843, this issue p. 457

Aerosols from wildfire smoke, pictured here in Southern California, generate a weather feedback loop that can intensify fires.

ORGANIC CHEMISTRY

Making the most of synthesis algorithms

Software that predicts synthetic routes to complex molecules has been rapidly increasing in sophistication. The extent to which the algorithms replicate or complement human intuition nonetheless remains uncertain. Lin *et al.* challenged a commercial retrosynthesis program with an alkaloid for which more than 30 syntheses had been reported in the literature. The algorithm consistently proposed a Mannich reaction that no prior approach had featured, although drawbacks in the rest of the route benefited from human intervention. By devising a supplemental graph-based method of prioritizing key steps, the authors achieved the shortest synthesis of this target. —JSY

Science, ade8459, this issue p. 453

NEUROSCIENCE

Attention alters cortical feedback

The neural underpinnings of attention are still incompletely understood. Debes and Dragoi present causal evidence that the attentional modulation of individual neurons and cell populations is performed by cortical feedback projections. Suppressing cortical area V4 feedback axons to area V1 without altering local and feedforward intracortical inputs virtually abolished the attention-induced benefits on response gain, the accuracy of network computations, and the attentional modulation of postsynaptic area V4 neuron responses. These findings indicate that feedback signals modulate visual cortical responses only when stimuli are attended. Because feedback has been hypothesized

to control other top-down processes, these results could have implications for a broad range of phenomena across many modalities. —PRS

Science, ade1855, this issue p. 468

CIRCADIAN RHYTHMS

Tracking human circadian gene expression

Rhythmic circadian changes in gene expression have been well documented in model organisms, but data are limited from primates and particularly humans. Talamanca *et al.* developed an algorithm that allowed them to assign a circadian phase to each individual in a set of about 900 human donors. This approach allowed them to detect circadian changes in gene expression in samples from 46 tissues. Women showed higher rhythmicity of transcripts, especially in liver

and the adrenal gland. The results also confirmed that rhythmicity was generally damped in older individuals. —LBR

Science, add0846, this issue p. 478

ORGANIC CHEMISTRY

Photoredox with chiral counterions

Photoredox catalysis uses light-induced electron transfer between a chromophore and substrate to promote chemical reactivity. In cases in which the substrate does not coordinate to the chromophore, it can be challenging to control stereoselectivity. Das *et al.* report a highly stereoselective approach that pairs a cationic chromophore with a chiral anion. After chromophore reduction, the anion pairs with the activated substrate, in this case an oxidized styrene derivative poised

for [2+2] cycloaddition, and thereby favors the formation of just one of two possible mirror-image products. —JSY

Science, ade8190, this issue p. 494

CELL BIOLOGY

A tale of two Beclin homologs

Cells reclaim nutrients from macromolecules and organelles through the process of autophagy. Quiles *et al.* examined the roles of the highly homologous Beclin1 and Beclin2 in autophagy and mitophagy, the autophagic degradation of mitochondria. Both homologs were required for basal autophagy but were dispensable for stress-induced autophagy. Beclin1 specifically promoted mitophagy, a function that required the phosphorylation of an evolutionarily conserved serine residue in Beclin1 that is not found in Beclin2. —WW

Sci. Signal. **16**, eabo4457 (2023).

ICE STRUCTURE

Milling around glassy ice

Water ice has many crystalline phases, along with a few amorphous structures. The complex structural diagram is important to understand because of the widespread importance of ice. Rosu-Finsen *et al.* discovered a medium-density amorphous ice formed by ball milling hexagonal ice at low temperatures. The distinct density and



Grinding ice in a ball mill, pictured here, at low temperature yielded a new amorphous ice form.

structure helped to identify it as a new form of ice, opening up questions as to the stable amorphous structure of this important material. —BG

Science, abq2105, this issue p. 474

GEOLOGY

Carbon on the early Earth

Black cherts have long been targets for preserved fossils of the oldest microbial organisms, but whether the carbon (which provides the black color) in these cherts is derived from organic activity is controversial. Rasmussen and Muhling have restudied one of the most controversial localities, 3.5-billion-year-old black cherts from the Pilbara region of Northwest Australia. Earlier reports of fossils from this location have been challenged by proposed abiotic sources for the dispersed carbon. Using studies of these rocks and younger analogs, the authors report an abiotic origin from organic-rich hydrothermal fluids. This study has implications for the origins of other black cherts and suggests that hydrothermal fluids may have been a source of organics on the early earth. —DHE

Sci. Adv. 10.1126/sciadv.add7925 (2023).

FLEXIBLE DEVICES

Stretchable hermetic seals

An often overlooked aspect of stretchable electronics and technology is the choice of materials to hermetically protect them. Shen *et al.* devised liquid metal hermetic seals based on eutectic gallium indium for stretchable devices. The low gas permeability and fluidic properties of liquid metals overcome the tradeoff between permeability and modulus that arises with other materials. The authors demonstrate the protection of a stretchable battery and a heat-transfer device that uses volatile liquids. —MSL

Science, ade7341, this issue p. 488

IN OTHER JOURNALS

Edited by Caroline Ash and Jesse Smith

ENVIRONMENTAL ECONOMICS

Water markets boost farms' output

Trading among farmers in the world's largest and most valuable water market enabled 4 to 6% additional irrigated agricultural output from 2007 to 2015. Rafey estimates that in the absence of water trading in Australia's southern Murray-Darling basin (that is, if users had been held to their initial water allocations), farm output would have been as low as if there had been an overall 8 to 12% decline in water. Gains from water trade were particularly substantial during periods of drought. As societies face increased water variability due to climate change, the estimated \$1.5 billion in flow benefits from this market reflect potential returns to public investments in necessary monitoring and coordination in support of a market. —BW

Amer. Econ. Rev. 10.1257/aer.20201434 (2023).

PHOTOCATALYSIS

Toward N₂O emissions abatement

Because of their complex nonequilibrium and ultrafast nature, photoinduced molecular dissociation processes at metal and semiconductor surfaces remain difficult to characterize experimentally. An example is the low-temperature photodecomposition of nitrous oxide (N₂O), the third most potent trace greenhouse gas, on transition-metal oxides, which is poorly understood despite being one of the most promising technologies to reduce N₂O emissions. Using *ab initio* adiabatic and nonadiabatic molecular dynamics, Cheng *et al.* comprehensively investigated N₂O photodissociation on the reduced rutile TiO₂(110) surface. Their simulations revealed the key role of the N₂O^{•-} radical anion lifetime and provide a

fundamental atomistic understanding of the competition and synergy among N₂O photolysis, photothermolysis, and pyrolysis that could be useful in the design of high-performance heterogeneous catalysts for this important photocatalytic reaction. —YS

J. Am. Chem. Soc. **145**, 476 (2022).

METALLOPROTEINS

A crystal ball for metal sites

Metal ions within proteins often form crucial structural or catalytic sites and are thus typically associated with conserved sequence motifs. Cheng *et al.* developed MetalNet, a metal site prediction algorithm that is based on residue co-evolution, an approach that has been used successfully in other contexts for structure and protein complex prediction. MetalNet



Water trading in Australia has significantly benefited farm output there.

recovered many predicted sites consistent with known motifs, and experimental validation of a previously unknown site in a metabolic enzyme revealed a bound zinc ion. —MAF

Nat. Chem Biol. 10.1038/s41589-022-01223-z (2023).

SEED DISPERSAL Through the gut of a duck

Animals are important seed dispersers, and some seeds even benefit from passing through animal guts. These phenomena have been mostly studied in plants with fleshy fruits that have evolved to attract animal dispersers. However, some animals, such as waterbirds, ingest large quantities of seeds that lack fleshy fruit, potentially transporting them long distances during migration. van Leeuwen

et al. created a bioassay to simulate the mechanical and chemical processes of digestion in Anseriformes waterbirds (ducks, geese, and swans) to examine how digestion affects seed survival and germination of 48 plant species. They found that digestive processes aided germination more in plants from wetter habitats, suggesting that some aquatic plants may have evolved to end seed dormancy after digestion by waterbirds. —BEL

Ecography 1, e06470 (2022).

IMMUNOLOGY Unlinked recognition in alloreactivity?

Some individuals who receive blood transfusions develop alloantibodies against donor red blood cells (RBCs) for reasons that are not entirely clear. B cells are typically activated by

CD4⁺ T cells that recognize the same antigen, but not necessarily the same structures or epitopes on that antigen, in a process called linked recognition. Jajosky *et al.* used a model for human blood transfusion and found that linked recognition may not be the whole story. Green fluorescent protein (GFP) was given as an alloantigen to mice, which then received transfusions of RBCs that expressed both intracellular GFP and another unrelated surface alloantigen. These mice subsequently developed antibody responses against the unrelated surface antigen, suggesting that previous priming events against intracellular antigens that are not physically linked to B cell target antigens may enhance naïve B cell responses to their targets. —STS

Blood 10.1182/blood.2022016588 (2023).

GENE EXPRESSION

The demographics of gene expression

Variation in gene expression is known to exist across tissues. It is also influenced by the environment and factors such as age, although this has been difficult to quantify. Using human data from the Genotype-Tissue Expression project, Garcia-Perez *et al.* assessed the effects of age, sex, ancestry, body mass index, and disease state on gene expression and splicing in 46 tissues. The authors found that diseases such as type 1 and type 2 diabetes can have large effects on gene expression, particularly in disease-related tissues, but that ancestry tends to have the strongest effects on RNA splicing. —CNS

Cell Genom. 3, 100244 (2023).

PHENOLOGY

Uncoupling interactions

The coordination of seasonal natural history events (phenology) governs species interactions within ecosystems. For example, when a migratory bird returns from its wintering range, the evolutionary expectation is that the animals or plants that it feeds on will have emerged after postwinter dieback or diapause. Climate change can alter phenology and species interactions. Prather *et al.* analyzed a suite of taxa that have been studied at a field station in Colorado's Rocky Mountains for decades and found that species' responses varied significantly across different climate components. Whereas first activity dates for most species became earlier in response to earlier snowmelt and warmer springs, species' responses to other climatic traits varied. Responses in some cases can occur in opposite directions; for example, root damage from increased freeze-thaw cycles can delay plant growth in the spring. Such mismatches have the potential to uncouple long-persisting interactions, leading to possible ecosystem instability. —SNV

Proc. R. Soc. London Ser. B 10.1098/rspb.2022.2181 (2023).

ALSO IN SCIENCE JOURNALS

Edited by Michael Funk

CORONAVIRUS

Learning from uncertainty in a pandemic

The COVID-19 pandemic has highlighted the importance of mathematical modeling to analyze surveillance data and of epidemiological investigations to inform public health policy. In a Perspective, Cauchemez *et al.* discuss the importance of accurate data collection and the types of data that are most helpful for assessing important health measures such as infection incidence, severity, population immunity, and vaccine effectiveness. Mathematical models have been essential in estimating key parameters, building short-term forecasts and medium-term intervention scenarios, and anticipating the impact of variants and of vaccination, but the modeling toolbox requires more development to ensure robust preparations for future pandemics. —GKA

Science, add3173, this issue p. 437

PLANT SCIENCE

Forces and fibers

Surrounded by cell walls, plant cells are constrained in shape and mobility as they develop. Coen and Cosgrove review the latest insights into plant morphogenesis and how mechanical constraints build complex plant shapes. They thus explain how mechanical forces act on plant tissues at scales from molecular to macro. —PJH

Science, ade8055, this issue p. 452

ORGANIC CHEMISTRY

Pulling C out of NHCs

Methods to generate free carbon atoms are typically incompatible with the selective solution-phase chemistry pertinent to pharmaceutical synthesis. Kamitani *et al.* now report that heating N-heterocyclic carbene (NHC) compounds can result in clean carbon atom transfer to unsaturated amides, producing lactams

with concurrent loss of diamine (see the Perspective by Nakano and Lupton). This reactivity mode is somewhat surprising given the comparative stability of NHCs and offers a potentially versatile means of introducing unadorned carbon centers to complex molecules. —JSY

Science, ade5110, this issue p. 484;
see also adf2201, p. 439

BATTERIES

An enabling composite electrolyte

Lithium-air batteries have scope to compete with gasoline in terms of energy density. However, in most systems, the reaction pathways either involve one- or two-electron transfer, leading to lithium peroxide (Li_2O_2) or lithium superoxide (LiO_2), respectively. Kondori *et al.* investigated a lithium-air battery that uses a ceramic-polyethylene oxide-based composite solid electrolyte and found that it can undergo a four-electron redox reaction through lithium oxide (Li_2O) formation and decomposition (see the Perspective by Dong and Lu). The composite electrolyte embedded with $\text{Li}_{10}\text{GeP}_2\text{S}_{12}$ nanoparticles shows high ionic conductivity and stability and high cycle stability through a four-electron transfer process. —MSL

Science, abq1347, this issue p. 499;
see also ade2302, p. 436

VOLCANOLOGY

A magmatic nexus

The island of Hawai'i is shaped by its well-known volcanoes, Mauna Kea, Mauna Loa, and Kilauea. Although Kilauea is currently by far the most active, the other volcanoes could still erupt as well. Wilding *et al.* used more than 200,000 seismic events to map out the geometry of the magma feeding into these volcanoes at a 40-kilometer depth (see the Perspective by Flinders).

The magma forms a sill complex that connects Kilauea and Mauna Loa, and there is some evidence of connection to Mauna Kea. The observations suggest far greater underground connections between the volcanoes and provide an interesting insight into magma transport. —BG

Science, ade5755, this issue p. 462;
see also adf2993, p. 434

DEVICES

Lending the shoulder a hand

Developing upper-limb soft robotic wearables for people with physical impairments is still in its infancy. Proietti *et al.* fashioned a soft, lightweight, portable robotic wearable to assist shoulder movements. They tested their device in 10 individuals with the neurodegenerative disease amyotrophic lateral sclerosis who had different degrees of limb impairment. Participants using the robotic wearable showed improvements in the shoulder's range of motion while undertaking tasks simulating activities of daily living. This device reduced shoulder muscle activity and also perceived muscular exertion and increased endurance. This device is a step forward in the development of soft robotic wearables for everyday use. —OMS

Sci. Transl. Med. **15**, eadd1504 (2023).

B CELLS

Tracing T-independent responses

T-independent (TI) B cell responses develop without T cell help and are mostly directed against repetitive structures such as surface polysaccharides derived from encapsulated bacteria. Using high-throughput B cell receptor repertoire sequencing, Weller *et al.* studied the B cell subsets contributing to human TI responses in healthy individuals vaccinated with the

pneumococcal polysaccharide vaccine Pneumovax. The most expanded plasma cells were clonally related to previously mutated peripheral blood B cell precursors, including marginal zone B cells, and these cells remained stable without acquiring further mutations up to 2 months after vaccination. Antibodies specific to bacterial capsular polysaccharides isolated from vaccine-elicited plasma cells cross-reacted with gut bacterial antigens, supporting a model in which human TI responses mobilize marginal zone B cells that are prediversified in gut-associated lymphoid tissues. —CO

Sci. Immunol. **8**, eade1413 (2023).

Your Legacy to Science

AN ESTATE GIFT TO THE
AMERICAN ASSOCIATION FOR THE ADVANCEMENT OF SCIENCE



Since 1848, our founding year, the American Association for the Advancement of Science (AAAS) has been deeply committed to advancing science, engineering and innovation around the world for the benefit of all people.

By making AAAS a beneficiary of your will, trust, retirement plan or life insurance policy, you become a member of our 1848 Society, joining Thomas Edison, Alexander Graham Bell and the many distinguished individuals whose vision led to the creation of AAAS and our world-renowned journal, *Science*, so many years ago.

Unlike many of its peers, *Science* is not for-profit. Your estate gift would provide long-term financial stability and durable annual income that will support operations and competitive innovation for years to come. **This support is vital.**

"As a teacher and instructor, I bear responsibility for the younger generations. If you have extra resources, concentrate them on organizations, like AAAS, that are doing work for all."

—Prof. Elisabeth Ervin-Blankenheim, 1848 Society member

If you intend to include AAAS in your estate plans, provide this information to your lawyer or financial adviser:

Legal Name: American Association for the Advancement of Science

Federal Tax ID Number: 53-0196568

Address: 1200 New York Avenue, NW, Washington, DC 20005

If you would like more information on making an estate gift to AAAS, cut out and return the form below or send an email to philanthropy@aaas.org. Additional details are also available online at www.aaas.org/1848Society.

cut here ✂

Yes, I would like more information about joining the AAAS 1848 Society.

PLEASE CONTACT ME AT:

Name: _____

Address: _____

City: _____ State: _____ Zip code: _____ Country: _____

Email: _____ Phone: _____

RETURN THIS FORM TO:

AAAS Office of Philanthropy and Strategic Partnerships • 1200 New York Avenue, NW • Washington, DC 20005 USA



REVIEW SUMMARY

PLANT SCIENCE

The mechanics of plant morphogenesis

Enrico Coen* and Daniel J. Cosgrove*

BACKGROUND: The growth and shape of plants depend on the mechanical properties of the plant's mesh of interconnected cell walls. Because adhering cell walls prevent cell migrations, morphogenesis is simpler to study in plants than in animals. Spatiotemporal variations in the rates and orientations at which cell walls yield to mechanical stresses—ultimately powered by cell turgor pressure—underlie the development and diversity of plant forms. Here, we review new insights and points of current contention in our understanding of plant morphogenesis, starting from wall components and building up to cells and tissues.

ADVANCES: Recent modeling and experimental studies have enabled advances at four levels: fiber, wall, cell, and tissue. In moving up levels, a population of discrete components is typically abstracted to a continuum at the next level (e.g., fibers to wall, walls to cell, cells to tissue). These abstractions help to both clarify concepts and simplify simulations. Mechanical stresses operate at each level, but values are typically not the same from one level to the next.

At the fiber level, growth corresponds to cellulose microfibrils sliding past each other, which is passively driven by turgor-induced tension. The rate of sliding depends on adhesion between microfibrils, whereas anisotropy reflects differences in the proportion of fibers in different orientations. Growth occurs preferentially in the direction of maximal microfibril stress.

At the wall level, microfibril sliding corresponds to cell wall creep, at rates dependent on turgor, wall extensibility, thickness, and yield thresholds. Anisotropic mechanical properties can arise through orientation-selective synthesis of cellulose microfibrils, guided by microtubules. Creep is stimulated by the wall-

loosening action of expansins, which increase extensibility and lower the yield threshold. Wall synthesis and loosening influence growth in complementary ways. Wall loosening increases growth rate with almost immediate effect, but unless wall synthesis increases in parallel, wall thickness declines over time, potentially weakening the wall. Wall synthesis requires a longer time scale to have a discernible growth effect but is critical for maintaining wall thickness and orienting anisotropy. By regulating loosening and synthesis separately, plants have the flexibility to produce rapid growth responses as well as control longer-term growth patterns and mechanical strength.

At the cellular level, growth corresponds to irreversible deformations that are catalyzed by expansins and physically driven by mechanical stresses that arise from turgor acting on cell walls. Oriented cell growth depends on wall anisotropy and cell geometry, which in turn depend on the dynamics of microtubule alignment. Collisions between microtubules lead to self-organized alignments that may be influenced by cellular cues and cell geometry.

At the tissue level, cell-cell adhesion combined with differential wall properties can lead to tissue-wide stresses. Tissue morphogenesis depends on coupling the mechanical properties of walls, cells, and tissues to regional patterning. Coupling may occur by regional gene activity that modifies rates of microfibril deposition, wall extensibility, and/or yield thresholds, and thus wall growth through creep. Regional gene activity may also provide tissue cues that orient microtubule alignments, and thus the orientations of growth anisotropy. Computational modeling, informed by developmental genetics, live imaging, and growth analysis, has shown how these principles can

account for morphogenetic changes through mechanically connected tissue regions irreversibly growing at specified rates and orientations. Taken as a whole, the cellulose network at the fiber and wall level provides elastic resistance to deformation while allowing growth through creep, which enables morphogenesis at the cell and tissue level while maintaining mechanical strength.

OUTLOOK: A key question is how patterns of gene expression at the tissue level modify behaviors and mechanics at other levels to generate tissue morphogenesis. Although we outline broad principles for how this may operate, many of the underlying molecular mechanisms remain unresolved. Controversies remain over the role of pectins in controlling wall mechanics and in the role of mechanosensing, chemical signaling, and polarity in controlling orientations of growth. And although tissue-level models have been proposed to account for morphogenetic changes, many of the underlying components remain hypothetical. A further challenge is to determine how interactions across levels have been modified during evolution to give rise to the diversity of plant forms.

Many of the principles described here may also be applicable to microbial and animal morphogenesis. Similar to plants, rates and orientations of cellular growth in these organisms depend on fibers in the wall or cell cortex that resist turgor. Controlled fiber sliding may play a key role, though in animals such sliding can be driven actively as well as passively. In animal tissues where cell rearrangements are limited, as during organogenesis, growth coordination and tissue stresses may operate similarly to plants. Thus, although the molecular players that control plant, animal, and microbial development are different, the mechanics of morphogenesis may share common principles. ■

The list of author affiliations is available in the full article online.

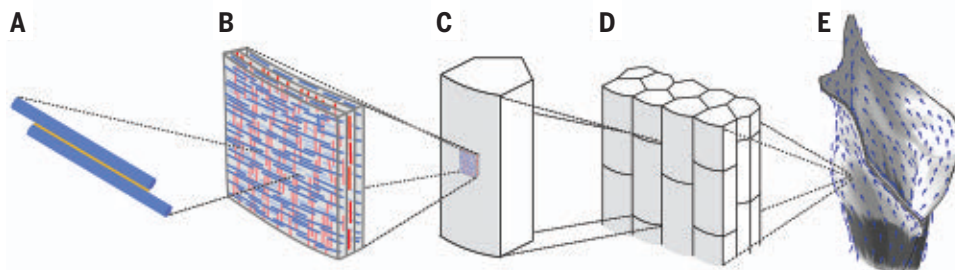
*Corresponding author. Email: enrico.coen@jic.ac.uk (E.C); dcogrove@psu.edu (D.J.C.)

Cite this article as E. Coen and D. J. Cosgrove, *Science* 379, eade8055 (2023). DOI: 10.1126/science.ade8055

S READ THE FULL ARTICLE AT
<https://doi.org/10.1126/science.ade8055>

Plant morphogenesis, from nano- to

macroscale. (A to E) Growth begins with the sliding of cellulose fibers (A) within the cohesive, extensible, and layered networks of cell walls [(B); layers with different fiber orientations are color coded]. Sliding is physically driven by turgor pressure, which generates stress patterns in cells (C) and across tissues (D). Patterned tissue growth may be oriented by polarity fields (arrows) to generate complex forms (E).



REVIEW

PLANT SCIENCE

The mechanics of plant morphogenesis

Enrico Coen^{1*} and Daniel J. Cosgrove^{2*}

Understanding the mechanism by which patterned gene activity leads to mechanical deformation of cells and tissues to create complex forms is a major challenge for developmental biology. Plants offer advantages for addressing this problem because their cells do not migrate or rearrange during morphogenesis, which simplifies analysis. We synthesize results from experimental analysis and computational modeling to show how mechanical interactions between cellulose fibers translate through wall, cell, and tissue levels to generate complex plant tissue shapes. Genes can modify mechanical properties and stresses at each level, though the values and pattern of stresses differ from one level to the next. The dynamic cellulose network provides elastic resistance to deformation while allowing growth through fiber sliding, which enables morphogenesis while maintaining mechanical strength.

The growth and shape of plants depend on the mechanical properties of the plant's mesh of interconnected cell walls. Because adhering cell walls prevent cell migrations, morphogenesis is simpler to study in plants than in animals. Spatiotemporal variations in the rates and orientations at which cell walls yield to mechanical stresses—ultimately powered by cell turgor pressure—underlie the development and diversity of plant forms. Considerable progress has been made in understanding the molecular genetic basis of plant morphogenesis, but confusion and controversies remain over how these findings relate to the mechanics of development. Here, we review new insights and points of current contention in our understanding of the mechanics of plant morphogenesis, starting from wall components and building up to cells and tissues.

At the heart of morphogenesis is a trade-off between mechanical stiffness and deformability. As a plant develops, it must resist external mechanical forces, such as gravity and wind, while also growing by several orders of magnitude and deforming to produce its characteristic shapes. Plant materials therefore need to be strong while also pliant enough to grow and deform. These conflicting requirements are partly met by restricting morphogenesis to protected areas such as embryos, growing tips (apical meristems), and cambial zones, which reduces the extent to which they weaken the plant. However, even within these zones, mechanical strength needs to be maintained. A key problem is how such strength is achieved in the face of growth.

Fiber mechanics

The mechanical properties of plant tissues largely depend on how fibers in cell walls are organized. These fibers experience tensile stress caused by turgor pressure of several atmospheres within each cell, which provides the primary driving force for plant growth (1–3). Non-turgor-based mechanisms, in which growth is driven by active insertion of cell wall material, have been proposed (4, 5), but their contribution to plant growth remains contentious (1, 6).

The main load-bearing fibers are cellulose microfibrils, each comprising many linear β 1,4-glucan chains packed into a crystalline array, with stiffness comparable to steel. Aligned microfibrils bind strongly to each other laterally, forming two-dimensional networks that resist being stretched (7). Microfibrils are embedded in a hydrophilic matrix of pectins and hemicelluloses that make up

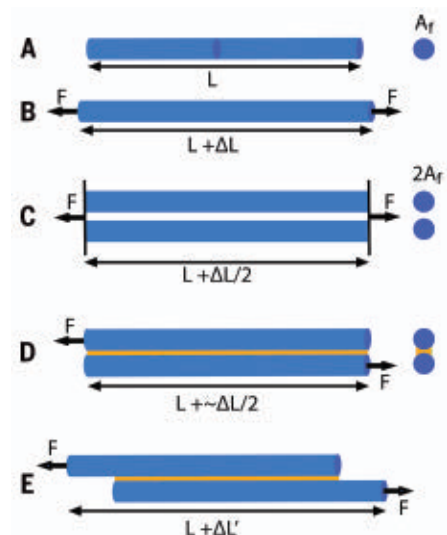
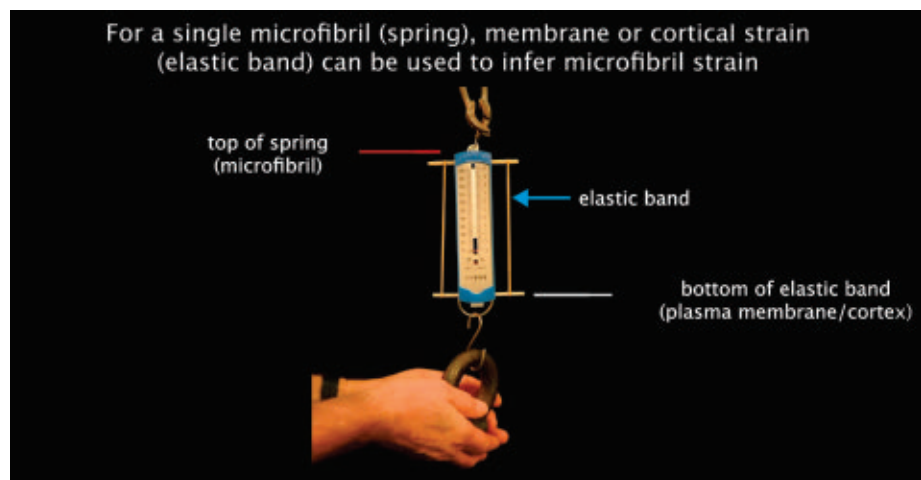


Fig. 1. Fiber growth in one dimension. (A) Fiber of length L and cross-sectional area A_f . (B) Tensile force, F , leads to extension ΔL . Strain $\epsilon_f = \Delta L/L$. For an idealized linear elastic fiber, $\epsilon_f = \sigma_f/E_f$, where σ_f is the fiber tensile stress F/A_f , and E_f is the Young's modulus of the fiber. (C) Doubling fiber number halves stress and strain. (D) Shear stress, τ_f , generated at the fiber interface (yellow), equals F/A_c , where A_c is the contact area along the length of the fibers. If the cross-sectional area of the interface is small relative to A_f , $\epsilon_f \sim \Delta L/2L$. (E) Slippage caused by shear stress. Fiber extension $\Delta L'$ increases with time.

most of the cross-sectional area of the growing cell wall yet bear little tensile stress (8).

We first consider growth in one dimension. Wall growth involves two types of fiber stress: tensile and shear. If a tensile force F is applied to a fiber of length L and causes extension by



Movie 1. For a single microfibril (spring), membrane or cortical strain (elastic band) can be used to infer microfibril strain. When a weight is applied, extension of a spring (equivalent to a fiber in Fig. 1B) is the same as the extension of a less stiff elastic band attached to the spring.

¹Department of Cell and Developmental Biology, John Innes Centre, Norwich Research Park, Colney Lane, Norwich NR4 7UH, UK. ²Department of Biology, Pennsylvania State University, University Park, PA 16870, USA.

*Corresponding author. Email: enrico.coen@jic.ac.uk (E.C.); dcogrove@psu.edu (D.J.C.)

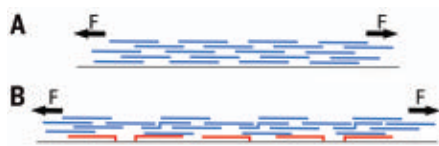


Fig. 2. Wall growth in one dimension. (A and B) Schematic of fibers in a wall cross section with the plasma membrane shown as a gray line and newly deposited fibers shown in red. Before growth is shown in (A). After growth by fiber slippage, newly deposited fibers (red) maintain wall thickness, as shown in (B).

ΔL , the proportionate increase in length, or fiber strain, is defined as $\epsilon_f = \Delta L/L$. For an idealized linear elastic fiber, fiber strain is proportional to fiber tensile stress, $\sigma_f = F/A_f$, where A_f is the fiber cross-sectional area (Fig. 1, A and B). The constant of proportionality is $1/E_f$, where E_f is Young's modulus of the fiber. If we introduce a second fiber in parallel and apply the same force, the tensile stress in each fiber is halved and fiber strain is halved (Fig. 1C), as is the strain of the entire structure or wall ϵ_w . Thus, for a given tensile force, stress and strain are inversely proportional to fiber number, N . Because of the proportionality between wall strain and fiber tensile stress, strain in cellular components that deform together with the wall, such as the plasma membrane or cortex, can be used to infer fiber stress (Movie 1).

If fibers are firmly stuck together at an interface along their length and force is applied to only one end of each fiber (Fig. 1D), a shear stress, τ_f , acts at the interface. Shear stress equals F/A_c , where A_c is the contact area along the length of the fibers. As fiber number N increases, there are more fibers and interfaces to resist the tensile force, so τ_f and σ_f decrease. As above, plasma membrane or cortical strain can be used to infer σ_f (Movie 2).

So far, we have assumed an elastic regime in which all deformations are reversible. Cell wall enlargement during growth, however, is largely irreversible, arising through slow sliding of the fiber network. Suppose τ_f exceeds a slippage threshold, such that sliding occurs at the fiber interface (yellow in Fig. 1E). In this situation, wall strain, ϵ_w , is no longer proportional to stress because wall strain continually increases in time, whereas stress does not. Thus, plasma membrane or cortical strain can no longer be used to infer fiber tensile stress (Movie 3). For a simple linear case, the rate of increase in ϵ_w , or strain rate, $\dot{\epsilon}_w$, is proportional to shear stress above the slippage threshold. The constant of proportionality, a type of “extensibility,” depends on the strength with which fibers adhere to each other (i.e., fiber-fiber binding energy). If forces are removed, individual fibers relax to their

resting lengths, but wall strain due to slippage does not reverse.

From fibers to walls

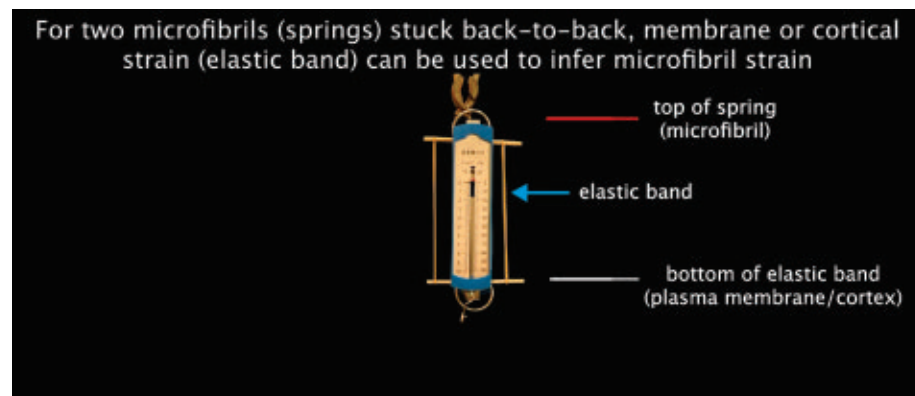
A simplified mechanical view of a growing cell wall is a network of overlapping cellulose microfibrils sticking to each other and stretched by a turgor-based tensional force F , which is maintained by cellular water uptake (Fig. 2A). Irreversible wall enlargement (~5 to 10% per hour in rapidly growing tissue) occurs at approximately constant turgor pressure through slow microfibril sliding that is facilitated by a nonenzymatic wall-loosening protein, expansin (9). As the growing wall thins through extension, wall thickness is maintained by addition of new microfibrils (red in Fig. 2B), which are synthesized at the plasma membrane, together with the incorporation of additional matrix materials. Each nascent microfibril begins to bear tensile load when it binds to overlying microfibrils that it straddles, becoming part of the cohesive cellulose network. As the overlying microfibrils slide, the nascent fiber is put under tension, “taking up the slack.”

This simplified account is consistent with the structure and nanoscale mechanics of primary cell walls (10, 11) but omits the mechanical role of matrix polysaccharides. Hemicelluloses, such as xyloglucan, bind strongly to cellulose surfaces in extended conformations and as random coils, whereas pectins form a soft hydrogel that binds weakly to cellulose surfaces (12–14). Microindentation measurements of various growing organs and pectin-rich pollen tubes have implicated pectins in the control of wall stiffness (15), whereas other experimental and computational results indicate that tensile stress is borne mainly by the cellulose network, with a minor contribution by matrix polymers (8, 16). The apparent contradiction may be partly resolved by recognizing that the in-

plane stretching of walls involves different modes of polymer deformation than out-of-plane indentation (12), with the cellulose network dominating in-plane tensile stretching and pectins contributing substantially to out-of-plane mechanics (16, 17). Pectins and xyloglucan may also influence tensile mechanics indirectly by modulating the formation of cellulose-cellulose contacts during wall assembly and remodeling, thereby shaping the cellulose network and its mechanical properties (12). Another proposal is that enzymatic swelling of pectin may supply an additional driving force for wall enlargement (14).

In addition to their structural role, pectins and xyloglucan participate in local signaling by auxin and brassinosteroid (18–20), thereby influencing many downstream pathways. Direct mechanical effects of these matrix polysaccharides may therefore be confounded with indirect hormonal responses, which complicates the interpretation of genetic studies and possibly accounts for divergent views on the effects of pectin modifications (12–14, 21–24). The role of pectins in wall mechanics and growth therefore remains contentious, and further results will be needed to reach a unified view.

In growing cell walls, lateral interfaces between aligned cellulose microfibrils are heterogeneous, involving direct cellulose-cellulose contacts, contacts mediated by a thin layer of water, and bonding through a monolayer of hemicelluloses (12, 25). The relative importance of these different interfaces for cellulose slippage has not been established. The major endogenous catalysts of cell wall extension, α -expansins, loosen noncrystalline cellulose-cellulose interactions in vitro (9), but molecular details are lacking. The loosening action of α -expansins may be restricted to infrequent sites of slippage, dubbed “biomechanical hot-spots” (12, 26). Tethering between cellulose



Movie 2. For two microfibrils (springs) stuck back to back, membrane or cortical strain (elastic band) can be used to infer microfibril strain. When a weight is applied to two firmly attached springs, extension of the springs (equivalent to fibers in Fig. 1D) is the same as the extension of a less stiff elastic band attached to the springs.

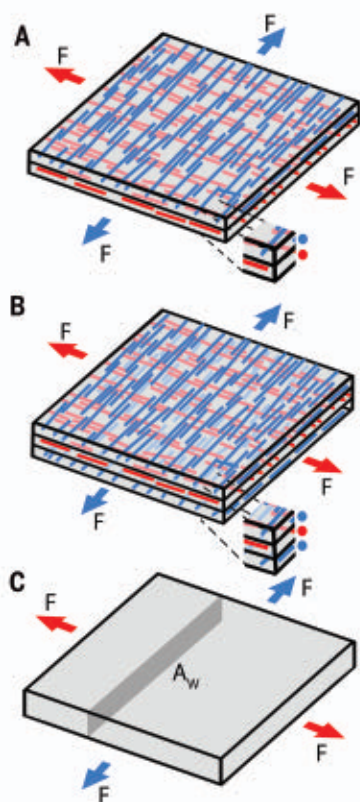


Fig. 3. Wall growth in two dimensions. (A) Two layers of microfibrils, with an equal number of microfibrils in red and blue orientations. (B) Three layers of microfibrils, with twice as many microfibrils in blue orientations than in red orientations. (C) Continuum perspective.

microfibrils by xyloglucan may also occur but contributes little to steady-state tensile mechanics (8, 26). However, mechanical responses of isolated cell walls to exogenous β 1,4-endoglucanases implicate regions of intertwined cellulose-xyloglucan in limiting cellulose sliding (16, 26).

We may also consider the wall as a continuum, rather than being made up of discrete fibers. From this perspective, wall stress, σ_w , equals F/A_w , where A_w is the wall cross-sectional area. Wall stress is less than fiber stress, because matrix contributes to the cross-sectional wall area while not bearing the main tensile load (8). Microfibril sliding, facilitated by α -expansin, can account for wall creep, which is readily observed as slow, irreversible extension of a wall held at constant force above a yield threshold (the minimum where creep begins) (9). Such sliding can dissipate wall stresses, termed wall stress relaxation, which is most apparent when wall enlargement is physically constrained (12). Stress relaxation generates the slight water potential disequilibrium required for sustained water uptake during cell enlargement (27). The stimulation of wall stress relaxation

and creep by α -expansins is maximal at acidic pH and entails changes in both the strain-rate proportionality constant, which is commonly called “wall extensibility” (2), and the yield threshold (28). This pH dependence enables rapid and local control of wall loosening by a signaling pathway that activates plasma membrane H^+ -adenosine triphosphatases (H^+ -ATPases), which acidify the wall space to activate α -expansins and promote wall creep (29). The biological control of wall pH and thereby expansin activity, which does not occur in mechanical measurements of isolated cell walls, may result in dynamic shifts in wall extensibility and the yield thresholds observed in vivo (3, 30), consistent with pH-dependent expansin action measured in vitro (28).

In addition to elasticity and creep, cell walls may also display plasticity, which is observable as an immediate irreversible deformation when tensile force is suddenly increased beyond a threshold (9, 31). Although both plasticity and creep involve cellulose-cellulose sliding, they differ in time scale and microsites of cellulose movements. Plastic deformation, unlike wall creep, is nearly independent of time and expansins and does not occur during normal cell growth, which occurs at steady turgor (steady wall stress). Sudden changes in wall tensile force (e.g., in a mechanical tester) also reveal transient mechanical responses termed viscoelastic or viscoplastic deformations. These are material responses that generally subside within a few minutes of the change in force, which reflects the short time constants of most physical rearrangements of matrix polymers and the cellulose network (other than expansin-mediated creep). Developmental patterns of wall or tissue viscoelasticity and plasticity are sometimes associated with growth (1, 15, 23), but in other cases, the correlations are poor or nonexistent (12, 32). Consequently,

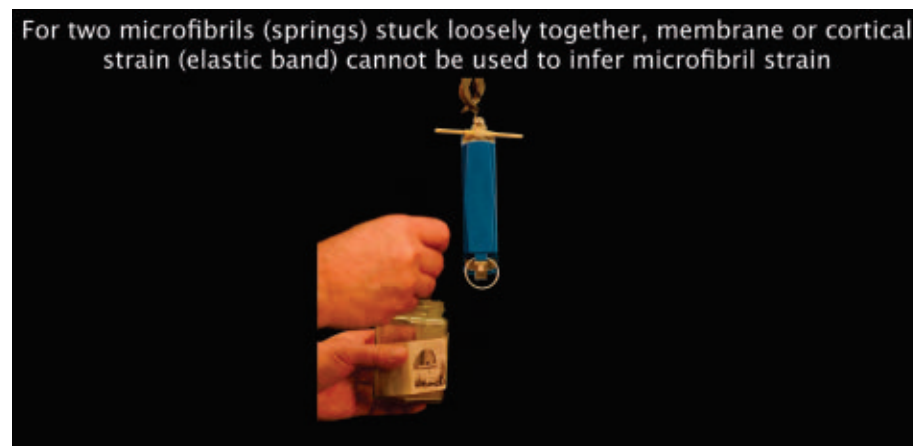
the interpretation of viscoelastic-plastic measurements in relation to wall growth is a point of contention. Contrasting ideas of cell wall structure and whether tensile forces are transmitted between cellulose fibers through direct cellulose-cellulose contacts or through matrix polysaccharides lie at the heart of these divergent views (12).

Wall synthesis and loosening influence cell growth through wall creep in complementary ways (33, 34). Wall loosening increases growth rate with almost immediate effect (35), but unless wall synthesis increases in parallel, wall thickness declines over time, potentially weakening the wall. Wall synthesis requires a longer time scale to have a discernible growth effect but is critical for maintaining wall thickness and orienting anisotropy (see next section). By regulating loosening and synthesis separately, plants have the flexibility to produce rapid growth responses as well as control longer-term growth patterns and mechanical strength.

Anisotropic wall growth

Plant morphogenesis involves differential orientations and rates of growth. Such growth anisotropy is evident at the wall level, as shown by marking walls of the classically studied alga *Nitella axillaris*, whose internodes are one cell wide and grow about four times faster in length than circumference (36, 37). A key question is how growth anisotropy is determined and regulated.

Growth anisotropy depends on the three-dimensional structure of the cell wall. Consider a square piece of wall with two layers of microfibrils (colored blue and red in Fig. 3A) that are oriented perpendicular to each other. A tensile force, F , is applied to the ends of the wall equally in both microfibril orientations. If microfibrils are the main load-bearing



Movie 3. For two microfibrils (springs) stuck loosely together, membrane or cortical strain (elastic band) cannot be used to infer microfibril strain. When a weight is applied to two springs held together with honey, slippage (as in Fig. 1E) increases with time and leads to greater strain for the elastic band than for the individual springs.

components, the average microfibril stress σ_f equals F/NA_f , where N is the number of microfibrils cut transversely in the cross section. Without microfibril slippage, wall strain, ϵ_w , equals fiber strain, ϵ_f , and is the same in both orientations. As F increases, shear stress may exceed the slippage threshold, and the wall grows at a strain rate, $\dot{\epsilon}_w$, which is the same in both orientations, giving isotropic growth.

To introduce anisotropy, we add a second layer of blue microfibrils (Fig. 3B). There are now half as many red microfibrils resisting the red force as blue resisting the blue force, so red tensile stress is twice that of blue. Red microfibrils are also under twice the shear stress of blue. As F increases, microfibrils begin to slip and exhibit faster slippage in the red direction compared with the blue direction. Thus, the orientation of maximal growth rate is aligned with the orientation of maximal microfibril stress.

Yet from a continuum perspective, wall stress, σ_w , is equal in both orientations, because A_w is the same for each (Fig. 3C). The wall Young's modulus and yield threshold (proportional to fiber slippage threshold times N) in the blue direction are twice those in the red direction. As F increases, the wall begins to yield and exhibits faster creep in the red direction compared with the blue direction. Thus, from a continuum perspective, the direction of maximal growth is coaligned with the direction of the lowest Young's modulus and wall yield threshold, whereas from a fiber perspective, maximal growth occurs in the direction of the highest microfibril stress.

From walls to cells

Modulation of wall properties can lead to formation of diverse cell geometries (38). Cell geometry may in turn feed back to influence stresses (39). In a turgid spherical cell with isotropic walls, tensile stresses are equal in all directions in the plane of the wall. However, in a cylindrical cell with isotropic walls, both wall stress and microfibril stress in the circumferential direction are twice those in the axial direction (40), which would lead to greater growth in cell diameter than length. Yet elongated cells often exhibit axial growth. Such growth may be achieved through the preferential loosening and synthesis of the wall at one end: tip growth (41). However, the cylindrical internode cells of *Nitella* grow faster axially than circumferentially even though growth is distributed throughout the wall: diffuse growth (36). Diffuse growth is common to most cells of the plant body (42).

Diffuse axial growth can be explained by wall anisotropy. Assume the wall of the cylindrical cell has twice as many circumferential microfibrils as axial microfibrils (Fig. 4). Although tensile force is twice as great in the circumferential orientation (blue arrows), there are

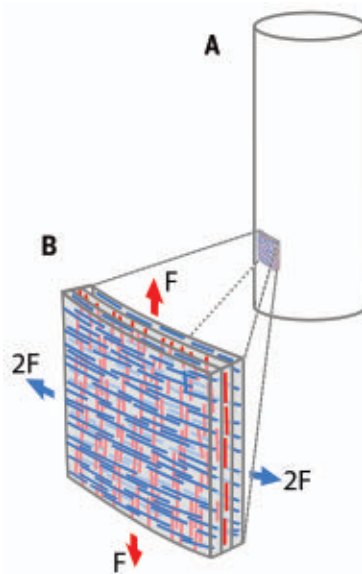


Fig. 4. Mechanics of a cylindrical cell. (A) Cell outline. (B) Microfibril composition and tensile forces on a small region of anisotropic wall with two layers of circumferential microfibrils (blue) and one layer of axial microfibrils (red).

twice as many microfibrils to resist it, and therefore microfibril stress is equal in both orientations. The wall will therefore grow equally along both the circumferential and axial directions. If the number of circumferential microfibrils is more than twice that of axial microfibrils, microfibril stress will be higher in the axial orientation and the cell grows faster in length than circumference. From a continuum perspective, resistance to wall creep is more than twice as high in the circumferential direction compared with the axial direction, leading to low circumferential growth despite twice the wall stress. Measurements on *Nitella* internode cells confirm that they have a greater proportion of circumferential to axial microfibrils and have more than twice the wall yield stress threshold in the circumferential orientation (36, 37, 43, 44).

Control of microtubule orientation in individual cells

Microfibril orientation is primarily determined by microtubules guiding cellulose synthases (45), although feedback from microfibrils can also guide cellulose synthases where microtubules are absent (46). When the growing end of a microtubule collides with another microtubule, it may turn to follow the microtubule (zippering) or undergo depolymerization (collision-induced catastrophe) (47). Computer simulations show that such interactions in a population of microtubules can generate alignments (i.e., near-parallel arrangements) that maximize microtubule survival

probability (48, 49). In a spherical cell without cues, such alignments are randomly oriented. For an elongated cell, orientations along the cell's long axis can be favored, which is consistent with longitudinal microtubule orientations that are observed in wall-less plant cells (protoplasts) deformed in rectangular microwells (50).

The predominant microtubule orientation in microwell-constrained protoplasts changes from longitudinal to transverse under high turgor, which has been explained by microtubules responding to the direction of maximal tension in the cell cortex (51). There has been confusion, however, over how stress-sensing in the cell cortex relates to sensing stresses in the wall. Stress-sensing depends on cells being able to sense strain (31), which is proportional to stress for elastic deformations (Fig. 1, A to D). Thus, for elastic deformations, cortical strain can be a proxy for measuring wall stress (Movies 1 and 2). However, in a walled cell that grows by creep, strain and wall stress are not proportional (strain can increase for a fixed stress; Fig. 1E and Movie 3). The direction of maximal strain therefore need not correspond to the direction of maximal wall stress (e.g., axially growing cylindrical cell). Thus, for an intact growing plant cell, stress-sensing in the cortex relates to wall strain, not wall stress. In principle, sudden changes in wall stress could be detected by membrane or cortical strain because creep is slow, but the relevance of such rapid stress changes to plant growth, which occurs under steady turgor, is unclear.

Various hypotheses have been proposed for how microtubules, and thus microfibrils, are oriented in intact plant cells. Classic studies on cylindrical *Nitella* cells suggested that microtubules are aligned passively by early-stage circumferential growth (52). This model was later disproved, leading to the hypothesis that microfibrils determine the directionality of cell expansion in accord with wall stress (37). One hypothesis is that membrane-spanning receptors have two domains: an extracellular domain that preferentially binds to more highly stressed microfibrils and an intracellular domain that binds to microtubules, aligning them with the direction of the bound microfibrils (53). By connecting to both microfibrils and microtubules, such receptors would allow the direction of the maximal wall stress to orient microtubules, avoiding the problem of indirect sensing through cortical or plasma membrane strain. However, enzymatic treatments, or mutants that modify mechanical properties of walls by interfering with cellulose content, have no discernible effect on microtubule patterning (54, 55), which argues against this mechanism.

Another microtubule-orienting hypothesis is based on asymmetric localization of molecules

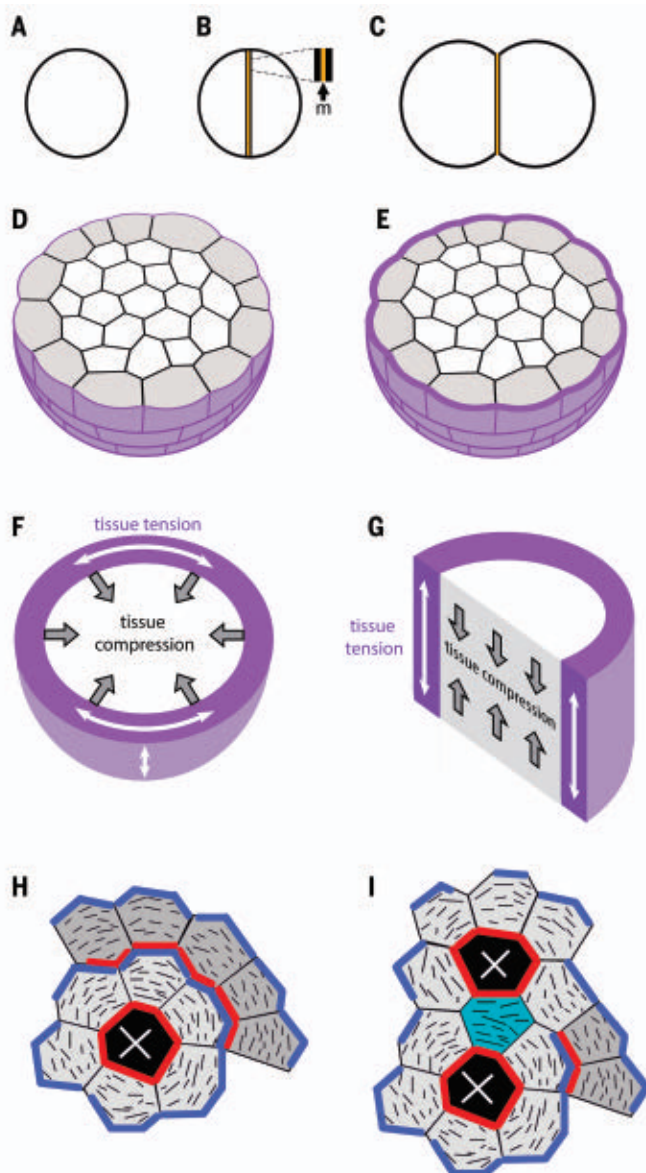


Fig. 5. Multicellular interactions. (A to C) Spherical cell (A) divides to give two daughters (B) separated by a middle lamella (yellow, m). Isotropic growth and strong adhesion lead to the formation of two cells with a flattened interface (C). (D) In a spherical tissue with isotropic walls of uniform width (shown in cross section), all walls experience similar tensile stress. The outer wall of the epidermal cells (gray) is shown in purple. (E and F) With thickened outer walls (E), growth leads to higher tensile force on the outer walls, corresponding to tissue tension in an outer region (purple) and tissue compression in the inner region of a continuous tissue (F). (G) With a cylindrical tissue that grows axially (half section shown), thickened outer walls lead to axial outer tissue tension and axial inner tissue compression. (H) With single-cell ablation (black cell with cross), microtubules (black lines) become oriented circumferentially around the wound in cells directly bordering the wound (light gray) and cells further out (dark gray). This could be explained by circumferential stresses caused by the wound orienting microtubules. Alternatively, cells could have polarity proteins (red and blue) that localize at opposite cell ends. If red polarity proteins are activated adjacent to the wound by a chemical signal, polarity proteins in cells bordering the wound would localize to faces oriented circumferentially around the wound. This polarity pattern could propagate further out (dark gray cells) through molecular signaling. Destabilization of microtubules by red and blue polarity proteins would favor microtubule orientations parallel to the red and blue faces (i.e., circumferential to the wound) because this increases microtubule survival probability. (I) In a double ablation, microtubules in the bridging cell (cyan) are oriented parallel to the cell faces adjoining the wounds, which could be explained by mechanosensing. Alternatively, red polarity proteins could be activated at both faces of the bridging cell that are adjacent to the wounds, destabilizing microtubules and favoring microtubule orientations in the bridging cell that are parallel to its two red faces.

across a cell, as exhibited by several plant polarity proteins (56–62). A cell polarity protein in protoplasts gives a polarity axis that aligns with subsequent growth orientation (63). Computer simulations show that microtubules tend to adopt orientations parallel to faces or edges where they are preferentially destabilized, because such orientations increase microtubule survival probability (48, 64). If polarity proteins at opposite end-faces or edges of a cylindrical cell destabilize microtubules, microtubule orientations parallel to the edges (i.e., circumferential) would therefore be favored. This hypothesis remains to be further explored.

Microtubule-orienting mechanisms have also been investigated for jigsaw puzzle-shaped epidermal cells (pavement cells). Microtubules on the outer face of these cells form arrays that fan out from the neck tips, which has been explained through response to stresses, localized protein activity, and/or cell geometry (65).

From cells to tissues

Morphogenesis of multicellular tissues depends not only on properties of individual cells but also on mechanical interactions between them. Consider a spherical turgid cell with isotropic walls that undergoes division (Fig. 5, A and B). With strong adhesion at the middle lamella (labeled m and colored yellow in Fig. 5B), the cells would grow to form two partial spheres joined by a flat interface (Fig. 5C). With reduced adhesion, a degree of cell separation may occur, leading to two spherical daughters in the extreme case. The extent of cell-cell adhesion is influenced by wall matrix components, such as pectins (66).

Suppose our cells continue to grow, divide, and adhere to form a spherical tissue (Fig. 5D), with an epidermal layer (gray) and all cells maintaining the same turgor. All walls have the same thickness, the same isotropic material properties, and similar tensile stress. However, if the outer epidermal walls are thicker (purple in Fig. 5E), as is common for many tissues, tensile stress is reduced in these walls because their cross-sectional area, A_w , is greater. The outer walls therefore create a growth constraint. Turgor force is then transferred from inner to outer walls, increasing the tensile force on outer walls.

Such tensile forces, or tissue tensions, have been inferred from the way tissues bend or gape after being cut or by the formation of epidermal cracks when adhesion between cells is weakened (67–69). Tissue tension can be quantified by stretching detached epidermal tissue to the point that it restores its original length (70). Epidermal tissue tension is counterbalanced by internal tissue compression—internal tissue expands when the epidermal constraint is removed. Thus, tissue stresses can be either tensile or compressive. They

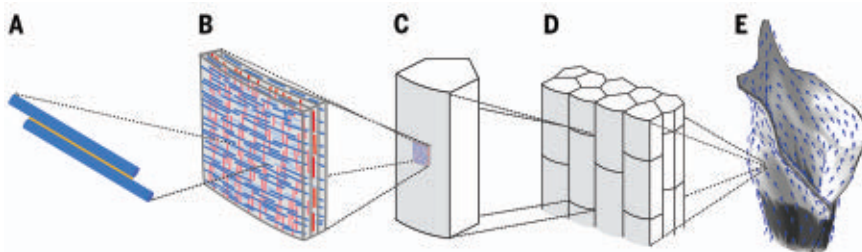


Fig. 6. Plant morphogenesis, from nano- to macroscale. (A to E) Growth begins with the sliding of cellulose fibers (A) within the cohesive, extensible, and structurally biased networks of cell walls (B). Sliding is physically driven by turgor pressure, which generates stress patterns in single cells (C) and across tissues (D). Growth may be oriented by polarity fields (blue arrows) to generate complex forms, as illustrated by a tissue-level model of grass leaf development (E), with the tubular sheath region in darker gray (93).

impose additional forces on cells that can increase or decrease wall stresses, as a result of connectivity with other cells with different mechanical or growth properties (71).

Just as wall stress is based on the notion of the wall as a continuum, tissue stress is based on the notion of tissue as a continuum (70, 72). If all regions of a continuous uniformly growing sphere have the same isotropic mechanical and growth properties, there are no tissue stresses (corresponding to all cell walls having the same thickness and wall stress). However, if the outer region of the sphere (purple in Fig. 5F) is more resistant to growth (e.g., because of thick outer cell walls), the tissue effectively behaves as a continuous pressurized vessel, with the outer region under tissue tension and the inner region under tissue compression (73) (Fig. 5F). Tissue stress does not equate to wall stress: Although tensile tissue stress is higher in the outer region, outer wall tensile stress may be reduced because of increased A_w . Similarly, although the inner region is under tissue compression, inner cell walls may partially resist some turgor force and thus be stretched in tension.

If the tissue has the form of a cylinder, thickened outer walls will lead to circumferential tissue tension being twice that of axial tissue tension. Outer wall and fiber stresses will also be greater in the circumferential orientation, resulting in axial cracks when cell adhesion is compromised, as observed with shoot apices (68).

So far, we have assumed that cell walls in our tissue have isotropic properties. Each cell would therefore grow spherically if mechanically isolated from its neighbors. If walls have anisotropic properties (e.g., biased microfibril orientations), cells in mechanical isolation would grow to form other shapes, such as ellipsoids. Oriented tissue growth may arise by coordination of such growth anisotropies between cells. For instance, if cell growth of interior cells is preferentially axial for a cylindrical tissue, thicker outer cell walls would

lead to axial outer tissue tension and axial inner tissue compression (72) (Fig. 5G), as observed in hypocotyls (67–69). Growth anisotropy of hypocotyls may be enhanced through increasing wall extensibility by brassinosteroid (32) or by selective weakening of axial walls (23).

Correlation between tissue stresses and microtubule orientations

In multicellular tissues, microtubules are typically aligned with maximal tissue tension (74, 75). For example, in shoot apical meristems, microtubules are oriented circumferentially around the apex and are aligned with organ-meristem junctions, which is the predicted orientation of maximal tissue tension (73). Wounding leads to microtubules orienting circumferentially around the wound, in alignment with predicted tissue tension (73, 76) (black lines in Fig. 5H). Mechanically bending, stretching, restraining, or compressing tissue also promotes alignments along the orientation of increased tissue tension (73, 77–80). These observations support the hypothesis that the orientation of maximal tissue tension can be sensed by cells to orient microtubules (74). Additionally, the cellulose synthesis inhibitor isoxaben alters microtubule alignments, which has been explained by wall weakening causing altered stress patterns (81, 82). However, the mechanism for sensing maximal wall-stress orientation remains speculative (74).

Another explanation may be offered for the correlation between tissue stress and microtubule orientation. Circumferential reorientation of microtubules after tissue damage may be a response that evolved to mechanically reinforce cells at the wound site, mediated by chemical signaling and cell polarity. For example, suppose cells contain two types of polarity protein, red and blue, that localize at opposite cell ends. If a wound-induced chemical signal causes the red polarity proteins to be activated in the plasma membrane adjacent to the wound site, polarity proteins in cells directly

bordering the wound would localize to cell faces oriented circumferentially around the wound (Fig. 5H). This polarity pattern could propagate further out to surrounding cells (darker gray) through cell-cell signaling (83). If red and blue polarity proteins destabilize microtubules, microtubules would become oriented circumferentially around the wound because this orientation would increase microtubule survival probability. This hypothesis is consistent with an induced pattern of cell polarity markers, which either face toward or away from the wound site (56, 82). Disruption of auxin dynamics does not prevent damage-induced cell polarity (82), indicating that polarity signaling is not auxin dependent.

Double-ablation experiments, with an intact cell between two ablated cells (cyan in Fig. 5I), were originally thought to preclude polarity as a microtubule-orienting mechanism because the cell bridging the two ablations shows circumferential microtubule orientations, even though that cell has no polarity (73). However, red polarity proteins could still be activated in the wound-facing plasma membranes of the bridging cell, destabilizing microtubules and thus orienting microtubules in the bridging cell parallel to its two red faces. Whether polarity proteins are localized in this manner for double ablations remains to be tested. Cell polarity in shoot apices may similarly provide the cue for orienting microtubules.

The effects of mechanical manipulations (bending or compressing of tissue), and of isoxaben treatment, may also have explanations that do not depend on stress sensing. Mechanical manipulations cause cells to be stretched in the direction of maximal tension, changing cell geometry. Such changes in geometry can modify microtubule orientations (50), potentially accounting for the effects of mechanical manipulations on microtubule patterns. Changes in cell geometry may be viewed as an indirect form of stress sensing in the case of mechanical manipulations. However, changes in cell geometry cannot be used as a general mechanism to infer stresses in growing plant cells. For example, in an axially growing cylindrical cell, the cell elongates axially, but wall stress is maximal circumferentially.

Isoxaben depletes cellulose synthase complexes from the plasma membrane. Because these complexes are tethered to microtubules, their depletion may affect microtubules directly rather than through the weakening of walls (54). Cellulase treatment, which weakens the wall without targeting the cellulose synthase complex, does not influence microtubule patterning (54). Similarly, mutants that reduce the amount of cellulose without impairing cellulose-synthase tethering to microtubules have little effect on microtubule patterns (55). Thus, although wall-stress sensing is often invoked to explain microtubule orientations,

the mechanosensing mechanisms remain elusive and the results may be accounted for by alternative mechanisms based on chemical signaling and cell geometry.

Stresses have also been proposed to play a role in orienting cell polarity (82). According to this view, stresses orient microtubules along the axis of maximal tension and orient cell polarity through stress gradients. However, spherical protoplasts can become polarized in the absence of mechanical asymmetries, which shows that stress gradients are not needed for polarization (63). Thus, the role of stresses versus chemical signals in the control of growth, microtubule orientation, and polarity remains controversial.

Tissue patterning and morphogenesis

Tissue morphogenesis depends on coupling the growth properties of walls, cells, and tissues to regional patterning. Coupling may occur by regional gene activity that modifies rates of microfibril deposition and/or wall extensibility and yield thresholds, and thus wall growth through creep. Regional gene activity may also provide tissue cues that orient microtubule alignments, and thus the orientations of growth anisotropy.

Computational modeling—informed by developmental genetics, live imaging, and growth analysis—has been used to determine whether such principles could account for tissue morphogenesis. From a modeling perspective, we may distinguish between two types of growth (84). “Specified growth” is how a small region of tissue would grow in isolation and therefore free from tissue stresses. “Resultant growth” is the way a small region grows when mechanically connected to the rest of the tissue. Computational models allow resultant growth, and thus tissue deformation, to be calculated from an input pattern of specified growth rates and orientations. As tissue deforms, so do the regional patterns that determine the rates and orientations of specified growth, creating a feedback loop. If cell divisions are incorporated, they are typically based on division rules and are a consequence rather than cause of growth (85–87). Such a view follows naturally from plant growth mechanics, where growth rates depend on turgor, wall extensibility, and yield thresholds instead of on the introduction of new walls, which act mechanically to restrain rather than promote growth.

Models based on regionally varying isotropic specified growth rates can account for the formation of bulges on the flanks of an apex, simulating early development of lateral appendages (primordia) (88). However, to account for more complex morphogenetic events, tissue-wide cues are needed to orient anisotropic specified growth. Use of tissue stresses to orient growth is problematic: If regions are reinforced in the direction of maximal stress,

growth will be retarded in that direction, thwarting coherent changes in tissue shape (84, 89). Tissue-stress sensing may reinforce a shape, such as leaf flatness (90), but generating a new tissue shape is more difficult. To circumvent this problem, it has been proposed that global stresses across the developing organ may be sensed (89), though how global and local stresses might be discriminated by cells remains unclear.

The stress-feedback problem does not apply when polarity controlled by chemical cues (83) is used to orient specified growth. Although tissue-wide stresses are generated through differential growth (because of tissue connectivity), they do not disrupt growth-orienting polarity fields. Moreover, tissue-wide polarity fields have been described for several polarity proteins (91). The formation of flattened structures, like leaves, can be modeled with two orthogonal polarity fields, which act in combination to orient regionally varying specified growth rates (92, 93). Leaf formation involves anisotropic growth oriented by a polarity field pointing from the tissue surface toward the ad-abaxial boundary (orthoplanar field). Orienting growth in this manner generates an initial primordial bulge followed by the development of an extended flat or curved sheet. Growth and shaping of the sheet are oriented by a second (planar) polarity field (93, 94) (Fig. 6E). Modulation of planar polarity and growth rates at the leaf margins can generate serrated forms (95). Thus, regional variation in specified growth rates, oriented by tissue-wide polarity fields, can account for a range of plant morphogenetic behaviors.

Growth arrest

Tissue growth slows down and finally arrests as plant cells mature and differentiate. Growth typically does not stop abruptly after the cessation of cell division but continues for a period, leading to cell enlargement. Growth arrest may eventually occur throughout a tissue, as with determinate organs such as leaves, or may be restricted to regions displaced away from meristems, as in stems or roots. For determinate structures, such as leaves, sepals, and the apical hook of seedlings, growth rates decline gradually with time in a defined spatial pattern (89, 94, 96–98). This decline could arise through reduced wall extensibility, an increase in yield threshold, an increase in wall thickness, and/or reduced turgor, but the contribution of each mechanism, and thus the control of final organ size, remains unclear.

Conclusion

We have reviewed the mechanics of plant morphogenesis at different interrelated levels, from fiber (Fig. 6, A and B) to wall (Fig. 6, B and C) to cell (Fig. 6, C and D) to tissue (Fig. 6, D and E). In moving up levels, a population of

discrete components is typically abstracted to a continuum at the next level (e.g., fibers to wall, walls to cell, cells to tissue). These abstractions help to both clarify concepts and simplify simulations. Mechanical stresses operate at each level, but values are typically not the same from one level to the next. By viewing the levels together, the cellulose network at the fiber and wall level provides elastic resistance to deformation while allowing growth through creep, which enables morphogenesis at the cell and tissue level while maintaining mechanical strength.

A key question is how patterns of gene expression at the tissue level modify behaviors and mechanics at other levels to generate tissue morphogenesis. Although we have outlined broad principles for how this may operate, many of the underlying molecular mechanisms are unresolved. Controversies remain over the role of pectins in controlling wall mechanics and over the role of mechanosensing or chemical signaling in controlling orientations of growth. And although tissue-level models have been proposed to account for morphogenetic changes (e.g., Fig. 6E), many of the underlying components remain hypothetical. A further challenge is to determine how interactions across levels have been modified during evolution to give rise to the diversity of plant forms (99).

To what extent can the principles of plant morphogenesis be extended to microbial and animal development? Like plants, bacteria and fungi have cell walls with fibers that confer mechanical strength but that correspond to peptidoglycans, glycans, or chitin rather than cellulose (100, 101). Growth depends on turgor, though the extent to which turgor and/or insertion of new wall material drives growth remains to be clarified (102). Animal cells have a network of fibers, the actin cortex, that lies immediately beneath the plasma membrane and plays a comparable role to a cell wall in mechanics: conferring mechanical stiffness and resistance to external mechanical stresses and turgor (103, 104). Sliding of these fibers likely plays a key role in animal morphogenesis but, unlike plants, can be active (e.g., contractile) as well as passive (caused by turgor or tissue stresses). Animal cells can rearrange and migrate during morphogenesis, but the extent of rearrangement is limited for many growing tissues, as evidenced by the coherence of clonal sectors (105–107). Thus, organogenesis presents similar issues for coordination of growth and division orientation as in plants, such as the role of polarity and stresses (108). Animal morphogenesis is also influenced mechanically and chemically by the extracellular matrix, which contains fibers, such as collagen, that may slide past each other to stretch irreversibly (109, 110). Thus, although the molecular players and interactions are different, many of

the mechanical principles and issues outlined in this review may also be applicable to microbial and animal morphogenesis.

REFERENCES AND NOTES

1. A. N. J. Heyn, The physiology of cell elongation. *Bot. Rev.* **6**, 515–574 (1940). doi: [10.1007/BF02879296](#)
2. J. A. Lockhart, An analysis of irreversible plant cell elongation. *J. Theor. Biol.* **8**, 264–275 (1965). doi: [10.1016/0022-5193\(65\)90077-9](#); pmid: 5876240
3. P. B. Green, R. O. Erickson, J. Buggy, Metabolic and physical control of cell elongation rate: In vivo studies in *Nitella*. *Plant Physiol.* **47**, 423–430 (1971). doi: [10.1104/pp.47.3.423](#); pmid: 16657635
4. K. T. Haas, R. Wightman, E. M. Meyerowitz, A. Peaucelle, Pectin homogalacturonan nanofilament expansion drives morphogenesis in plant epidermal cells. *Science* **367**, 1003–1007 (2020). doi: [10.1126/science.aaz5103](#); pmid: 32108107
5. A. Ursprung, G. Blum, Eine Methode zur Messung des Wandturgordruckes der Zelle nebst Anwendungen. *Jahrb. Wiss. Bot.* **63**, 1–110 (1924).
6. D. J. Cosgrove, C. T. Anderson, Plant cell growth: Do pectins drive lobe formation in arabidopsis pavement cells? *Curr. Biol.* **30**, R660–R662 (2020). doi: [10.1016/j.cub.2020.04.007](#); pmid: 32516619
7. M. C. Jarvis, Structure of native cellulose microfibrils, the starting point for nanocellulose manufacture. *Philos. Trans. R. Soc. London Ser. A* **376**, 20170045 (2018). doi: [10.1098/rsta.2017.0045](#); pmid: 29277742
8. Y. Zhang *et al.*, Molecular insights into the complex mechanics of plant epidermal cell walls. *Science* **372**, 706–711 (2021). doi: [10.1126/science.abf2824](#); pmid: 33986175
9. D. J. Cosgrove, Catalysts of plant cell wall loosening. *F1000 Res.* **5**, 119 (2016). doi: [10.12688/f1000research.7180.1](#); pmid: 26918182
10. T. Zhang, D. Vavylonis, D. M. Durachko, D. J. Cosgrove, Nanoscale movements of cellulose microfibrils in primary cell walls. *Nat. Plants* **3**, 17056 (2017). doi: [10.1038/nplants.2017.56](#); pmid: 28452988
11. W. J. Nicolas *et al.*, Cryo-electron tomography of the onion cell wall shows bimodally oriented cellulose fibers and reticulated homogalacturonan networks. *Curr. Biol.* **32**, 2375–2389.e6 (2022). doi: [10.1016/j.cub.2022.04.024](#); pmid: 35508170
12. D. J. Cosgrove, Building an extensible cell wall. *Plant Physiol.* **189**, 1246–1277 (2022). doi: [10.1093/plphys/kiac184](#); pmid: 35460252
13. A. M. Saffer, Expanding roles for pectins in plant development. *J. Integr. Plant Biol.* **60**, 910–923 (2018). doi: [10.1111/jipb.12662](#); pmid: 29727062
14. K. T. Haas, R. Wightman, A. Peaucelle, H. Höfte, The role of pectin phase separation in plant cell wall assembly and growth. *Cell Surf.* **7**, 100054 (2021). doi: [10.1016/j.tcsu.2021.100054](#); pmid: 34141960
15. A. J. Bidhendi, A. Geitmann, Relating the mechanics of the primary plant cell wall to morphogenesis. *J. Exp. Bot.* **67**, 449–461 (2016). doi: [10.1093/jxb/erv535](#); pmid: 26689854
16. T. Zhang, H. Tang, D. Vavylonis, D. J. Cosgrove, Disentangling loosening from softening: Insights into primary cell wall structure. *Plant J.* **100**, 1101–1117 (2019). doi: [10.1111/tpj.14519](#); pmid: 31469935
17. M. C. Jarvis, Control of thickness of collenchyma cell walls by pectins. *Planta* **187**, 218–220 (1992). doi: [10.1007/BF00201941](#); pmid: 24178046
18. J. Du, C. T. Anderson, C. Xiao, Dynamics of pectic homogalacturonan in cellular morphogenesis and adhesion, wall integrity sensing and plant development. *Nat. Plants* **8**, 332–340 (2022). doi: [10.1038/s41477-022-01120-2](#); pmid: 35411046
19. K. Jonsson, O. Hamant, R. P. Bhalerao, Plant cell walls as mechanical signaling hubs for morphogenesis. *Curr. Biol.* **32**, R334–R340 (2022). doi: [10.1016/j.cub.2022.02.036](#); pmid: 35413265
20. Z. L. Yue *et al.*, The receptor kinase OsWAK11 monitors cell wall pectin changes to fine-tune brassinosteroid signaling and regulate cell elongation in rice. *Curr. Biol.* **32**, 2454–2466.e7 (2022). doi: [10.1016/j.cub.2022.04.028](#); pmid: 35512695
21. G. Levesque-Tremblay, J. Pelloux, S. A. Braybrook, K. Müller, Tuning of pectin methylesterification: Consequences for cell wall biomechanics and development. *Planta* **242**, 791–811 (2015). doi: [10.1007/s00425-015-2358-5](#); pmid: 26168980
22. S. A. Braybrook, A. Peaucelle, Mechano-chemical aspects of organ formation in *Arabidopsis thaliana*: The relationship between auxin and pectin. *PLOS ONE* **8**, e57813 (2013). doi: [10.1371/journal.pone.0057813](#); pmid: 23554870
23. F. Bou Daher *et al.*, Anisotropic growth is achieved through the additive mechanical effect of material anisotropy and elastic asymmetry. *eLife* **7**, e38161 (2018). doi: [10.7554/eLife.38161](#); pmid: 30226465
24. A. Peaucelle, R. Wightman, H. Höfte, The control of growth symmetry breaking in the arabidopsis hypocotyl. *Curr. Biol.* **25**, 1746–1752 (2015). doi: [10.1016/j.cub.2015.05.022](#); pmid: 26073136
25. M. C. Jarvis, Hydrogen bonding and other non-covalent interactions at the surfaces of cellulose microfibrils. *Cellulose* **30**, 667–687 (2022). doi: [10.1007/s10570-022-04954-3](#)
26. Y. B. Park, D. J. Cosgrove, A revised architecture of primary cell walls based on biomechanical changes induced by substrate-specific endoglucanases. *Plant Physiol.* **158**, 1933–1943 (2012). doi: [10.1104/pp.111.192880](#); pmid: 22362871
27. D. J. Cosgrove, Relaxation in a high-stress environment: The molecular bases of extensible cell walls and cell enlargement. *Plant Cell* **9**, 1031–1041 (1997). doi: [10.1105/tpc.9.7.1031](#); pmid: 9254929
28. K. Takahashi, S. Hirata, N. Kido, K. Katou, Wall-yielding properties of cell walls from elongating cucumber hypocotyls in relation to the action of expansin. *Plant Cell Physiol.* **47**, 1520–1529 (2006). doi: [10.1093/pcp/pcl017](#); pmid: 17012740
29. W. Lin *et al.*, TMK-based cell-surface auxin signalling activates cell-wall acidification. *Nature* **559**, 278–282 (2021). doi: [10.1038/s41586-021-03976-4](#); pmid: 34707287
30. K. Nakahori, K. Katou, H. Okamoto, Auxin changes both the extensibility and the yield threshold of the cell wall of *Vigna* hypocotyls. *Plant Cell Physiol.* **32**, 121–129 (1991).
31. B. Mouila, Plant biomechanics and mechanobiology are convergent paths to flourishing interdisciplinary research. *J. Exp. Bot.* **64**, 4617–4633 (2013). doi: [10.1093/jxb/ert320](#); pmid: 24193603
32. T. W. Wang, D. J. Cosgrove, R. N. Arteca, Brassinosteroid stimulation of hypocotyl elongation and wall relaxation in pakchoi (*Brassica chinensis* cv Lei-Choi). *Plant Physiol.* **101**, 965–968 (1993). doi: [10.1104/pp.101.3.965](#); pmid: 12231748
33. G. Réfrégier, S. Pelletier, D. Jaillard, H. Höfte, Interaction between wall deposition and cell elongation in dark-grown hypocotyl cells in *Arabidopsis*. *Plant Physiol.* **135**, 959–968 (2004). doi: [10.1104/pp.104.038711](#); pmid: 15181211
34. J. Verbančič, J. E. Lunn, M. Stitt, S. Persson, Carbon supply and the regulation of cell wall synthesis. *Mol. Plant* **11**, 75–94 (2018). doi: [10.1016/j.molp.2017.10.004](#); pmid: 29054565
35. H. Edelmann, R. Bergfeld, P. Schonfer, Role of cell-wall biogenesis in the initiation of auxin-mediated growth in coleoptiles of *Zea mays* L. *Planta* **179**, 486–494 (1989). doi: [10.1007/BF00397588](#); pmid: 24201772
36. P. B. Green, The spiral growth pattern of the cell wall in *Nitella axillaris*. *Am. J. Bot.* **41**, 403–409 (1954). doi: [10.1002/j.1537-2197.1954.tb14356.x](#)
37. P. A. Richmond, Patterns of cellulose microfibril deposition and rearrangement in *Nitella*: In vivo analysis by a birefringence index. *J. Appl. Polym. Sci.* **37**, 107–122 (1983).
38. A. J. Bidhendi, A. Geitmann, Finite element modeling of shape changes in plant cells. *Plant Physiol.* **176**, 41–56 (2018). doi: [10.1104/pp.17.01684](#); pmid: 29229695
39. A. J. Bidhendi, B. Altartouri, F. P. Gosselin, A. Geitmann, Mechanical stress initiates and sustains the morphogenesis of wavy leaf epidermal cells. *Cell Rep.* **28**, 1237–1250.e6 (2019). doi: [10.1016/j.celrep.2019.07.006](#); pmid: 31365867
40. E. S. Castle, Membrane tension and orientation of structure in the plant cell wall. *J. Cell. Comp. Physiol.* **10**, 113–121 (1937). doi: [10.1002/jcp.1030100110](#)
41. C. M. Rounds, M. Bezanilla, Growth mechanisms in tip-growing plant cells. *Annu. Rev. Plant Biol.* **64**, 243–265 (2013). doi: [10.1146/annurev-arplant-050312-120150](#); pmid: 23451782
42. D. J. Cosgrove, Diffuse growth of plant cell walls. *Plant Physiol.* **176**, 16–27 (2018). doi: [10.1104/pp.17.01541](#); pmid: 29138349
43. P. B. Green, Mechanism for plant cellular morphogenesis. *Science* **138**, 1404–1405 (1962). doi: [10.1126/science.138.3548.1404](#); pmid: 17753861
44. J. P. Métraux, L. Taiz, Transverse viscoelastic extension in *Nitella*: I. Relationship to growth rate. *Plant Physiol.* **61**, 135–138 (1978). doi: [10.1104/pp.61.2.135](#); pmid: 16660247
45. A. R. Paredes, C. R. Somerville, D. W. Ehrhardt, Visualization of cellulose synthase demonstrates functional association with microtubules. *Science* **312**, 1491–1495 (2006). doi: [10.1126/science.1126551](#); pmid: 16627697
46. J. Chan, E. Coen, Interaction between autonomous and microtubule guidance systems controls cellulose synthase trajectories. *Curr. Biol.* **30**, 941–947.e2 (2020). doi: [10.1016/j.cub.2019.12.066](#); pmid: 32037093
47. R. Dixit, R. Cyr, Encounters between dynamic cortical microtubules promote ordering of the cortical array through angle-dependent modifications of microtubule behavior. *Plant Cell* **16**, 3274–3284 (2004). doi: [10.1105/tpc.104.026930](#); pmid: 15539470
48. B. Chakraborty, I. Bilou, B. Scheres, B. M. Mulder, A computational framework for cortical microtubule dynamics in realistically shaped plant cells. *PLOS Comput. Biol.* **14**, e1005959 (2018). doi: [10.1371/journal.pcbi.1005959](#); pmid: 29394250
49. S. H. Tindemans, R. J. Hawkins, B. M. Mulder, Survival of the aligned: Ordering of the plant cortical microtubule array. *Phys. Rev. Lett.* **104**, 058103 (2010). doi: [10.1103/PhysRevLett.104.058103](#); pmid: 20366797
50. P. Durand-Smet, T. A. Spelman, E. M. Meyerowitz, H. Jönsson, Cytoskeletal organization in isolated plant cells under geometry control. *Proc. Natl. Acad. Sci. U.S.A.* **117**, 17399–17408 (2020). doi: [10.1073/pnas.2003184117](#); pmid: 3264513
51. L. Colin *et al.*, Cortical tension overrides geometrical cues to orient microtubules in confined protoplasts. *Proc. Natl. Acad. Sci. U.S.A.* **117**, 32731–32738 (2020). doi: [10.1073/pnas.2008895117](#); pmid: 33288703
52. P. B. Green, A. King, A mechanism for the origin of specifically oriented textures in development with special reference to *Nitella* wall texture. *Aust. J. Biol. Sci.* **19**, 421–437 (1966). doi: [10.1071/BI9660421](#)
53. R. E. Williamson, Alignment of cortical microtubules by anisotropic wall stresses. *Aust. J. Plant Physiol.* **17**, 601–613 (1990).
54. A. R. Paredes, S. Persson, D. W. Ehrhardt, C. R. Somerville, Genetic evidence that cellulose synthase activity influences microtubule cortical array organization. *Plant Physiol.* **147**, 1723–1734 (2008). doi: [10.1104/pp.108.120196](#); pmid: 18583534
55. R. Schneider, D. W. Ehrhardt, E. M. Meyerowitz, A. Sampathkumar, Tethering of cellulose synthase to microtubules dampens mechano-induced cytoskeletal organization in *Arabidopsis* pavement cells. *Nat. Plants* **8**, 1064–1073 (2022). doi: [10.1038/s41477-022-01218-7](#); pmid: 35982303
56. M. Bringmann, D. C. Bergmann, Tissue-wide mechanical forces influence the polarity of stomatal stem cells in *Arabidopsis*. *Curr. Biol.* **27**, 877–883 (2017). doi: [10.1016/j.cub.2017.01.059](#); pmid: 28285992
57. P. Křeček *et al.*, The PIN-FORMED (PIN) protein family of auxin transporters. *Genome Biol.* **10**, 249 (2009). doi: [10.1186/gb-2009-10-12-249](#); pmid: 20053306
58. J. Dong, C. A. MacAlister, D. C. Bergmann, BASL controls asymmetric cell division in *Arabidopsis*. *Cell* **137**, 1320–1330 (2009). doi: [10.1016/j.cell.2009.04.018](#); pmid: 19523675
59. E. Truernit *et al.*, High-resolution whole-mount imaging of three-dimensional tissue organization and gene expression enables the study of phloem development and structure in *Arabidopsis*. *Plant Cell* **20**, 1494–1503 (2008). doi: [10.1105/tpc.107.056069](#); pmid: 18523061
60. S. Yoshida *et al.*, A SOSEKI-based coordinate system interprets global polarity cues in *Arabidopsis*. *Nat. Plants* **5**, 160–166 (2019). doi: [10.1038/s41477-019-0363-6](#); pmid: 30737509
61. L. J. Pillitteri, K. M. Peterson, R. J. Horst, K. U. Torii, Molecular profiling of stomatal meristemoids reveals new component of asymmetric cell division and commonalities among stem cell populations in *Arabidopsis*. *Plant Cell* **23**, 3260–3275 (2011). doi: [10.1105/tpc.111.088583](#); pmid: 21963668
62. E. Truernit, H. Bauby, K. Belcram, J. Barthélémy, J. C. Palauqui, OCTOPUS, a polarly localised membrane-associated protein, regulates phloem differentiation entry in *Arabidopsis thaliana*. *Development* **139**, 1306–1315 (2012). doi: [10.1242/dev.072629](#); pmid: 22395740
63. J. Chan, C. Mansfield, F. Clouet, D. Dorussen, E. Coen, Intrinsic cell polarity coupled to growth axis formation in tobacco BY-2 cells. *Curr. Biol.* **30**, 4999–5006.e3 (2020). doi: [10.1016/j.cub.2020.09.036](#); pmid: 33035485

64. C. Ambrose, J. F. Allard, E. N. Cytrynbaum, G. O. Wasteneys, A CLASP-modulated cell edge barrier mechanism drives cell-wide cortical microtubule organization in *Arabidopsis*. *Nat. Commun.* **2**, 430 (2011). doi: [10.1038/ncomms1444](https://doi.org/10.1038/ncomms1444); pmid: [21847104](https://pubmed.ncbi.nlm.nih.gov/21847104/)
65. S. Liu, F. Robert, Z. Rahnesan, S. M. Doyle, S. Robert, Solving the puzzle of shape regulation in plant epidermal pavement cells. *Annu. Rev. Plant Biol.* **72**, 525–550 (2021). doi: [10.1146/annurev-arplant-080720-081920](https://doi.org/10.1146/annurev-arplant-080720-081920); pmid: [34143651](https://pubmed.ncbi.nlm.nih.gov/34143651/)
66. F. B. Daher, S. A. Braybrook, How to let go: Pectin and plant cell adhesion. *Front. Plant Sci.* **6**, 523 (2015). doi: [10.3389/fpls.2015.00523](https://doi.org/10.3389/fpls.2015.00523); pmid: [26236321](https://pubmed.ncbi.nlm.nih.gov/26236321/)
67. W. S. Peters, A. D. Tomos, The history of tissue tension. *Ann. Bot.* **77**, 657–665 (1996). doi: [10.1093/aob/77.6.657](https://doi.org/10.1093/aob/77.6.657); pmid: [11541099](https://pubmed.ncbi.nlm.nih.gov/11541099/)
68. S. Verger, Y. Long, A. Boudaoud, O. Hamant, A tension-adhesion feedback loop in plant epidermis. *eLife* **7**, e34460 (2018). doi: [10.7554/eLife.34460](https://doi.org/10.7554/eLife.34460); pmid: [29683428](https://pubmed.ncbi.nlm.nih.gov/29683428/)
69. U. Kutschera, K. J. Niklas, The epidermal-growth-control theory of stem elongation: An old and a new perspective. *J. Plant Physiol.* **164**, 1395–1409 (2007). doi: [10.1016/j.jplph.2007.08.002](https://doi.org/10.1016/j.jplph.2007.08.002); pmid: [17905474](https://pubmed.ncbi.nlm.nih.gov/17905474/)
70. Z. Hejnowicz, A. Sievers, Tissue stresses in organs of herbaceous plants II. Determination in three dimensions in the hypocotyl of sunflower. *J. Exp. Bot.* **46**, 1045–1053 (1995). doi: [10.1093/jxb/46.8.1045](https://doi.org/10.1093/jxb/46.8.1045)
71. Z. Hejnowicz, A. Sievers, Tissue stresses in organs of herbaceous plants I. Poisson ratios of tissues and their role in determination of the stresses. *J. Exp. Bot.* **289**, 1035–1043 (1995). doi: [10.1093/jxb/46.8.1035](https://doi.org/10.1093/jxb/46.8.1035)
72. A. Goriely, *The Mathematics and Mechanics of Biological Growth* (Springer, 2017).
73. O. Hamant *et al.*, Developmental patterning by mechanical signals in *Arabidopsis*. *Science* **322**, 1650–1655 (2008). doi: [10.1126/science.1165594](https://doi.org/10.1126/science.1165594); pmid: [19074340](https://pubmed.ncbi.nlm.nih.gov/19074340/)
74. O. Hamant, D. Inoue, D. Bouchez, J. Dumais, E. Mjølness, Are microtubules tension sensors? *Nat. Commun.* **10**, 2360 (2019). doi: [10.1038/s41467-019-10207-y](https://doi.org/10.1038/s41467-019-10207-y); pmid: [31142740](https://pubmed.ncbi.nlm.nih.gov/31142740/)
75. M. G. Heisler, Integration of core mechanisms underlying plant aerial architecture. *Front. Plant Sci.* **12**, 786338 (2021). doi: [10.3389/fpls.2021.786338](https://doi.org/10.3389/fpls.2021.786338); pmid: [34868186](https://pubmed.ncbi.nlm.nih.gov/34868186/)
76. J. M. Hush, C. R. Hawes, R. L. Overall, Interphase microtubule re-orientation predicts a new cell polarity in wounded pea roots. *J. Cell Sci.* **96**, 47–61 (1990). doi: [10.1242/jcs.96.1.47](https://doi.org/10.1242/jcs.96.1.47)
77. Z. Hejnowicz, A. Rusin, T. Rusin, Tensile tissue stress affects the orientation of cortical microtubules in the epidermis of sunflower hypocotyl. *J. Plant Growth Regul.* **19**, 31–44 (2000). doi: [10.1007/s003440000005](https://doi.org/10.1007/s003440000005); pmid: [11010990](https://pubmed.ncbi.nlm.nih.gov/11010990/)
78. A. Burian, Z. Hejnowicz, Strain rate does not affect cortical microtubule orientation in the isolated epidermis of sunflower hypocotyls. *Plant Biol.* **12**, 459–468 (2010). doi: [10.1111/j.1438-8677.2009.00228.x](https://doi.org/10.1111/j.1438-8677.2009.00228.x); pmid: [20522182](https://pubmed.ncbi.nlm.nih.gov/20522182/)
79. S. Robinson, C. Kuhlemeier, Global compression reorients cortical microtubules in *Arabidopsis* hypocotyl epidermis and promotes growth. *Curr. Biol.* **28**, 1794–1802.e2 (2018). doi: [10.1016/j.cub.2018.04.028](https://doi.org/10.1016/j.cub.2018.04.028); pmid: [29804811](https://pubmed.ncbi.nlm.nih.gov/29804811/)
80. K. Zandomeni, P. Schopfer, Mechanosensory microtubule reorientation in the epidermis of maize coleoptiles subjected to bending stress. *Protoplasma* **182**, 96–101 (1994). doi: [10.1007/BF01403471](https://doi.org/10.1007/BF01403471); pmid: [11540618](https://pubmed.ncbi.nlm.nih.gov/11540618/)
81. D. D. Fisher, R. J. Cyr, Extending the microtubule/microfibril paradigm: Cellulose synthesis is required for normal cortical microtubule alignment in elongating cells. *Plant Physiol.* **116**, 1043–1051 (1998). doi: [10.1104/pp.116.3.1043](https://doi.org/10.1104/pp.116.3.1043); pmid: [9501137](https://pubmed.ncbi.nlm.nih.gov/9501137/)
82. M. G. Heisler *et al.*, Alignment between PIN1 polarity and microtubule orientation in the shoot apical meristem reveals a tight coupling between morphogenesis and auxin transport. *PLOS Biol.* **8**, e1000516 (2010). doi: [10.1371/journal.pbio.1000516](https://doi.org/10.1371/journal.pbio.1000516); pmid: [20976043](https://pubmed.ncbi.nlm.nih.gov/20976043/)
83. K. Abley *et al.*, An intracellular partitioning-based framework for tissue cell polarity in plants and animals. *Development* **140**, 2061–2074 (2013). doi: [10.1242/dev.062984](https://doi.org/10.1242/dev.062984); pmid: [23633507](https://pubmed.ncbi.nlm.nih.gov/23633507/)
84. E. Coen, R. Kennaway, C. Whitewoods, On genes and form. *Development* **144**, 4203–4213 (2017). doi: [10.1242/dev.151910](https://doi.org/10.1242/dev.151910); pmid: [29183934](https://pubmed.ncbi.nlm.nih.gov/29183934/)
85. L. Errera, Sur une condition fondamentale d'équilibre des cellules vivantes. *C.R. Acad. Sci.* **103**, 822–824 (1886).
86. P. Prusinkiewicz, A. Runions, Computational models of plant development and form. *New Phytol.* **193**, 549–569 (2012). doi: [10.1111/j.1469-8137.2011.04009.x](https://doi.org/10.1111/j.1469-8137.2011.04009.x); pmid: [22235985](https://pubmed.ncbi.nlm.nih.gov/22235985/)
87. S. Yoshida *et al.*, Genetic control of plant development by overriding a geometric division rule. *Dev. Cell* **29**, 75–87 (2014). doi: [10.1016/j.devcel.2014.02.002](https://doi.org/10.1016/j.devcel.2014.02.002); pmid: [24684831](https://pubmed.ncbi.nlm.nih.gov/24684831/)
88. F. Boudon *et al.*, A computational framework for 3D mechanical modeling of plant morphogenesis with cellular resolution. *PLOS Comput. Biol.* **11**, e1003950 (2015). doi: [10.1371/journal.pcbi.1003950](https://doi.org/10.1371/journal.pcbi.1003950); pmid: [25569615](https://pubmed.ncbi.nlm.nih.gov/25569615/)
89. N. Hervieux *et al.*, A mechanical feedback restricts sepal growth and shape in *Arabidopsis*. *Curr. Biol.* **26**, 1019–1028 (2016). doi: [10.1016/j.cub.2016.03.004](https://doi.org/10.1016/j.cub.2016.03.004); pmid: [27151660](https://pubmed.ncbi.nlm.nih.gov/27151660/)
90. F. Zhao *et al.*, Microtubule-mediated wall anisotropy contributes to leaf blade flattening. *Curr. Biol.* **30**, 3972–3985.e6 (2020). doi: [10.1016/j.cub.2020.07.076](https://doi.org/10.1016/j.cub.2020.07.076); pmid: [32916107](https://pubmed.ncbi.nlm.nih.gov/32916107/)
91. V. Gorelova, J. Sprakel, D. Weijers, Plant cell polarity as the nexus of tissue mechanics and morphogenesis. *Nat. Plants* **7**, 1548–1559 (2021). doi: [10.1038/s41477-021-01021-w](https://doi.org/10.1038/s41477-021-01021-w); pmid: [34887521](https://pubmed.ncbi.nlm.nih.gov/34887521/)
92. C. D. Whitewoods *et al.*, Evolution of carnivorous traps from planar leaves through simple shifts in gene expression. *Science* **367**, 91–96 (2020). doi: [10.1126/science.aay5433](https://doi.org/10.1126/science.aay5433); pmid: [31753850](https://pubmed.ncbi.nlm.nih.gov/31753850/)
93. A. E. Richardson *et al.*, Evolution of the grass leaf by primordium extension and petiole-lamina remodeling. *Science* **374**, 1377–1381 (2021). doi: [10.1126/science.abf9407](https://doi.org/10.1126/science.abf9407); pmid: [34882477](https://pubmed.ncbi.nlm.nih.gov/34882477/)
94. S. Fox *et al.*, Spatiotemporal coordination of cell division and growth during organ morphogenesis. *PLOS Biol.* **16**, e2005952 (2018). doi: [10.1371/journal.pbio.2005952](https://doi.org/10.1371/journal.pbio.2005952); pmid: [30383040](https://pubmed.ncbi.nlm.nih.gov/30383040/)
95. D. Kierzkowski *et al.*, A growth-based framework for leaf shape development and diversity. *Cell* **177**, 1405–1418.e17 (2019). doi: [10.1016/j.cell.2019.05.011](https://doi.org/10.1016/j.cell.2019.05.011); pmid: [31130379](https://pubmed.ncbi.nlm.nih.gov/31130379/)
96. M. Zhu *et al.*, Robust organ size requires robust timing of initiation orchestrated by focused auxin and cytokinin signalling. *Nat. Plants* **6**, 686–698 (2020). doi: [10.1038/s41477-020-0666-7](https://doi.org/10.1038/s41477-020-0666-7); pmid: [32451448](https://pubmed.ncbi.nlm.nih.gov/32451448/)
97. P. Žádníková *et al.*, A model of differential growth-guided apical hook formation in plants. *Plant Cell* **28**, 2464–2477 (2016). doi: [10.1105/tpc.15.00569](https://doi.org/10.1105/tpc.15.00569); pmid: [27754878](https://pubmed.ncbi.nlm.nih.gov/27754878/)
98. Q. Zhu, P. Žádníková, D. Smet, D. Van Der Straeten, E. Benková, Real-time analysis of the apical hook development. *Methods Mol. Biol.* **1497**, 1–8 (2017). doi: [10.1007/978-1-4939-6469-7_1](https://doi.org/10.1007/978-1-4939-6469-7_1); pmid: [27864752](https://pubmed.ncbi.nlm.nih.gov/27864752/)
99. D. Wilson-Sánchez, N. Bhatia, A. Runions, M. Tsiantis, From genes to shape in leaf development and evolution. *Curr. Biol.* **32**, R1215–R1222 (2022). doi: [10.1016/j.cub.2022.09.021](https://doi.org/10.1016/j.cub.2022.09.021); pmid: [36347226](https://pubmed.ncbi.nlm.nih.gov/36347226/)
100. N. A. R. Gow, M. D. Lenardon, Architecture of the dynamic fungal cell wall. *Nat. Rev. Microbiol.* **10**, 1038/s41579-022-00796-9 (2022). doi: [10.1038/s41579-022-00796-9](https://doi.org/10.1038/s41579-022-00796-9); pmid: [36266346](https://pubmed.ncbi.nlm.nih.gov/36266346/)
101. T. Dörr, P. J. Moynihan, C. Mayer, Editorial: Bacterial cell wall structure and dynamics. *Front. Microbiol.* **10**, 2051 (2019). doi: [10.3389/fmicb.2019.02051](https://doi.org/10.3389/fmicb.2019.02051); pmid: [31551985](https://pubmed.ncbi.nlm.nih.gov/31551985/)
102. E. R. Rojas, K. C. Huang, Regulation of microbial growth by turgor pressure. *Curr. Opin. Microbiol.* **42**, 62–70 (2018). doi: [10.1016/j.mib.2017.10.015](https://doi.org/10.1016/j.mib.2017.10.015); pmid: [29125939](https://pubmed.ncbi.nlm.nih.gov/29125939/)
103. G. Salbreux, G. Charras, E. Paluch, Actin cortex mechanics and cellular morphogenesis. *Trends Cell Biol.* **22**, 536–545 (2012). doi: [10.1016/j.tcb.2012.07.001](https://doi.org/10.1016/j.tcb.2012.07.001); pmid: [22871642](https://pubmed.ncbi.nlm.nih.gov/22871642/)
104. T. Kim, M. L. Gardel, E. Munro, Determinants of fluidlike behavior and effective viscosity in cross-linked actin networks. *Biophys. J.* **106**, 526–534 (2014). doi: [10.1016/j.bpj.2013.12.031](https://doi.org/10.1016/j.bpj.2013.12.031); pmid: [24507593](https://pubmed.ncbi.nlm.nih.gov/24507593/)
105. L. Marcon, C. G. Arqués, M. S. Torres, J. Sharpe, A computational clonal analysis of the developing mouse limb bud. *PLOS Comput. Biol.* **7**, e1001071 (2011). doi: [10.1371/journal.pcbi.1001071](https://doi.org/10.1371/journal.pcbi.1001071); pmid: [21347315](https://pubmed.ncbi.nlm.nih.gov/21347315/)
106. S. M. Meilhac *et al.*, A retrospective clonal analysis of the myocardium reveals two phases of clonal growth in the developing mouse heart. *Development* **130**, 3877–3889 (2003). doi: [10.1242/dev.00580](https://doi.org/10.1242/dev.00580); pmid: [12835402](https://pubmed.ncbi.nlm.nih.gov/12835402/)
107. F. Germani, C. Bergantinos, L. A. Johnston, Mosaic analysis in *Drosophila*. *Genetics* **208**, 473–490 (2018). doi: [10.1534/genetics.117.300256](https://doi.org/10.1534/genetics.117.300256); pmid: [29378809](https://pubmed.ncbi.nlm.nih.gov/29378809/)
108. L. LeGoff, T. Lecuit, Mechanical forces and growth in animal tissues. *Cold Spring Harb. Perspect. Biol.* **8**, a019232 (2015). doi: [10.1101/cshperspect.a019232](https://doi.org/10.1101/cshperspect.a019232); pmid: [26261279](https://pubmed.ncbi.nlm.nih.gov/26261279/)
109. B. Sun, The mechanics of fibrillar collagen extracellular matrix. *Cell Rep. Phys. Sci.* **2**, 100515 (2021). doi: [10.1016/j.xcrp.2021.100515](https://doi.org/10.1016/j.xcrp.2021.100515); pmid: [34485951](https://pubmed.ncbi.nlm.nih.gov/34485951/)
110. M. L. Wood, G. E. Lester, L. E. Dahners, Collagen fiber sliding during ligament growth and contracture. *J. Orthop. Res.* **16**, 438–440 (1998). doi: [10.1002/jor.1100160407](https://doi.org/10.1002/jor.1100160407); pmid: [9747784](https://pubmed.ncbi.nlm.nih.gov/9747784/)

ACKNOWLEDGMENTS

We thank P. Robinson for filming and editing the movies and J. Chan, P. Durand-Smet, A. Hanner, R. Kennaway, R. Smith, and S. Zhang for helpful comments on the manuscript. **Funding:** We acknowledge support from the Human Frontier Science Program (HFSP) for a collaborative research grant RGP0005/2022 awarded to the authors of this review. E.C. was supported by grants from the UK Biotechnology and Biological Sciences Research Council (BB/M023117/1, BB/W007924/1, BBS/E/J/000PR9787, BBS/E/J/00000152, BB/L008920/1, and BBS/E/J/000PR9789). D.J.C. was supported by the US Department of Energy under awards #DE-SC0001090 for work on wall structure and #DE-FG2-84ER13179 for work on expansins and wall mechanics. **Competing interests:** The authors have no competing interests. **License information:** Copyright © 2023 the authors, some rights reserved; exclusive licensee American Association for the Advancement of Science. No claim to original US government works. <https://www.science.org/about/science-licenses-journal-article-reuse>

Submitted 3 October 2022; accepted 15 December 2022
10.1126/science.ade8055

Pushing the Boundaries of Knowledge

As AAAS's first multidisciplinary, open access journal, *Science Advances* publishes research that reflects the selectivity of high impact, innovative research you expect from the *Science* family of journals, published in an open access format to serve a vast and growing global audience. Check out the latest findings or learn how to submit your research: **[ScienceAdvances.org](https://www.scienceadvances.org)**

Science
Advances
AAAS

GOLD OPEN ACCESS, DIGITAL, AND FREE TO ALL READERS

RESEARCH ARTICLES

ORGANIC CHEMISTRY

Computer-aided key step generation in alkaloid total synthesis

Yingfu Lin¹, Rui Zhang², Di Wang¹, Tim Cernak^{1,2*}

Efficient chemical synthesis is critical to satisfying future demands for medicines, materials, and agrochemicals. Retrosynthetic analysis of modestly complex molecules has been automated over the course of decades, but the combinatorial explosion of route possibilities has challenged computer hardware and software until only recently. Here, we explore a computational strategy that merges computer-aided synthesis planning with molecular graph editing to minimize the number of synthetic steps required to produce alkaloids. Our study culminated in an enantioselective three-step synthesis of (–)-stemoamide by leveraging high-impact key steps, which could be identified in computer-generated retrosynthesis plans using graph edit distances.

Efficient total synthesis converts commercially available starting materials into complex target molecules in as few steps as possible. In practice, this is often achieved by optimizing key steps to simultaneously form many of the requisite target bonds, thereby rapidly generating structural complexity. Common examples include cycloadditions, cascades (1), or multicomponent coupling reactions (2). Although the notion of a key step is well known to practitioners of total synthesis, it has not been formalized in computer-aided synthesis planning (CASP). Modern CASP strategies aim to minimize protecting-group manipulations and maximize convergence, but the focus of automated retrosynthesis has been on encoding reaction rules for maximum reliability in experimental realization of predicted routes, which favors robust, well-precedented reactions. Meanwhile, state-of-the-art human synthetic strategies maximize step and atom economy by targeting innovative but riskier key steps and minimizing low-impact concession steps such as protecting group manipulations (3), unnecessary redox operations (4), and functional group interconversions (5). Here we explore the synergy of automatically generating many plausible key steps using CASP, with manual selection for high-impact steps, which are encoded as the reduction in graph edit distance, to minimize overall step count in total synthesis.

Experimental demonstration of routes designed with modern CASP has been achieved in pharmaceutical synthesis (6–9) but has seen considerably less use in the complex setting of alkaloid total synthesis. Notable

exceptions include a recent 30-step synthesis of weisaconitine D (10) and a 15-step synthesis of (+)-tacamonidine (11), representing the state of the art. We chose stemoamide (1, Fig. 1), isolated from *Stemonaceae* plants (12), as an ideal target molecule because its four stereocenters and fused-ring structure would challenge modern CASP (11), while its precedence in thirty-two historic and contemporary syntheses (13–21) provides a strong benchmark for comparison.

Computer-aided retrosynthetic plans

The first retrosynthetic plan removes the α -methyl group and breaks the C–N bond of the azepine ring to give cyclized alkene 2 (Fig. 1), which was itself produced by a key organocatalyzed Mannich-allylation-lactonization sequence recommended by CASP. Advanced intermediate 2 was further simplified to starting materials 3, 4 and two equivalents of aldehyde 5. A second route to 1 resulted from the evolution of our CASP and graph editing strategy. In this route, a Schmidt–Aubé rear-

angement recommended by CASP is a key simplifying element. The resultant cyclobutanone intermediate 6 was further broken down into 7, 8, 9, and 10, leveraging a key Michael addition and alkylation sequence, which was identified as a key step in a separate CASP search of 1. The computationally discovered routes were edited and experimentally realized as described below.

Revelation of the Mannich reaction as a key step

Modern CASP platforms favor reactions with well-established conditions. As a result, predicted routes generally have lower risk but can be biased toward low-impact transformations. A system for recognizing synthetic ideality (22, 23) could synergize with the power of modern CASP platforms even though additional experimental optimization may be required to realize riskier high-impact key steps.

As a first attempt to minimize step count from CASP-generated routes, (–)-1 was subjected to automated retrosynthesis in the software SYNTHIA with a scoring function that promoted chemoselectivity, regioselectivity, and stereoselectivity and demoted the use of protecting groups. An organocatalyzed Mannich reaction appeared as a proposed transformation in every predicted route (Fig. 2A), an unexpected outcome because this well-known reaction had not featured in any of the 32 prior syntheses of 1. Nonetheless, even the shortest calculated route (fig. S1) was seven steps long, which was competitive with, but not better than, the shortest human-derived enantioselective route (14). We thus chose to logically edit calculated routes for brevity by maximizing high-impact transformations and minimizing low-impact transformations. This required a new system to measure step impact.

Obvious inefficiencies such as protecting-group manipulations could be minimized by the CASP software in the calculated routes,

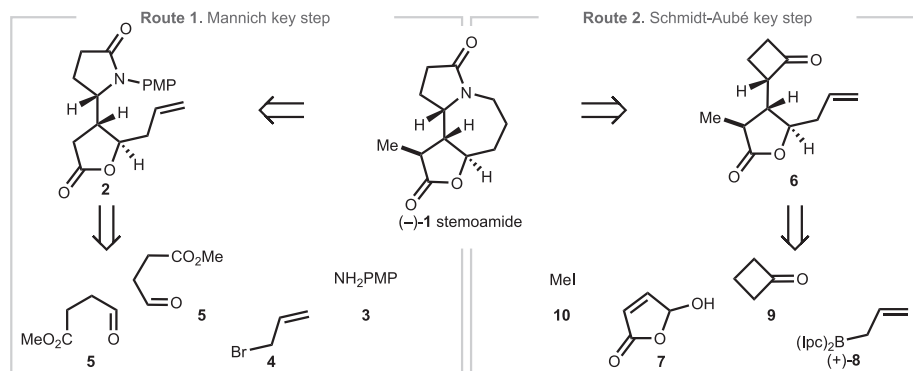


Fig. 1. Two retrosynthetic plans of 1 with computer-aided key step generation. PMP, *p*-methoxyphenyl; lpc, isopinocampheyl.

¹Department of Medicinal Chemistry, University of Michigan, Ann Arbor, MI 48109, USA. ²Department of Chemistry, University of Michigan, Ann Arbor, MI 48109, USA.

*Corresponding author. Email: tcernak@med.umich.edu

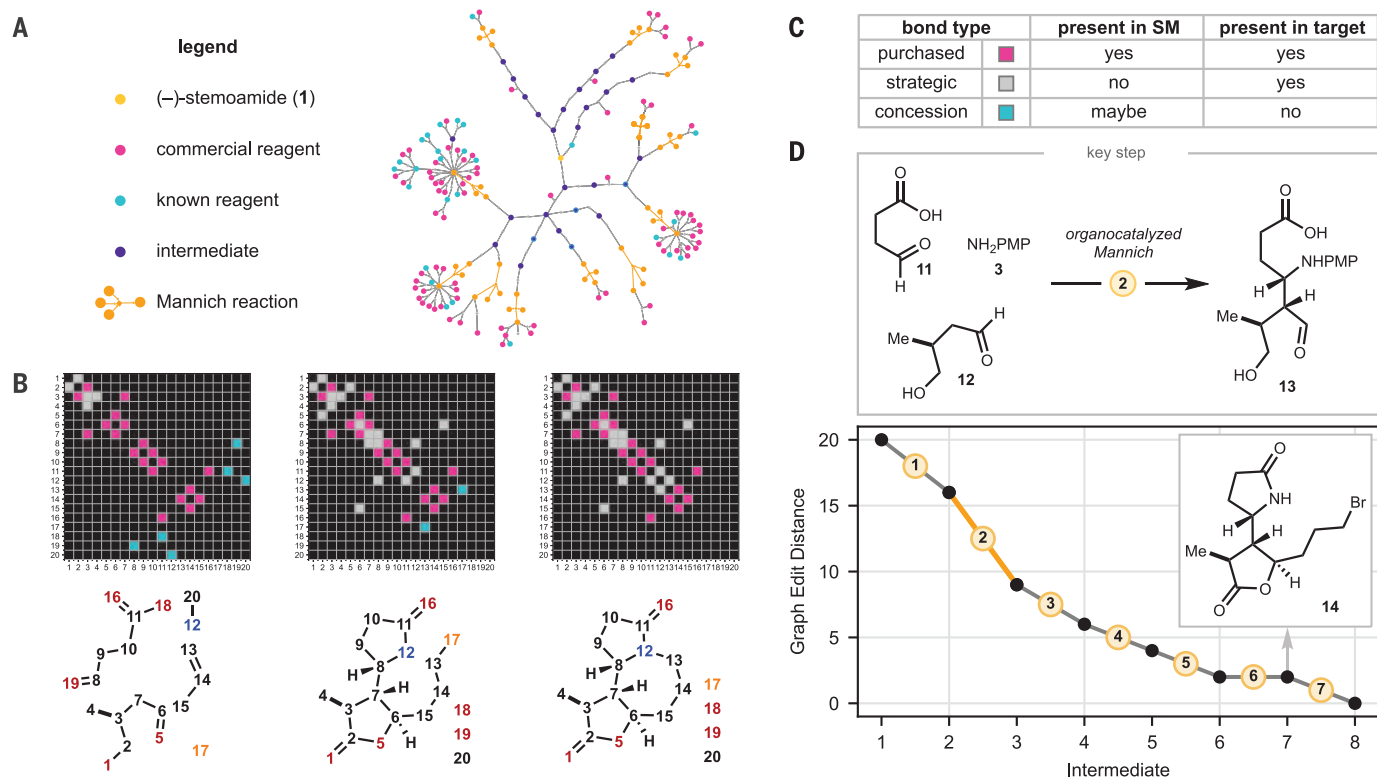


Fig. 2. Identifying key steps by graph edit analysis. (A) Network analysis of 50 SYNTHIA-predicted routes to (–)-**1**. In this search result, the Mannich reaction featured as a consistent disconnection, as highlighted by a cluster of four orange dots in each route. (B) Adjacency matrices of **3**, **11**, **12**, **8**, and HBr (left); **14** and disconnected concession atoms (middle); and **1** with

disconnected concession atoms (right). Matrix width and length are determined by the total number of heavy atoms in the overall synthesis. For concession groups, only the attached atom is considered in the graph. (C) Classification of bond type used in graph edit analysis. (D) Graph edit distance plots of a retrosynthetic route to **1**, produced by CASP, highlighting Mannich key step.

but it was nonobvious whether other specific steps among the hundreds of calculated retrosynthetic routes analyzed were impactful or not. In principle, the impact of a given synthetic step in a multistep sequence can be measured by the reduction in graph edit distance (24) between molecular graphs (25) of intermediates and the target molecule. Efficient multistep synthesis converts the bonds and atoms of commercially available starting materials into those of the target with key steps assembling a large portion of the target bonds and stereocenters simultaneously. Thus, high-impact reaction steps should have a steep slope in a molecular graph edit distance plot between given intermediates en route to the final target.

We encoded molecular graphs of each intermediate, including starting materials and the final target, as individual adjacency matrices (Fig. 2B and fig. S2) in which the number of rows and columns is equal to the total number of heavy atoms and groups used in the entire synthetic route. In this way, all bonds of the final target and their progression from starting materials, as well as any concession groups used in the synthesis, are mapped exactly in each individual matrix and in rela-

tion to the final target's matrix (Fig. 2C). A simple comparison of the matrix for **1** (Fig. 2B, right) reveals that it shares more entries in common (99%) with the calculated penultimate intermediate **14** (Fig. 2B, middle) than it does with the matrix for starting materials **3**, **11**, **12**, **8**, and HBr (Fig. 2B, left) (93%). Accordingly, key steps maximize the reduction in graph edit distance from a given intermediate to the target, which is equivalent to maximizing formation of target bonds while minimizing reaction manipulations on concession groups. This graph formalization shares similarity with established concepts of synthetic ideality but is machine readable, carries exact atom and bond mapping, and requires no labeling of reaction type to separate low-impact reactions such as redox manipulations from impactful cycloadditions or cascade reactions. Because graphs capture the exact location of every bond, graph edit distance was superior to other metrics, such as Tanimoto distance based on Morgan fingerprints (fig. S3), at highlighting the impact of key transformations. A survey of published total syntheses by graph edit distance (fig. S4) shows that diverse key steps are readily visualized. A full graph analysis of the shortest calculated route to **1** (fig. S5)

reveals the impact of the Mannich coupling (Fig. 2D), which appears as the steepest declining step (yellow) in the graph edit distance plot.

Six-step total synthesis of stemoamide

Although the computed routes to **1** focused our attention on the Mannich disconnection (Fig. 2A) as an impactful key step, we recognized opportunities for improvement. For instance, C2 and C11 are both in the carboxyl oxidation state in **1**, so by considering redox economy (4), the oxidation state of **11** and **12** could be harmonized to excise two calculated steps. This realization unveiled a hidden symmetry element within **1**, where two equivalents of commercially available aldehyde **5** (Fig. 3A) unite in a self-Mannich reaction (26, 27). This would require installation of the chiral α -methyl group at a later stage, and fortuitously a diastereoselective methylation had already been reported as a viable final step in several syntheses of **1** (13, 14).

In experimental practice (Fig. 3A), stirring **3** with a fourfold excess of aldehyde **5** and 20 mol % L-proline in *N,N*-dimethylformamide at -15°C , then adding a mixture of allyl bromide **4**, zinc, and bismuth chloride directly to

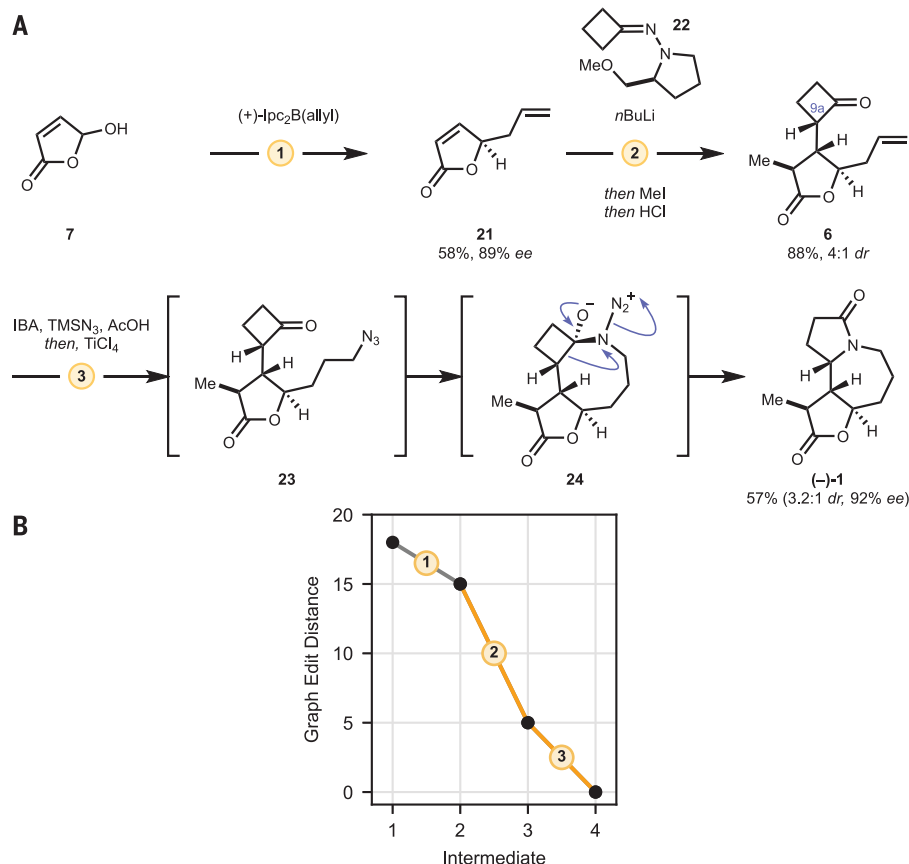


Fig. 4. Total synthesis of **1** featuring a Schmidt-Aubé rearrangement. (A) Total synthesis of (–)-**1** in three steps. (+)-Ipc₂B(allyl), (+)-*B*-allyldiisopinocampheylborane; IBA, iodosobenzoic acid; TMS, trimethylsilyl. (B) Graph edit distance analysis of the route.

Step impact can be readily observed in our six-step synthesis of **1**, where the first organocatalyzed Mannich-allylation step markedly increases the graph similarity of **3**, **5**, and **4** to **1**, installing 45% of the bonds required to produce **1** (Fig. 3B). This high-impact step is then followed by a series of low-impact steps, such as protecting-group manipulations and functional-group interconversions, which are easily recognized by their shallow slope in Fig. 3B. Meanwhile, our 3-step route is much more efficient with the sequence of steps contributing 17, 55, and 28%, respectively, to the graph similarity of intermediates to **1** (Fig. 4B). The key steps that we used were selected from an analysis of more than a thousand calculated retrosynthetic routes.

In addition to highlighting key steps, the graph edit distance technique can be used to highlight shortcuts in the route, which may require the invention of new reactions. This is easily achieved by grouping neighboring transformations with a modest slope in the graph edit plot into a single shortcut step. For instance, steps 3, 4 and 5 in our Mannich route (Fig. 3) could in principle be grouped into an overall *anti*-Markovnikov hydroamidation

(Fig. S7). It was possible to quench the TFA-promoted lactamization (step 2) with ceric ammonium nitrate (CAN) to produce an analog of **17** with the PMP group removed in 33% overall yield from **3**. This analog could be converted to **20** in a single step following invention of an *anti*-Markovnikov hydroamidation reaction, ultimately leading to a four-step synthesis of **1**. This strategy can be generally applied to suggest specific new reactions, with their respective atom mappings, that provide a shortcut in any synthetic route.

Modern CASP has demonstrated the ability to produce practicable routes to modestly complex targets, but to date route proposals do not challenge the brevity of modern human-derived routes. Our method shows that it is possible to unite multiple high-impact steps from diverse CASP route proposals, as shown for (–)-**1** in Fig. 4, to arrive at concise synthetic routes. We focused on step count as a sole optimization metric in the current study, but important real-world metrics such as reagent cost, building block availability, or predicted yield could be easily incorporated as a weighted distance metric. As advances in automated retrosynthesis make complex molecules more accessi-

ble, it is likely that precision pharmaceuticals will become increasingly available.

REFERENCES AND NOTES

- K. C. Nicolaou, D. J. Edmonds, P. G. Bulger, *Angew. Chem. Int. Ed.* **45**, 7134–7186 (2006).
- B. B. Touré, D. G. Hall, *Chem. Rev.* **109**, 4439–4486 (2009).
- T. Newhouse, P. S. Baran, R. W. Hoffmann, *Chem. Soc. Rev.* **38**, 3010–3021 (2009).
- N. Z. Burns, P. S. Baran, R. W. Hoffmann, *Angew. Chem. Int. Ed.* **48**, 2854–2867 (2009).
- S. W. M. Crossley, R. A. Shenvi, *Chem. Rev.* **115**, 9465–9531 (2015).
- T. Klucznik et al., *Chem* **4**, 522–532 (2018).
- Y. Lin et al., *Nat. Commun.* **12**, 7327 (2021).
- A. Wolos et al., *Nature* **604**, 668–676 (2022).
- C. W. Coley et al., *Science* **365**, eaax1566 (2019).
- C. J. Marth et al., *Nature* **528**, 493–498 (2015).
- B. Mikulak-Klucznik et al., *Nature* **588**, 83–88 (2020).
- L. Wang et al., *Phytochem. Rev.* **21**, 835–862 (2022).
- G. A. Brito, R. V. Pirovani, *Org. Prep. Proced. Int.* **50**, 245–259 (2018).
- M. Yoritate et al., *J. Am. Chem. Soc.* **139**, 18386–18391 (2017).
- X. Yin, K. Ma, Y. Dong, M. Dai, *Org. Lett.* **22**, 5001–5004 (2020).
- J. H. Siitonen, D. Csókás, I. Pápai, P. M. Pihko, *Synlett* **31**, 1581–1586 (2020).
- Z. Guo et al., *Angew. Chem. Int. Ed.* **60**, 14545–14553 (2021).
- F. Cao et al., *Org. Lett.* **23**, 6222–6226 (2021).
- T. Shi et al., *Org. Chem. Front.* **9**, 771–774 (2022).
- X. Wang et al., *Org. Chem. Front.* **9**, 3818–3822 (2022).
- G. Bernardi Rosso, B. Matos Paz, R. Aloise Pilli, *Eur. J. Org. Chem.* **2022**, e202200585 (2022).
- D. S. Peters et al., *Acc. Chem. Res.* **54**, 605–617 (2021).
- J. B. Hendrickson, *J. Am. Chem. Soc.* **97**, 5784–5800 (1975).
- A. Sanfeliu, K. Fu, *IEEE Trans. Syst. Man Cybern. SMC-13*, 353–362 (1983).
- L. David, A. Thakkar, R. Mercado, O. Engkvist, *J. Cheminform.* **12**, 56 (2020).
- W. Notz et al., *J. Org. Chem.* **68**, 9624–9634 (2003).
- Y. Hayashi et al., *Angew. Chem. Int. Ed.* **42**, 3677–3680 (2003).
- P. J. Kropp et al., *J. Am. Chem. Soc.* **112**, 7433–7434 (1990).
- D. Hazeldar, A. Fadel, *Tetrahedron Asymmetry* **16**, 2067–2070 (2005).
- H. Li, S.-J. Shen, C.-L. Zhu, H. Xu, *J. Am. Chem. Soc.* **141**, 9415–9421 (2019).
- X. Li, P. Chen, G. Liu, *Sci. China Chem.* **62**, 1537–1541 (2019).
- J. Aube, G. L. Milligan, *J. Am. Chem. Soc.* **113**, 8965–8966 (1991).
- G. L. Milligan, C. J. Mossman, J. Aube, *J. Am. Chem. Soc.* **117**, 10449–10459 (1995).
- K. J. Frankowski, R. Liu, G. L. Milligan, K. D. Moeller, J. Aubé, *Angew. Chem. Int. Ed.* **54**, 10555–10558 (2015).
- Y. Lin, R. Zhang, D. Wang, T. Cernak, Code and Data for Computer-Aided Key Step Generation in Alkaloid Total Synthesis, version 1.1, Zenodo (2022): <https://doi.org/10.5281/zenodo.7449332>.

ACKNOWLEDGMENTS

The authors thank N. Brugger, S. Jasty, A. Tathe, R. Turnbull, and L. Rickershauser (MilliporeSigma) for helpful discussions and assistance with graphics. We also thank S. Trice (previously of MilliporeSigma) for early discussions and support of the work. **Funding:** This work was funded by MilliporeSigma, start-up funds from the University of Michigan College of Pharmacy, and the National Science Foundation (CHE-2236215). **Author contributions:** Y.L. performed synthetic chemistry experiments, Y.L. and T.C. performed SYNTHIA searches. R.Z. and D.W. developed the graph edit distance technique. All authors reviewed and interpreted the data and wrote the manuscript. T.C. supervised the work. **Competing interests:** The Cernak Lab has received research funding or in-kind donations from MilliporeSigma, Relay Therapeutics, Janssen Therapeutics, SPT Labtech, and Merck & Co., Inc. T.C. holds equity in Scorpion Therapeutics.

and is a cofounder of and equity holder in Entos, Inc. The Regents of the University of Michigan have filed a provisional patent on some aspects of this work. **Data and materials availability:** Code for graph editing techniques is available at Zenodo (35). SYNTHIA is available at <https://www.synthiaonline.com>. **License information:** Copyright © 2023 the authors, some rights reserved; exclusive licensee American Association for the Advancement

of Science. No claim to original US government works. <https://www.science.org/about/science-licenses-journal-article-reuse>

SUPPLEMENTARY MATERIALS

science.org/doi/10.1126/science.ade8459
Materials and Methods

Figs. S1 to S71
Table S1
NMR Spectra
References (36–59)

Submitted 14 September 2022; accepted 4 January 2023
10.1126/science.ade8459

WILDFIRES

Smoke-weather interaction affects extreme wildfires in diverse coastal regions

Xin Huang^{1,2†*}, Ke Ding^{1,2†}, Jingyi Liu¹, Zilin Wang¹, Rong Tang¹, Lian Xue¹, Haikun Wang^{1,2}, Qiang Zhang³, Zhe-Min Tan¹, Congbin Fu¹, Steven J. Davis^{3,4}, Meinrat O. Andreae^{5,6,7}, Aijun Ding^{1,2*}

Extreme wildfires threaten human lives, air quality, and ecosystems. Meteorology plays a vital role in wildfire behaviors, and the links between wildfires and climate have been widely studied. However, it is not fully clear how fire-weather feedback affects short-term wildfire variability, which undermines our ability to mitigate fire disasters. Here, we show the primacy of synoptic-scale feedback in driving extreme fires in Mediterranean and monsoon climate regimes in the West Coast of the United States and Southeastern Asia. We found that radiative effects of smoke aerosols can modify near-surface wind, air dryness, and rainfall and thus worsen air pollution by enhancing fire emissions and weakening dispersion. The intricate interactions among wildfires, smoke, and weather form a positive feedback loop that substantially increases air pollution exposure.

In recent decades, wildfires have increasingly threatened lives and infrastructure, degraded air quality, and damaged ecosystem services (1–3). Globally, wildfires account for ~25% of the world's forest loss and ~8% of premature deaths from poor air quality (4, 5). The intensity of wildfires is extremely heterogeneous and largely determined by meteorology on a range of temporal scales (6, 7). Meteorology affects vegetation productivity (fuel availability), determines the length of fire seasons (fuel flammability), and influences the spread of the fires (fire behavior), yet prior studies of the fire-meteorology relationship have mostly focused on long-term climate scale (8, 9) rather than short-term weather processes. Anomalous synoptic weather conditions at time scales of ~1 to 2 weeks, such as exceptionally strong winds that drive rapid fire spread (10) and intense hydrological droughts that make vegetation extremely combustible (11), have important impacts on the behavior of extreme wildfires (12, 13). The recent

increase in catastrophic wildfires globally (6, 14) calls into question our understanding of the drivers of extreme wildfire events, as well as our capacity to manage the most severe fires, especially in regions with dense populations.

In general, wildfires exhibit great variability on temporal scales, ranging from days to years, but extreme wildfires (i.e., >90th percentile of daily burned area in one specific fire-prone region) are tightly linked to synoptic fluctuations (15, 16). To quantitatively understand the temporal scales of wildfires, we applied empirical mode decomposition and Fourier transform to daily burned area in major wildfire regions during 2002–2021 (see the materials and methods). Figure 1 shows that synoptic-scale (<20 days) variation of wildfires is evident in most fire-prone areas across the globe. Among them, the US West Coast and Southeastern Asia are characterized by the most pronounced fluctuations down to 1 to 2 weeks, corresponding to the time period of extreme fires that have repeatedly ravaged both regions (17). Given the dense populations in these regions, the impacts of these fires on air quality and the associated human health exposure are enormous (18, 19).

During extreme fire events, weather conditions show distinct patterns in both regions with respect to key meteorological drivers such as relative humidity, wind speed, and precipitation (Fig. 1). In the US West Coast, which has a Mediterranean climate, extreme fires

usually begin when near-surface humidity is very low and wind speeds are at their highest. During these periods, dry air rapidly lowers vegetation moisture while strong winds accelerate the rate of fire spread, and the compounding effect of these two drivers gives rise to large and severe fires (10). By contrast, the variability of rainfall in the monsoon climate of Southeastern Asia largely determines the magnitude of the fire activity, with rainfall deficits making fuels flammable and drying peatlands (20).

Meteorological parameters such as humidity, wind speed, and precipitation are key factors modulating extreme wildfires (14, 21), whereas radiatively active aerosols such as black carbon (BC) in fire smoke may create feedback by substantially altering meteorology (22–24). However, relatively little attention has been paid to the complex interactions among smoke aerosols, weather, and wildfire behaviors on a synoptic scale. We used a coupled meteorology-chemistry model together with multiple satellite and ground-based observational datasets to investigate the role of fire-weather feedback in the spread and impacts of extreme wildfires for the two regions with the largest synoptic-scale variability in wildfires.

The US West Coast is suffering from increasingly destructive wildfires, with records broken every few years (10, 25), and the wildfire-induced severe haze pollution has long been a top air-quality concern there (26). In September 2020, a series of wildfires in Oregon and California burned 1.2 million acres (defined as a “gigafire” for an area >1 million acres; fig. S1). Fire smoke stretched from the Pacific Ocean over most of Oregon, California, and even Canada (Fig. 2), and hazardous haze pollution engulfed valley cities (10). During this gigafire, the observed near-surface specific humidity and wind speed reached unprecedented levels of 3.3 g/m³ and 13.1 m/s, respectively, in the western Oregon Cascades. Correspondingly, there were strong anomalies compared with the climatic mean in the large fire potential (LFP) index (see the supplementary materials).

To explore the interaction mechanism among smoke aerosols, meteorology, and this gigafire, we conducted meteorology-chemistry-coupled simulations using the WRF-Chem model (see the supplementary materials). Smoke aerosols modify meteorology through impacts on

¹School of Atmospheric Sciences, Nanjing University, Nanjing 210023, China. ²Frontiers Science Center for Critical Earth Material Cycling, Nanjing University, Nanjing 210023, China. ³Department of Earth System Science, Tsinghua University, Beijing 100084, China. ⁴Department of Earth System Science, University of California, Irvine, CA 92697, USA. ⁵Max Planck Institute for Chemistry, 55128 Mainz, Germany. ⁶Scripps Institution of Oceanography, University of California, San Diego, La Jolla, CA 92093, USA. ⁷Department of Geology and Geophysics, King Saud University, Riyadh 14511, Saudi Arabia.

*Corresponding author. Email: dingaj@nju.edu.cn (A.D.); xinhuang@nju.edu.cn (X.H.)

†These authors contributed equally to this work.

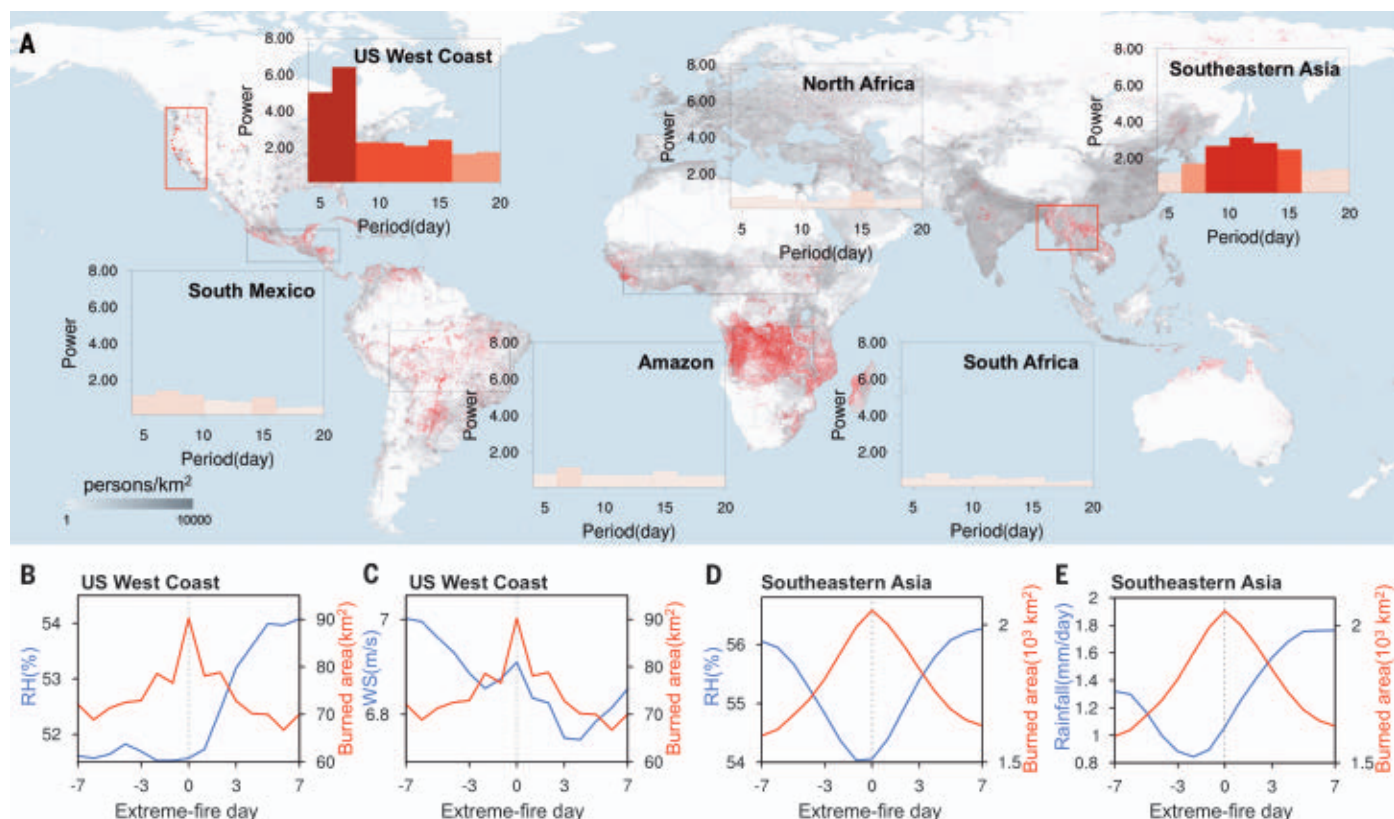


Fig. 1. Synoptic-scale variability of wildfires and meteorology during extreme fires in typical fire regions in the globe. (A) Global map of population density and power spectra of burned area variation at synoptic scale in main fire-prone regions based on empirical mode decomposition and Fourier transform (see the materials and methods). The Fourier power at different oscillation periods is color coded. Six typical wildfire regions are marked by rectangles. (B and C) Two-week

evolution of 2-m relative humidity (RH) and 10-m wind speed (WS₁₀) derived from ERA5 reanalysis data around extreme fires (daily burned area >90th percentile) in the US West Coast during 2002–2021. The day with the largest fire area is indicated as a dashed line in the middle (day 0). (D and E) Two-week evolution of RH and rainfall rate around extreme fires in Southeastern Asia. The US West Coast and Southeastern Asia regions are outlined by red rectangles in (A).

both radiation transfer and clouds. Given the cloudless skies over the US West Coast during the gigafire (fig. S2), we performed two parallel experiments, one with an aerosol-radiation interaction (EXP_ARI) and the other without (EXP_nARI), and validated the model with in situ and remote sensing measurements (figs. S3 and S4). During the most severe haze pollution (10 to 13 September 2020), aerosol optical depth (AOD) sharply increased from ~0.2 to >2. Such a high aerosol loading substantially perturbed the radiation energy balance by trapping >100 W/m² (~32%) of incoming solar energy in the atmosphere and in turn altered thermal stratification (fig. S5).

The light absorption by aerosol tended to warm the smoke layer and cool the land surface over the US West Coast, thereby suppressing the development of the planetary boundary layer (PBL), a phenomenon known as the aerosol-PBL interaction (27). On 12 September 2020, the decrease in near-surface temperature was 6°C in Salem, Oregon, accompanied by a decline in daytime PBL height of >500 m (~63%). Further, our results show that the

aerosol-PBL interaction increased near-surface fine particle concentrations (PM_{2.5}) by >100 µg/m³ on the western slope of the Cascade Mountains during 10 to 13 September 2020 (Fig. 2D), due mainly to the smoke-stabilized PBL trapping pollution in a much shallower PBL.

The fire smoke also substantially modified vertical and horizontal winds because the re-allocated radiative energy caused a katabatic and offshore wind anomaly. Specifically, land cooling led to a strong easterly wind anomaly of 3 to 4 m/s in near-surface wind, especially at the western slope of the Cascade Mountains. Furthermore, the aerosol-PBL interaction over the land area with high AOD prevented the onshore transport of water vapor from the Pacific Ocean. Thus, the near-surface air was dried out over the fire-prone areas, which is exactly the area with abnormally intense wildfires and severe pollution compared with the climatological average (fig. S6). Associated with the enhanced downslope wind, the wind-speed was amplified (Fig. 2D). The specific humidity deficit and wind speed increase induced by the smoke aerosols correlated well

with AOD (Fig. 2E). Such synchronous reinforcements in the two major meteorological drivers of extreme wildfires are tightly coupled. The Mediterranean climate and topography in the US West Coast shape a marked meridional humidity gradient in summer (fig. S6C), so the enhanced easterly winds would further dry out the air (28). Decreased humidity combined with stronger wind greatly enhanced the fire potential, especially over the Cascade Mountains, where fires were the most intense, and the LFP index increased by >100% (Fig. 2F).

With wildfire emissions scaled according to their correlation with LFP, we conducted another simulation by excluding the smoke-induced perturbations in meteorology. As illustrated in Fig. 2G, fire-weather feedback, including both fire emission enhancement and the aerosol-PBL interaction, substantially aggravated the smoke pollution, with a PM_{2.5} increment exceeding 300 µg/m³ in the Oregon Cascades. Such an aggravation of air pollution substantially increased human smoke exposure, especially in densely populated valley cities. Our estimation shows that fire-weather

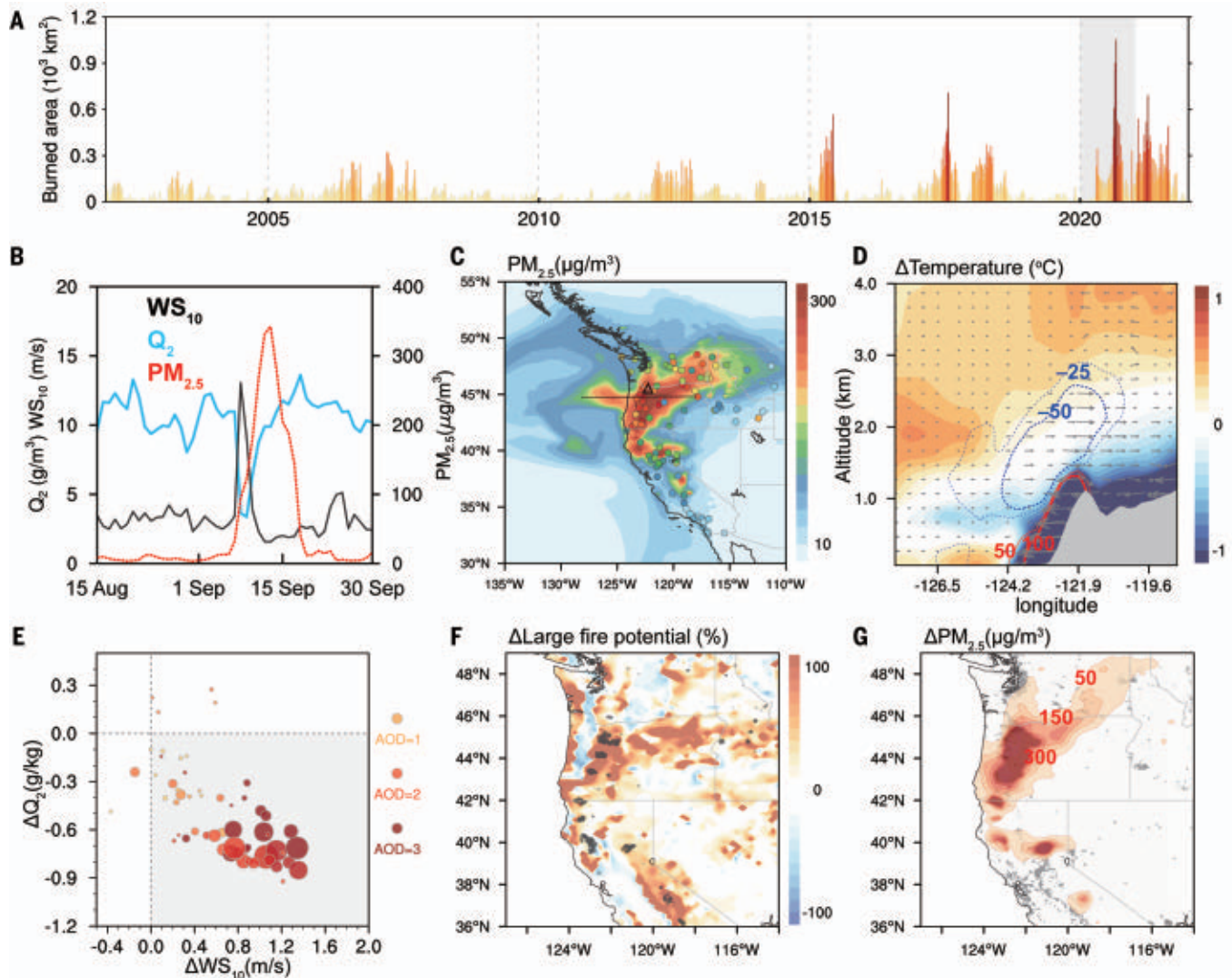


Fig. 2. Fire-weather feedback and aggravated smoke pollution in the US West Coast. (A) Time series of satellite-observed daily burned area in the US West Coast (red rectangle in Fig. 1A) in August and September of 2002–2021. (B) Daily $PM_{2.5}$, 2-m humidity (Q_2), and WS_{10} observations in the Oregon Cascades in August and September of 2020 [gray shading in (A)]. $PM_{2.5}$ and meteorological observational stations are marked by dots and triangle in (C). (C) Simulated (contour) and observed (dots) $PM_{2.5}$ concentrations during 10 to 13 September 2020 in the US West Coast. (D) Cross section of ARI-induced

temperature, wind, and $PM_{2.5}$ changes (isolines in units of $\mu g/m^3$) along the dashed line in (C) based on model simulations. Red and blue isolines show the increase and decrease due to ARI in $PM_{2.5}$ concentrations, respectively. (E) Scatter plot of simulated changes in near-surface wind speed and specific humidity due to the radiative effect of aerosol with different AOD levels. (F) Changes in LFP caused by the radiative effect of smoke aerosol. Gray dots mark fire spots. (G) Population density (gray) and simulated near-surface $PM_{2.5}$ increase (red contour) due to fire-weather feedback.

feedback increased the $PM_{2.5}$ exposure by ~77% in the US West Coast ($40 \mu g/m^3$), 48% of which was directly caused by emission enhancement and the other 29% by the aerosol-PBL interaction (fig. S7).

Likewise, monsoon-dominated Southeastern Asia suffers from intense wildfires in spring (23), which also features an obvious interannual and synoptic-scale variability (figs. S8 and S9). Comparatively, the fluctuation of wildfires in Southeastern Asia is highly sensitive to rainfall (Fig. 1E) (20, 29). The meteorological evolution during the extreme wildfire events

demonstrates that the burned area is inversely correlated with precipitation with a time period of ~2 weeks (Fig. 3B). On a daily basis, the burned area of wildfires in this region shows a good correlation with the fire weather index (FWI) (see the supplementary materials), and the most important contributor to the fire risk is rainfall rate (fig. S10).

Extreme wildfires hit Southeastern Asia in the spring every few years (Fig. 3A). Here, we mainly focused our modeling on the most devastating fire, which engulfed the Indo-China Peninsula in March 2004. On the basis of the

validated model simulations (figs. S11 and S12), we found that the prevailing westerlies transported fire-emitted pollutants at an altitude of ~3 km, leading to a thick, BC-containing plume covering almost all of Southeastern Asia (23). The light-absorbing fire smoke aloft trapped the radiative energy that would otherwise have warmed the ground surface, causing atmospheric heating and a surface dimming (Fig. 3), which even reached up to $+3.0^\circ C$ and $-3.2^\circ C$, respectively, averaged over the 2-week burning period (13 to 21 March 2004) (fig. S11C). The opposite temperature responses

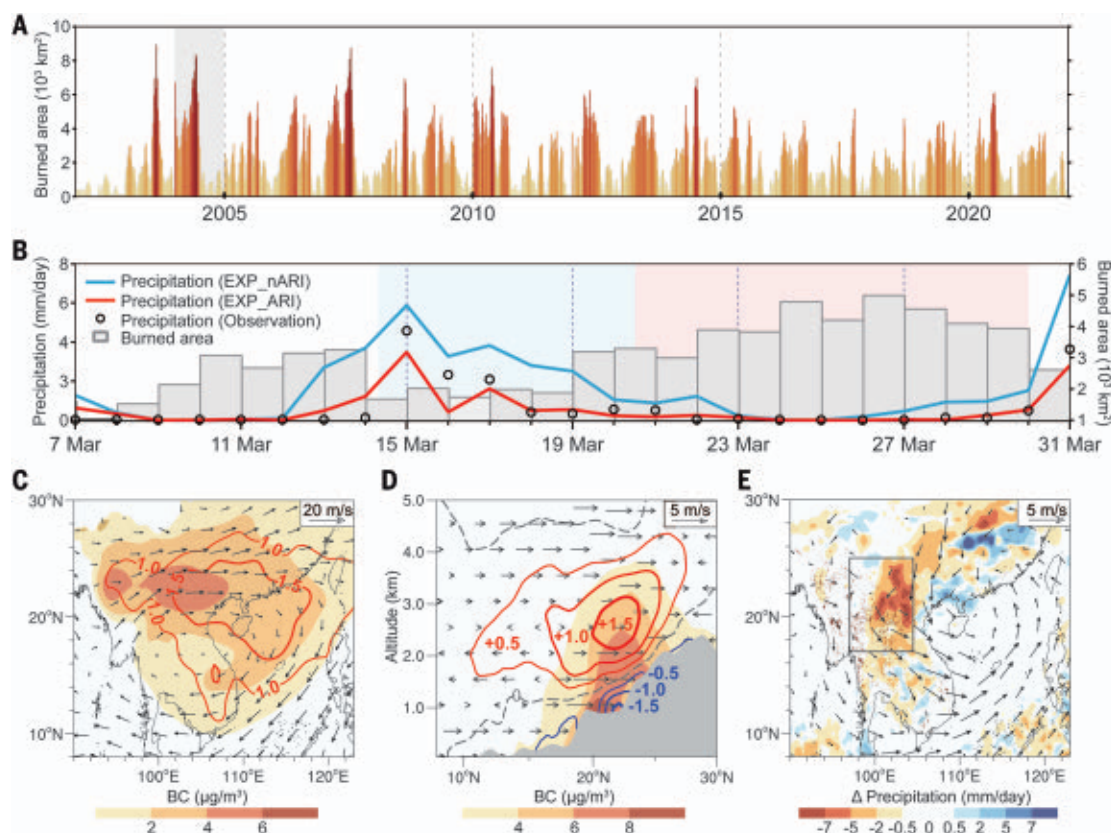


Fig. 3. Fire-weather feedback in Southeastern Asia. (A) Time series of satellite-observed daily burned area of Southeastern Asian wildfires (red rectangle in Fig. 1A) in March and April of 2002–2021. (B) Daily satellite-detected burned area, precipitation observations from the TRMM multi-satellite product, and corresponding simulations with and without aerosol feedback in March 2004 in the fire-intensive region [black rectangle in (E)]. (C) Simulated BC concentration and atmospheric heating (isolines in

units of °C) at an altitude of 3 km over Southeastern Asia during the burning period (13 to 21 March 2004). (D) Cross section of simulated BC aerosol, air temperature (isolines in units of °C), and wind changes due to the radiative effect of smoke aerosols between longitudes outlined in (E). (E) Simulated changes in precipitation and wind due to the radiative effect of aerosols overlaid by 850-hPa wind. Red dots mark the fire spots from satellite observations.

in the vertical dimension then formed a very stable stratification in the lower troposphere. Meanwhile, the pronounced cooling over the land surface and warming over the sea substantially narrowed the temperature difference between land and sea, forcing a cyclonic circulation anomaly along the coast (Fig. 3E and fig. S13).

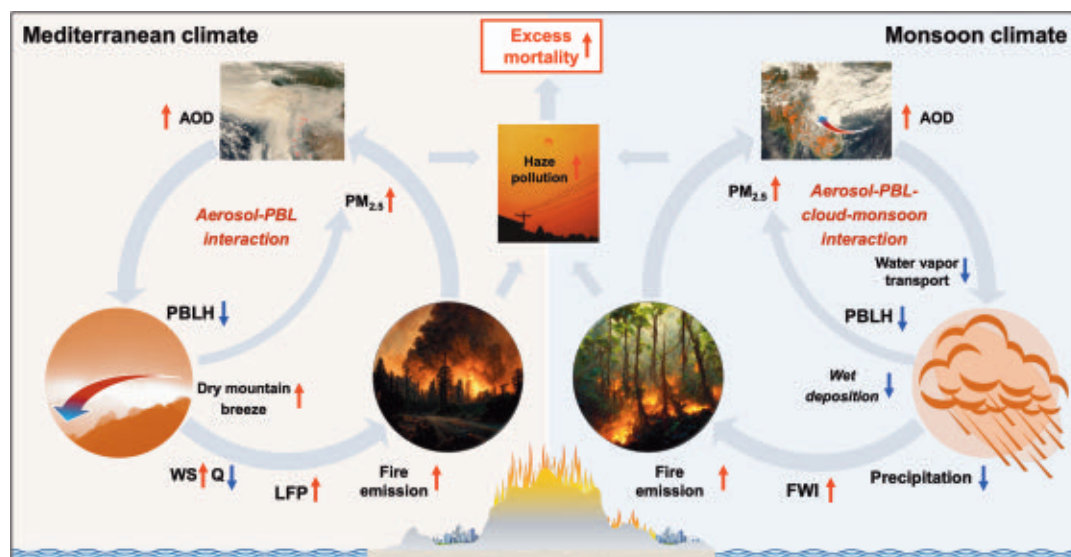
The mechanism of the smoke-PBL-cloud-monsoon interaction in this region has been thoroughly discussed (23), and our simulations suggest that such feedback could also strongly influence precipitation and promote more intense wildfires in Southeastern Asia. As shown in Fig. 3E, the precipitation was substantially diminished (~7 mm/day), which could be attributed to weakened convection and less moisture transport with anomalous offshore winds. The adjusted circulation blocked the water vapor supply from the South China Sea, thereby leading to a moisture deficit and much less rainfall in the fire-intensive region. Compared with the aerosol-cloud interaction, the radiative effects of smoke aerosol

dominated the precipitation suppression (fig. S14). Subsequently, less rainfall was conducive to fire ignition and expansion, further corroborated by the exponential relationship between FWI and burned area (fig. S8). On the basis of this relationship, we estimated the enhanced smoke pollution resulting from the reduction in precipitation. As shown in fig. S15, $PM_{2.5}$ concentration soared by $300 \mu\text{g}/\text{m}^3$ in the fire-prone areas. Such a spike in smoke pollution caused by fire-weather feedback would increase $PM_{2.5}$ exposure by ~17% in Southeastern Asia. Similar fire-weather feedback through precipitation suppression also holds true in other years with extreme wildfires (fig. S16).

These results provide a comprehensive demonstration of unexpectedly strong feedback between wildfire and weather in diverse coastal regions. Increasing wildfire severity is not just a consequence of fire-prone weather, it is also an active participant. In a Mediterranean climate with dry and hot summers, such as that in the US West Coast, increased aerosol

loading from wildfire suppresses the development of the PBL and enhances orographic winds, thereby increasing the large fire potential at the western slope of the Cascade Mountains through higher wind speed and lower humidity. Conversely, in the fire-intensive region of Southeastern Asia, which has a monsoon climate, thick fire smoke tends to cool the land surface but warm the atmosphere over the sea. The opposite air temperature responses over the land and sea modify the monsoon circulation and block the onshore transport of moisture, thereby suppressing rainfall. More flammable vegetation due to the hydrologic drought intensifies the fire activities and prolongs the burning period. Moreover, in both regions, the aerosol-PBL interaction exacerbates $PM_{2.5}$ concentrations near the surface by suppressing convection and weakening diffusion. The strengthened wildfire emission further enhances the haze pollution and reinforces the positive feedback loops, and thus human exposure to smoke pollution could be greatly amplified (Fig. 4).

Fig. 4. Conceptual model of the fire-weather feedback in the Mediterranean and monsoon climate regimes. Gray arrows indicate the linkage among wildfire, air quality, and thermal circulations. Red and blue arrows show the increase and decrease, respectively, of each parameter. Q, specific humidity; PBLH, planetary boundary layer height.



Although the feedbacks for the two different climatic zones on the east and west coasts appear different, in essence, they can be well explained by a unified mechanism. Both are driven by the radiative effects of fire smoke over different land covers and terrains, which cause thermal contrast and thus enhanced fire emission by modifying circulations and water vapor transport.

Our findings emphasize the complexity of fire-weather feedback in the Earth system and the critical importance of improving our understanding of such mechanisms to prioritize fire prevention and suppression efforts and thus mitigate the impacts of extreme wildfires. The results indicate a potential nonlinear benefit from early fire suppression efforts. Given the persistence and spread of wildfires and fire-weather feedback, early-stage fire suppression at preidentified amplifier regions based on near-real-time forecasting could avert some extreme wildfires. Moreover, strategic and early fire management, e.g., more effort on fire suppression in the forests upslope of populated areas, could reduce the impacts of wildfire-related air pollution and save lives (30). As extreme wildfires become increasingly common, coordinated and effective management of fire risks is vital. Meanwhile, growing supercomputing resources and innovative methods are making chemical-weather forecasts ever more feasible. Our results thus suggest that seamless meteorology-chemistry-coupled modeling may be a practical approach for mitigating extreme and damaging fires in populated coastal regions.

REFERENCES AND NOTES

1. M. O. Andreae, *Atmos. Chem. Phys.* **19**, 8523–8546 (2019).
2. D. A. Jaffe et al., *J. Air Waste Manag. Assoc.* **70**, 583–615 (2020).

3. R. Aguilera, T. Corringham, A. Gershunov, T. Benmarhnia, *Nat. Commun.* **12**, 1493 (2021).
4. J. Lelieveld, J. S. Evans, M. Fnais, D. Giannadaki, A. Pozzer, *Nature* **525**, 367–371 (2015).
5. P. G. Curtis, C. M. Slay, N. L. Harris, A. Tyukavina, M. C. Hansen, *Science* **361**, 1108–1111 (2018).
6. W. M. Jolly et al., *Nat. Commun.* **6**, 7537 (2015).
7. M. R. Alizadeh et al., *Proc. Natl. Acad. Sci. U.S.A.* **118**, e2009717118 (2021).
8. N. Andela et al., *Science* **356**, 1356–1362 (2017).
9. A. B. Leverkus, S. Thorn, D. B. Lindenmayer, J. G. Pausas, *Science* **370**, 416–417 (2020).
10. J. T. Abatzoglou, D. E. Rupp, L. W. O'Neill, M. Sadegh, *Geophys. Res. Lett.* **48**, e2021GL092520 (2021).
11. J. L. Crockett, A. L. Westerling, *J. Clim.* **31**, 341–354 (2018).
12. W. C. Bessie, E. A. Johnson, *Ecology* **76**, 747–762 (1995).
13. B. M. Collins, *Agric. For. Meteorol.* **189–190**, 30–35 (2014).
14. M. Goss et al., *Environ. Res. Lett.* **15**, 094016 (2020).
15. D. A. Peterson et al., *Bull. Am. Meteorol. Soc.* **96**, 229–247 (2015).
16. R. D. Field, G. R. Van Der Werf, S. S. P. Shen, *Nat. Geosci.* **2**, 185–188 (2009).
17. N. J. Nauslar, J. T. Abatzoglou, P. T. Marsh, *Fire (Basel)* **1**, 18 (2018).
18. X. Zhou et al., *Sci. Adv.* **7**, eabi8789 (2021).
19. I. C. Yadav et al., *Environ. Pollut.* **227**, 414–427 (2017).
20. M. J. Wooster, G. L. W. Perry, A. Zoumas, *Biogeosciences* **9**, 317–340 (2012).
21. M. G. Pereira, J. Parente, M. Amraoui, A. Oliveira, P. M. Fernandes, in *Extreme Wildfire Events and Disasters: Root Causes and New Management Strategies*, F. Tedim, V. Leone, T. K. McGee, Eds. (Elsevier, 2019); pp. 55–72.
22. T. C. Bond et al., *J. Geophys. Res. Atmos.* **118**, 5380–5552 (2013).
23. K. Ding et al., *Nat. Commun.* **12**, 6416 (2021).
24. A. J. Ding et al., *Atmos. Chem. Phys.* **13**, 10545–10554 (2013).
25. M. S. Khorshidi et al., *Environ. Res. Lett.* **15**, 104002 (2020).
26. C. D. McClure, D. A. Jaffe, *Proc. Natl. Acad. Sci. U.S.A.* **115**, 7901–7906 (2018).
27. A. J. Ding et al., *Geophys. Res. Lett.* **43**, 2873–2879 (2016).
28. T. Rolinski, S. B. Capps, W. Zhuang, *Weather Forecast.* **34**, 257–275 (2019).
29. D. L. A. Gaveau et al., *Sci. Rep.* **4**, 6112 (2014).
30. M. A. Moritz et al., *Nature* **515**, 58–66 (2014).

ACKNOWLEDGMENTS

We are grateful to the High-Performance Computing (HPC) and the Massive Data Center (MDC) of the School of Atmospheric Sciences at Nanjing University, for doing the numerical

calculations for this study on its Blade cluster system; the Jiangsu Collaborative Innovation Center for Climate Change for support; and the National Aeronautics and Space Administration (NASA) for the use of imagery from the NASA Worldview application, part of the NASA Earth Observing System Data and Information System (EOSDIS). **Funding:** This work was supported by the National Natural Science Foundation of China (grant 41725020 to A.D., grant 41922038 to X.H., and grant 13001146 to K.D.), by Fundamental Research Funds for the Central Universities (grant 14380187 to X.H.), and by the Tencent Foundation through the XPLOER PRIZE to A.D. **Author contributions:** Conceptualization: X.H., A.D.; Funding acquisition: X.H., A.D.; Investigation: X.H., K.D., J.L., Z.W., L.X.; Methodology: X.H., K.D., J.L., R.T., H.W., Q.Z.; Project administration: X.H., A.D.; Supervision: X.H., A.D.; Visualization: X.H., K.D., J.L.; Writing – original draft: X.H., A.D.; Writing – review and editing: X.H., A.D., Q.Z., S.J.D., Z.-M.T., C.F., M.O.A. **Competing interests:** The authors declare no competing interests. **Data and materials availability:** MODIS thermal anomalies and aerosol products are available at <https://ladsweb.modaps.eosdis.nasa.gov/archive/allData/6/MOD14A1/> and https://ladsweb.modaps.eosdis.nasa.gov/archive/allData/61/MOD04_L2/. Fire emissions data are openly accessible at <https://www.acom.ucar.edu/Data/fire/>. The gridded anthropogenic emission data EDGAR are available from <https://edgar.jrc.ec.europa.eu/>. Ambient air quality monitoring data can be obtained at https://aqswb.epa.gov/aqswb/airdata/download_files.html. The radiosonde and surface meteorological observations are archived at the National Center for Environmental Information, available at <ftp://ftp.ncdc.noaa.gov/pub/data/noaa/> and <ftp://ftp.ncdc.noaa.gov/pub/data/igra>. The gridded population density data are available at <https://sedac.ciesin.columbia.edu/data/collection/gpw-v4>. Code used to analyze the data are available from <https://github.com/xinhuang415/extremewildfire>. The source code of the WRF-Chem model is archived in the UCAR data repository (<https://www2.mmm.ucar.edu/wrf/users/download>). **License information:** Copyright © 2023 the authors, some rights reserved; exclusive licensee American Association for the Advancement of Science. No claim to original US government works. <https://www.science.org/about/science-licenses-journal-article-reuse>

SUPPLEMENTARY MATERIALS

science.org/doi/10.1126/science.add9843
Materials and Methods
Figs. S1 to S16
Tables S1 and S2
References (31–37)

Submitted 17 July 2022; accepted 3 January 2023
10.1126/science.add9843

VOLCANOLOGY

The magmatic web beneath Hawai'i

John D. Wilding^{*†}, Weiqiang Zhu[†], Zachary E. Ross, Jennifer M. Jackson

The deep magmatic architecture of the Hawaiian volcanic system is central to understanding the transport of magma from the upper mantle to the individual volcanoes. We leverage advances in earthquake monitoring with deep learning algorithms to image the structures underlying a major mantle earthquake swarm of nearly 200,000 events that rapidly accelerated after the 2018 Kīlauea caldera collapse. At depths of 36 to 43 kilometers, we resolve a 15-kilometers-long collection of near-horizontal sheeted structures that we identify as a sill complex. These sills connect to the lower depths of Kīlauea's plumbing by a 25-kilometers-long belt of seismicity. Additionally, a column of seismicity links the sill complex to a shallow décollement near Mauna Loa. These findings implicate the mantle sill complex as a nexus for magma transport beneath Hawai'i and furthermore indicate widespread magmatic connectivity in the volcanic system.

The structures responsible for transporting magma from the upper mantle to crustal storage chambers have great influence on the dynamical behavior of a volcanic system. These transport structures also encode details about the processes that created them and therefore document the system's history and evolution. The Hawaiian volcanic system has served as a global case study in how many volcanoes grow, erupt, and collapse (1, 2) because of the frequent eruptive activity, the abundance of seismicity, the wealth of instrumentation, and the presence of many volcanoes spanning various stages of life. These factors have led to Hawai'i's Kīlauea Volcano being among the best understood volcanoes in the world, with detailed knowledge of the locations and extent of the magma chambers that supply it (3, 4); detailed knowledge of the geometry of its rift zones (5); and a physical understanding of the eruptive patterns, accompanying seismicity, and geodetic deformation signals (6–8). Despite these major successes, the structures and processes by which magma is transported to these shallow crustal depths remain rather elusive.

Kīlauea's magma supply system is generally believed to follow a near-vertical pathway at shallow depths (9). Although there is geochemical evidence for subcrustal magma storage (10), the magmatic architecture beyond this depth is far less clear, particularly because the current position of the Hawaiian hot spot is believed to be offset from Kīlauea by tens of kilometers (10). A leading idea to explain lateral deep magma transport from the hot spot to Kīlauea is through a set of structures making up a mantle fault zone (11). These structures were first proposed after observations of a persistent, near-horizontal belt of mantle seismicity at ~30- to 35-km depth to the southwest of Kīlauea. This idea was built upon further

by other studies (9, 10, 12, 13) that have argued for the existence of these structures in the upper mantle.

In 2018, Kīlauea experienced its largest caldera collapse and major summit eruption in more than two centuries (2, 14). In August of 2019, ~1 year after the conclusion of this collapse sequence, a marked increase in earthquake swarms at 30- to 40-km depth occurred ~30 km southwest of Kīlauea, near the town of Pāhala (Fig. 1) (15). The depth to the Moho has been estimated at 13 and 18 km underneath Kīlauea and Mauna Loa, respectively, which indicates that the swarms occurred well into the upper mantle (16). The swarms were scattered across a region ~15 km in diameter and close to the area thought to be the current position of the Hawaiian hot spot (9).

To better understand the origin of these Pāhala swarms and how they might relate to the deeper magmatic architecture, we used an earthquake monitoring workflow with deep learning algorithms to reprocess the continuous seismic waveforms across the island and build an extremely detailed seismicity catalog. Imaging the magma plumbing systems from mantle to crust remains challenging for most geophysical methods, such as seismic tomography, geodetic inversion, and gravity and electromagnetic surveys, because these methods typically are unable to resolve the distribution and transportation pathways of magma (17). High-resolution earthquake catalogs built with deep learning provide an unprecedented opportunity to study the detailed spatial and temporal evolution of volcanic earthquake swarms and to characterize the driving mechanisms of magma plumbing systems. The improved picture of magma migration from mantle to crust could thus provide important information for estimating magma intrusion and forecasting volcanic eruption.

Pāhala sill complex

The Pāhala mantle swarm region experienced a notable ~192,000 events over the 3.5-year period. These events span the depth range of

36 to 51 km and can be organized into two main bodies of seismicity that are vertically offset from each other by ~2 km. The upper body (36- to 43-km depth) is primarily composed of volcano-tectonic (VT) earthquakes, whereas the lower body (45- to 51-km depth) is formed of almost exclusively long-period (LP) volcanic earthquakes. The lower body is within the tremor source region identified by Wech and Thelen (12), who interpreted it as a magma-rich volume. The bulk of the seismicity is in the upper body and consists of discrete layered, near-horizontal sheets with typical separation of ~500 m (Fig. 2). Individually, these sheeted structures are as large as 6 km by 5 km with a thickness of up to 300 m. The collection of sheets forms a major regional seismicity feature that extends 17 km laterally across the region and dips ~25° to the west. Although the sheets are predominantly made up of VT earthquakes, they are interspersed with LP volcanic earthquakes. From the totality of these observations, we conclude that the sheeted seismicity structures form a massive complex of mantle sills. Hereafter, we refer to this set of structures as the Pāhala sill complex (PSC), and we subsequently show that it likely serves as a nexus for magmatic activity in the volcanic system.

The seismicity within the PSC exhibits prominent spatiotemporal patterns at multiple scales. The entire volume of seismicity undergoes system-wide surges in the rate of earthquakes along with large-scale migration of seismicity. The largest sills within the PSC, however, individually demonstrate strong variations in event rates and complex patterns of migrating seismicity and quiescence. The disjoint nature of the sills makes them easily extracted with a clustering algorithm. We show the spatial and temporal evolution of the events within four different sills in Fig. 3, with the colors corresponding to the sills in Fig. 2. Spatially migrating swarms initiate within the sills at a single point and expand up, down, or bilaterally along the feature. After their most active phase, many swarms display a back-front of seismic quiescence. Assuming a homogeneous diffusion process from a point source, we can estimate the diffusivity of migrating seismicity (dashed lines in Fig. 3). The estimated point sources, or injection points, are plotted as stars in Fig. 2. We observe a common diffusivity value of ~0.05 m²/s in Fig. 3, A to C, whereas some clusters can migrate at a much faster speed with a diffusivity of 0.54 m²/s (Fig. 3D). In many of the sills, multiple migrating swarms initiate at different times; these later swarms often take place more than a year after the initial swarm began. These repeat episodes in many cases expand the size of the sills beyond the previous dimensions.

Several observations suggest that seismicity within the PSC itself is related to the migration

Seismological Laboratory, California Institute of Technology, Pasadena, CA, USA.

^{*}Corresponding author. Email: jwilding@caltech.edu

[†]These authors contributed equally to this work.

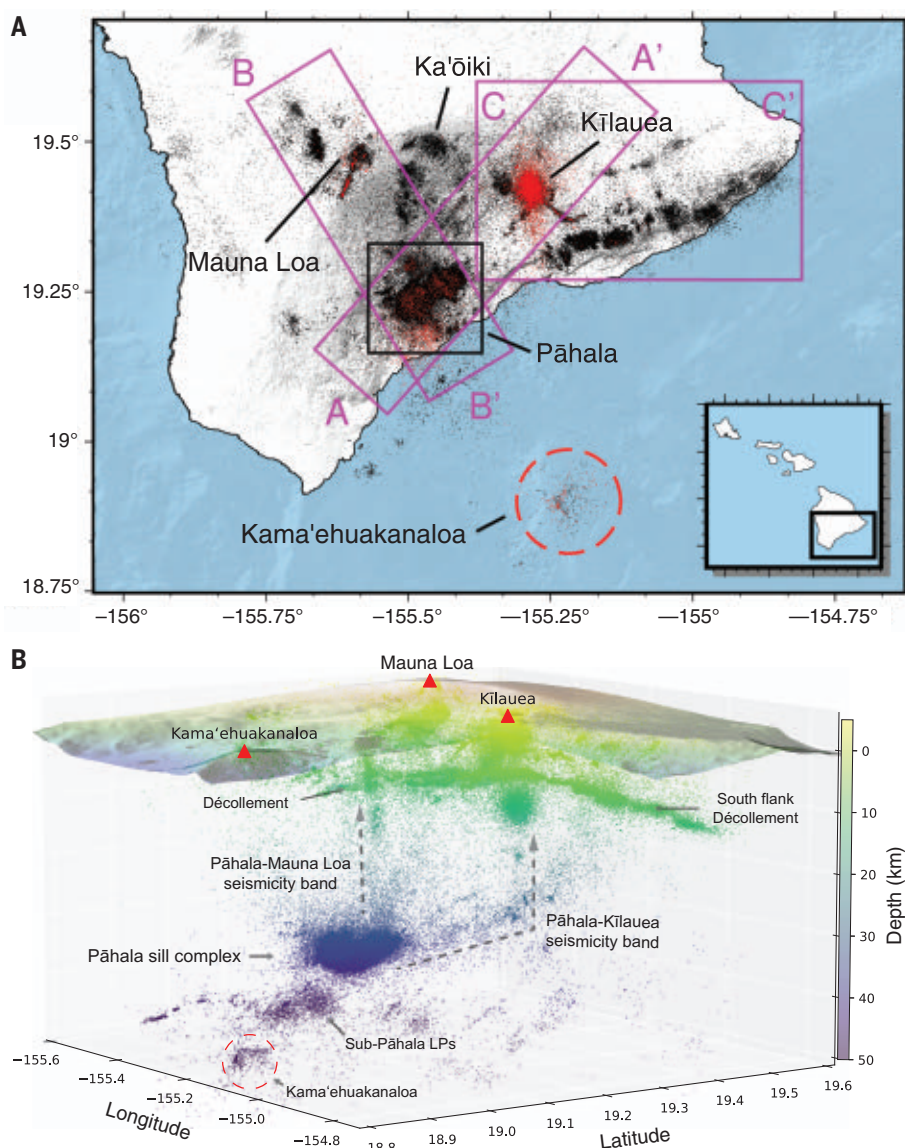


Fig. 1. Overview of seismicity of Hawai'i. (A) Map view of the Island of Hawai'i. Regular earthquakes are colored black, and LP earthquakes are colored red. Cross sections of labeled boxes are plotted in Fig. 5. (B) Three-dimensional view of seismicity colored by depth. Volcanoes are indicated with red triangles.

of magma. Spatiotemporal diffusion of seismicity with accompanying backfracts has previously been linked to transient fluid injection (18). Although static stress transfer (15) could be responsible for generating some of the earthquakes outside of the sills, the multiple discrete fronts of seismicity suggest that seismogenic processes within the structures are more localized. We propose that the observed swarms are generated by the injection of magma into the sills.

The diffuse body of LP earthquake swarms situated beneath the sills at 45- to 51-km depth is the most likely source region for these injected fluids. This LP volume broadly overlaps with a previously identified source region of

impulsive tremor signals and LP seismicity (9, 12, 19). Source mechanisms for LP earthquakes in this volume have been posited as either magma flux through cracks (19) or a volumetrically dispersed stress response to magma influx (12). Degassing of volatile-saturated magmas during decompression has also been proposed as a source mechanism for deep LP earthquakes (20). Any of these source mechanism models allows us to interpret the swarm-like behavior between January 2019 and December 2020 as magmatic unrest preceding apparent fluid injection into the sill complex above. Although LP seismicity is broadly distributed within the sills, its rate of occurrence is highly nonstationary—surges of

LP earthquakes within the sills are only observed after January 2021 (Fig. 4E). This temporal shift in source properties suggests a change in the physical properties of the source region, consistent with growing fluid enrichment in the sills over the time span of our catalog.

The distinctive, sustained intensity of seismic activity within the PSC suggests that material conditions in the source volume are particularly favorable to seismogenesis. Sills in the complex are likely to be composed of mafic magmas with olivine precipitates hosted in a lherzolite matrix (21). The plagioclase-spinel transition in this assemblage has previously been invoked to explain localized seismicity along the mantle fault zone (9). Phase equilibria studies place the maximum depth of this boundary at 30 to 35 km, proximal to the top of the sill complex at 36-km depth (21–23). Over their full depth extent (36 to 43 km), the sills may traverse this boundary, with their uppermost components located in the plagioclase stability region, or they may otherwise be emplaced within a broad plagioclase-spinel coexistence region (21). The location of the sills in this mineralogically complex region suggests that the pronounced seismic activity could be attributed to processes occurring within polyphase magma conduits. Polyminerals assemblages can exhibit transient weakening arising from coupled deformation and metamorphic reactions; this transformation weakening has been observed to promote diffusion creep-based deformation (24) and could facilitate crack growth or fault activation. Although the time scale of this weakening would be limited by the duration of the reaction and the counteracting effect of grain growth, sustained deformation in the PSC may be promoted by recurrent upward injections of magma into the sills. These injections would continuously modulate grain sizes in the PSC, prolonging conditions for seismic deformation in the host rock. This process could exploit lateral variations in strength (25) to produce the laterally compact seismogenic features that we observe.

The speed and intensity with which seismicity migrates throughout the complex suggests the existence of high-permeability paths that can support rapid magma transport. Laboratory experiments on partially molten rocks have demonstrated that melt can segregate into narrow, melt-enriched channels under deformation (26). The substantial melt content of these channels could provide the requisite permeability for the rapid magma transport that we observe; because of their weakness relative to the surrounding mantle, the channels may also serve to localize deformation (27). Our observations suggest that transport channels in the sill complex have attained an advanced stage of development under the

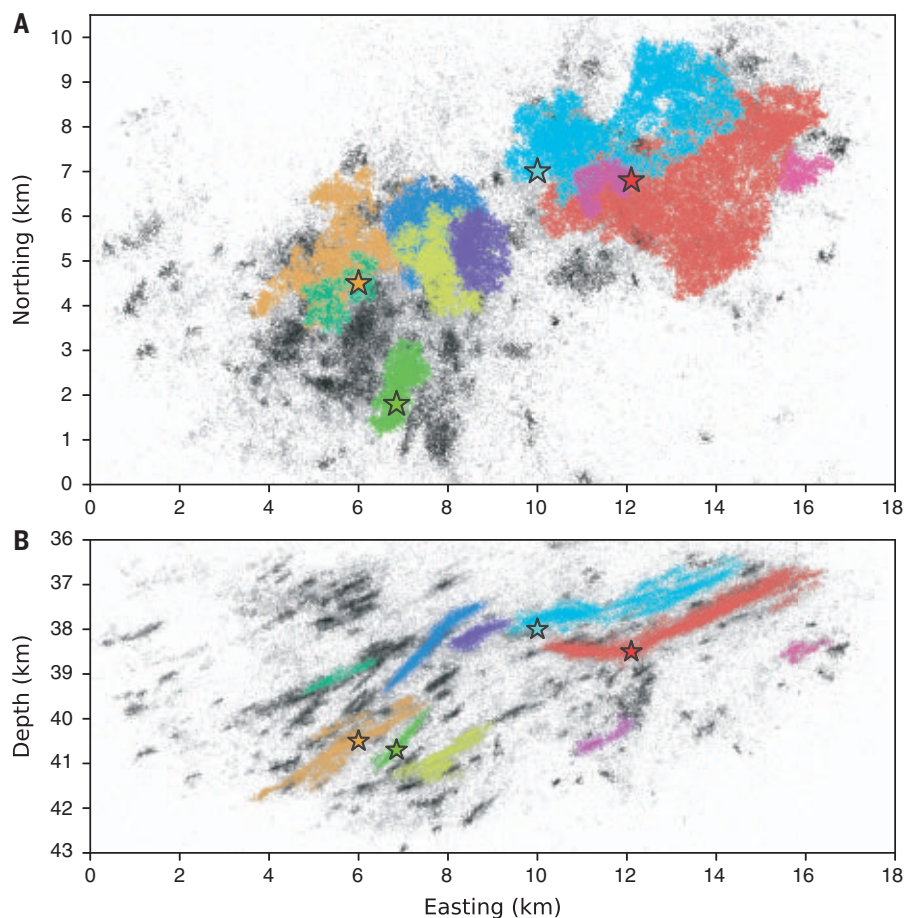


Fig. 2. The geometry of the PSC. (A and B) The map view (A) and cross-sectional view (B) correspond to the black boxed region in Fig. 1. The largest 10 clusters are colored for clarity. The spatiotemporal evolution of four clusters is shown in Fig. 3; the four colored stars are the approximate injection points of each cluster.

effects of long-term shear, possibly from island loading or the motion of the Pacific plate over the hot spot.

The web of seismicity beneath Hawai'i

At a regional scale, our high-resolution catalog of earthquakes elucidates an interconnected system of seismicity beneath the island of Hawai'i. Notably, we identify structures emerging from the PSC that connect to the edifices of both Kīlauea and Mauna Loa, which indicates a link between the PSC and both volcanoes.

The sills in the PSC are coplanar with a subhorizontal band of seismicity that extends laterally from the PSC to beneath Kīlauea. These observations are consistent with the hypothesis of a mantle fault zone existing in this region, which has been suggested to serve as a pathway for lateral transport of magma between Kīlauea and the plume (9, 11). Most of the seismicity in this band is characterized by VT earthquakes, but a small cluster of LP earthquakes is present on the seismicity band directly beneath Kīlauea, at 30-km depth. Above these LP earthquakes, there is a near-

vertical trend of seismicity that extends upward to ~20-km depth. This trend terminates just below a large cluster of LP seismicity at 10- to 15-km depth (Fig. 5A). To the northeast of Kīlauea, another branch of the structure abruptly deflects upward and rises nearly vertically to meet the surface. We refer to this overall band of seismicity as the Pāhala-Kīlauea seismicity band (Fig. 5A).

A second distinct seismicity structure connects the PSC to the Mauna Loa edifice, which we refer to as the Pāhala-Mauna Loa seismicity band. This 25-km-long column of seismicity rises from the northern edge of the PSC to the décollement beneath the Ka'ōiki seismic zone at a depth of 10 km, 20 km south of the Mauna Loa summit (Fig. 5B). The location of the Pāhala-Mauna Loa seismicity band is consistent with a previously proposed magma transport path between the PSC region and the Mauna Loa edifice (9). Although this path was inferred from the geometry of seismicity at 30-km depth, our catalog captures the first identified continuous structure that connects the two regions.

We also observe a collection of deep LP earthquakes almost directly beneath Kama'e-huakanalao Volcano (formerly Lō'ihi) at 50-km depth (Fig. 1). Although deep seismicity has been observed beneath Kama'e-huakanalao, it has previously been interpreted as belonging to a diffuse zone of seismicity between 20- and 60-km depth (28). Our catalog allows us to identify these events as LPs that are distinctly concentrated deep beneath the summit of Kama'e-huakanalao. On the basis of their colocation with the Kama'e-huakanalao summit, we suggest that these deep LPs represent a deep part of the volcano's magma system, as has been similarly inferred from LPs detected beneath Kīlauea and Mauna Loa (9, 29). Our catalog also reproduces a concentrated volume of deep LP seismicity beneath Mauna Kea that has previously been attributed to second boiling of a stalled magma body (fig. S4) (30).

Systemic interconnectivity

The spatiotemporal patterns of seismicity within the aforementioned structures are closely linked. The rates of earthquake activity and their source properties are seen to undergo rapid changes in response to distal eruptive activity or changes elsewhere in the system (Fig. 4).

Several episodic LP earthquake swarms took place in the seismicity body beneath the PSC between January and August 2019 (Fig. 4F). In July 2019, a week-long swarm of LP earthquakes occurred on the Pāhala-Kīlauea seismicity band, directly beneath Pāhala at 30-km depth (Fig. 4B). This episode coincided with an order-of-magnitude increase of VT seismicity rates within the PSC, 25 km away (Fig. 4D). During this phase of activity, multiple discrete swarms of VT seismicity migrated upward and to the east along the sills; this activity represents the first activation of these structures in our catalog. Simultaneously, the rate of earthquakes in Kīlauea's east rift zone steadily began to increase, from a mean of 15 events per week to values as high as 436 events per week during December 2020 (Fig. 4A).

After this activity, Kīlauea experienced two eruptions in late December 2020 and September 2021 (31, 32). Several features throughout the volcanic system responded immediately to these eruptions. At the onset of both eruptions, the rate of activity at Kīlauea's summit shut down and remained quiescent for months. After the 2020 eruption, the PSC immediately experienced a substantial increase in the rate of VT and LP earthquakes, which formed migrating swarms suggestive of fluid injection into the sills. After the 2021 eruption, the PSC experienced another episode of migratory swarms along with acceleration in the rate of LP earthquakes. These LP earthquakes occur

along the same sill structures generated during the previous stages of VT seismicity.

Both the Kīlauea and Mauna Loa seismicity bands experienced earthquake rate increases after the 2020 and 2021 Kīlauea eruptions. The rate increases after the 2020 eruption were gradual and occurred over months. After the 2021 eruption, the rate increases in both structures instead occurred over weeks (Fig. 4).

Discussion

Although our findings have important implications for large-scale magma transport in the system, particularly with regards to the forecasting of eruptive activity, magma transport in the Hawaiian mantle is likely not the sole process behind seismogenesis at these depths. Flexural or loading stresses are a viable mechanism for generating VT mantle seismicity (3, 13). In contrast to the broadly distributed seismicity expected from these stresses (3, 13), the Pāhala-Kīlauea and Pāhala-Mauna Loa seismicity bands revealed by our catalog are spatially concentrated features along previously theorized magma transport routes. In particular, the columnar structures beneath both volcanoes are suggestive of an additional, localized source of stress at depth.

Furthermore, previously observed or theorized magmatic structures are connected along the seismicity bands. Both bands originate from the magmatic PSC. The Pāhala-Kīlauea band rises to meet a concentrated volume of LP seismicity beneath Kīlauea's summit at 10- to 15-km depth (Fig. 5A), a persistent feature that has been interpreted as part of its magma system (33). LP earthquakes at 30-km depth additionally suggest the presence of magma or magmatic fluids deeper within the vertical column beneath the volcano. The Pāhala-Mauna Loa band terminates at the décollement within the Ka'ōiki seismic zone; a concentration of LP earthquakes is present within this intersecting region at 10-km depth (Fig. 5B). Although seismicity above this intersection is diffuse, the location of these LPs is connected to the summit by a positive *P*-wave velocity anomaly that has been interpreted as ultramafic cumulates associated with crustal magma storage (9, 34).

From these observations, we interpret the seismicity bands as magmatic structures connecting Kīlauea and Mauna Loa to a common source in the mantle (Fig. 6). Earthquakes occurring throughout the bands could be stimulated by the localized addition of magmatic stressing to background flexural and tectonic stress (11). The rapid response of the PSC to the July 2019 LP earthquake swarm and Kīlauea's 2020 and 2021 eruptions would suggest that system-wide pressure gradients can propagate quickly through the system, as observed in other regions, such as beneath Kamchatka volcanoes (35, 36).

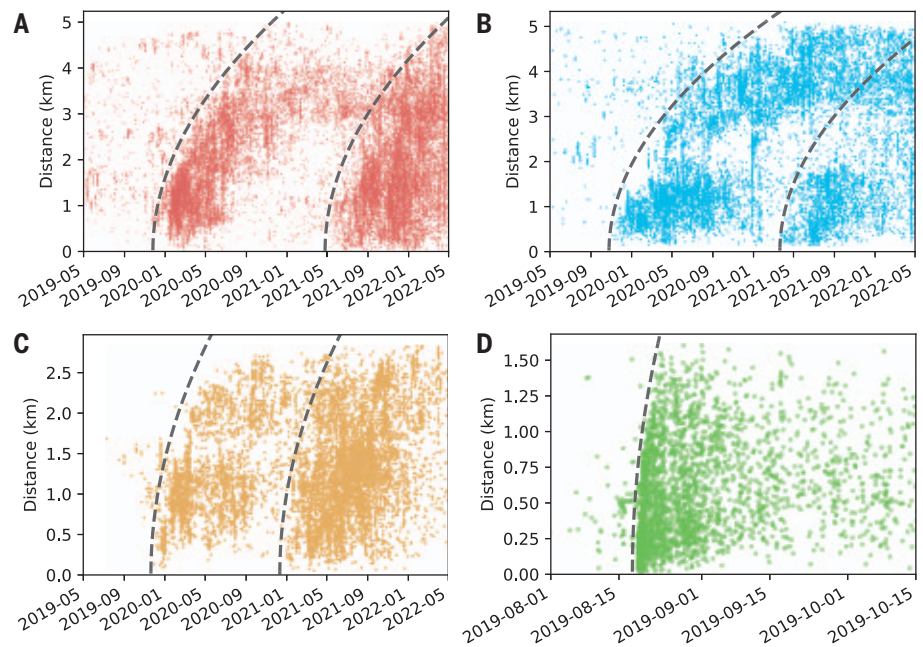


Fig. 3. Spatiotemporal evolution of the Pāhala sill seismicity. (A to D) The distance is calculated from the injection points indicated by stars in Fig. 2. The dashed lines are the diffusion fronts, assuming a homogeneous media with a diffusivity value of 0.05 m²/s [(A) to (C)] and 0.54 m²/s (D).

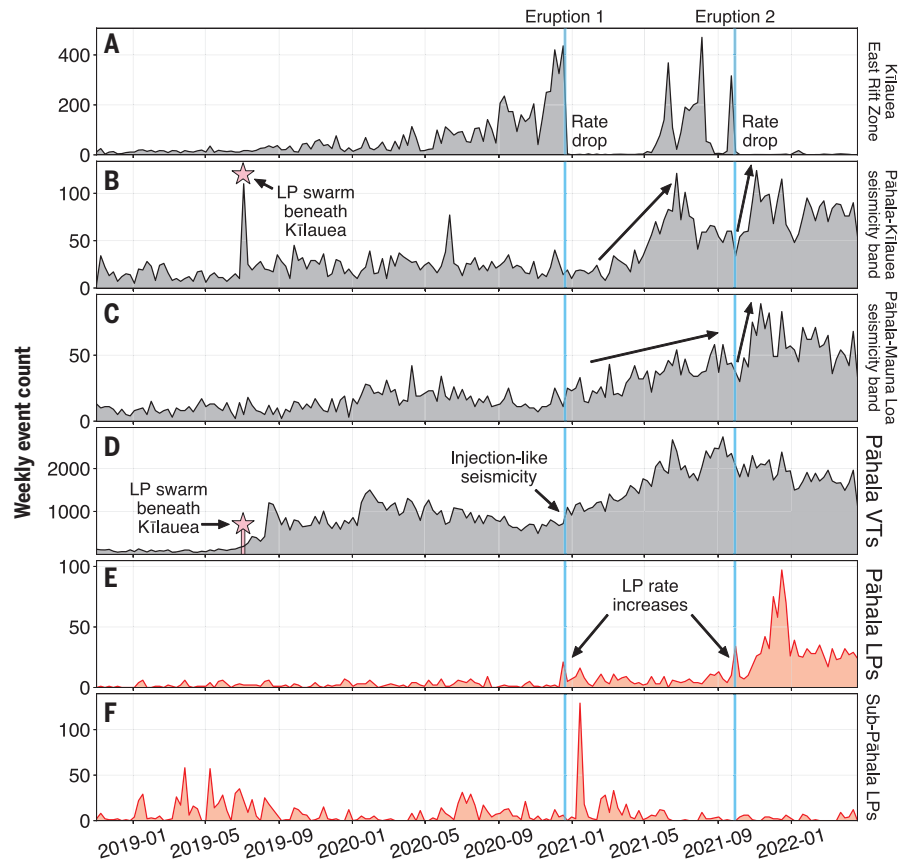
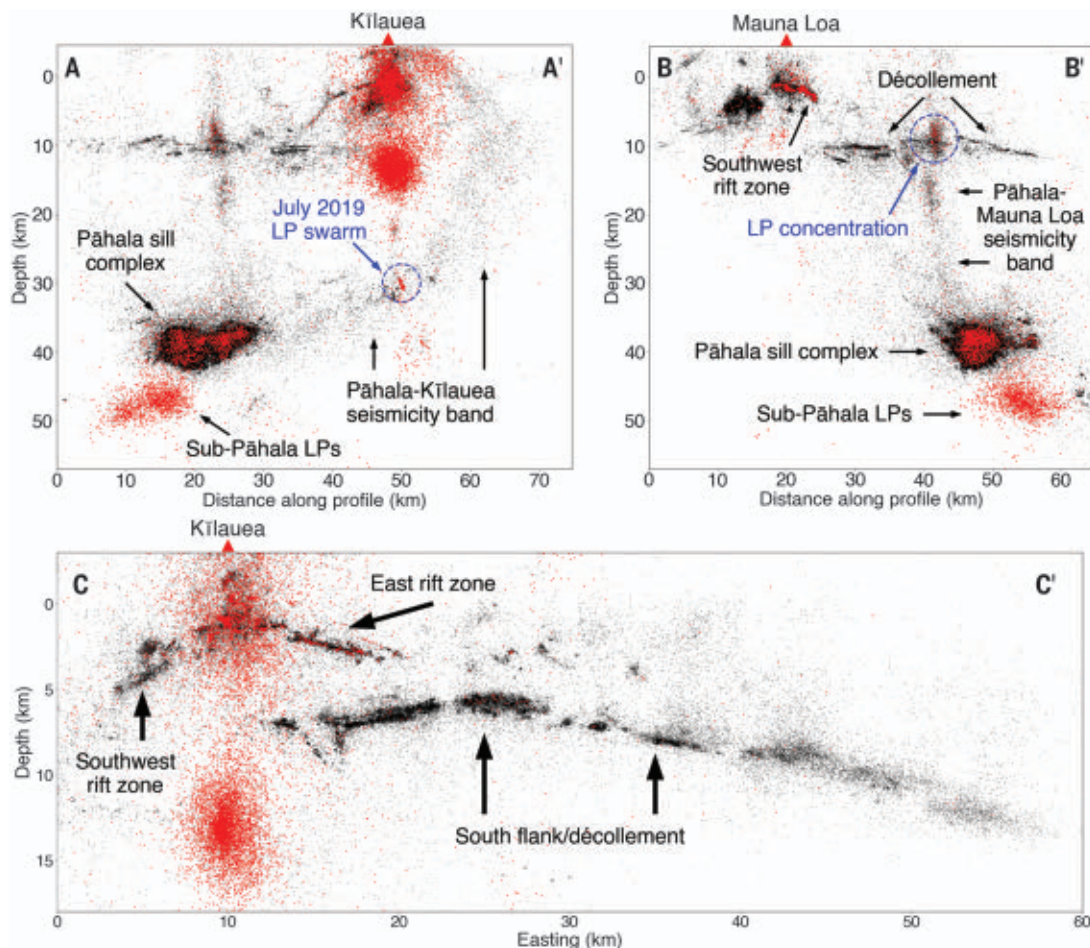


Fig. 4. Temporal variation of event counts for various regions making up the magmatic system. (A to F) The 2020 and 2021 eruptions at Kīlauea are demarcated by cyan lines. Pāhala VTs and Pāhala LPs refer to VT and LP earthquakes within the PSC, respectively. Sub-Pāhala LPs refers to the distributed volume of LP earthquakes beneath the sill complex.

Fig. 5. Depth sections of seismicity. The individual cross sections show seismicity within the boxes plotted in Fig. 1. VT seismicity is shown in black; LP seismicity is shown in red with larger marker size to emphasize its distribution. (A) Seismicity along the Pāhala-Kīlauea profile, A to A'. (B) Seismicity along the Pāhala-Mauna Loa profile, B to B'. (C) Shallow seismicity within the Kīlauea edifice, C to C'.



After PSC intrusions, increasing earthquake rates within the Pāhala-Kīlauea and Pāhala-Mauna Loa seismicity bands could plausibly be attributed to increased flux of magma or magmatic fluids between the PSC and the surface. Alternatively, accelerating earthquake rates within the seismicity bands could reflect intensifying VT activity within the crustal edifices of Kīlauea and Mauna Loa accompanied by broad-scale deformation that may stress the mantle below (3).

The PSC may serve as a common magma source at 40-km depth for Kīlauea and Mauna Loa. This degree of volcanic interconnectivity is noteworthy in light of geochemical and past seismological results that imply Hawaiian volcanoes have distinct plumbing systems sourced from distinct regions of the underlying plume (9, 29, 37–39). The seismic structures we observe suggest that previously posited magma transport routes may be nonunique; the connection between the deep tremor region (12) and the volcanoes may represent one part of a distributed network of structures.

Temporal clustering of eruptive behavior between neighboring volcanoes is well documented (40). In the absence of evidence of shallow magmatic connections, such cluster-

ing has been attributed to stress transfer (40, 41) or has been proposed to be an artifact caused by spatial clustering of volcanoes in plate boundary regions (42). Our results suggest that many neighboring volcanoes might have more extensively connected magma systems than has previously been appreciated.

The apparent absence of large, seismogenic magma structures beneath Kama'ehuakanaloa could reflect the volcano's distance from the hot spot. The local geotherm might not intersect the solidus above 50-km depth so that persistent magma storage at shallower depths is not thermodynamically viable. A purely vertical magmatic architecture beneath Kama'ehuakanaloa would suggest that formation of lateral transport structures in the uppermost mantle (<50 km) is not favored at earlier stages of a Hawaiian volcano's life cycle. Such connections might only become favorable after the development of laterally extensive magma systems (43) under the effects of long-term shear.

Many prior attempts to image magmatic structures underneath the island of Hawai'i have used seismic tomography methods (44), which have limited sensitivity to fine-scale structure. However, microseismicity enables us to characterize connections between mag-

matic structures with high precision (45). Our seismicity catalog also captures detailed patterns of unrest in the shallow magma systems of Kīlauea and Mauna Loa. A substantial proportion of LP earthquakes are detected within Kīlauea's summit and east rift zone, as well as Mauna Loa's summit and southwest rift zone. LP earthquake locations in these features are spatially concentrated, consistent with previous observations (33, 46). Although rift zone swarms may be triggered tectonically (7) and do not necessarily portend eruptive activity, the patterns of activity that we observe highlight the possibility of enhanced monitoring and eruptive forecasting with microseismicity catalogs as well as the improved characterization of shallow reservoir systems.

Our analysis of the Pāhala swarm is the first in situ observation of magma dynamics in the mantle at the resolution of individual structures. These measurements represent a rich opportunity to study diffusion and emplacement models at remote depths in future work. Although the observed swarm in the PSC should be viewed as a major sequence in this volcanic system, it is probably not unique. Comparable mantle swarms occurred during 1953 to 1960 beneath Kīlauea, a period of

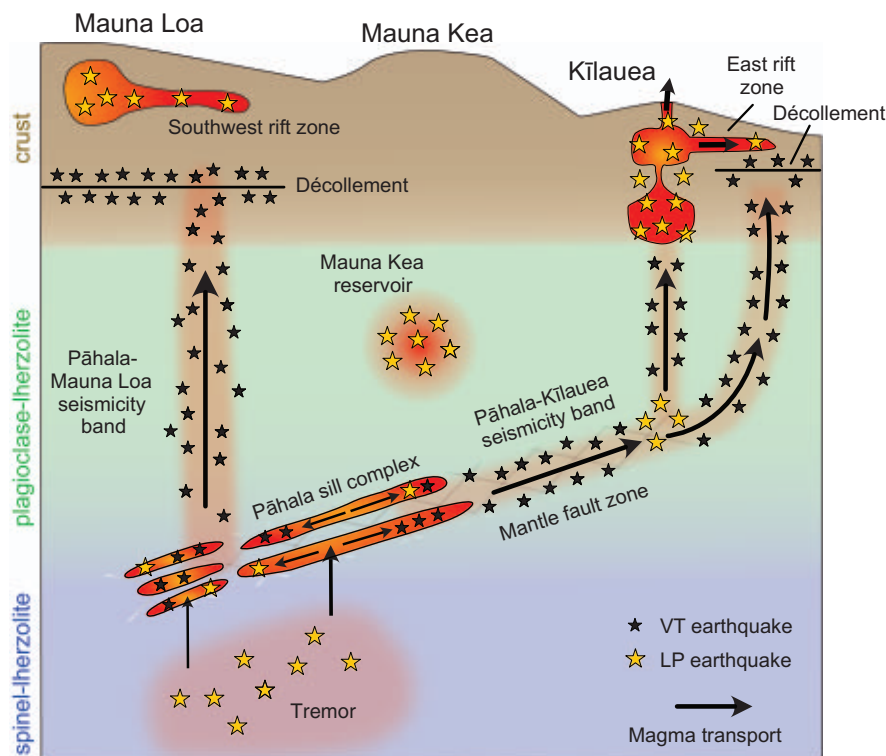


Fig. 6. Cartoon summarizing observations. Eruptions and intrusions at Kīlauea cause pressure gradients to rapidly propagate through the Kīlauea transport structure to the PSC. Magma is injected into the PSC from the underlying magma-bearing volume; the sills are proximal to the plagioclase-spinel phase boundary, possibly in a polyphase coexistence region. The sills are connected to Kīlauea and the décollement or Ka'ōiiki region within the Mauna Loa edifice along continuous bands of seismicity.

time that includes the 1959 to 1960 Kīlauea Iki eruption. Although hypocenters from this era of Hawai'i monitoring are not well constrained by modern standards, the depth of this swarm sequence has been estimated at 45 to 65 km, well into the mantle (47). Although this earlier swarm might have originated in the structures that we image, the apparent nonuniqueness of deep magma transport paths under Hawai'i raises the possibility of activity within a distinct set of structures. The size and level of activity observed within the PSC suggest that these features may be important contributors to the growth process of Hawaiian volcanoes and therefore may encode valuable historical information about plume-surface interaction.

Similar mantle earthquake swarms have been reported at several other ocean island volcanoes, including Fogo, El Hierro, and La Reunion (48–50). In particular, the Fogo swarm took place at similar depths (38 to 44 km) to the PSC swarm and has been interpreted as sill emplacement. These observations hint that large-scale mantle magma transport structures like the PSC may be present under many other ocean island volcanoes. Future improvements to earthquake monitoring capabilities

could facilitate better identification of connections between deep magma and surface volcanoes, with important implications for real-time monitoring.

REFERENCES AND NOTES

1. J. G. Moore, D. A. Clague, *Geol. Soc. Am. Bull.* **104**, 1471–1484 (1992).
2. C. A. Neal *et al.*, *Science* **363**, 367–374 (2019).
3. F. W. Klein, R. Y. Koyanagi, J. S. Nakata, W. R. Tanigawa, in *Volcanism in Hawaii: Volume 2*, R. W. Decker, T. L. Wright, P. H. Stauffer, Eds. (US Geological Survey, professional paper 1350, 1987), pp. 1019–1185.
4. A. F. Flinders *et al.*, *Geophys. Res. Lett.* **40**, 3367–3373 (2013).
5. D. Gillard, A. M. Rubin, P. Okubo, *Nature* **384**, 343–346 (1996).
6. E. K. Montgomery-Brown, A. Miklius, *Geology* **49**, 397–401 (2020).
7. C. Wauthier, D. C. Roman, M. P. Poland, *Geology* **47**, 820–824 (2019).
8. B. Chouet, P. Dawson, *J. Geophys. Res.* **116**, B12317 (2011).
9. T. L. Wright, F. W. Klein, *Lithos* **87**, 50–79 (2006).
10. K. Putirka, *Geology* **25**, 69 (1997).
11. C. J. Wolfe, P. G. Okubo, P. M. Shearer, *Science* **300**, 478–480 (2003).
12. A. G. Wech, W. A. Thelen, *Geophys. Res. Lett.* **42**, 7090–7097 (2015).
13. M. E. Pritchard, A. M. Rubin, C. J. Wolfe, *Geophys. J. Int.* **168**, 419–430 (2007).
14. K. R. Anderson *et al.*, *Science* **366**, eaaz1822 (2019).
15. M. K. Burgess, D. C. Roman, *Geophys. Res. Lett.* **48**, e2020GL091096 (2021).

16. D. P. Hill, J. J. Zucca, in *Volcanism in Hawaii: Volume 2*, R. W. Decker, T. L. Wright, P. H. Stauffer, Eds. (US Geological Survey, professional paper 1350, 1987), pp. 903–917.
17. C. Magee *et al.*, *J. Petrol.* **59**, 1217–1251 (2018).
18. Z. E. Ross, E. S. Cochran, *Geophys. Res. Lett.* **48**, e2021GL092465 (2021).
19. K. Aki, R. Koyanagi, *J. Geophys. Res.* **86**, 7095–7109 (1981).
20. O. Melnik, V. Lyakhovsky, N. M. Shapiro, N. Galina, O. Bergal-Kuvikas, *Nat. Commun.* **11**, 3918 (2020).
21. G. Sen, *Earth Planet. Sci. Lett.* **62**, 215–228 (1983).
22. G. Borghini, P. Fumagalli, E. Rampone, *J. Petrol.* **51**, 229–254 (2010).
23. P. Wyllie, *Geol. Rundsch.* **70**, 128–153 (1981).
24. H. Stünitz *et al.*, *J. Struct. Geol.* **139**, 104129 (2020).
25. A. Bellas, S. J. Zhong, *Geochem. Geophys. Geosyst.* **22**, e2020GC009547 (2021).
26. B. K. Holtzman, N. J. Groebner, M. E. Zimmerman, S. B. Ginsberg, D. L. Kohlstedt, *Geochem. Geophys. Geosyst.* **4**, 8607 (2003).
27. M. E. Zimmerman, D. L. Kohlstedt, *J. Petrol.* **45**, 275–298 (2004).
28. F. W. Klein, *J. Geophys. Res.* **87**, 7719–7726 (1982).
29. P. G. Okubo, C. J. Wolfe, *J. Volcanol. Geotherm. Res.* **178**, 787–794 (2008).
30. A. G. Wech, W. A. Thelen, A. M. Thomas, *Science* **368**, 775–779 (2020).
31. P. Segall, K. Anderson, T. A. Wang, *Geophys. Res. Lett.* **49**, e2022GL099270 (2022).
32. Global Volcanism Program, “Report on Kīlauea (United States),” K. L. Bennis, E. Venzke, Eds., *Bulletin of the Global Volcanism Network*, 47:1 (Smithsonian Institution, 2022).
33. R. S. Matoza, P. M. Shearer, P. G. Okubo, *Geophys. Res. Lett.* **41**, 3413–3421 (2014).
34. P. G. Okubo, H. M. Benz, B. A. Chouet, *Geology* **25**, 867 (1997).
35. C. Journeau *et al.*, *Sci. Adv.* **8**, eabj1571 (2022).
36. N. M. Shapiro *et al.*, *Nat. Geosci.* **10**, 442–445 (2017).
37. J. E. Dixon, D. A. Clague, E. M. Stolper, *J. Geol.* **99**, 371–394 (1991).
38. J. M. Rhodes, K. P. Wenz, C. A. Neal, J. W. Sparks, J. P. Lockwood, *Nature* **337**, 257–260 (1989).
39. F. A. Frey, J. M. Rhodes, K. G. Cox, D. P. McKenzie, R. S. White, *Phil. Trans. R. Soc. A* **342**, 121–136 (1993).
40. A. T. Linde, I. S. Sacks, *Nature* **395**, 888–890 (1998).
41. H. M. Gonnermann *et al.*, *Nat. Geosci.* **5**, 826–829 (2012).
42. D. M. Palladino, G. Sottili, *Geophys. Res. Lett.* **39**, L12308 (2012).
43. R. S. J. Sparks *et al.*, *Phil. Trans. R. Soc. A* **377**, 20180019 (2019).
44. G. Lin, P. M. Shearer, F. Amelung, P. G. Okubo, *J. Geophys. Res. Solid Earth* **120**, 2510–2524 (2015).
45. A. J. Hotovec-Ellis *et al.*, *Sci. Adv.* **4**, eaat5258 (2018).
46. J. Battaglia, J.-L. Got, P. Okubo, *J. Geophys. Res.* **108**, 2553 (2003).
47. J. P. Eaton, D. H. Richter, H. L. Krivoy, in *Volcanism in Hawaii: Volume 2*, R. W. Decker, T. L. Wright, P. H. Stauffer, Eds. (US Geological Survey, professional paper 1350, 1987), pp. 1307–1335.
48. C. Leva, G. Rümpeker, F. Link, I. Wölbern, *J. Volcanol. Geotherm. Res.* **386**, 106672 (2019).
49. A. Klügel, M.-A. Longpré, L. García-Cañada, J. Stix, *Earth Planet. Sci. Lett.* **431**, 140–149 (2015).
50. Z. Duputel *et al.*, *C. R. Geosci.* **353**, 237–255 (2021).

ACKNOWLEDGMENTS

The authors acknowledge comments by A. Flinders and an anonymous reviewer that substantially improved the manuscript. The facilities of IRIS Data Services, and specifically the IRIS Data Management Center (DMC), were used for access to waveforms, related metadata, and/or derived products used in this study. IRIS Data Services are funded through the Seismological Facilities for the Advancement of Geoscience (SAGE) Award of the National Science Foundation under cooperative support agreement EAR-1851048. The computations presented in this work were conducted

in the Resnick High Performance Computing Center, a facility supported by the Resnick Sustainability Institute at the California Institute of Technology. **Funding:** Z.E.R. and J.D.W. received support from NSF award EAR-2034167. J.M.J. acknowledges the JPL Strategic Research & Technology Development Program, "Venus Science Into The Next Decade." **Author contributions:** W.Z. performed phase picking. Z.E.R. and J.D.W. performed quality control on the phase picks and constructed the catalog. Z.E.R. and W.Z. performed earthquake relocation. J.D.W. performed the frequency index calculations. J.D.W., W.Z., Z.E.R., and J.M.J.

contributed to data analysis and writing. All authors contributed to the revised version of the manuscript. **Competing interests:** All authors declare no competing interests. **Data and materials availability:** Seismic data are publicly available from the IRIS DMC. The seismicity catalog developed in this study will be made publicly available. **License information:** Copyright © 2023 the authors, some rights reserved; exclusive licensee American Association for the Advancement of Science. No claim to original US government works. <https://www.science.org/about/science-licenses-journal-article-reuse>

SUPPLEMENTARY MATERIALS

science.org/doi/10.1126/science.ade5755
Materials and Methods
Figs. S1 to S12
References (51–89)
Movie S1
Data S1

Submitted 24 August 2022; accepted 8 December 2022
10.1126/science.ade5755

NEUROSCIENCE

Suppressing feedback signals to visual cortex abolishes attentional modulation

Samantha R. Debes¹ and Valentin Dragoi^{1,2*}

Attention improves perception by enhancing the neural encoding of sensory information. A long-standing hypothesis is that cortical feedback projections carry top-down signals to influence sensory coding. However, this hypothesis has never been tested to establish causal links. We used viral tools to label feedback connections from cortical area V4 targeting early visual cortex (area V1). While monkeys performed a visual-spatial attention task, inactivating feedback axonal terminals in V1 without altering local intracortical and feedforward inputs reduced the response gain of single cells and impaired the accuracy of neural populations for encoding external stimuli. These effects are primarily manifested in the superficial layers of V1 and propagate to downstream area V4. Attention enhances sensory coding across visual cortex by specifically altering the strength of corticocortical feedback in a layer-dependent manner.

Selective attention is a critical brain mechanism that enhances the processing of relevant sensory information. Attentional modulation of sensory encoding, intensively studied over the past several decades, has long been hypothesized to originate from downstream areas carrying top-down feedback signals to early cortex such as to increase response gain, sensitivity, and accuracy of network computations (1–4). Understanding the neural mechanisms of attentional modulation depends on our ability to activate or silence presynaptic downstream areas and subsequently assess their impact on the target network. However, separating the impact of feedback inputs from local intracortical and bottom-up inputs, which is necessary for examining the mechanism of top-down attentional modulation, has been challenging when using traditional neuromodulation methods (1–11). Here, we combined in vivo electrophysiology in behaving monkeys with an optogenetic protocol to perturb construct-expressing neuronal processes and modulate feedback signals without altering the strength of feedforward and intracortical inputs that are not directly caused by feedback.

To examine the function of corticocortical feedback for attentional modulation of sensory coding, we have chosen a major pathway

involving primary and midlevel visual cortical areas V1 and V4 in behaving monkeys. Neurons in V4 carry top-down signals related to behavioral context and attention to V1 via direct, monosynaptic feedback projections (12–16). Although V1 also receives feedback inputs from area V2, neurons in V4 are more strongly modulated by attention and are hierarchically closer to decision-making areas; hence, they are ideally suited to examine the impact of cortical feedback on the transmission of attentional signals to early cortex (17, 18).

Results

We developed a sensitive assay based on viral-mediated labeling of feedback connections arising from midlevel cortical area V4 that target area V1. The construct leveraged a halorhodopsin-derived chloride pump, Jaws, in adeno-associated virus serotype 8 (AAV8) under the control of the promoter human synapsin (19, 20). AAV8-hSyn-Jaws-GFP-ER2 was expressed within an approximately 12.6-mm³ cortical volume in area V4 (Fig. 1A) (see materials and methods). This allowed us to simultaneously place a linear electrode array and fiber optic in V1 to record neural activity at multiple sites (fig. S1) and selectively suppress axonal feedback terminals of V4 neurons targeting V1 while macaques performed a spatial attention task. Because the viral construct was injected in V4, we reasoned that shining red light in the superficial layers of V1 would specifically inactivate feedback inputs while leaving un-

perturbed local intracortical and feedforward inputs to V1 neurons (Fig. 1A). This allowed us to examine whether the attentional modulation of neural populations in V1 is impaired when suppressing cortical feedback from V4 and whether the hypothesized reduction in attentional modulation in V1 is further transmitted to postsynaptic V4 targets.

Optogenetic suppression of V4 feedback axons in V1

Two monkeys performed a spatial-attention contrast detection task (Fig. 1B and fig. S2) whereby various contrast stimuli were displayed at two symmetric spatial locations on a computer screen. One location covered the receptive fields of the neurons being recorded and the other location was outside the receptive fields, diametrically opposed at the same eccentricity. Only one spatial location was behaviorally relevant on a given trial: Monkeys were cued by the color of the fixation point to attend to the stimuli covering the neurons' receptive fields or to those presented on the contralateral side (see materials and methods) (Fig. 1B). On 50% of trials in each condition, optical stimulation was applied to selectively suppress V4 feedback axons in the upper layers of V1. To maintain equal behavioral performance in the "laser" and control conditions, we restricted laser power to a low level such that behavioral performance at the attended side was not significantly different between control and laser trials ($P = 0.52$) (Fig. 1B); these effects were consistent across animals (fig. S3), and perceptual performance was unaffected by the stimuli flashed at the unattended location (fig. S4). If light stimulation would change behavioral performance across conditions, the obtained unequal reward across conditions could possibly alter behavioral context and hence introduce additional top-down feedback signals besides those related to attention. The lack of a behavioral effect in the laser condition may be due to the fact that in monkey cortex, only a fraction of neurons at the injection site are typically transfected (21), and this likely resulted in a small number of cells that were perturbed relative to the entire V1 population encoding the stimuli.

We first placed the electrode array and fiber optic at the injection site in V4, which was associated with a direct suppression of local

¹Department of Neurobiology and Anatomy, McGovern Medical School, University of Texas at Houston, Houston, TX 77030, USA. ²Department of Electrical and Computer Engineering, Rice University, Houston, TX 77005, USA.
*Corresponding author: Email: valentin.dragoi@uth.tmc.edu

neural activity ($P = 4.22 \times 10^{-5}$) (Fig. 1C and fig. S6). When the recording array and fiber optic were placed at the V1 sites with overlapping receptive fields corresponding to the V4 injection sites, responses were significantly reduced, indicating a selective suppression of V4 axons terminating in V1 ($P = 3.85 \times 10^{-10}$) (Fig. 1D and fig. S5). We confirmed that the differences in firing rates seen in V1 indeed reflect feedback modulation and hence performed electrical recordings in a control, likely nontransfected area ($P = 0.44$) (Fig. 1E). When we separated the electrode and fiber optic by several millimeters, V1 responses were not influenced by light ($P = 0.84$) (Fig. 1F). Light stimulation presented either alone or in combination with the visual stimulus did not change the mean eye position, eye velocity, or pupil size across trials (median eye X position, $P = 0.75$; median eye Y position,

$P = 0.71$; median pupil size, $P = 0.69$; median eye X velocity, $P = 0.68$; median eye Y velocity, $P = 0.73$, Wilcoxon rank sum test) (fig. S7).

V4 feedback pathways carry attentional signals to V1

We examined the role of cortical feedback in modulating attentional effects in V1 and isolated 239 neurons recorded across 16 sessions in two animals (Fig. 2A) that were both stimulus and light sensitive ($P < 0.05$, Wilcoxon rank sum test). If feedback projections carry attentional signals, inactivating axonal terminals in V1 would significantly reduce the strength of attentional modulation such that the responses of V1 cells in the attended laser condition would be indistinguishable from those in the unattended laser condition. Without laser stimulation (control, Fig. 2A, left), there

was a 7.2% (± 2.06) increase in neurons' mean firing rates when high-contrast stimuli were attended (relative to unattended, $P = 9.59 \times 10^{-10}$) (22–25). However, when we inactivated axonal feedback terminals (Fig. 2A, middle), the responses of neurons in the attended and unattended conditions became indistinguishable ($P = 0.95$). Attentional modulation was abolished when cortical feedback was inactivated [high-contrast, $P = 3.61 \times 10^{-9}$ (Fig. 2A, right, and fig. S8), i.e., a 7.4-fold decrease in attentional modulation]; the interaction between laser stimulation and attention was statistically significant ($P = 0.0022$, Kruskal-Wallis test, post hoc Fisher's least significant difference test). This result was also significant when computed by electrode penetration (fig. S9). In the absence of attention, there was no significant difference between laser and

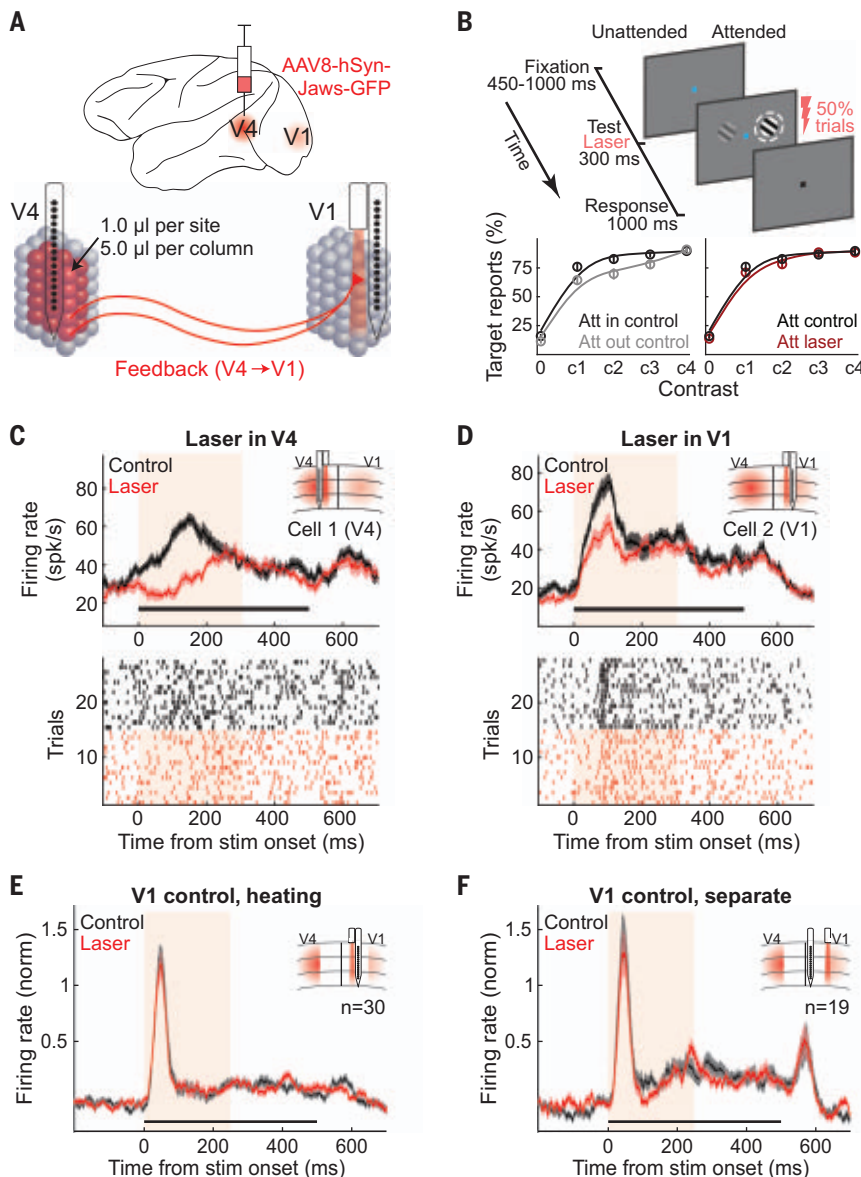


Fig. 1. Optogenetic suppression of V4 feedback axons in V1. (A) Schematic illustrating the AAV8-hSyn-Jaws-GFP-ER2 injection into area V4. Feedback terminals are inactivated by placing a fiber optic laser in V1. (B) Top: Schematic of spatial attention task. Bottom left: Behavioral performance during control (no laser) trials as a function of stimulus location, plotted with a spline curve fit (low- to high-contrast, $P = 0.11, 0.08, 0.09, 0.17, 0.56$, Wilcoxon signed-rank test). Bottom right: Behavioral performance in attended condition as a function of laser stimulation, plotted with a spline curve fit (low- to high-contrast, $P = 0.23, 0.37, 0.09, 0.59, 0.63$, Wilcoxon signed-rank test). (C) Peristimulus time histogram (PSTH) (top) and raster (bottom) plots for an example V4 cell when laser stimulation targets cell bodies at injection site. In all plots, the envelope represents SEM, black horizontal line represents stimulus duration, and shaded window represents laser stimulation. (D) PSTH (top) and raster (bottom) plots for an example V1 cell when laser stimulation targets V4 feedback terminals in V1. (E) Population PSTH of V1 cells ($n = 30$), recorded from a part of V1 likely not receiving transfected V4 feedback terminals. (F) Population PSTH of V1 cells ($n = 19$), recorded while the electrode and laser were separated (>2 mm).

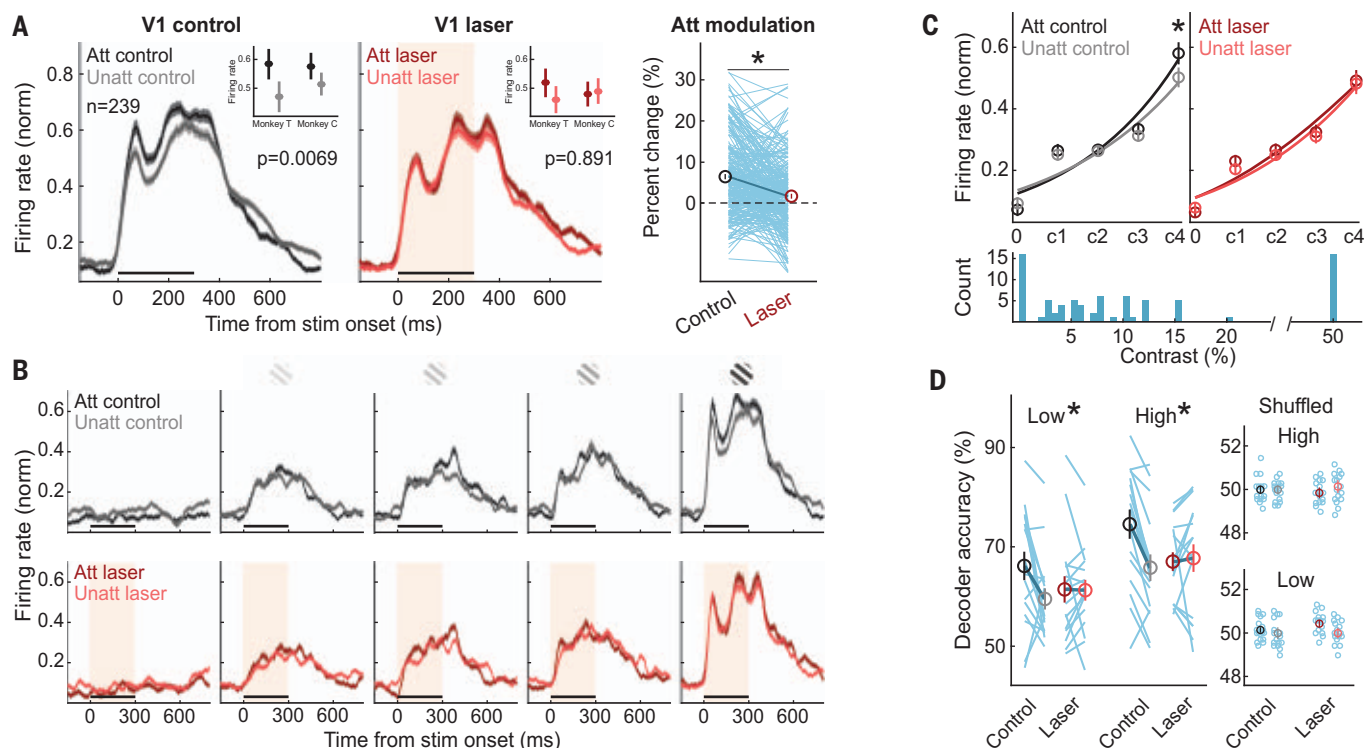


Fig. 2. V4 feedback carries attentional signals to V1. (A) Left: Neural responses to the high-contrast stimulus (50% contrast) flashed in cells' receptive field without laser stimulation. Population PSTH ($n = 239$) while animals attended the stimulus ("Att control," black) compared to when animals attended to the opposite side of the screen ("Unatt control," gray, $P = 9.59 \times 10^{-10}$, Wilcoxon signed-rank test). In all plots, the envelope represents SEM; black horizontal line represents stimulus duration. Inset shows per animal changes. Middle: Same as left panel, but during laser stimulation. Population PSTH while animals attended the stimulus ("Att laser," maroon) compared to when animals attended to the opposite side of the screen ("Unatt laser," pink, $P = 0.95$, Wilcoxon signed-rank test). In all plots, the shaded window represents laser stimulation. Right: Changes in attentional modulation with and without feedback as percent change of control condition effects (black) compared to laser

conditions (red, $P = 3.61 \times 10^{-9}$, Wilcoxon signed-rank test). Blue lines represent values from individual cells; dark line represents the mean. (B) Top: Population PSTHs across all contrasts without laser stimulation. Bottom: With laser stimulation. (C) Top left: Population contrast response functions for control conditions, plotted with a cumulative Gaussian fit (c0, $P = 0.051$; c1, $P = 0.20$; c2, $P = 0.89$; c3, $P = 0.25$; c4, $P = 9.59 \times 10^{-10}$, Wilcoxon signed-rank test). Top right: Contrast response functions for laser conditions (c0, $P = 0.055$; c1, $P = 0.011$; c2, $P = 0.081$; c3, $P = 0.50$; c4, $P = 0.95$, Wilcoxon signed-rank test). Bottom: Histogram of contrasts used in all experiments. (D) Left: Relative difference (control versus laser) in decoder accuracy for low- and high-contrast stimuli (low, $P = 0.02$; high, $P = 0.0023$, Wilcoxon signed-rank test). Right: "Shuffled" decoder performance for low- (bottom) and high- (top) contrast stimuli. Blue lines represent values from individual sessions; dark lines represent the mean.

control firing rates ($P = 0.057$, Wilcoxon signed-rank test).

Despite expectation that attention is most needed when stimuli are difficult to see, neuronal responses were primarily modulated at the highest stimulus contrast (Fig. 2, B and C, and fig. S10). When cortical feedback inputs from V4 were inactivated, we found a lack of attentional modulation across all contrasts ($P = 0.18$, Wilcoxon signed-rank test). However, although firing rates were only weakly modulated by attention at low stimulus contrasts, a linear decoder (classifying stimulus-present versus stimulus-absent trials) based on the population response in each session yielded a significant improvement in decoder accuracy when feedback signals were present [attended versus unattended conditions: low-contrast (c1-c2), $P = 0.0061$; high-contrast (c3-c4), $P = 0.00053$ (Fig. 2D)]. Inactivating cortical feedback inputs rendered decoder performance indistinguishable between attended

and unattended conditions (low-contrast, $P = 0.38$; high-contrast, $P = 0.50$). The relative difference in decoder performance (attended versus unattended) was significantly larger in control compared to laser condition (relative difference: low-contrast, decreased by 87.8%, $P = 0.02$; high-contrast, decreased by 93.4%, $P = 0.0023$; Wilcoxon signed-rank test). Our main results were consistent across animals (fig. S11) and stimulus contrast values (fig. S12, see supplementary materials). Analyzing the responses of all stimulus-responsive cells regardless of whether they were light-sensitive or not ($n = 309$ neurons) yielded highly significant effects of cortical feedback inactivation on attentional modulation of individual cell responses (fig. S13).

Laminar dependency of feedback inactivation effects

Because feedback axons from V4 preferentially terminate in the upper layers of V1 (12–16)

(Fig. 3A), we asked whether the effects of feedback inactivation are layer specific. Current source-density analysis was used to assign recorded cells on the linear array to laminar locations (26, 27) (Fig. 3B, see materials and methods). Out of 16 sessions, we identified the full laminar profile in 9 sessions, i.e., a total of 47, 44, and 32 cells in the supragranular (SG), granular (G), and infragranular (IG) layers, respectively. Attention influenced mean firing rates and decoder performance in the supragranular layers [attention modulation at c4 contrast, control versus laser, SG: $P = 0.00015$; Wilcoxon signed-rank test (Fig. 3C and fig. S14); SG decoder low-contrast (c1-c2): $P = 0.016$; SG decoder high-contrast (c3-c4): $P = 0.016$ (Fig. 3D and fig. S15)], although the effects in the other layers were weak and statistically nonsignificant (G attention modulation, $P = 0.26$; G decoder low-contrast, $P = 0.55$, G decoder high-contrast, $P = 0.11$; IG attention modulation, $P = 0.36$; IG decoder

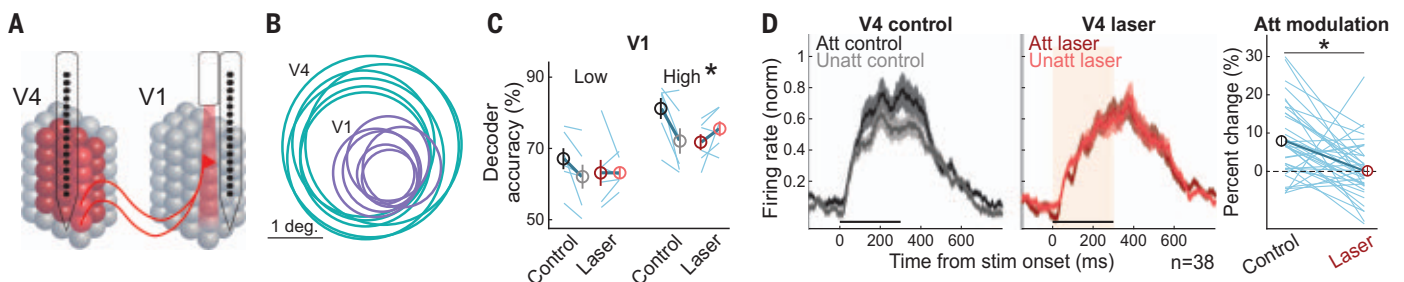
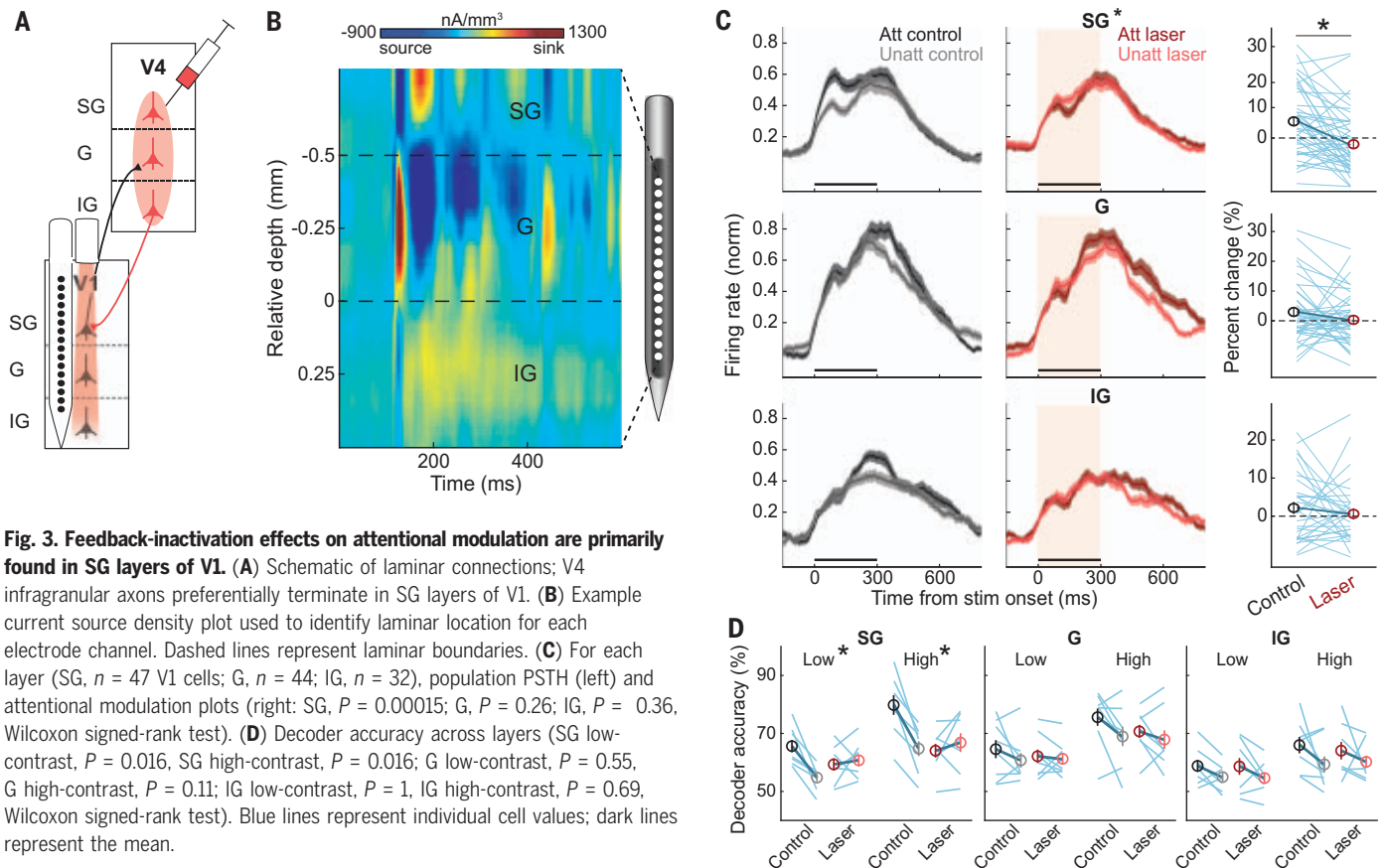


Fig. 4. Feedback-related attentional changes propagate to V4.

(A) Schematic for simultaneous V1-V4 recordings while suppressing V4 feedback terminals in V1. (B) Receptive field traces from V1 (purple) and V4 (green) cells for one example session. (C) Decoder accuracy for the V1 population (low-contrast, $P = 0.044$; high-contrast, $P = 0.031$, Wilcoxon signed-rank test). (D) Left: V4 responses to the high-contrast stimulus (50% contrast) flashed in cells' receptive field without laser stimulation. Population PSTH ($n = 38$ cells) while animals attended the stimulus ("Att control," black) compared to when animals attended to the opposite side of the screen ("Unatt control," gray). In all plots, envelope represents SEM; black horizontal line represents stimulus duration. Middle: Same as left panel, but during laser stimulation. Population PSTH while animals attended the stimulus ("Att laser," maroon) compared to when animals attended to the opposite side of the screen ("Unatt laser," pink). In all plots, the shaded window represents laser stimulation. Right: Changes in V4 attentional modulation with and without feedback suppression as percent change of effects in control conditions (black) compared to laser conditions (red, $P = 0.00033$, Wilcoxon signed-rank test). Blue lines represent values from individual cells; dark line represents the mean.

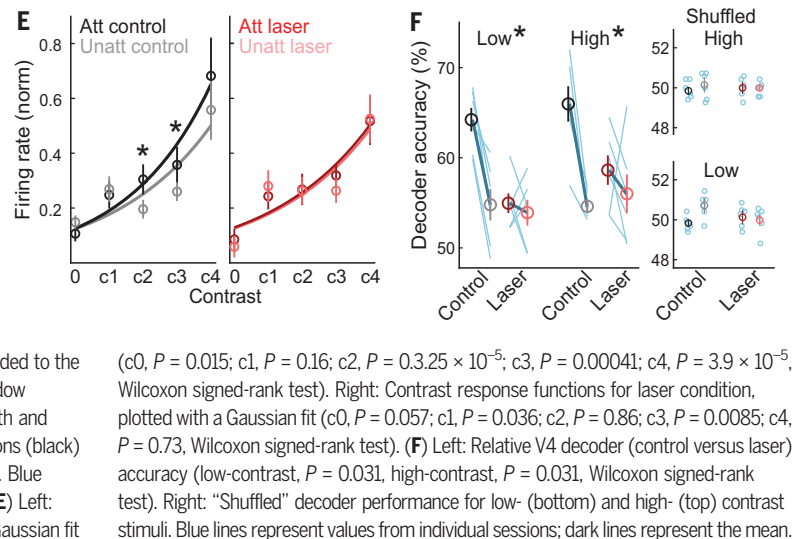
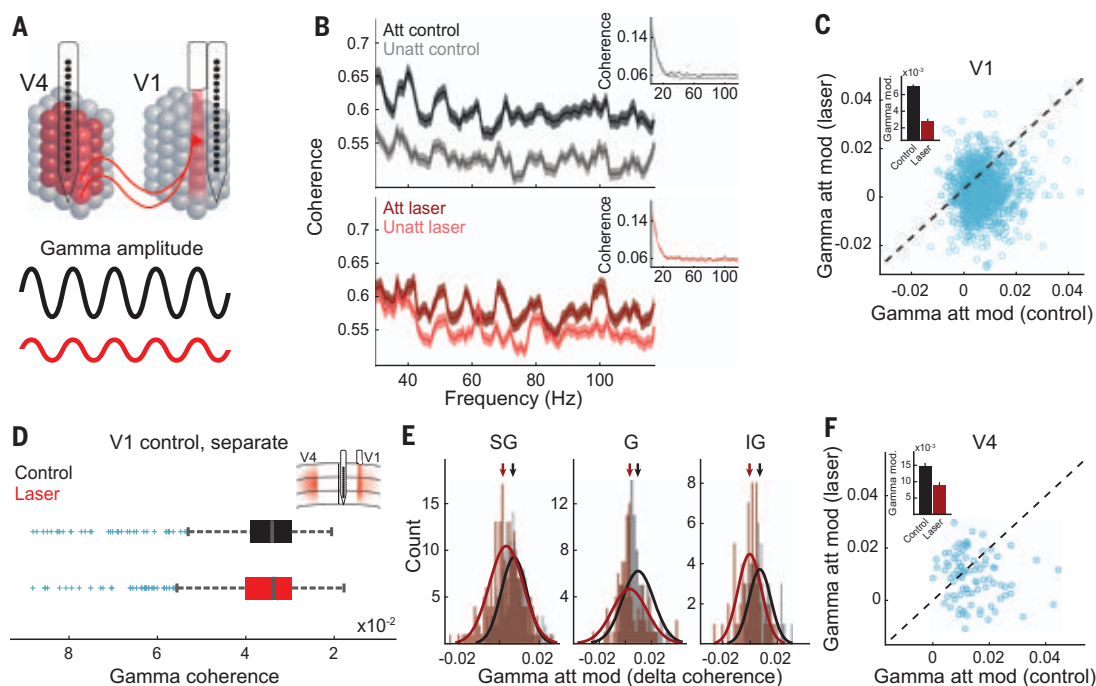


Fig. 5. Feedback-mediated attentional signals modulate gamma-coherence. (A) Top: Schematic of recording design. Bottom: Hypothesized changes in gamma amplitude across conditions, showing reduced gamma coherence during the laser condition. (B) Spike-spike gamma coherence. Insets show coherence across a wide frequency range. Top: Control conditions. Bottom: Laser conditions. For all plots, error bars reflect SEM. (C) Changes in V1 gamma modulation with and without feedback as attentional modulation in control versus laser conditions ($n = 1,315$ pairs, $P < 10^{-10}$, Wilcoxon signed-rank test). Each blue point represents one cell. Inset shows averages for control (black) and laser (red) conditions. (D) Box and whisker plot of gamma-coherence values during fixation (without attentional manipulation) for control (black) and laser (red) conditions while recording electrode and optic fiber were separated by >2 mm ($P = 0.95$, Wilcoxon signed-rank test). (E) Histograms show attentional modulation (relative difference between attended and unattended) of gamma coherence as a function of laser stimulation across the V1 laminae (SG: $n = 194$ pairs, G: $n = 91$, IG: $n = 66$), plotted with normal fits (SG: $P = 4.21 \times 10^{-7}$; G: $P = 1.20 \times 10^{-5}$; IG: $P = 2.01 \times 10^{-5}$, Wilcoxon



signed-rank test). Arrows represent the mean gamma modulation (attended versus unattended) for control and laser conditions. (F) Changes in V4 gamma modulation with and without feedback, computed as attentional modulation in control versus laser conditions ($n = 90$ pairs, $P = 0.00082$, Wilcoxon signed-rank test). Each blue point represents one cell. Inset shows average attentional modulation (relative difference between attended and unattended) for control (black) and laser (red) conditions.

low-contrast, $P = 1$, IG decoder high-contrast, $P = 0.69$). The supragranular layers were significantly more influenced by feedback suppression than the granular or infragranular layers (degree of attentional modulation in control versus laser: low-contrast, $P = 0.03$; high-contrast, $P = 0.0071$, Kruskal-Wallis test, post hoc Fisher's least significant difference test). Thus, cortical feedback-inactivation effects are not generalizable to the entire cortical column.

The effects seen in SG layers were not simply due to laser position. Light scatters and becomes absorbed by the neural tissue. The red light used to activate our Jaws construct is significantly less prone to these issues than are blue- or green-light anion channelrhodopsin alternatives (19, 28, 29). We positioned the laser to directly target granular layers, but this procedure did not elicit laser-mediated firing rate changes (fig. S16). Cortical feedback thus impacts attentional modulation in V1, primarily in the supragranular layers.

Feedback-related changes in attentional modulation propagate to V4

We further tested whether optogenetically altering V4→V1 cortical feedback induces effects that propagate downstream. We recorded the electrical activity of 38 V4 cells (six sessions in

two animals, Fig. 4A) by positioning the laminar electrode to target sites localized at least 800 μm below cortical surface to maximize the likelihood of reaching the middle layers, (i.e., the recipients of feedforward inputs from early visual cortex). Simultaneously, we recorded and optically stimulated the feedback axonal terminals in V1. Cells in V1 and V4 had overlapping receptive fields and were modulated by visual stimuli (Fig. 4B). We first confirmed that in the absence of feedback suppression, attention led to a significant increase in V1 firing rates (c4 contrast control, attended versus unattended, $P = 2.74 \times 10^{-13}$), and suppressing cortical feedback rendered attended- and unattended-trial firing rates indistinguishable from one another (c4 contrast laser, attended versus unattended, $P = 0.79$). Comparing the effect of attention as a function of laser stimulation, we found a significant change in both firing rates and decoder accuracy (attentional modulation at c4 contrast in control versus laser: firing rate, $P = 9.6 \times 10^{-11}$; decoder low-contrast, $P = 0.044$, decoder high-contrast, $P = 0.031$, Wilcoxon signed-rank test).

We further examined whether the feedback-inactivation effects observed in V1 are transmitted to V4. In control, attention increased the mean response of V4 neurons by 9.9% (± 7.49) at the highest contrast (Fig. 4D, left).

Overall, the attentional modulation of V4 firing rates was significant for three out of four contrasts displayed during the task (c1, $P = 0.72$; c2, $P = 0.00027$; c3, $P = 0.049$; c4, $P = 0.00033$), confirming the expectation that the effects of attention are more prominent in V4 compared to V1 (where firing rates were only significantly different for the high-contrast stimulus). Suppressing cortical feedback to V1 reduced the attentional gain response in V4 [c4 contrast: Fig. 4, D (middle) and E]. The relative differences between these conditions (control versus laser) indicate that the attention-induced increase in neural responses critically relies on feedback signals [firing rate: $P = 0.00033$ (Fig. 4D, right); decoder low-contrast: $P = 0.031$, high-contrast: $P = 0.031$ (Fig. 4F and fig. S17)]. This result is surprising, as downstream prefrontal areas also send feedback inputs to the superficial layers of V4 that are believed to carry attentional signals. However, our electrode penetrations have likely oversampled the granular layers to possibly explain the light-induced reduction in attentional modulation in V4.

Feedback-mediated attentional signals modulate gamma coherence

Because attention has been commonly associated with increased gamma activity in visual cortex (30–33), we investigated whether the

selective suppression of V4→V1 feedback terminals influences gamma spike–spike coherence in V1 (18, 34, 35) (Fig. 5A). In the absence of light, attention was associated with increased gamma coherence (attended versus unattended, 6.3%, $P < 10^{-10}$), both in the low- (30 to 80 Hz, $P < 10^{-10}$) and high-gamma frequency bands (80 to 120 Hz, $P = 2.16 \times 10^{-80}$). However, when cortical feedback was optogenetically suppressed (Fig. 5B, bottom), the attention-mediated changes were much reduced, leading to a 2.5-fold decrease in gamma coherence [control versus laser, $P = 1.01 \times 10^{-35}$, Wilcoxon signed-rank test (Fig. 5C); this effect was consistent across animals (fig. S18), and the attentional modulation of spike coherence in nearby frequency bands was not significantly influenced by feedback inactivation (beta, $P = 0.074$; alpha, $P = 0.97$, Wilcoxon signed-rank test)]. This effect was indeed driven by feedback signals, as separating the recording probe and optic fiber by several millimeters during a fixation task did not elicit significant changes in gamma coherence between the attended and unattended conditions ($P = 0.95$) (Wilcoxon signed-rank test, Fig. 5D).

We next investigated whether the attention-induced changes in gamma coherence are layer specific. The relative change in gamma coherence between control and laser conditions (attended versus unattended) was significantly modulated in all layers (SG: $P = 4.21 \times 10^{-7}$; G: $P = 1.20 \times 10^{-5}$; IG: $P = 2.01 \times 10^{-5}$) (Fig. 5E) despite the fact that the effects on neuronal responses and network performance are layer-dependent. Finally, we computed spike–spike coherence between pairs of V4 cells, as V4 responses were strongly influenced by cortical feedback suppression (Fig. 3). Suppressing cortical feedback to V1 significantly reduced attentional modulation (attended versus unattended) of gamma coherence across pairs of V4 cells ($P = 0.00082$, Fig. 5F).

Discussion

For the past several decades, neuroscientists have widely assumed that cortical feedback mediates attentional modulation in brain circuits. Because this hypothesis is intuitive, it has long dominated research in the field despite lack of direct support. Previous studies have either demonstrated attention-related interactions between cortical areas without establishing causality (5, 36–39) or used causal manipulations to perturb cortical feedback without measuring attentional signals (1, 3, 8, 9, 40). Furthermore, previous studies have largely ignored laminar-specific changes, although it is well accepted that feedback connections are layer-specific, and hence their effects on neuronal responses may vary across the targeted cortical column.

Our findings provide causal evidence of attentional modulation in individual neurons

and cell populations induced by cortical feedback projections. Optogenetically suppressing V4 feedback axons to V1, without inherently altering local and feedforward intracortical inputs, significantly diminished the attention-induced benefits on response gain and accuracy of network computations, abolished attentional modulation of postsynaptic V4 neuron responses, and greatly reduced gamma coherence when attention was deployed. Our results further indicate that feedback signals modulate visual cortical responses only when stimuli are attended.

It has been hypothesized that the pulvinar may constitute one source of attentional modulation of neuronal responses in early cortex (41, 42). Specifically, the pulvinar may synchronize neuronal responses across cortical areas by attention allocation and hence regulate information transmission. However, although our results do not challenge this view, they raise the possibility that cortical feedback and the pulvinar could work together to fulfill optimal attentional requirements during visual perception. Further research is needed to tease apart attentional influences due to pulvinar and cortical feedback sources.

Our findings may have general implications applicable to the entire cortex, because they suggest that cortical feedback connections carry attentional signals via laminar-specific mechanisms. Thus, our results could set the stage for further investigations probing large-scale feedback circuits across species to study the effects of attention at multiple stages of thalamic and cortical processing. Because feedback has been hypothesized to control other top-down processes, such as expectation and behavioral context, our results could have widespread implications for a broad range of phenomenology across many modalities.

REFERENCES AND NOTES

1. J. M. Hupé et al., *Nature* **394**, 784–787 (1998).
2. T. Moore, K. M. Armstrong, *Nature* **421**, 370–373 (2003).
3. J. J. Nassi, S. G. Lomber, R. T. Born, *J. Neurosci.* **33**, 8504–8517 (2013).
4. L. B. Ekstrom, P. R. Roelfsema, J. T. Arsenault, G. Bonmassar, W. Vanduffel, *Science* **321**, 414–417 (2008).
5. B. Dagnino, M.-A. Gariel-Mathis, P. R. Roelfsema, *J. Neurophysiol.* **113**, 730–739 (2015).
6. A. F. Rossi, N. P. Bichot, R. Desimone, L. G. Ungerleider, *J. Neurosci.* **27**, 11306–11314 (2007).
7. B. Noudoost, K. L. Clark, T. Moore, *J. Neurosci.* **34**, 3687–3698 (2014).
8. J.-M. Hupé, A. C. James, P. Girard, J. Bullier, *J. Neurophysiol.* **85**, 146–163 (2001).
9. J. H. Sandell, P. H. Schiller, *J. Neurophysiol.* **48**, 38–48 (1982).
10. T. van Kerkoerle et al., *Proc. Natl. Acad. Sci. U.S.A.* **111**, 14332–14341 (2014).
11. P. C. Klink, B. Dagnino, M. A. Gariel-Mathis, P. R. Roelfsema, *Neuron* **95**, 209–220.e3 (2017).
12. L. G. Ungerleider, T. W. Galkin, R. Desimone, R. Gattass, *Cereb. Cortex* **18**, 477–499 (2008).
13. D. J. Felleman, D. C. Van Essen, *Cereb. Cortex* **1**, 1–47 (1991).
14. K. S. Rockland, K. S. Saleem, K. Tanaka, *Vis. Neurosci.* **11**, 579–600 (1994).
15. J. Bullier, H. Kennedy, W. Salinger, *J. Comp. Neurol.* **228**, 329–341 (1984).

16. G. H. Henry, P. A. Salin, J. Bullier, *Eur. J. Neurosci.* **3**, 186–200 (1991).
17. E. A. Buffalo, P. Fries, R. Landman, H. Liang, R. Desimone, *Proc. Natl. Acad. Sci. U.S.A.* **107**, 361–365 (2010).
18. J. F. Mitchell, K. A. Sundberg, J. H. Reynolds, *Neuron* **63**, 879–888 (2009).
19. A. S. Chuong et al., *Nat. Neurosci.* **17**, 1123–1129 (2014).
20. L. Acker, E. N. Pino, E. S. Boyden, R. Desimone, *Proc. Natl. Acad. Sci. U.S.A.* **113**, E7297–E7306 (2016).
21. X. Han et al., *Neuron* **62**, 191–198 (2009).
22. C. D. Gilbert, W. Li, *Nat. Rev. Neurosci.* **14**, 350–363 (2013).
23. B. C. Motter, *J. Neurophysiol.* **70**, 909–919 (1993).
24. J. H. Reynolds, L. Chelazzi, *Annu. Rev. Neurosci.* **27**, 611–647 (2004).
25. Y. Chen et al., *Nat. Neurosci.* **11**, 974–982 (2008).
26. C. E. Schroeder, A. D. Mehta, S. J. Givre, *Cereb. Cortex* **8**, 575–592 (1998).
27. K. H. Pettersen, A. Devor, I. Ulbert, A. M. Dale, G. T. Einevoll, *J. Neurosci. Methods* **154**, 116–133 (2006).
28. O. Yizhar, L. E. Fenna, T. J. Davidson, M. Mogri, K. Deisseroth, *Neuron* **71**, 9–34 (2011).
29. T. Vo-Dinh, Ed., *Biomedical Photonics Handbook* (CRC Press, ed. 2, 2003).
30. P. Fries, J. H. Reynolds, A. E. Rorie, R. Desimone, *Science* **291**, 1560–1563 (2001).
31. P. Fries, T. Womelsdorf, R. Oostenveld, R. Desimone, *J. Neurosci.* **28**, 4823–4835 (2008).
32. T. Womelsdorf, P. Fries, P. P. Mitra, R. Desimone, *Nature* **439**, 733–736 (2006).
33. N. P. Bichot, A. F. Rossi, R. Desimone, *Science* **308**, 529–534 (2005).
34. J. L. Herrero, M. A. Gieselmann, M. Sanayei, A. Thiele, *Neuron* **78**, 729–739 (2013).
35. S. Ray, J. H. R. Maunsell, *Neuron* **67**, 885–896 (2010).
36. D. Ferro, J. van Kempen, M. Boyd, S. Panzeri, A. Thiele, *Proc. Natl. Acad. Sci. U.S.A.* **118**, e2022097118 (2021).
37. J. D. Semedo et al., *Nat. Commun.* **13**, 1099 (2022).
38. J. Moran, R. Desimone, *Science* **229**, 782–784 (1985).
39. A. Speed, J. Del Rosario, N. Mikail, B. Haider, *Nat. Commun.* **11**, 505 (2020).
40. L. Nurminen, S. Meril, M. Bijanzadeh, F. Federer, A. Angelucci, *Nat. Commun.* **9**, 2281 (2018).
41. Y. B. Saalmann, M. A. Pinsk, L. Wang, X. Li, S. Kastner, *Science* **337**, 753–756 (2012).
42. I. C. Fiebelkorn, S. Kastner, *Annu. Rev. Psychol.* **71**, 221–249 (2020).

ACKNOWLEDGMENTS

We thank A. Andrei for technical assistance, A. Asadollahi for help with control experiments, R. Janz for help with virus handling and expression, S. Pojoga for help with the design of the behavioral task, and A. Parajuli for discussions on control analyses. **Funding:** National Eye Institute grant 1F31EY030735-01 (S.R.D.), NIH BRAIN Initiative grant 1R34NS116829 (V.D.). **Author contributions:** Conceptualization: S.R.D., V.D. Methodology: S.R.D., V.D. Investigation: S.R.D., V.D. Visualization: S.R.D., V.D. Funding acquisition: S.R.D., V.D. Project administration: S.R.D., V.D. Supervision: V.D. Writing – original draft: S.R.D., V.D. Writing – review and editing: S.R.D., V.D. **Competing interests:** The authors declare no competing financial interests. Correspondence and requests for materials should be addressed to V.D. (valentin.dragoi@uth.tmc.edu). **Data and materials availability:** All data supporting the findings from this study are openly available at <https://zenodo.org/record/7297037/files/Y2g5uHbMKUk>. **License information:** Copyright © 2023 the authors, some rights reserved; exclusive licensee American Association for the Advancement of Science. No claim to original US government works. <https://www.science.org/about/science-licenses-journal-article-reuse>

SUPPLEMENTARY MATERIALS

science.org/doi/10.1126/science.adel1855
Materials and Methods
Supplementary Text
Figs. S1 to S18
References (43–46)
MDAR Reproducibility Checklist

Submitted 29 July 2022; accepted 23 December 2022
10.1126/science.adel1855

ICE STRUCTURE

Medium-density amorphous ice

Alexander Rosu-Finsen¹, Michael B. Davies^{2,3}, Alfred Amon¹, Han Wu,⁴ Andrea Sella¹, Angelos Michaelides^{2,3*}, Christoph G. Salzmann^{1*}

Amorphous ices govern a range of cosmological processes and are potentially key materials for explaining the anomalies of liquid water. A substantial density gap between low-density and high-density amorphous ice with liquid water in the middle is a cornerstone of our current understanding of water. However, we show that ball milling “ordinary” ice *Ih* at low temperature gives a structurally distinct medium-density amorphous ice (MDA) within this density gap. These results raise the possibility that MDA is the true glassy state of liquid water or alternatively a heavily sheared crystalline state. Notably, the compression of MDA at low temperature leads to a sharp increase of its recrystallization enthalpy, highlighting that H₂O can be a high-energy geophysical material.

Water has a complex phase diagram with 20 crystalline phases and at least two families of amorphous forms (1–7). Although three new crystalline phases have been discovered in the past 5 years alone (2–6), the discovery of amorphous states is much less common. The current complement of amorphous forms comprises low-density amorphous ice (LDA), first made through vapor deposition in the 1930s (8). By compression of ice *Ih* or LDA at low temperatures, high-density amorphous ice (HDA) was made in the 1980s (9, 10). Heating HDA under pressure gives either expanded high-density (eHDA) or very high-density amorphous ice (vHDA), as reported in the early years of this century (11, 12). As their names suggest, amorphous ices are distinguished principally by their densities, with LDA having a density of 0.94 g cm^{−3} and the HDAs starting from 1.13 g cm^{−3} at ambient pressure and 77 K (7). This leaves a conspicuous gap in densities around the density of liquid water (1 g cm^{−3}) which is not filled by any known crystalline phases, and it is unclear whether homogeneous amorphous ice can display a density in this gap (13–15). This gap, and the question of whether the amorphous ices have corresponding liquid states below a liquid-liquid critical point, is a topic of great interest with respect to explaining water’s many anomalies (16–26). Moreover, the fact that amorphous ice is the most common form of ice in the Universe (27) underpins the need to understand the structurally disordered states of H₂O.

In addition to previously reported techniques for making amorphous ices, ball milling is an established technique for making amorphous materials in general (28). This method is widely used for metallic alloys, inorganic

compounds, and pharmaceuticals (28–30) but has not been applied to ice. At the heart of the amorphization processes are ball-crystal-ball impact events that exert a combination of compressive and shear forces on the crystalline starting materials (Fig. 1A). Although local melting effects have been discussed as the origin of amorphization the introduction of dislocation defects seems to be the main driving force (31). In general, amorphization through ball milling is most effective at low temperatures (32).

We show that low-temperature ball milling of ice *Ih* leads to an amorphous ice with a density in the gap between LDA and HDA. We cooled a grinding jar to 77 K with liquid nitrogen, filled it with ice and stainless-steel balls, and firmly closed it (Fig. 1B). To achieve amorphization, the entire assembly was shaken vigorously for a range of ball-milling cycles at 77 K (33).

We see the formation of amorphous ice after 80 ball-milling cycles from the broad x-ray diffraction features with peak maxima at 1.93 and 3.04 Å^{−1} (Fig. 1C). The shift of the first strong diffraction peak (FSDP) at 1.93 Å^{−1} away from the most intense Bragg peaks of ice *Ih* signifies major structural changes. For comparison, cryogenic ball milling of the isostructural NH₄F *Ih* results in broadening—without shifting—of the Bragg peaks indicating only a reduction of the crystallite sizes (fig. S1). Ball milling the ice II, IX, and V high-pressure phases does also not yield any amorphous materials (fig. S2), suggesting that the low-density ice *Ih* crystal structure is particularly susceptible to amorphization. Similar observations of ice *Ih* occur in the context of pressure-induced amorphization to HDA (9).

A comparison with the diffraction patterns of other amorphous ices highlights that the amorphous ice obtained through ball milling is structurally unique (fig. S3). The closest match in terms of peak positions is HDA. Yet, in contrast to HDA (10), the ball-milled amorphous ice does not transform to LDA upon heating at ambient pressure (Fig. 1C). Instead, the diffraction patterns collected upon heating show

recrystallization to stacking disordered ice I (ice *Isd*) above ~140 K which later transforms to the stable ice *Ih*. We performed a quantitative analysis of the cubic/hexagonal stacking disorder of the ice *Isd* using the MCDIFFaX software (34) (fig. S4). The ice *Isd* obtained by heating the ball-milled ice contains 31% cubic stacking. The fact that the amorphous ice does not recrystallize to the fully hexagonal ice *Ih* starting material highlights substantial structural changes upon amorphization.

We monitored the progress of the ball milling quantitatively with differential scanning calorimetry (DSC) (Fig. 1D). The recrystallization of the amorphous ice manifests itself as an exothermic phase transition at ~150 K which increases in area with increasing milling cycles. We obtained an enthalpy of -1.16 ± 0.09 kJ mol^{−1} (SD, *N* = 3) after 40 milling cycles. Further increase to 80 milling cycles gives a heat release of -1.21 ± 0.15 kJ mol^{−1} (SD, *N* = 3) indicating that the amorphization process is close to completion after 40 milling cycles. The areas of the exotherms are independent of the diameters of the stainless-steel balls in the 10- to 20-mm range (fig. S5), illustrating that the amorphization process takes place robustly within a range of different ball-milling conditions. Stainless-steel balls give the best results in terms of amorphization compared with Teflon-coated or hardened-steel balls (fig. S6).

The progressive amorphization upon ball milling was also followed quantitatively by fully crystallizing the amorphous samples through heating and analyzing the changes in the intensities of the ice *Ih* Bragg peaks (fig. S7). Consistent with the increases in the areas of the exotherms (Fig. 1D), the amorphous content from the x-ray diffraction analysis increases steadily up to 40 milling cycles and then levels off at ~70% (Fig. 1E).

Analysis of the half-widths of the ice *Ih* Bragg peaks reveals no systematic change in particle size of the ice *Ih* contaminant as its amount decreases during ball milling (fig. S8). Consistent with an amorphous material, optical microscopy of the ball-milled sample after 80 milling cycles primarily shows a disordered, opaque material (Fig. 1F). A minor fraction of transparent particles with sharp edges—and hence likely crystalline ice *Ih*—were also observed (Fig. 1F, arrows). The overall appearance of the ball-milled ice is that of large chunks consisting of a densely compacted powder. Inevitably, as more amorphous ice forms, a small fraction of the ice *Ih* crystals will become increasingly shielded from the effects of ball milling. A small contribution from vapor condensation toward the ice *Ih* content during the x-ray diffraction analysis cannot be excluded. The possibility that the incomplete amorphization is due to recrystallization caused by local heating effects during ball

¹Department of Chemistry, University College London, London WC1H 0AJ, UK. ²Department of Physics and Astronomy, University College London, London WC1E 6BT, UK. ³Yusuf Hamied Department of Chemistry, University of Cambridge, Cambridge CB2 1EW, UK. ⁴Department of Chemical Engineering, University College London, London WC1E 7JE, UK.

*Corresponding author. Email: c.salzmann@ucl.ac.uk (C.G.S.); am452@cam.ac.uk (A.M.)

milling seems unlikely as the crystalline contaminant is ice *Ih* and not ice *Isd* to which the amorphous material recrystallizes upon heating (fig. S4).

We collected Raman spectra of a ball-milled sample in the spectral range of the O-H stretching modes (Fig. 1G). Whereas the x-ray diffraction data was closest to HDA, the Raman spectrum of the ball-milled ice was closer to LDA than to HDA. Consistent with the earlier x-ray diffraction analysis, we show that a maximal contribution of ~30% ice *Ih* can be subtracted from the spectrum before the baseline below 3000 cm^{-1} begins to display an unphysical negative slope (fig. S9). The main effect of the subtraction is a decrease in relative intensity of the most intense peak, which shifts slightly by 4 cm^{-1} to 3100 cm^{-1} .

We determined the bulk densities of ball-milled samples using buoyancy measurements in liquid nitrogen. The samples become denser as the amorphization progresses closely following the trend of the amorphous content (Fig. 1E). After 80 milling cycles, the ball-milled ice has a density of $1.02 \pm 0.03 \text{ g cm}^{-3}$ (SD, $N = 3$) at 77 K. Because the sample is $69 \pm 5\%$ (SD, $N = 3$) amorphous, it follows that the amorphous fraction has a density of $1.06 \pm 0.06 \text{ g cm}^{-3}$ (SD, $N = 3$). This density falls into the gap between LDA (0.94 g cm^{-3}) and HDA (1.15 g cm^{-3}) (10, 12). We therefore name the amorphous ice obtained from ball milling medium-density amorphous ice (MDA).

A continuous shift of the FSDP to lower Q values was previously observed during the HDA to LDA transition upon heating at ambient pressure (13, 35). By contrast, the transitions of eHDA and vHDA to LDA appear to be sharper (14, 35, 36). The question arises whether MDA is equivalent to an HDA→LDA transition state. A major argument against this is that the transition states all transform to LDA upon heating whereas MDA transforms to ice *Isd* at higher temperatures (~20 K). The transition state at 114 K in the x-ray diffraction data (36) shows the best fit with MDA in terms of the peak position of the FSDP (fig. S10). However, the FSDP of the transition state is broader compared with MDA and displays asymmetry. Overall, on the basis of different phase transitions, thermal stability, and diffraction characteristics, MDA is a different material compared with the HDA→LDA transition states.

Using small-angle scattering experiments, HDA itself as well as the HDA→LDA transition states have been suggested to be structurally inhomogeneous and contain nanoclusters of different densities (15). Our two-dimensional small-angle x-ray scattering (SAXS) data in fig. S11 shows that MDA displays isotropic scattering, which is an important prerequisite for testing its structural homogeneity. The radially integrated SAXS data recorded upon heating MDA

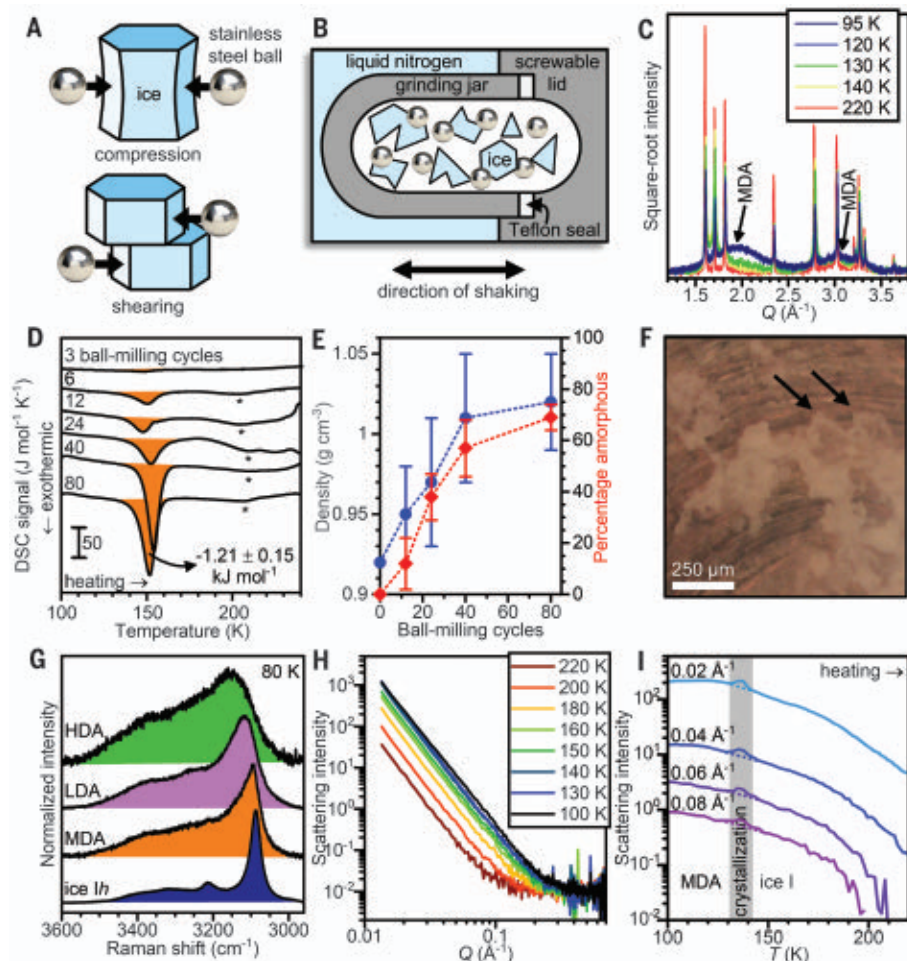


Fig. 1. Preparation and physical properties of MDA. (A) Illustration of the ball-crystal-ball impact events upon ball milling. (B) Schematic of the low-temperature ball-milling setup. (C) X-ray diffraction patterns (square-root intensities) upon heating MDA after 80 ball-milling cycles. (D) Differential scanning calorimetry of ice ball milled for increasing numbers of ball-milling cycles. Asterisks mark weak exotherms from the ice *Isd* to ice *Ih* phase transitions. (E) Density (blue circles) and amorphous content (red diamonds) at 77 K as a function of the ball-milling cycles. Data are mean \pm standard deviation and $N \geq 3$. (F) Optical microscopy image of MDA powder pressed against a copper substrate. Arrows indicate transparent crystalline ice *Ih* impurities. Circular features are part of the substrate. (G) Comparison of the Raman spectra of HDA, LDA, MDA, and ice *Ih* at 80 K in the O-H stretching spectral region. (H) Small angle x-ray scattering data of MDA upon heating from 100 to 220 K. (I) Scattering intensities at constant Q values as a function of temperature. Dashed lines illustrate continuous intensity changes across crystallization.

is shown in a double-logarithmic plot (Fig. 1H). Following a linear negative decrease, consistent with Porod's law (fig. S12), a flat region is observed above $\sim 0.3 \text{ \AA}^{-1}$ for MDA at 100 K. For the vapor-deposited version of LDA, a similar crossover was observed at $\sim 0.5 \text{ \AA}^{-1}$ (37). Upon heating, the crossover between the two different scattering regimes shifts toward lower Q values. The SAXS intensities at constant Q upon heating (Fig. 1I) show small peaks during the MDA to ice *I* phase transition, which we attribute to the additional scattering contrast as two phases with different densities coexist. The important point is that the scattering intensities change continuously across crystallization

implying that the structural origin of the scattering is the same before and after crystallization. After crystallization, the crystalline material is structurally homogeneous implying that the low- Q scattering arises solely from surface effects. On the basis of the continuous crossover from MDA to ice *I*, MDA is therefore also structurally homogeneous as far as its bulk structure is concerned. Furthermore, the scattering intensity levels in the flat scattering regime, which was used as a criterion for structural homogeneity by Koza and co-workers for HDA (15), are the same within error for MDA and ice *I*. Overall, the decreases in the low-angle scattering intensities upon heating MDA

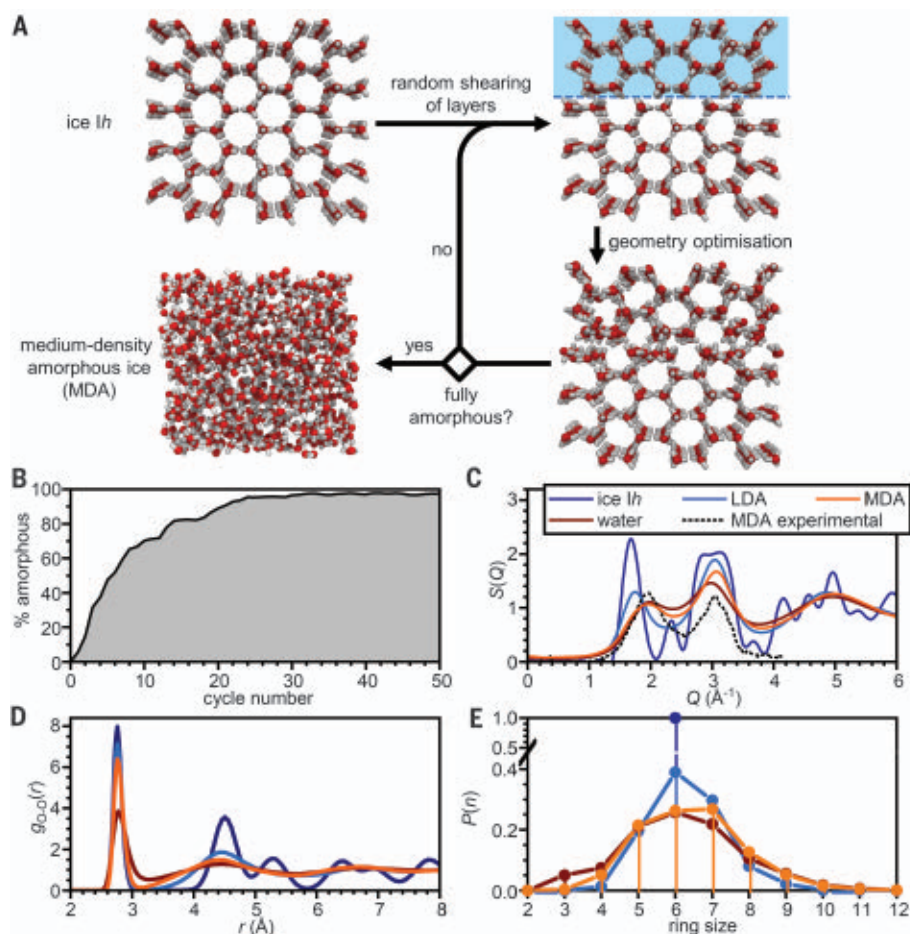


Fig. 2. Computational investigation into the mechanism of formation of MDA. (A) Schematic of the computational protocol that yields MDA upon repeated shearing and geometry-optimization steps. (B) Percentage amorphous with increasing computational cycles using the local structural analysis shown in fig. S18. (C) Experimental and computational x-ray structure factors of MDA, water, LDA, and ice Ih. (D) Corresponding oxygen-oxygen pair distribution functions and (E) primitive ring-size distributions. All simulations were carried out using periodic boxes with approximate dimensions of 4.5 nm in *x*, *y*, and *z*.

and ice I are a result of continuous reductions in surface area of otherwise homogeneous materials. Structural heterogeneity is only observed during the MDA→ice I phase transition where two phases of different density coexist within a small temperature window.

We investigated the structural mechanism of the amorphization process through ball milling computationally (33). The computational protocol started with a periodically repeated ice Ih simulation box containing 2880 water molecules. This box was then subjected to random shearing of layers followed by geometry optimization of the local molecular environments (Fig. 2A and fig. S13). These steps were repeated until the calculated structure factors and other structural characteristics converged (figs. S14 and S15). The simulations show the evolution of an amorphous fraction (Fig. 2B). We verified the robustness of the computational approach in terms of both path dependence and system size (figs. S16 and S17).

During the computational amorphization process, we found a density increase from 0.92 to 0.97 g cm⁻³ (fig. S19), in line with our experimental observations. The somewhat lower density of the computational MDA compared with the experimental value is attributed to the rigid water molecules in the TIP4P/Ice computer model (38), which underestimates the bending of hydrogen bonds in dense structures. Good agreement exists between the calculated and experimental diffraction patterns of MDA in terms of the peak positions of the diffraction features (Fig. 2C). This illustrates that dislocation processes are essential for achieving the amorphization of ice Ih to the denser MDA. The higher relative peak intensity of the FSDP in the experimental *S(Q)* with respect to the second peak at ~3 Å⁻¹ indicates somewhat more pronounced intermediate-range structural order within the experimental sample compared with the computational structure. The computational recipe for making

MDA involves shearing along random directions resulting in a maximally disordered amorphous structure. However, the experimental situation may be slightly different because shearing is likely to proceed at least initially along the characteristic cleavage planes of the crystal leading to a somewhat more ordered amorphous structure. The computational amorphization process goes along with a partial collapse of the second coordination shell of the water molecules (Fig. 2D). This means that water molecules that are not directly hydrogen bonded move toward the first coordination shell which is a well-known structural mechanism for achieving higher densities in ice (1, 39).

Notably, the computational structure of MDA is closer to liquid water than to LDA. This observation can be seen from the positions of the FSDPs, which are indicators for the intermediate-range structure (Fig. 2C). The FSDPs of MDA and liquid water are found at similar positions whereas the FSDP of LDA is close to ice Ih. A comparison of the experimental positions of the FSDPs of water and the various amorphous ices as a function of temperature including a possible extrapolation from MDA to water is shown in fig. S20. From the oxygen-oxygen pair-distribution functions (Fig. 2D), we observed a progressive collapse of the second coordination shell upon going from ice Ih to LDA, to MDA, and to liquid water. The same progression can also be seen in the statistics of the primitive ring sizes (Fig. 2E).

The experimental identification of MDA shows that the polymorphism of H₂O—the existence of multiple distinct amorphous states—is more complex than previously appreciated. A key question is whether MDA should be regarded as a glassy state of liquid water. The glassy natures of LDA and HDA are still debated and a range of different scenarios is possible with the discovery of MDA. One notable possibility is that MDA represents the glass of liquid water, which would be supported by the similar densities and diffraction characteristics (40). This would not necessarily violate the well-known liquid-liquid critical point hypothesis (16, 17, 20, 24, 26), but MDA would need to have a glass transition temperature above the liquid-liquid critical point. Accordingly, MDA would represent liquid water before the phase separation into LDA and HDA takes place at temperatures below the liquid-liquid critical point. Consistent with this scenario, MDA does not show a glass transition below the recrystallization temperature at ~150 K despite extensive annealing at a range of different temperatures (fig. S21). Accordingly, MDA would be metastable with respect to either LDA or HDA at low temperatures and at all pressures.

Alternatively, a pressure range might exist at low temperatures within which MDA is more stable than LDA and HDA. However, as

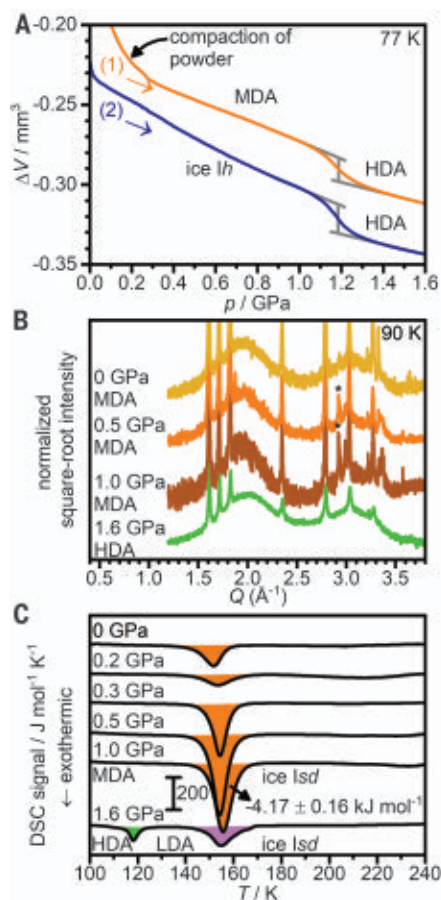


Fig. 3. Effect of pressure on MDA. (A) In situ volume changes upon compression of equal amounts of MDA and ice Ih to 1.6 GPa at 77 K. Gray lines indicate the stepwise volume changes during the transition to HDA. (B) X-ray diffraction patterns at 90 K and ambient pressure after compression of MDA to the indicated pressures at 77 K. (C) DSC scans upon heating at 10 K min⁻¹ at ambient pressure after compression of MDA at 77 K. The x-ray diffraction patterns and DSC scans after compression to 1.6 GPa correspond to HDA.

a result of the generally slow kinetics at low temperatures the two scenarios are difficult to distinguish. Heating MDA at ambient pressure does not lead to the formation of LDA (Fig. 1C) and MDA remained stable upon heating to the p/T conditions of eHDA (fig. S22). The compression of MDA at 77 K, by contrast, shows a transition to HDA with a stepwise change in volume at an onset pressure of ~1.1 GPa (Fig. 3A). Consistent with the higher density of MDA compared with ice Ih, the stepwise change in volume is smaller compared with the corresponding transition of the same amount of ice Ih. The onset pressure of the MDA to HDA transition upon compression is at a higher pressure than the LDA to HDA transition at ~0.5 GPa (47).

A third scenario is that MDA is not a glassy liquid but rather a heavily sheared crystalline

state that lacks a connection with the liquid phase. Whatever the precise structural nature of MDA, we expect it to play a role in the geology of ice at low temperatures, for example, in the many ice moons of the Solar system and beyond. Tidal forces in the interiors of ice moons induced by the gravitational forces of gas giants may cause similar shear forces as those found in ball milling and could therefore facilitate the transition of ice Ih to MDA, provided these occur across a similar temperature and pressure range.

Finally, we show that MDA displays one notable property not found for any of the other amorphous or crystalline forms of ice. The x-ray diffraction patterns (Fig. 3B) show that the structure of MDA remains unchanged upon compression at 77 K up to 1.0 GPa. However, the area of the recrystallization exotherm upon heating at ambient pressure increases substantially from $-1.21 \pm 0.15 \text{ kJ mol}^{-1}$ (SD, $N = 3$) for the uncompressed material to $-4.02 \pm 0.14 \text{ kJ mol}^{-1}$ (SD, $N = 3$) after compression to 0.5 GPa (Fig. 3C). Compression to 1.0 GPa leads to a further small increase to $-4.17 \pm 0.16 \text{ kJ mol}^{-1}$ (SD, $N = 3$). This value is a substantial amount of heat that corresponds to ~70% of the heat released upon freezing liquid water to ice Ih. Because MDA is prepared through ball milling, the amorphous sample is expected to display a high surface area. Given that the x-ray diffraction data remains unchanged upon compression, the increase in the recrystallization enthalpy can be rationalized by the formation of pressure-induced strain at the grain boundaries as has been observed for ball-milled metals (42). Similar processes could potentially take place in the ice layers of moons as they are subjected to tidal forces. If this is the case, heat released from the recrystallization of MDA could play a role in activating tectonic motions.

The identification of MDA shows that H₂O is more complex at low temperatures than previously recognized. The possibility that MDA may represent the true glass of liquid water and its many anomalies. Even if it is not, any valid computer model of water should be able to explain the existence of MDA and its relationship with LDA and HDA. Regardless of the exact nature of MDA, this material has the potential to store mechanical energy from compression, which can be released upon warming at low pressure.

REFERENCES AND NOTES

1. C. G. Salzmann, *J. Chem. Phys.* **150**, 060901 (2019).
2. M. Millot et al., *Nature* **569**, 251–255 (2019).
3. R. Yamane et al., *Nat. Commun.* **12**, 1129 (2021).
4. C. G. Salzmann, J. S. Loveday, A. Rosu-Finsen, C. L. Bull, *Nat. Commun.* **12**, 3162 (2021).
5. T. M. Gasser, A. V. Thoeny, A. D. Fortes, T. Loerting, *Nat. Commun.* **12**, 1128 (2021).

6. V. B. Prakapenka, N. Holtgrewe, S. S. Lobanov, A. F. Goncharov, *Nat. Phys.* **17**, 1233–1238 (2021).
7. T. Loerting et al., *Phys. Chem. Chem. Phys.* **13**, 8783–8794 (2011).
8. E. F. Burton, W. F. Oliver, *Proc. R. Soc. Lond.* **153**, 166–172 (1935).
9. O. Mishima, L. D. Calvert, E. Whalley, *Nature* **310**, 393–395 (1984).
10. O. Mishima, L. D. Calvert, E. Whalley, *Nature* **314**, 76–78 (1985).
11. R. J. Nemes et al., *Nat. Phys.* **2**, 414–418 (2006).
12. T. Loerting, C. Salzmann, I. Kohl, E. Mayer, A. Hallbrucker, *Phys. Chem. Chem. Phys.* **3**, 5355–5357 (2001).
13. C. A. Tulk et al., *Science* **297**, 1320–1323 (2002).
14. O. Mishima, Y. Suzuki, *Nature* **419**, 599–603 (2002).
15. M. M. Kozá, R. P. May, H. Schöber, *J. Appl. Cryst.* **40**, s517–s521 (2007).
16. P. H. Poole, F. Sciortino, U. Essmann, H. E. Stanley, *Nature* **360**, 324–328 (1992).
17. O. Mishima, H. E. Stanley, *Nature* **392**, 164–168 (1998).
18. J. S. Tse et al., *Nature* **400**, 647–649 (1999).
19. H. Schöber et al., *Phys. Rev. Lett.* **85**, 4100–4103 (2000).
20. P. G. Debenedetti, *J. Phys. Condens. Matter* **15**, R1669–R1726 (2003).
21. B. Geil, M. M. Kozá, F. Fujara, H. Schöber, F. Natali, *Phys. Chem. Chem. Phys.* **6**, 677–679 (2004).
22. D. T. Limmer, D. Chandler, *Proc. Natl. Acad. Sci. U.S.A.* **111**, 9413–9418 (2014).
23. J. J. Shephard et al., *J. Phys. Chem. Lett.* **8**, 1645–1650 (2017).
24. P. G. Debenedetti, F. Sciortino, G. H. Zerze, *Science* **369**, 289–292 (2020).
25. C. A. Tulk, J. J. Molaison, A. R. Makhlof, C. E. Manning, D. D. Klug, *Nature* **569**, 542–545 (2019).
26. K. H. Kim et al., *Science* **370**, 978–982 (2020).
27. S. Kwok, *Physics and Chemistry of the Interstellar Medium*. (Univ. Science Books, 2007).
28. P. Baláz et al., *Chem. Soc. Rev.* **42**, 7571–7637 (2013).
29. A. W. Weeber, H. Bakker, *Physica B* **153**, 93–135 (1988).
30. M. Descamps, J. F. Willart, *Adv. Drug Deliv. Rev.* **100**, 51–66 (2016).
31. F. Delogu, G. Cocco, *J. Alloys Compd.* **465**, 540–546 (2008).
32. M. Descamps, J. F. Willart, E. Dudognon, V. Caron, *J. Pharm. Sci.* **96**, 1398–1407 (2007).
33. Materials and methods are available as supplementary materials.
34. T. L. Malkin et al., *Phys. Chem. Chem. Phys.* **17**, 60–76 (2015).
35. F. Perakis et al., *Proc. Natl. Acad. Sci. U.S.A.* **114**, 8193–8198 (2017).
36. D. Mariedahl et al., *Philos. Trans. R. Soc. A* **377**, 20180164 (2019).
37. C. Mitterdorfer et al., *Phys. Chem. Chem. Phys.* **16**, 16013–16020 (2014).
38. J. L. F. Abascal, E. Sanz, R. García Fernández, C. Vega, *J. Chem. Phys.* **122**, 234511 (2005).
39. J. L. Finney, A. Hallbrucker, I. Kohl, A. K. Soper, D. T. Bowron, *Phys. Rev. Lett.* **88**, 225503 (2002).
40. N. Esmailidoost et al., *J. Chem. Phys.* **155**, 214501 (2021).
41. O. Mishima, *J. Chem. Phys.* **100**, 5910–5912 (1994).
42. H. Gleiter, *Prog. Mater. Sci.* **33**, 223–315 (1989).
43. A. Rosu-Finsen et al., Experimental data for research article “Medium-density amorphous ice”, *Dryad* (2023); <https://doi.org/10.5061/dryad.7sqv9s4wk>.
44. M. B. Davies, A. Michaelides, Research Data Supporting “Medium Density Amorphous Ice”, *Apollo* (2023); <https://doi.org/10.17863/CAM.78718>.

ACKNOWLEDGMENTS

We thank M. Vickers for help with the x-ray diffraction measurements, J. K. Cockcroft for access to a Cryojet, Z. X. Guo for making a cryomill available, and G. Sosso, M. Fitzner, A. Goodwin, and P. F. McMillan for discussions. The authors also acknowledge the use of the UCL Kathleen High Performance Computing Facility (Kathleen@UCL) and associated support services as well as the EPSRC CNIE research facility service at University College London for SAXS data collection. **Funding:** This work was funded by the following: European Research Council (ERC) under the European Union's Horizon 2020 research innovation program grant 725271 (to A.R.F. and C.G.S.), Austrian Science Funds (FWF) grant J4325 (to A.A.), Materials Chemistry Consortium grant EP/L000202 (to M.B.D. and A.M.), UK Materials and Molecular Modelling Hub grants EP/P020194/1 and EP/T022231/1 (to M.B.D. and A.M.) Engineering and Physical Sciences Research Council (EPSRC) grant EP/S03305X/1 (to H.W.). **Author contributions:** Conceptualization: C.G.S. and A.S. Investigation: A.R.F., M.B.D., A.A., and H.W. Formal Analysis: A.R.F., C.G.S., M.B.D., and A.M. Funding acquisition: C.G.S. and A.M. Software: M.B.D. Visualization: A.R.F., C.G.S., and M.B.D. Writing – original draft: C.G.S. Writing – review and editing: A.R.F., M.B.D.

A.A., H.W., A.S., A.M., and C.G.S. **Competing interests:** Authors declare that they have no competing interests. **Data and materials availability:** All data needed to evaluate the conclusions in the paper are present in the paper and/or the Supplementary Materials. Experimental data are archived at Dryad (43). Computer code and computational data are available at (44). **License information:** Copyright © 2023 the authors, some rights reserved; exclusive

licensee American Association for the Advancement of Science. No claim to original US government works. <https://www.sciencemag.org/about/science-licenses-journal-article-reuse>

SUPPLEMENTARY MATERIALS

science.org/doi/10.1126/science.abq2105
Materials and Methods

Figs. S1 to S22
Movies S1 and S2
References (45–63)

Submitted 7 April 2022; resubmitted 9 October 2022
Accepted 29 December 2022
[10.1126/science.abq2105](https://doi.org/10.1126/science.abq2105)

CIRCADIAN RHYTHMS

Sex-dimorphic and age-dependent organization of 24-hour gene expression rhythms in humans

Lorenzo Talamanca[†], Cédric Gobet[†], Felix Naef^{*}

The circadian clock modulates human physiology. However, the organization of tissue-specific gene expression rhythms and how these depend on age and sex is not defined in humans. We combined data from the Genotype-Tissue Expression (GTEx) project with an algorithm that assigns circadian phases to 914 donors, by integrating temporal information from multiple tissues in each individual, to identify messenger RNA (mRNA) rhythms in 46 tissues. Clock transcripts showed conserved timing relationships and tight synchrony across the body. mRNA rhythms varied in breadth, covering global and tissue-specific functions, including metabolic pathways and systemic responses. The clock structure was conserved across sexes and age groups. However, overall gene expression rhythms were highly sex-dimorphic and more sustained in females. Rhythmic programs generally dampened with age across the body.

The circadian clock allows evolutionary adaptation of life to the 24-hour periodicity of Earth's rotation. The clock synchronizes internal body rhythms in behavior and physiology with 24-hour environmental, societal, or feeding cues (1–3). Perturbations of the clock, such as those caused by sleep disruption and shift work, can lead to pathologies (4). Sexual dimorphism exists in gene expression levels across the body (5), and many complex phenotypes, including diseases, exhibit sex-dependent characteristics (6). However, interactions between sexual dimorphism and molecular circadian rhythms in humans are unexplored (7). Likewise, the effects of aging on human physiology are well studied (8), but the interplay between circadian oscillations and aging processes is still poorly understood (9).

We combined Genotype-Tissue Expression (GTEx) project transcriptomes with an algorithm that assigns circadian times to individuals and tissues (10–12) to obtain a whole-organism view of 24-hour gene expression rhythms in 46 human tissues. A stratification by sex and age revealed a rich picture of group-specific rhythms, especially in metabolic and cardiovascular tissues, that may provide insights into differential disease incidence rates.

Results

Comprehensive 24-hour gene expression rhythms in 46 human tissues

To study the breadth of rhythmic mRNA programs across the human body, we used data from 16,000 human RNA sequencing (RNA-seq) experiments from 914 donors in the GTEx collection and computed one circadian reference phase for each donor. This phase corresponds to the expected circadian phase in skeletal muscle, hereafter named the donor internal phase (DIP). The algorithm exploits the fact that the circadian phases of tissue samples (typically 10 to 20 per individual) from the same donor are correlated and assumes that relative circadian phases of tissues are conserved across donors. Time of death (TOD) (available from GTEx) may not reflect circadian phase because of the individuals' varying chronotypes (2), positions in a time zone, and type of death. In relation to the TOD, clock genes such as *PER2* and *NR1D1* exhibited arrhythmic profiles in most tissues (fig. S1A), and mRNA rhythmicity at the genome-scale was nearly absent (fig. S1B). However, the pairwise correlations between clock transcripts were indicative of a functional clock (fig. S1C). We therefore developed an algorithm to assign DIPs to all donors (Fig. 1A). After correcting for sample covariates to reduce variability that was not due to circadian oscillations (fig. S1D), we applied two steps. For each tissue independently, we used CHIRAL, an algorithm we developed to estimate the tissue internal phases (TIPs) of all samples, which uses a set of seed genes

and their assigned weights (fig. S1, E and F). We tested several sets of seed genes and benchmarked CHIRAL using time-labeled human samples from muscle (13) (fig. S1G and table S1). We identified a set of 12 genes, consisting of mechanistically well-characterized circadian time-telling transcripts, that performed better than other sets composed of genes showing rhythmicity across mouse tissues. In particular, performance decreases with the set size (fig. S1, H to J) (14, 15). The TIPs from one donor often showed one primary mode, which we assigned as the DIPs (fig. S2, A to D). With the DIPs, we characterized gene expression rhythmicity in 46 tissues by harmonic regression.

DIPs were distributed fairly uniformly along the 24-hour cycle (table S2). TODs and DIPs showed better concordance for fast death compared with slow death (Hardy scale) (fig. S2E). With the DIPs, *PER2* and *NR1D1* showed clear circadian oscillations across all donors (fig. S2F), indicating that the DIPs captured circadian phase more reliably than TODs. Clock transcript oscillations across all tissues showed that although the amplitudes varied, the peak times were aligned, with the tightest being *TEF* and *ARNTL* (*BMAL1*) and the most variable being *NR1D1* (*REVERBA*) (fig. S2G). We used the complex-valued singular value decomposition (cSVD) to summarize the multigene structure of clocks across multiple conditions. The first mode, which captured >95% of the variance, showed that the human clock module comprises two main groups of anti-phasic genes, plus fewer genes with a phase angle (Fig. 1B). Clocks across tissues were well synchronized, showing relative offsets of only a few hours; the adrenal gland had the earliest phase, perhaps related to the distinct role of adrenal glucocorticoids in systemic clock organization (16). Metabolic tissues (adipose tissue, esophagus, cardiovascular tissues) showed the highest amplitudes, whereas brain tissues and testis had the lowest (Fig. 1B) (17), as reflected by the clock genes *PER3* and *ARNTL* (Fig. 1C).

To test whether the DIPs also unveil mRNA rhythms associated with systemic signals, we considered heat shock response genes, which exhibit rhythmic activity in mice (18). Heat shock genes (HSF1 targets) showed clear diurnal expression patterns; the highest oscillatory amplitude was observed in brain tissues, which peaked between 8 and 10 p.m., near the time of highest body temperature in humans

Institute of Bioengineering, School of Life Sciences, Ecole Polytechnique Fédérale de Lausanne (EPFL), CH-1015 Lausanne, Switzerland.

^{*}Corresponding author. Email: felix.naef@epfl.ch

[†]These authors contributed equally to this work.

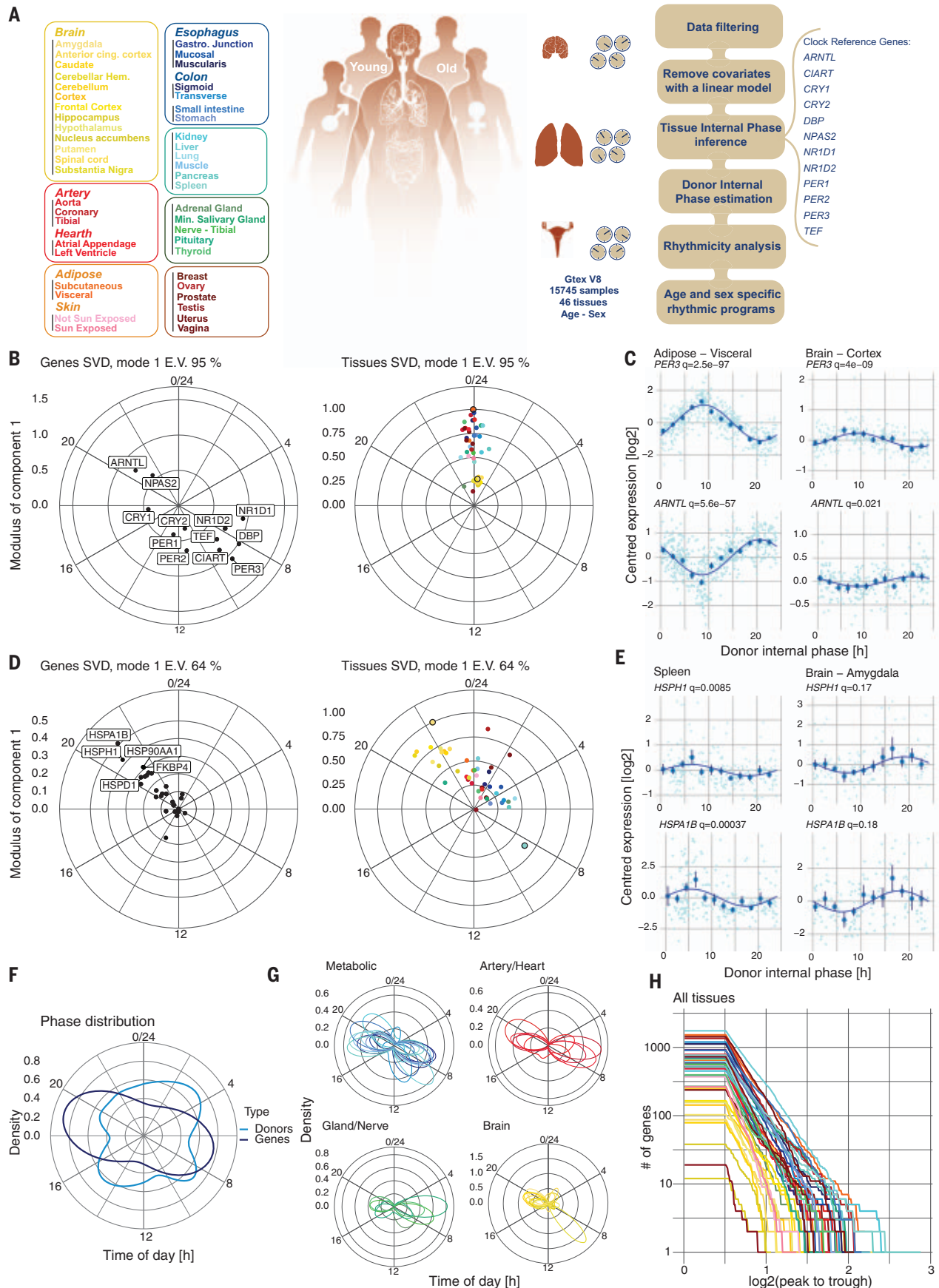


Fig. 1.

Fig. 1. Global circadian ordering of GTEx project data identifies synchronous circadian clocks in 46 human tissues. (A) Algorithm to assign one donor internal phase (DIP) to 914 individuals in the GTEx v8 RNA-seq dataset. The list of all tissues studied and the color scheme used in the figures are shown on the left. Anterior cing. cortex, anterior cingulate cortex; cerebellar hem., cerebellar hemisphere; gastro. junction, gastrointestinal junction; min. salivary gland, minor salivary gland. (B) First gene (left) and tissue (right) complex (eigen-)vectors from the cSVD performed on clock reference genes (first module explains 95% of the 24-hour variance; E.V., explained variance). In the polar plots, phases have been converted to 24-hour time, and time runs clockwise. (C) mRNA expression levels (\log_2 , centered) of two clock

genes (*PER3* and *ARNTL*) in two representative tissues. Mean and standard error (SE) were computed in 2-hour bins, and harmonic regression fits are shown (dark blue). Benjamini-Hochberg (BH) adjusted p values [$q(\text{BH})$] are reported. (D) Heat shock gene module (top 20 HSF1 targets), displayed as in (B). (E) mRNA expression levels (\log_2 , centered) for two heat shock response genes (*HSPH1* and *HSPA1B*), represented as in (C). (F) Polar density plot of the DIPs and of the peak times of rhythmic genes. (G) Phase densities of rhythmic genes [$q(\text{BH}) < 0.2$ and \log_2 peak-trough > 0.5] for various groups of tissues. (H) Number of rhythmic genes [$q(\text{BH}) < 0.2$ and \log_2 peak-trough > 0.5], with peak-trough amplitude higher than a threshold (x axis, \log_2) plotted as a function of the threshold across 46 tissues.

(19) (Fig. 1D). Compared with the clock, we observed a larger spread in peak phases across tissues; the peak times of both *HSPH1* and *HSPA1B* were almost antiphasic in spleen and amygdala (Fig. 1E). The high-amplitude heat shock program in many brain regions may reflect a pressure for high proteome integrity in nonrenewing tissues (20).

Genome-wide 24-hour rhythmicity (fig. S3A and tables S3 and S4) across tissues showed morning (centered on 7 a.m.) and evening (7 p.m.) waves of gene expression throughout the body (Fig. 1, F and G), with metabolic tissues showing the most rhythmicity and brain tissues the least, a property that was stable across the different seed gene sets (15, 21) (fig. S3B). These waves showed slight temporal shifts that followed the phases of the core clock (Fig. 1B): Several glands showed early phases, followed by cardiovascular, metabolic, and brain tissues (Fig. 1G). Depending on the tissue, we found between tens and several hundreds of rhythmic transcripts with peak-to-trough ratios greater than 2 (Fig. 1H). Besides clock genes, more than 100 transcripts were rhythmic in at least 20 tissues, including known rhythmic genes such as *NFIL3* and *PDK4* as well as glucocorticoid-responsive genes such as *FKBP5* and the proinflammatory cytokine receptors interleukin 1 receptor–like 1 and 2 (*IL1RL1*, *IL1R2*) (table S5). Twelve-hour ultradian mRNA rhythms were detected in several tissues, notably in ovary and liver (fig. S3C).

To characterize regulatory mechanisms, we used cSVD to integrate transcription factor (TF) targets. Putative regulators of both the morning and evening waves were involved in immunity, core clock, carbohydrate metabolism, and cell proliferation (fig. S3D and table S5). Among TFs that explained the most variance were the core clock dimer CLOCK:BMAL1 (peak target accumulation at 10 a.m.) and glucocorticoid receptor (GR) NR3C1 (5 p.m.) that corresponded to GR-repressed genes (22). In the evening, MYC and MYCN (7 p.m., cell proliferation), X-box-binding protein 1 (XBP1) (8 p.m., response to unfolded protein response), and peroxisome proliferator-activated receptor gamma coactivator 1 (PPARGC1) (8 p.m., energy metabolism) were activated. During the night, IRF2 (2 a.m., interferon regulatory factor) and STAT2 (3 a.m., cytokine response)

activities peaked. Similar TFs showed rhythmic activities in mouse liver (23). Enriched gene functions showed coherence across many tissues (fig. S4A and table S5). Starting at midnight, immune response genes peaked early during the night, consistent with the above IRF2 and STAT2 TFs, followed by a response to cholesterol in the early day that coincided with peak times of serum cholesterol levels (24). Around 9 a.m., we observed a peak for caffeine response, followed by energy homeostasis, gluconeogenesis, and lipid metabolism genes. mRNAs involved in amino acid and glucose metabolism, as well as protein synthesis and folding, peaked in the early afternoon, which extended into the evening. Cell-cycle pathways peaked in the evening to late night, which coincided with the predicted MYC and MYCN activities. Therefore, pan-rhythmic gene functions in humans largely consist of timed metabolic processes that reflect a switch between low- and high-energy states during the rest-activity cycle. Among functions that showed tissue specificity, lipid metabolism was particularly rhythmic in the liver, as was amino acid metabolism in the intestine and heat shock response across the brain tissues (fig. S4B).

Human sexual dimorphism in circadian rhythms

We leveraged DIPs to analyze sex-dimorphic mRNA rhythms. The relative phases and amplitudes of clock genes were conserved in males and females (Fig. 2A), and the distributions of DIPs were similar for males and females (Fig. 2B). To analyze sex-dimorphic clock output programs, we used a model selection approach to classify each transcript into five statistical scenarios (models) depending on the rhythmic behavior in both sexes (25). The number of rhythmic genes was higher in females by about twofold at all amplitude thresholds (Fig. 2C and fig. S5). Although tissues such as esophagus, skeletal muscle, and adipose tissue did not differ much, the stratification by sex unveiled several highly dimorphic tissues (Fig. 2D). Notably, females had considerably more rhythmic transcripts in the adrenal gland and liver (Fig. 2D).

Cardiovascular tissues are known sites of circadian regulation (26) that exhibit circadian rhythmicity in data from the GTEx project (12). In the heart (atrial appendage), the total number of rhythmic genes and their peak phases

were similar in males and females (Fig. 2, E and F). However, only about 50% of rhythmic genes were shared between male and female, with the remaining rhythms either being specific to one sex or showing different rhythmic patterns (Fig. 2G).

Liver exhibits marked circadian physiology and sex-dependent gene expression in humans (5). We found a strong enrichment of mRNA rhythms in females at all amplitudes, mostly as an extensive morning wave (Fig. 2, H to J). Three pathways, with sex-dependent mRNA rhythms in mice (27), showed enriched rhythmicity in female livers: xenobiotic detoxification, fatty acid oxidation, and cholesterol synthesis (fig. S6A). In the latter, nearly all enzymes, including the rate-limiting and statin target 3-hydroxy-3-methylglutaryl-CoA reductase (HMGCR), showed rhythmicity in females that was damped or absent in males (fig. S6C). In detoxification, many phase I and II enzymes were strongly enriched in female-specific cyclers (Fig. 2L) (28). Female-specific rhythms in the liver were predicted to be driven by heat shock transcription factor 1 (HSF1) and peroxisome proliferator-activated receptor gamma (PPARG) (fig. S6A).

The adrenal gland also exhibited more rhythmic mRNAs in females than in males, centered at midday (Fig. 2K). Among those, GR targets were enriched, which could reflect autocrine signaling (fig. S6B). Because glucocorticoid signaling is a systemic synchronizer and organizer of peripheral rhythms (16), this might corroborate with the overall increased rhythmicity in females at transcriptional and physiological levels (7).

Age-dependent circadian reprogramming of human gene expression

We analyzed how aging reprograms daily rhythmic gene expression across the human body. Donors were divided into two age groups: less than 50 years of age (38 ± 9 years) and more than 60 years of age (65 ± 3 years). The overall amplitudes, phases, and relative relationships of the clock genes were conserved with age (Fig. 3A). Rhythmic transcripts showed two waves in both age groups (Fig. 3B) but were overall strongly damped in the older donors (Fig. 3C and fig. S7) (29). The latter showed one-third of rhythmic genes with peak-to-trough ratios greater than 4 (Fig. 3C); such loss of rhythmicity with aging occurred in most but

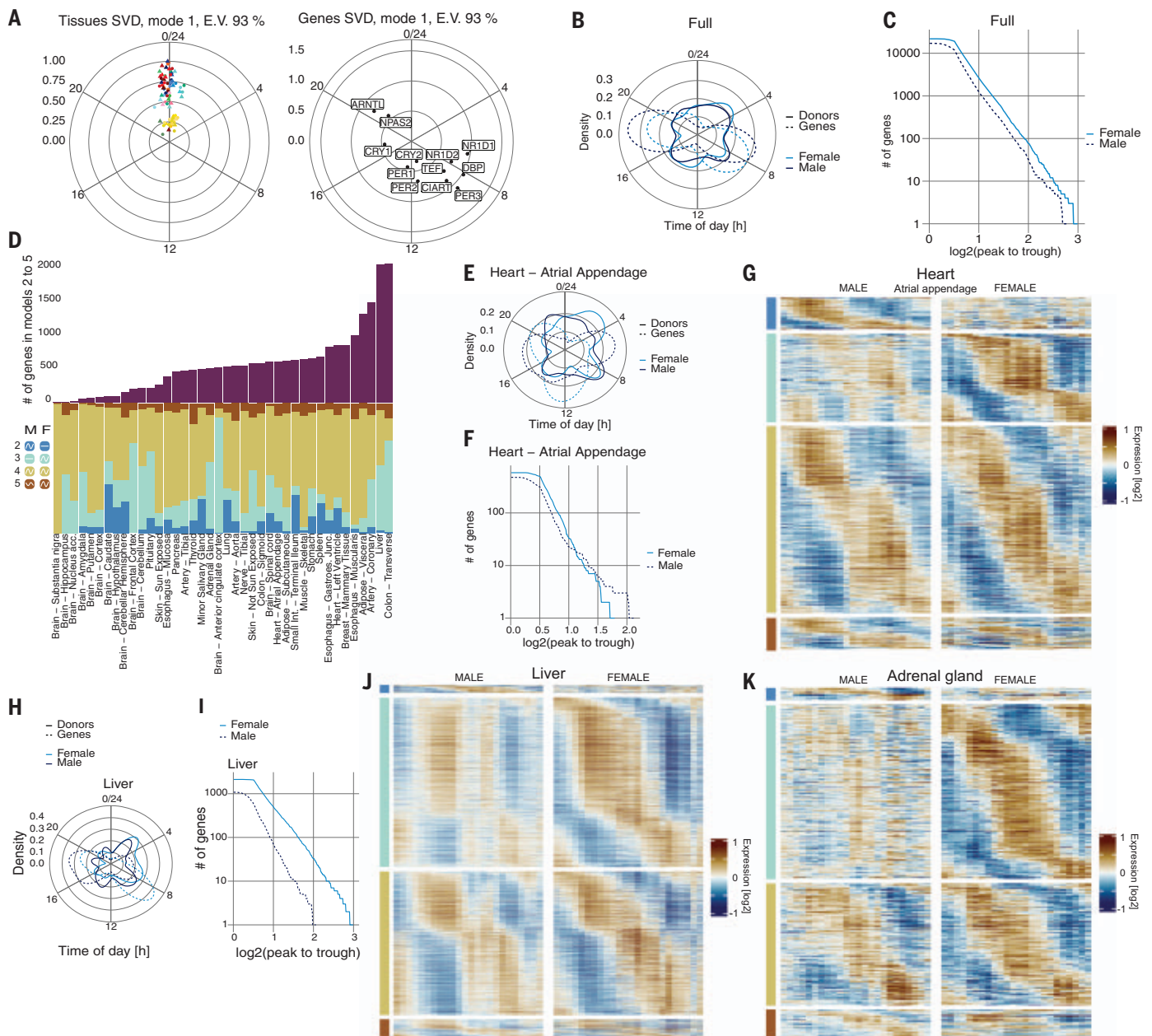


Fig. 2. Human sexual dimorphism in circadian mRNA rhythms.

(A) First gene (left) and tissue (right) vectors of cSVD performed on clock reference genes for males (triangle) and females (circle). The first module explains 93% of the 24-hour variance (E.V.). (B) Polar densities of DIPS (solid line) and gene peak phases (dashed line) in males (dark blue) and females (light blue). (C) Number of 24-hour rhythmic genes with an amplitude higher than a threshold as a function of the threshold in all tissues combined. (D) Summary of total number of rhythmic genes in each tissue (top) divided according to four statistical models (bottom): model 2 (blue), model 3 (cyan), model 4 (mustard), and model 5 (brick). M, male; F, female. (E) Heart atrial appendage represented as in (B). (F) Heart atrial appendage illustrated as in (C). (G) Heart atrial appendage: Heatmap of mRNA levels for genes in models 2 to 5 illustrates model selection. Log₂ (mean centered) expression of all samples in the two categories, low (blue) to high (brown), represented by 1-hour bins plotted with a 4-hour window moving average. (H) Liver tissue summarized as in (E). (I) Liver as in (F). (J) Liver as in (G). (K) Adrenal gland as in (G). (L) Liver: Visualization of rhythmic genes in the biotransformation meta pathway (WP702) colored according to amplitude of genes in males (blue) and females (red). All genes shown satisfy $q(BH) < 0.2$ and peak-trough > 0.5 (log₂) in one or both sexes (see methods).



gene phase (dashed line). **(C)** Number of 24-hour-rhythmic genes with an amplitude higher than a threshold as a function of the threshold in all tissues combined for younger (dark blue) and older (light blue) donors. **(D)** Summary of the number of rhythmic genes in each tissue divided according to the model selection approach [model 2 (blue), model 3 (cyan), model 4 (mustard), and model 5 (brick)]. Y, younger; O, older. **(E)** Adipose subcutaneous tissue represented as in (C). **(F)** Adipose subcutaneous tissue illustrated as in (B). **(G)** Adipose subcutaneous tissue: Heatmap of genes in models 2 to 5. Log₂ (mean-centered) expression of all samples in the two categories, low (blue) to

high (brown), represented by 1-hour bins plotted with a 4-hour window moving average. **(H)** Coronary artery: Polar density plot of DIPs (solid line) and peak phase of rhythmic genes (dashed line) for young (dark blue) and old (light blue). **(I)** Coronary artery: Number of genes with an amplitude higher than a threshold as a function of the threshold for young (dark blue) and old (light blue). **(J)** Coronary arteries as in (G). **(K)** Ovary as in (G). **(L)** Coronary artery: Visualization of cholesterol biosynthesis pathway (WP197) colored according to amplitude of genes in young (blue) and old (light red). All genes shown satisfy $q(\text{BH}) < 0.2$ and peak-trough > 0.5 (log₂) in one or both age groups (see methods).

not all tissues (Fig. 3D). For instance, adipose tissues, esophagus, and skeletal muscle showed conserved rhythmicity across age, with most genes exhibiting statistically identical rhythms in the two groups (model 4, colored mustard, in Fig. 3D). This is illustrated in subcutaneous adipose tissue, where the morning and evening waves are pronounced in both younger and older donors (Fig. 3E), with a majority of shared (model 4) mRNA rhythms (Fig. 3, F and G).

We next focused on the coronary arteries, a tissue that strongly lost rhythms with age. Although morning and evening transcript waves were observed in both groups (Fig. 3H), the number of rhythmic mRNAs in older donors was about half that in younger donors, across all amplitudes (Fig. 3, I and J). Programs that lost rhythmicity include cholesterol biosynthesis, fatty acid synthesis, and the regulation of glycolysis (Fig. 3L and fig. S8A), which are processes known to be deregulated in vascular smooth muscle cells in cardiovascular diseases (30). Most enzymes in the cholesterol biosynthesis pathway, including *HMGCR*, were rhythmically expressed in young coronary arteries but lost this feature with age (Fig. 3L).

Comparing the ovaries of pre- and postmenopausal women revealed that both lost and gained mRNA rhythms (Fig. 3K). Although rhythmicity in lipid and cholesterol biosynthesis was suppressed in older donors, as in the coronary arteries (fig. S8B), stress, and in particular heat shock response genes, became rhythmic, as supported by predicted HSF1 TF activity (fig. S8, B and C). This signature of a thermal stress response in postmenopausal women may reflect circadian patterns of temperature control (31).

In some tissues, genes switched from a 24-hour to a 12-hour ultradian periodicity with age. In the pituitary gland, liver, and colon, 12-hour rhythms arose in 30 to 50% of genes classified as only rhythmic in young donors (fig. S8, D and F). In humans, these tissues regulate rhythms of temperature, energy metabolism, and absorption. Such destabilization of 24-hour periodicity in favor of an ultradian state as a result of aging might reflect differences in the reception of external cues in older individuals (32).

Discussion

We developed an algorithm to temporally order GTEx samples that could overcome several

limitations of postmortem data through pre-processing, controlled statistics, and formulation in terms of a population-level phase model (DIP). Nevertheless, sensitivity to data quality, seed gene sets, complex covariate structures, or sampling bias cannot be fully ruled out, and the dataset is underpowered to comprehensively study the cross-interaction of sex and age. Clocks were largely in-phase in 46 analyzed tissues, with the adrenal gland peaking earliest. The concomitant signature of a sizable wave of negative GR targets in the afternoon suggests that released adrenal glucocorticoids play a crucial role in human body-wide circadian synchronization, including overall increased rhythmicity in females. HSF1 targets contributed a considerable portion of the body's 24-hour rhythms and showed sex and age dependency. The observation that rhythmic liver transcript levels, particularly in xenobiotic detoxification, were prevalent in females may reflect a sex-dimorphic incidence of liver diseases (33). Similarly, the loss of mRNA rhythms with age in coronary arteries correlates with age-dependent incidence rates of cardiovascular diseases (34). The identified differences in 24-hour rhythmic processes across sexes and ages may help improve patient-specific chronopharmacology (35).

REFERENCES AND NOTES

1. J. Aschoff, *Science* **148**, 1427–1432 (1965).
2. T. Roenneberg et al., *Sleep Med. Rev.* **11**, 429–438 (2007).
3. C. Dibner, U. Schibler, U. Albrecht, *Annu. Rev. Physiol.* **72**, 517–549 (2010).
4. C. R. Cederroth et al., *Cell Metab.* **30**, 238–250 (2019).
5. M. Oliva et al., *Science* **369**, eaba3066 (2020).
6. C. Ober, D. A. Loisel, Y. Gilad, *Nat. Rev. Genet.* **9**, 911–922 (2008).
7. S. T. Anderson, G. A. FitzGerald, *Science* **369**, 1164–1165 (2020).
8. R. Yamamoto et al., *Nat. Commun.* **13**, 5803 (2022).
9. V. A. Acosta-Rodríguez, F. Rijo-Ferreira, C. B. Green, J. S. Takahashi, *Nat. Commun.* **12**, 2862 (2021).
10. H. R. Ueda et al., *Proc. Natl. Acad. Sci. U.S.A.* **101**, 11227–11232 (2004).
11. R. C. Anafi, L. J. Francey, J. B. Hogenesch, J. Kim, *Proc. Natl. Acad. Sci. U.S.A.* **114**, 5312–5317 (2017).
12. M. D. Ruben et al., *Sci. Transl. Med.* **10**, eaat8806 (2018).
13. L. Perrin et al., *eLife* **7**, e34114 (2018).
14. J. Yeung et al., *Genome Res.* **28**, 182–191 (2018).
15. R. Zhang, N. F. Lahens, H. I. Ballance, M. E. Hughes, J. B. Hogenesch, *Proc. Natl. Acad. Sci. U.S.A.* **111**, 16219–16224 (2014).
16. P. Pezük, J. A. Mohawk, L. A. Wang, M. Menaker, *Endocrinology* **153**, 4775–4783 (2012).
17. D. Morse, N. Cermakian, S. Brancorsini, M. Parvinen, P. Sassone-Corsi, *Mol. Endocrinol.* **17**, 141–151 (2003).
18. H. Reinke et al., *Genes Dev.* **22**, 331–345 (2008).
19. J. Aschoff, *J. Therm. Biol.* **8**, 143–147 (1983).
20. R. San Gil, L. Ooi, J. J. Yebury, H. Ecroyd, *Mol. Neurodegener.* **12**, 65 (2017).

21. L. S. Mure et al., *Science* **359**, eaao0318 (2018).
22. H. M. Reichardt et al., *EMBO J.* **20**, 7168–7173 (2001).
23. J. Wang et al., *Cell Metab.* **25**, 102–117 (2017).
24. P. J. Jones, D. A. Schoeller, *J. Lipid Res.* **31**, 667–673 (1990).
25. B. D. Weger et al., *Proc. Natl. Acad. Sci. U.S.A.* **118**, e2015803118 (2021).
26. S. C. McLoughlin, P. Haines, G. A. FitzGerald, in *Circadian Rhythms and Biological Clocks*, Part B, A. Sehgal, Ed., vol. 552 of *Methods in Enzymology* (Elsevier, 2015), pp. 211–228.
27. B. D. Weger et al., *Cell Metab.* **29**, 362–382.e8 (2019).
28. Y.-F. Lu et al., *Chronobiol. Int.* **30**, 1135–1143 (2013).
29. C.-Y. Chen et al., *Proc. Natl. Acad. Sci. U.S.A.* **113**, 206–211 (2016).
30. J. Shi, Y. Yang, A. Cheng, G. Xu, F. He, *Am. J. Physiol. Heart Circ. Physiol.* **319**, H613–H631 (2020).
31. R. R. Freedman, D. Norton, S. Woodward, G. Cornélissen, *J. Clin. Endocrinol. Metab.* **80**, 2354–2358 (1995).
32. D. Weinert, *Chronobiol. Int.* **17**, 261–283 (2000).
33. S. Bellentani, F. Scaglioni, M. Marino, G. Bedogni, *Dig. Dis.* **28**, 155–161 (2010).
34. P. Jousilahti, E. Vartiainen, J. Tuomilehto, P. Puska, *Circulation* **99**, 1165–1172 (1999).
35. J. Bicker, G. Alves, A. Falcão, A. Fortuna, *Br. J. Pharmacol.* **177**, 2215–2239 (2020).
36. L. Talamana, C. Gobet, F. Naef, Sex-dimorphic and age-dependent organization of 24-hour gene expression rhythms in human, Zenodo (2022); <https://doi.org/10.5281/zenodo.7199055>.

ACKNOWLEDGMENTS

The GTEx project was supported by the Common Fund of the Office of the Director of the National Institutes of Health and by the National Cancer Institute (NCI); National Human Genome Research Institute (NHGRI); National Heart, Lung, and Blood Institute (NHLBI); National Institute on Drug Abuse (NIDA); National Institute of Mental Health (NIMH); and National Institute of Neurological Disorders and Stroke (NINDS). The data used in this manuscript were obtained from the GTEx Portal on 12 April 2020 and dbGaP accession number phs000424.GTEx.v8.p2.c1.GRU on 30 March 2022. We thank F. Gachon and P. De Los Rios for insightful discussions. **Funding:** This project was funded by a Swiss National Science Foundation individual project grant 310030B_201267 to F.N. **Author contributions:** Conceptualization: L.T., C.G., F.N.; Formal analysis: L.T., C.G.; Funding acquisition: F.N.; Methodology: L.T., C.G., F.N.; Investigation: L.T., C.G., F.N.; Software: L.T., C.G.; Supervision: F.N.; Writing – original draft: L.T., C.G., F.N.; Writing – review and editing: L.T., C.G., F.N. **Data and materials availability:** GTEx V8 (dbGaP Accession phs000424.v8.p2) is publicly available at <https://www.gtexportal.org/home/datasets>, and complete metadata can be requested from dbGaP. Table S3 is available at Zenodo (36). Code is available at <https://github.com/naef-lab/CHIRAL>. **Competing interests:** The authors declare that they have no competing interests. **License information:** Copyright © 2023 the authors, some rights reserved; exclusive licensee American Association for the Advancement of Science. No claim to original US government works. <https://www.science.org/about/science-licenses-journal-article-reuse>

SUPPLEMENTARY MATERIALS

science.org/doi/10.1126/science.add0846
Materials and Methods
Figs. S1 to S4
Tables S1 to S5
References (37–49)
MDAR Reproducibility Checklist
Appendix A

Submitted 13 June 2022; accepted 5 January 2023
10.1126/science.add0846

ORGANIC CHEMISTRY

Single-carbon atom transfer to α,β -unsaturated amides from N-heterocyclic carbenesMiharu Kamitani¹, Bunta Nakayasu¹, Hayato Fujimoto^{1,2}, Kosuke Yasui¹, Takuya Kodama^{1,2}, Mamoru Tobisu^{1,2*}

Single-carbon atom transfer reactions are lacking in organic synthesis, partly because of the absence of atomic carbon sources under standard solution-phase conditions. We report here that N-heterocyclic carbenes can serve as atomic carbon donors through the loss of a 1,2-diimine moiety. This strategy is applicable to single-carbon atom transfer to α,β -unsaturated amides, which can be converted into homologated γ -lactams through the formation of four single bonds to one carbon center in one operation.

One-carbon homologation reactions, in which a carbon chain or carbon ring is expanded by a one-carbon unit, underpin the synthesis of a variety of natural products, pharmaceuticals, and functional materials (1). Although several C1 reagents for use in homologation reactions have been developed to date (2–4), atomic carbon, the simplest C1 source, has not been trans-

ferred in a synthetic context because of the lack of a practical method for its generation in conventional solution phase. Such an atomic carbon source would enable the formation of four bonds at one carbon center in a single step (Fig. 1A). This specific type of transformation is referred to hereafter as a single-carbon atom doping (SCAD) reaction. The SCAD reaction was, in fact, reported to pro-

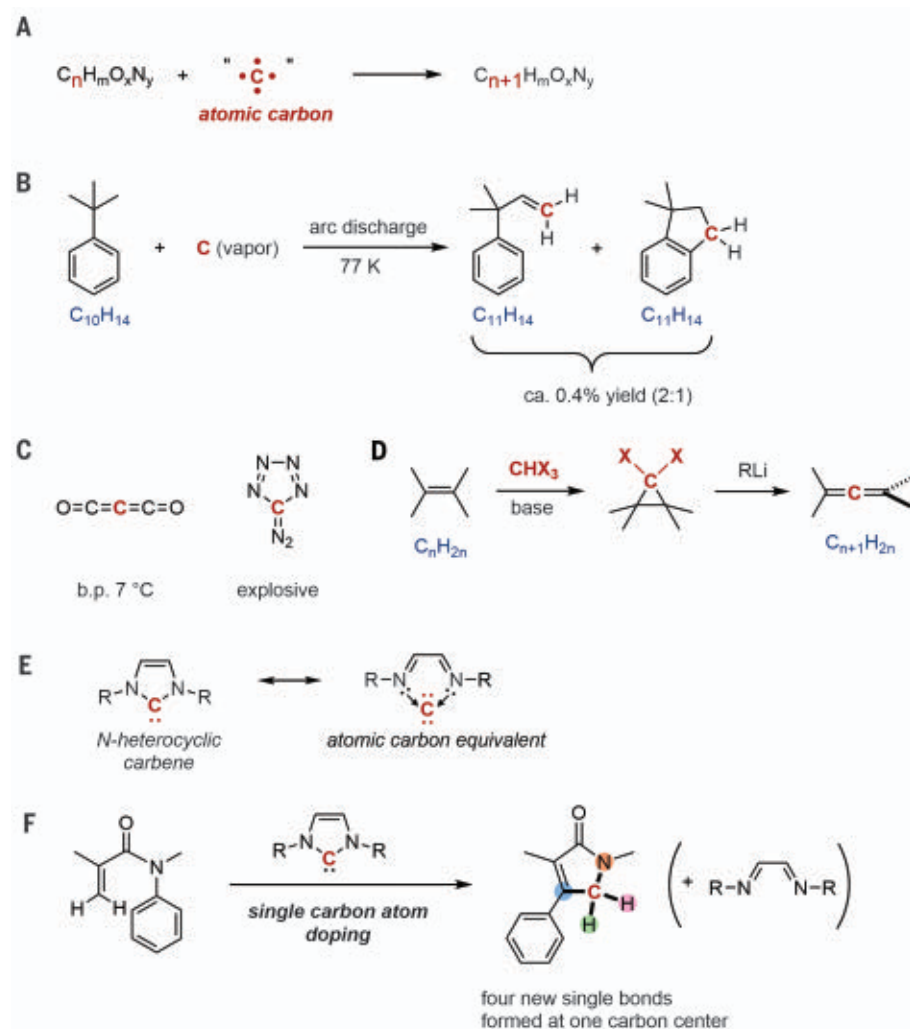
ceed in reactions of small organic molecules with atomic carbon that is generated by physical methods, such as an arc discharge, crossed molecular beam collision, and laser photolysis (5, 6). For example, the reaction of arc-generated carbon atoms with *tert*-butylbenzene ($C_{10}H_{14}$) gave 3-methyl-3-phenyl-1-butene ($C_{11}H_{14}$) and 1,1-dimethylindane ($C_{11}H_{14}$), in which four bonds were forged around the carbon that had been introduced (Fig. 1B) (7). Although substantial studies have appeared on the reactivity of physically generated carbon atoms (7–11), the need for a special apparatus as well as the extremely short lifetime of a naked atomic carbon limits the use of these protocols for practical synthetic purposes. Therefore, the development of a suitable synthetic equivalent of an atomic carbon is essential if synthetically useful SCAD reactions are

¹Department of Applied Chemistry, Graduate School of Engineering, Osaka University, Suita, Osaka 565-0871, Japan.

²Innovative Catalysis Science Division, Institute for Open and Transdisciplinary Research Initiatives, Osaka University, Suita, Osaka 565-0871, Japan.

*Corresponding author. Email: tobisu@chem.eng.osaka-u.ac.jp

Fig. 1. SCAD reactions. (A) Definition of a SCAD reaction. (B) Example of a SCAD reaction in which an atomic carbon generated by a physical method is used. (C) Reported carbon atom donors for SCAD reactions. b.p., boiling point. (D) Doering-LaFlamme allene synthesis: a two-step SCAD reaction. RLi, alkyl lithium. (E) NHC and its resonance structure as an atomic carbon coordinated with a 1,2-diimine. (F) This work: conversion of α,β -unsaturated amides into homologated γ -lactams by using NHCs as an atomic carbon donor.



to be realized. In fact, several organic molecules, such as carbon suboxide (12, 13) and diazotetrazole (14–18), were reported to decompose thermally or photochemically to generate atomic carbon (Fig. 1C). However, as in the case for physical methods, these molecules generate naked atomic carbon (or related highly reactive carbon species), thus rendering SCAD reactions using these molecules unselective and low yielding. Dihalocarbenes can serve as an atomic carbon equivalent via a two-step sequence. Thus, the overall insertion of an atomic carbon into an alkene double bond to form a homologated allene is possible via dihalocyclopropanation, followed by reductive treatment of the resulting 1,1-dihalocyclopropanes; this process is known as the Doering-LaFlamme allene synthesis (Fig. 1D) (19, 20). Although this two-step protocol represents a formal SCAD reaction, the method is limited to the synthesis of compounds derivatized from 1,1-dihalocyclopropanes. We report here that N-heterocyclic carbenes (NHCs) can be used as an atomic carbon equivalent, as represented by its limiting resonance structure of a nonbonded carbon ligated with a 1,2-diimine (Fig. 1E). The controlled doping of a single carbon atom into α,β -unsaturated amides was made possible by the action of an NHC, in which the carbon at the 2-position of the NHC is incorporated to form homologated γ -lactams with the formation of four σ -bonds at one carbon center in a single operation (Fig. 1F).

We previously reported on the NHC-catalyzed Truce-Similes-type rearrangement, in which **NHC1** mediates the conversion of α,β -unsaturated amide **1a** into cinnamide **2a** by means of nucleophilic aromatic substitution of an ylide intermediate (Fig. 2A) (27). During the course of our investigation regarding the effect of NHC structure on this rearrangement reaction, we observed the formation of γ -lactam **3a** (22) when **NHC2** was used as the catalyst. When **1a** was treated with 1 equiv. of **NHC2** in the presence of cesium fluoride (CsF) (2 equiv.) in toluene at 160°C for 12 hours, γ -lactam **3a** was formed in 52% yield. A comparison of the molecular formulas of **1a** ($C_{11}H_{13}NO$) and **3a** ($C_{12}H_{13}NO$), which were confirmed by high-resolution mass spectrometry (HRMS), clearly indicated that SCAD had occurred. In this reaction, 1,2-diimine **4a** was also formed in 55% yield, which suggests that the C2 carbon of **NHC2** served as an atomic carbon equivalent. Further screening of NHCs revealed that the use of *N*-alkyl-substituted derivatives improved the yield of **3a**, with the cyclohexyl-substituted derivative **NHC5** being the most effective among the NHCs that we examined (93% isolated yield of **3a**) (Fig. 2B). Regarding the bases, sodium carbonate (Na_2CO_3) or sodium *tert*-butoxide ($NaOtBu$) were much less effective (0 and 15%

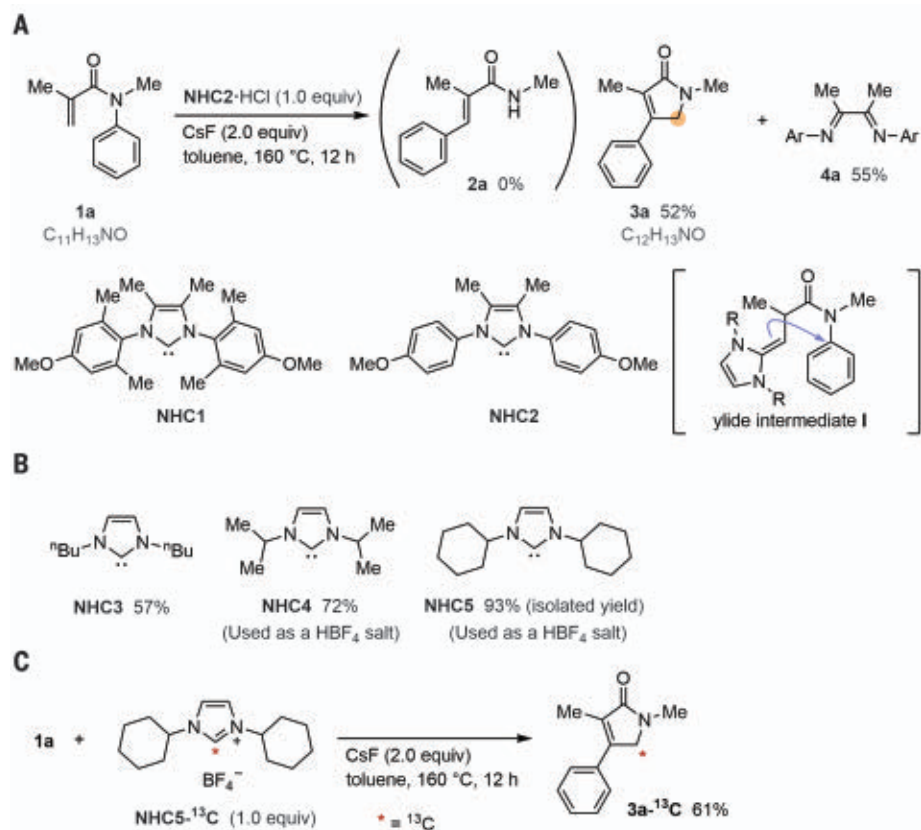


Fig. 2. NHC SCAD reactions with unsaturated amides. (A) Initial finding of SCAD reaction of amide **1a** using **NHC2**. Me, methyl; MeO, methoxy. (B) Effect of NHCs on the yield of lactam **3a** from amide **1a**. (C) ^{13}C -labeling experiment.

yields, respectively; fig. S2). The reaction also proceeded in the absence of CsF when pre-prepared free **NHC5** was used (53% yield; fig. S2). The reaction can be conducted at lower temperature by extending the reaction time (83% at 140°C for 24 hours; 49% at 120°C for 72 hours; fig. S3). When the reaction of **1a** was performed using **NHC5** labeled at the C2 position with ^{13}C , the resultant **3a** product contained ^{13}C at the C5 position, which was confirmed by ^{13}C nuclear magnetic resonance (NMR) spectroscopy (Fig. 2C). This observation unambiguously confirms that the carbon atom that is incorporated into **3a** is derived from the C2 site of **NHC5**. Considering that the overall transformation involves the cleavage of five single bonds (two C–H and three C–N bonds) and the formation of five single bonds (two C–C, two C–H, and one C–N bonds), multiple events occurred with a high degree of efficiency under these conditions.

This SCAD reaction can be used for the conversion of a diverse array of α,β -unsaturated amides into the corresponding γ -lactams (Fig. 3A). Halogens including bromides (**1b**, **1c**, and **1d**), fluorides (**1e** and **1j**), and chlorides (**1f**) are compatible under these conditions,

which allows for straightforward access to γ -lactams bearing these groups. The structure of **3b** was unambiguously determined by x-ray crystallography (fig. S8). Amide **3d**, which contains an *ortho*-Br group, was reported to undergo S_NAr at the Br site when an *N*-aryl-substituted NHC is used (21, 23), highlighting the profound impact of the nature of the NHC that is used on the course of the reaction. Although a styrene moiety would be predicted to be reactive toward NHCs (24), the reaction of **1l** selectively provided the corresponding lactam **3l** through the addition of NHC to the α,β -unsaturated amide moiety. In addition to benzene derivatives, π -extended analogs can also be used successfully as the migrating aryl group, as exemplified by the formation of biphenyl (**3k**–), naphthyl (**3m**–), and fluorenyl (**3n**–) substituted lactams. Although substrates bearing terminal and internal alkenes both failed to undergo this carbon atom doping reaction, alkenes with a substituent at the α -position (i.e., R' in Fig. 3A) were found to be compatible substrates. For example, ethyl-substituted amide **1o** participated successfully in this reaction to form the corresponding lactam **3o** in 81% yield. Regarding the substituents on the nitrogen, a range of groups,

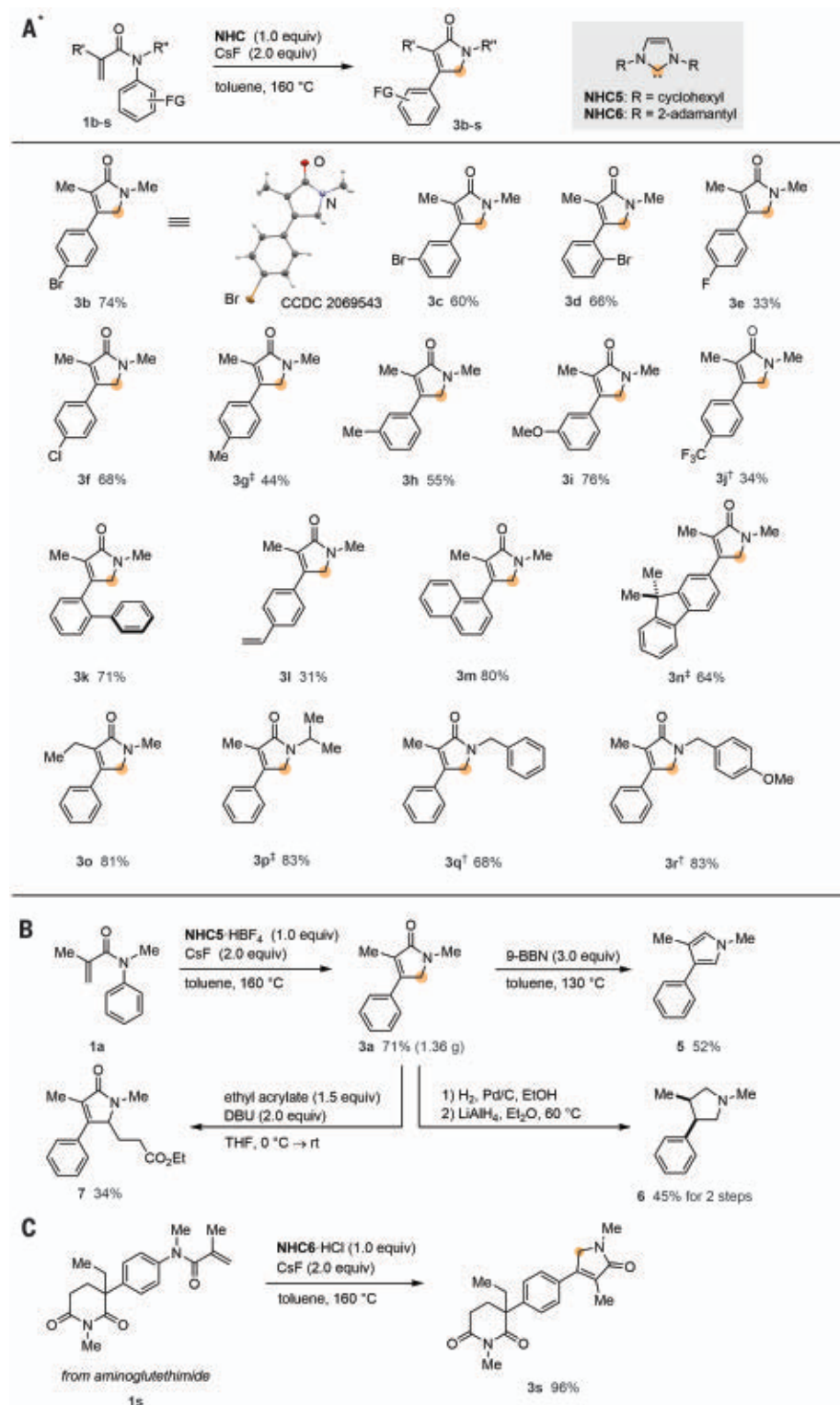


Fig. 3. Substrate scope exploration. (A) Scope of substrates. *Reaction conditions: amide **1** (0.20 mmol), **NHC5**-HBF₄ (0.20 mmol), CsF (0.40 mmol), and toluene (1.0 ml) in sealed tube at 160°C. Isolated yield is shown. †**NHC6**-HCl was used instead of **NHC5**-HBF₄. ‡**NHC6**-HBF₄ was used instead of **NHC5**-HBF₄. (B) Synthetic elaboration of **3a**. CO₂Et, ethoxycarbonyl; DBU, 1,8-diazabicyclo[5.4.0]undec-7-ene; EtOH, ethanol; Et₂O, diethyl ether; LiAlH₄, lithium aluminum hydride; Pd/C, palladium on activated charcoal; rt, room temperature; THF, tetrahydrofuran; 9-BBN, 9-borabicyclo[3.3.1]nonane. (C) Late-stage derivatization of aminoglutethimide derivatives by the SCAD reaction.

such as the isopropyl (**3p**), benzyl (**3q**), and *p*-methoxybenzyl (**3r**) groups, were compatible. The operational simplicity of this carbon atom doping reaction allows for the gram-scale synthesis of lactam **3a** by heating a mixture of amide **1a** and commercially available **NHC5**-HBF₄ (HBF₄, tetrafluoroboric acid) and CsF in toluene in a sealed tube (Fig. 3B). Although γ -lactams are valuable motifs in their own right (25), they can also be derivatized further into various useful compounds by classical organic reactions. Pyrroles (**5**) (26) and piperidines (**6**) are readily accessible from **3a** depending on the reducing agents used. Because the C–H bond α to the nitrogen atom in **3a** is relatively acidic, an additional substituent can readily be introduced at this position through a deprotonation/alkylation sequence (27), as exemplified by the formation of **7**. This SCAD reaction can also be used for the late-stage elaboration of intricate bioactive molecules (Fig. 3C). A derivative of aminoglutethimide (28), an aromatase inhibitor, **1s** can be converted into the corresponding γ -lactam derivative **3s** in 96% yield, demonstrating the utility of this SCAD reaction in complex settings.

A possible reaction pathway for the reaction of amide **1** with NHC to produce γ -lactam **3** is outlined in Fig. 4A. The reaction is initiated by the 1,4-addition of NHC across **1**, followed by a 1,2-proton shift, which leads to the formation of ylide intermediate **I** (29, 30). Ylide **I** serves as a carbanion equivalent, the β -carbon of which is sufficiently nucleophilic to attack the ipso carbon of the aromatic ring on the nitrogen, which results in a 1,4-aryl migration by means of an S_NAr reaction (27). The resulting intermediate **II** contains a nitrogen anion, which subsequently adds across a pendant imidazolium moiety to generate the spiro intermediate **III**. A similar spiro compound was reported to be formed by the reaction of an acrylamide derivative with the 1,2,4-triazole-based NHC (31). The spiro intermediate **III** subsequently collapses to yield γ -lactam **3** and 1,2-diimine **4** through the formal transfer of hydrogens at the α and β positions of the carbonyl to the spiro carbon with the cleavage of two C–N bonds. To verify the intermediacy of ylide **I**, imidazolium salt **8**, which is the protonated form of ylide **I**, was independently prepared and exposed to the reaction conditions (Fig. 4B). As a result, γ -lactam **3g** was, in fact, formed in 34% yield (with 66% of **8** being recovered), which supports that ylide **I** is involved in this SCAD process. To verify that the intermediates **II** and **III** are formed, the reaction of α,β -unsaturated amide **9** with NHC was next investigated in the hope that the intermediate similar to **II** (i.e., **II'**) would be directly generated and lead to the formation of a lactam product. When **9** was treated with 1 equiv. of **NHC5**, γ -lactam **10** was obtained

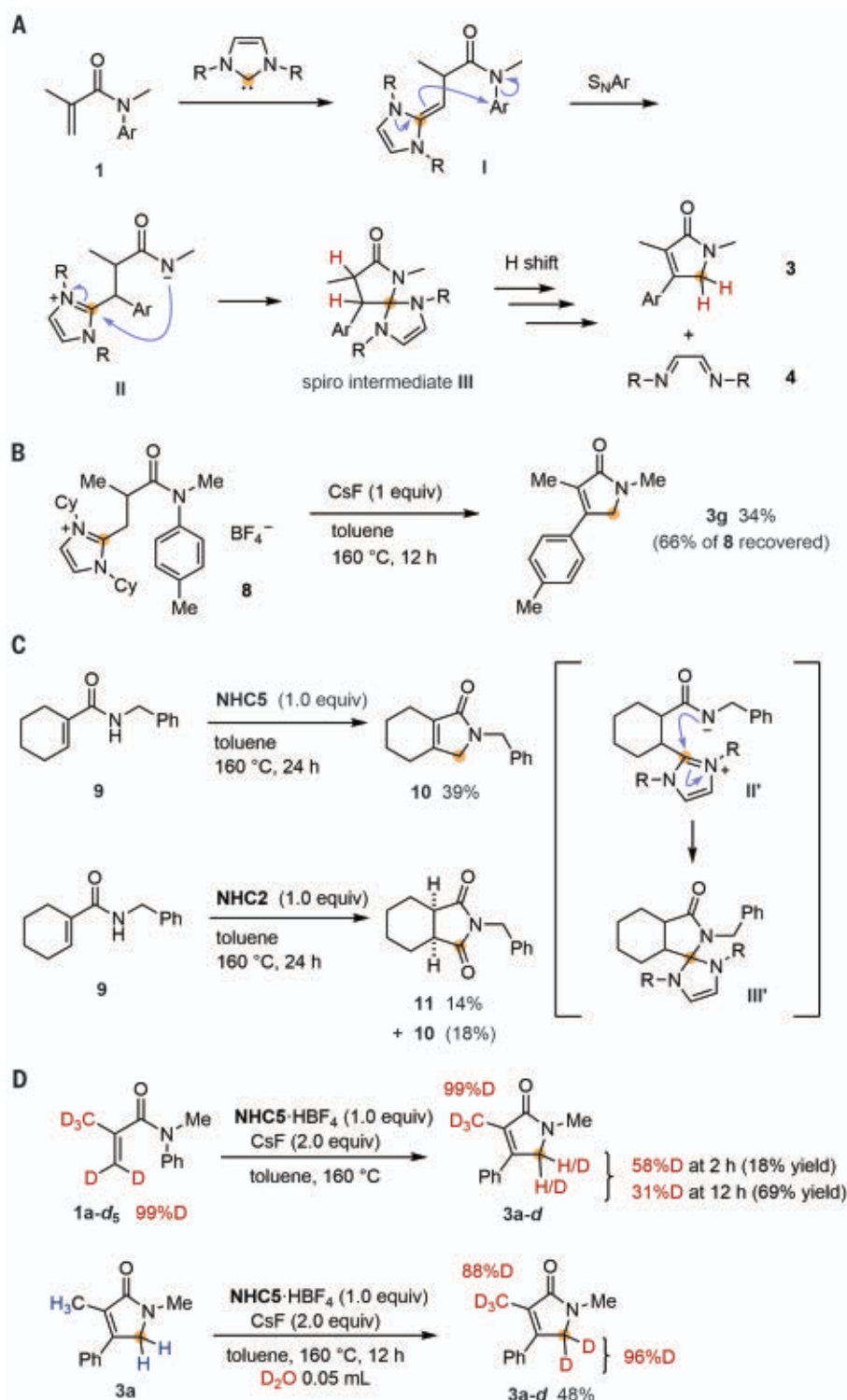


Fig. 4. Mechanistic studies. (A) Possible mechanism. (B) Experimental support for the intermediacy of **I**. (C) Experimental support for the intermediacy of **II** and **III**. (D) Deuterium labeling experiments. D_3C , methyl- d_3 ; H_3C , methyl.

in 39% yield (Fig. 4C). This result indicates that intermediate **II'**, which should be formed through the addition of NHC to **9**, followed by proton transfer, is involved in the conversion of **9** into **10**. In addition, when **NHC2**, in-

stead of **NHC5**, was used in the reaction of **9**, cyclic imide **11** was produced in 14% yield, along with **10**. This observation supports the intermediacy of spiro intermediate **III'**, which is susceptible to undergoing hydrolysis with

the formation of **11**. Deuterium-labeling experiments were performed to obtain additional insights into the mechanism that is responsible for the disassembly of spiro intermediate **III** into **3** and **4** (Fig. 4D). When amide **1a-d₅**, in which vinylic hydrogens and an α -methyl group are labeled with deuterium atoms, was exposed to the typical reaction conditions by using **NHC5**, γ -lactam **3a** was similarly obtained. Although deuterium was incorporated at the α -position relative to the nitrogen atom, the deuterium content decreased as the reaction proceeded, which was confirmed by 1H NMR spectroscopy (58% D at 2 hours and 31% D at 12 hours; figs. S5 and S6). In a separate experiment, when nonlabeled **3a**, **NHC5**· HBF_4 and CsF were heated in the presence of D_2O , the hydrogens at the α -position of nitrogen were completely substituted by deuterium atoms (fig. S7), thus demonstrating that hydrogen/deuterium (H/D) exchange at this position is rapid under the reaction conditions that are being used. We, therefore, conclude that the vinylic protons in **1a** are transferred to the methylene group in lactam **3a**, and the apparent deuterium content then decreases because of a rapid H/D exchange with trace amounts of endogenous water.

We demonstrate in this study that common NHCs can serve as an atomic carbon equivalent in synthetic organic reactions. This strategy allows for the scalable doping of a single carbon atom into α,β -unsaturated amides, which leads to the formation of homologated lactams through the formation of four single bonds in one operation.

REFERENCES AND NOTES

- J. J. Li, Ed., *Name Reactions for Homologations* (Wiley, 2009).
- N. R. Candeias, R. Paterna, P. M. P. Gois, *Chem. Rev.* **116**, 2937–2981 (2016).
- L. Castoldi, S. Monticelli, R. Senatore, L. Ielo, V. Pace, *Chem. Commun.* **54**, 6692–6704 (2018).
- J. Jurczyk et al., *Nat. Synth.* **1**, 352–364 (2022).
- C. Mackay, R. Wolfgang, *Science* **148**, 899–907 (1965).
- P. S. Skell, J. J. Havel, M. J. McGlinchey, *Acc. Chem. Res.* **6**, 97–105 (1973).
- B. M. Armstrong, F. Zheng, P. B. Shevlin, *J. Am. Chem. Soc.* **120**, 6007–6011 (1998).
- T. Rose, C. MacKay, R. Wolfgang, *J. Am. Chem. Soc.* **89**, 1529–1530 (1967).
- P. S. Skell, R. F. Harris, *J. Am. Chem. Soc.* **91**, 4440–4445 (1969).
- C. J. Emanuel, P. B. Shevlin, *J. Am. Chem. Soc.* **116**, 5991–5992 (1994).
- W. Pan, P. B. Shevlin, *J. Am. Chem. Soc.* **118**, 10004–10005 (1996).
- K. Bayes, *J. Am. Chem. Soc.* **83**, 3712–3713 (1961).
- C. Willis, K. D. Bayes, *J. Am. Chem. Soc.* **88**, 3203–3208 (1966).
- P. B. Shevlin, *J. Am. Chem. Soc.* **94**, 1379–1380 (1972).
- S. Kammula, P. B. Shevlin, *J. Am. Chem. Soc.* **96**, 7830–7832 (1974).
- P. B. Shevlin, S. Kammula, *J. Am. Chem. Soc.* **99**, 2627–2631 (1977).
- S. F. Dyer, P. B. Shevlin, *J. Am. Chem. Soc.* **101**, 1303–1304 (1979).
- T. S. Fabre et al., *J. Org. Chem.* **63**, 3522–3523 (1998).
- W. von E. Doering, P. M. LaFlamme, *Tetrahedron* **2**, 75–79 (1958).
- M. Fedorynski, *Chem. Rev.* **103**, 1099–1132 (2003).
- K. Yasui, M. Kamitani, H. Fujimoto, M. Tobisu, *Org. Lett.* **23**, 1572–1576 (2021).
- M. Shindo et al., *Chemistry* **12**, 524–536 (2005).
- K. Yasui, M. Kamitani, H. Fujimoto, M. Tobisu, *Bull. Chem. Soc. Jpn.* **93**, 1424–1429 (2020).
- S. Ito, H. Fujimoto, M. Tobisu, *J. Am. Chem. Soc.* **144**, 6714–6718 (2022).
- J. Caruano, G. G. Muccioli, R. Robiette, *Org. Biomol. Chem.* **14**, 10134–10156 (2016).

26. G. Verniest, N. De Kimpe, *Synlett* **13**, 2013–2016 (2003).
 27. N. E. Shepherd, H. Tanabe, Y. Xu, S. Matsunaga, M. Shibasaki, *J. Am. Chem. Soc.* **132**, 3666–3667 (2010).
 28. G. W. A. Milne, *Drugs: Synonyms and Properties* (Routledge, 2017).
 29. X. B. Nguyen, Y. Nakano, D. W. Lupton, *Aust. J. Chem.* **73**, 1–8 (2020).
 30. K. Yasui, M. Kamitani, M. Tobisu, *Angew. Chem. Int. Ed.* **58**, 14157–14161 (2019).
 31. O. Rajachan et al., *Tetrahedron Lett.* **56**, 6537–6540 (2015).

ACKNOWLEDGMENTS

We thank M. Shindo for providing the ^1H and ^{13}C NMR spectra of an authentic sample of **3a** for comparison. The Instrumental Analysis Center, Faculty of Engineering, Osaka University, is

acknowledged for their assistance with HRMS. **Funding:** This work was supported by JSPS KAKENHI grants JP21H04682 (M.T.) and JP22K19031 (M.T.). **Author contributions:** M.K. and B.N. performed and analyzed the experiments. M.K., B.N., H.F., K.Y., and M.T. designed the experiments. T.K. performed x-ray analysis of **3b**. M.T. prepared the manuscript. **Competing interests:** The authors declare that they have no competing interests. **Data and materials availability:** Crystallographic data for the structures reported in this article have been deposited at the Cambridge Crystallographic Data Centre, under the deposition number CCDC 2069543 (**3b**). Copies of the data can be obtained free of charge through <https://www.ccdc.cam.ac.uk/structures/>. All other data are available in the main text or the supplementary materials. **License information:** Copyright © 2023 the authors,

some rights reserved; exclusive licensee American Association for the Advancement of Science. No claim to original US government works. <https://www.science.org/about/science-licenses-journal-article-reuse>

SUPPLEMENTARY MATERIALS

science.org/doi/10.1126/science.ade5110
 Materials and Methods
 Supplementary Text
 Figs. S1 to S9
 References (32–45)

Submitted 21 August 2022; accepted 30 November 2022
 10.1126/science.ade5110

FLEXIBLE DEVICES

Liquid metal-based soft, hermetic, and wireless-communicable seals for stretchable systems

Qingchen Shen^{1,2†}, Modi Jiang^{1†}, Ruitong Wang^{1†}, Kexian Song^{1†}, Man Hou Vong^{2†}, Woojin Jung², Febby Krisnadi², Ruyu Kan¹, Feiyu Zheng¹, Benwei Fu¹, Peng Tao¹, Chengyi Song¹, Guoming Weng³, Bo Peng⁴, Jun Wang^{5*}, Wen Shang^{1*}, Michael D. Dickey^{2*}, Tao Deng^{1,3*}

Soft materials tend to be highly permeable to gases, making it difficult to create stretchable hermetic seals. With the integration of spacers, we demonstrate the use of liquid metals, which show both metallic and fluidic properties, as stretchable hermetic seals. Such soft seals are used in both a stretchable battery and a stretchable heat transfer system that involve volatile fluids, including water and organic fluids. The capacity retention of the battery was ~72.5% after 500 cycles, and the sealed heat transfer system showed an increased thermal conductivity of approximately 309 watts per meter-kelvin while strained and heated. Furthermore, with the incorporation of a signal transmission window, we demonstrated wireless communication through such seals. This work provides a route to create stretchable yet hermetic packaging design solutions for soft devices.

The rapid advancement of stretchable electronics promises to enable new types of human-machine interfaces and soft devices (1–3). Conventional rigid electronic devices are encased in packaging materials to keep reactive species, such as oxygen and water, away from sensitive materials and thereby ensure the long-term stability of the devices. There is, however, no equivalent stretchable packaging that provides a hermetic seal for stretchable devices and systems (4–7). Stretchable materials, such as elastomers, have large free volume and high chain mobility and therefore readily permeate gases. Consequently, materials with a low Young's modulus generally have high gas per-

meability (6, 7). The current approaches to addressing such challenges involve combining materials that have low Young's modulus, such as elastomers, with materials that have low gas permeability, such as inorganic or metallic materials, but these approaches show either limited stretchability or limited hermetic performance.

Liquid metals (LMs) have both metallic and fluidic properties and thus provide an opportunity to achieve stretchable and hermetic sealing. Metals, such as aluminum and steel, are known as excellent permeation barriers and therefore find use in the food industry in canned goods and liners in packaging (such as potato chip bags). Yet, metals are generally inextensible. LMs, especially gallium and its alloys, are an exception that have attracted increased attention from the research community recently (8–11). Their metallic electric conductivity and fluidic deformability make them suitable for applications in stretchable and soft electronics (8, 12, 13). Their metallic thermal conductivity and fluidic deformability also offer the potential of using them as thermal interface materials (14, 15) for dissipating heat from electronic devices. LMs should also have similar hermetic sealing performance as

that of metals, while at the same time show Young's modulus much lower than that of the common elastomers that have limited hermetic performances (Fig. 1A). Such a combination of low Young's modulus and low gas permeability makes LMs ideal candidates for the generation of stretchable and hermetic seals.

We studied the hermetic performance of LMs and demonstrated a stretchable and hermetic seal enabled by LMs with the integration of spacers. A common LM, eutectic gallium indium (EGaIn), was used in this study.

Gas permeability of LMs

To measure the gas permeability of EGaIn, we fabricated a barrier film (fig. S1A) by filling a chamber with EGaIn by the method of vacuum filling (fig. S1B) (16). We measured the permeability of two representative gases: water vapor and oxygen. We used a water vapor transmission rate (WVTR) permeation analyzer (AQUATRAN 3, AMETEK MOCON) to measure the water permeability. The sample was placed between the two chambers with different partial pressure of water vapor, and the vapor flux through the sample was measured. We used an oxygen transmission rate (OTR) permeation analyzer (OX-TRAN 2/22H, AMETEK MOCON) to measure the oxygen permeability.

The permeability, P , is defined by the following equation (7)

$$P = \frac{J * h}{s * \Delta p} \quad (1)$$

where J is the gas flux through the sample per unit time, h is the thickness of the sample, s is the surface area of the sample, and Δp is the difference of gas pressure between two sides of the sample.

Because of the low gas permeability of glass (7), the water and oxygen flux in the area with glass can be neglected. The part with EGaIn is a three-layer laminate structure that includes two layers of polydimethylsiloxane (PDMS) and one layer of EGaIn. When the gas flux reaches the steady state, the gas flux through

¹State Key Laboratory of Metal Matrix Composites, School of Materials Science and Engineering, Shanghai Jiao Tong University, Shanghai 200240, P. R. China. ²Department of Chemical and Biomolecular Engineering, North Carolina State University, Raleigh, NC 27695, USA. ³Shanghai Key Laboratory of Hydrogen Science, School of Materials Science and Engineering, Shanghai Jiao Tong University, Shanghai 200240, P. R. China. ⁴Wanxiang A123-Global Headquarters, A123 Systems, Hangzhou 311215, P. R. China. ⁵Research and Development Center, A123 Systems, Waltham, MA 02451, USA. *Corresponding author. Email: dengtao@sjtu.edu.cn (T.D.); mddickey@ncsu.edu (M.D.D.); shangwen@sjtu.edu.cn (W.S.); jwang.a123systems@gmail.com (J.W.)

†These authors contributed equally to this work.

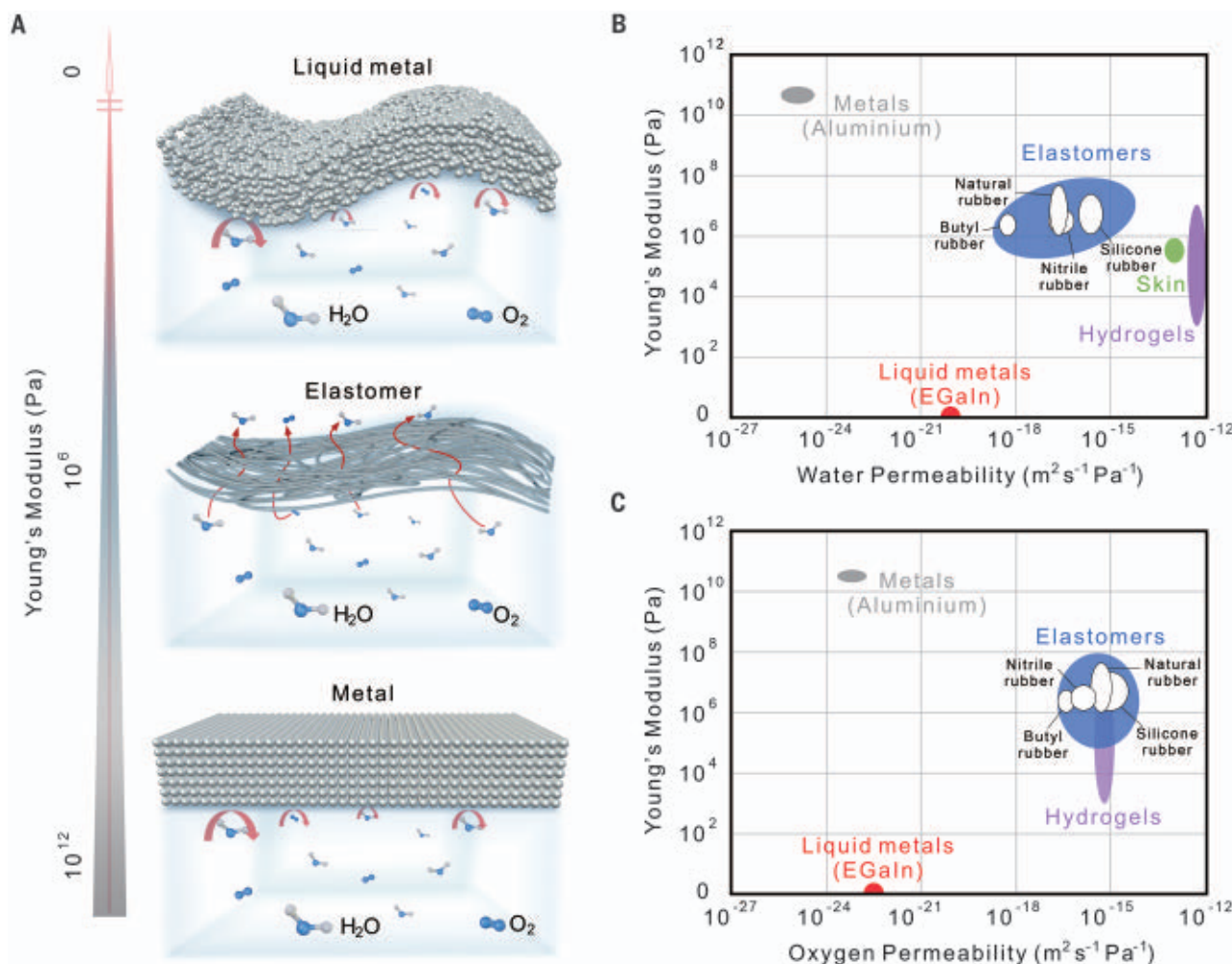


Fig. 1. Gas permeability of LMs. (A) Schematic of mechanical and hermetic properties of metals, elastomers, and LMs. Metals generally have rigidity (high Young's modulus) and low gas permeability. Elastomers have elasticity (low Young's modulus) and high gas permeability. LMs show both fluidity (effectively zero Young's modulus) and gas permeability that is as low as that

of other metals. (B) Young's modulus versus water permeability for various stretchable materials. (C) Young's modulus versus oxygen permeability for various stretchable materials. Except the data of EGaIn, the data points for all materials in (B) and (C) are from (7). A common metal barrier material (Al) is included as a reference in (B) and (C).

each layer is the same, and Eq. 1 can be converted to Eq. 2

$$\Delta\pi_{\text{tot}} = \Delta\pi_{\text{PDMS}_1} + \Delta\pi_{\text{EGaIn}} + \Delta\pi_{\text{PDMS}_2}$$

$$= \frac{J}{s} \left(\frac{h_{\text{PDMS}_1}}{P_{\text{PDMS}}} + \frac{h_{\text{EGaIn}}}{P_{\text{EGaIn}}} + \frac{h_{\text{PDMS}_2}}{P_{\text{PDMS}}} \right) \quad (2)$$

where h_{PDMS_1} , h_{PDMS_2} , and h_{EGaIn} are the thickness of the corresponding layers, and P_{PDMS} and P_{EGaIn} are the permeability of PDMS and EGaIn, respectively.

As shown in fig. S2A, the water flux through the sample with EGaIn reached a stable value, 4.0×10^{-7} cc/day, after about 94-hour measurement. This value is at the lower measurement limit of the WVTR permeation analyzer $[(2.5 \pm 2.5) \times 10^{-7}$ cc/day]. P_{EGaIn} of water was calculated to be $9.6 \times 10^{-21} \text{ m}^2/(\text{s Pa})$, which is more than four orders of magnitude smaller

than that of PDMS (6). The actual permeability of EGaIn may be smaller than the measured value if an instrument with better sensitivity can be used. As shown in fig. S2B, the oxygen flux through the sample with EGaIn reached 2.5×10^{-6} cc/day, which also reaches the measurement limit of the OTR permeation analyzer $[(2.5 \pm 2.5) \times 10^{-6}$ cc/day]. P_{EGaIn} of oxygen was calculated to be $5.0 \times 10^{-23} \text{ m}^2/(\text{s Pa})$, which is more than eight orders of magnitude smaller than that of PDMS (17).

Gas permeability versus Young's modulus for various stretchable materials are plotted in Fig. 1, B and C (7). In Fig. 1, B and C, the solid red dots indicate the measured values for EGaIn. The permeability of oxygen is measured to be close to that of metal [aluminum (Al)]. The permeability of water is relatively high compared with that of metal (Al), which is primarily due to the current limitation of the

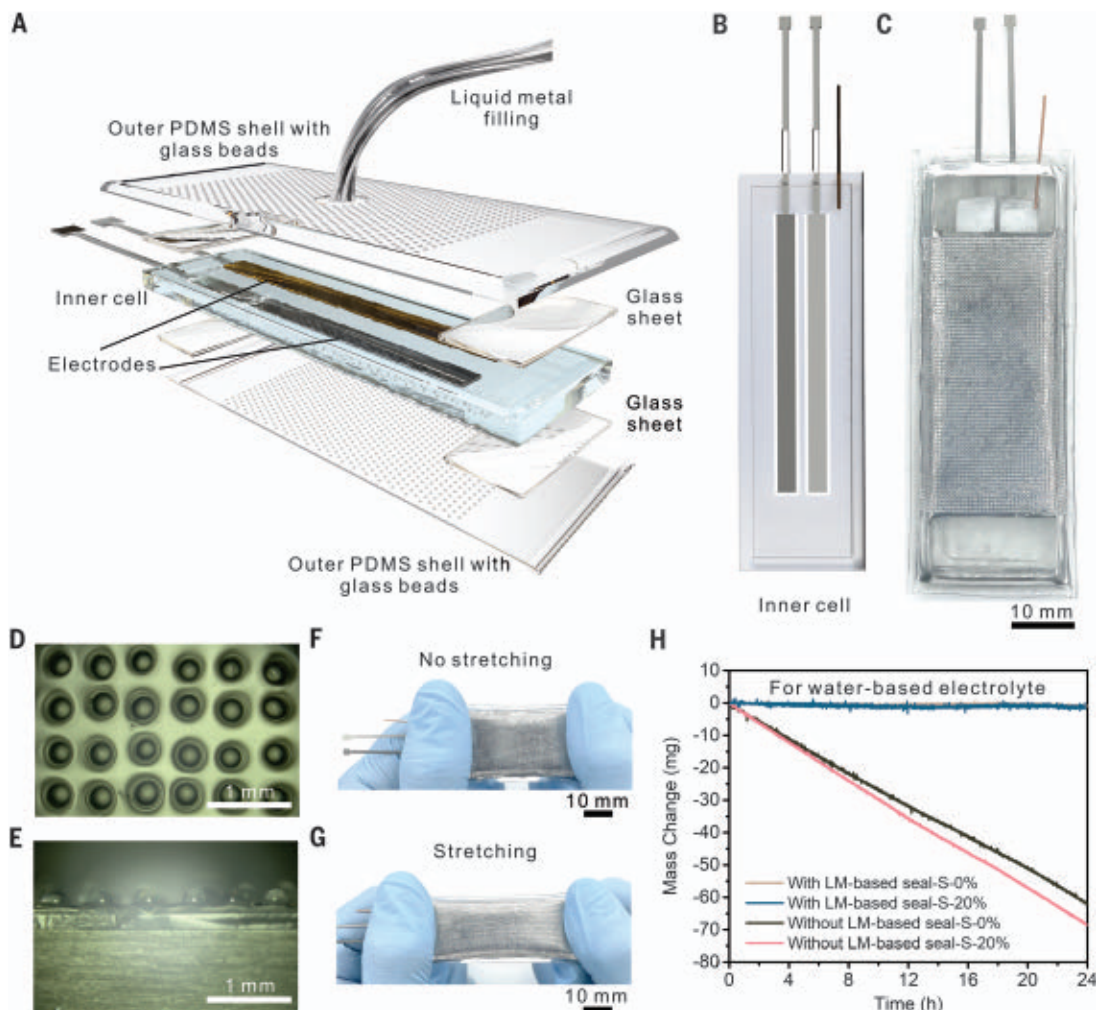
instrument we used for the water permeability measurement.

LM-based soft and hermetic seals

With the low gas permeability and soft mechanical properties, EGaIn opens possible design space to achieve stretchable and hermetic seals, which will help enable the practical long-term applications of stretchable and soft systems that are sensitive to the permeation of various gases, including flexible electronics systems, wearable systems, energy generation and storage systems, heat transfer systems, sensing systems, and biomedical systems (18–25). In this work, we demonstrated the design and fabrication of LM-based seals with the integration of spacers for stretchable batteries—specifically, lithium-ion batteries (LIBs) with a water-based electrolyte. Most research in stretchable batteries focuses on

Fig. 2. Stretchable and hermetic seals for LIBs.

(A) Exploded schematic showing the key components of the LM-based seal that is integrated into the stretchable LIB. (B) Schematic configuration of the inner cell of the stretchable LIB. (C) Photograph of the stretchable LIB with the LM-based seal. (D and E) Optical microscopy images of patterned glass beads on a PDMS sheet from (D) the top view and (E) the cross-sectional view. (F) Photograph of the LIB with the LM-based seal under no stretching. (G) Photograph of the LIB with the LM-based seal under stretching. (H) Mass change of LIBs with and without the LM-based seal. The inner cells for both LIBs were filled with a water-based electrolyte.



the stretchable current collector (26), electrode (27), and electrolyte (28). The stretchable packaging, which plays a critical role in the long-term stability and safe operation of the stretchable batteries, is usually overlooked, with limited performance reported (4, 5).

The exploded schematic in Fig. 2A shows the key components integrated into the stretchable LIB with the LM-based seal. The inner cell in Fig. 2B is a stretchable LIB without a LM-based seal. There are three steps in the fabrication of the LM-sealed LIB: fabrication of the electrodes (fig. S3A), fabrication of the inner cell (fig. S3B), and fabrication of the outer seal (fig. S3C). In the fabrication of the electrodes (fig. S3A), the premixed slurries of cathode materials, which are based on commercial lithium manganese oxide, were coated onto the current collector of stainless steel meshes through the blade coating process. The premixed slurries of anode materials, which are based on carbon-coated lithium titanate phosphate (cc-LTP) (fig. S4) (29), were coated onto stainless steel meshes by using a similar process. The fabri-

cated electrodes were then cut into strips with a size of 45 by 3 mm, which were wrapped by a hydrophilic porous polytetrafluoroethylene (PTFE) separator to avoid internal short-circuiting. The obtained electrodes were further connected with stainless steel tabs for the performance characterization. For the integration of the LM-based seal, parts of the stainless steel tabs that were in contact with LM were precoated with a thin layer of parylene (~10 μm in thickness) to prevent the LM-induced short-circuiting between the tabs. The assembled electrodes were attached onto a PDMS substrate and then sealed with another PDMS sheet to form the inner cell (fig. S3B). This pristine inner cell was further bonded with four glass sheets to create places to grasp on each end of the device during stretching. It was also integrated with a copper tube that worked as an inlet for injecting the electrolyte into the inner cell. In the fabrication of the outer seal (fig. S3C), two outer PDMS sheets patterned with arrays of glass beads, which served as the spacers between the top and bottom PDMS shell of the LM encapsulation,

were attached to the inner cell to form the outer PDMS chamber. With the use of the stretchable material such as PDMS as the encapsulation of the LM, the encapsulation shell might deform under the localized pressure, which will lead to the contact of the top and bottom PDMS shells and the possible failure of the hermetic seal (supplementary text, Deformation pressure and the critical role played by the spacers). The localized pressure is inevitable during the normal operation or deformation (stretching, bending, and twisting) of the soft devices, and the seal will deteriorate without the design of the spacers (30). To prevent the contact of the PDMS shells during operation, glass beads were used in the design to serve as spacers to avoid the failure of the seal from the contact of the PDMS shells. With the glass beads serving as the spacers between the PDMS shells, the PDMS between the neighboring glass beads ensure the stretchability of the integrated LM-based seal. There is a liquid-metal inlet in one of the outer PDMS sheets. EGaIn was filled into the chamber between the inner

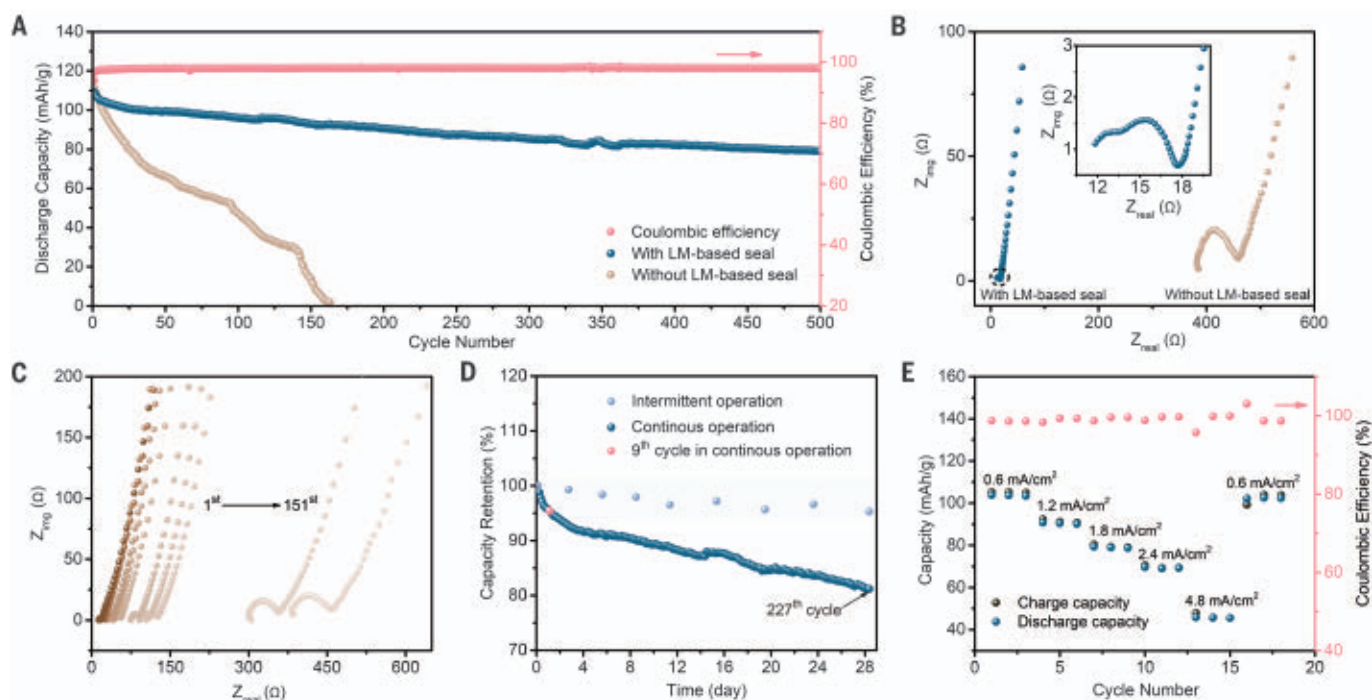


Fig. 3. Electrical performance of the stretchable LIBs under no deformation.

(A) Room-temperature-cycle life comparison at the current density of 0.6 mA/cm^2 for the LIBs with and without the LM-based seal. The pink dots indicate the corresponding coulombic efficiency of the LIB with the LM-based seal. (B) Comparison of EIS at the 100th cycle between LIBs with and without the LM-based seal. (Inset) A

detailed look at the low-impedance portion of the EIS for the LIB with the LM-based seal. (C) Cycle dependent EIS for the LIB without the LM-based seal. (D) Capacity retention comparison between continuous and intermittent operation of LIBs with the LM-based seal. (E) Charge and discharge rate capabilities (black and blue dots) and coulombic efficiency (pink dots) of the LIB with the LM-based seal.

cell and outer PDMS shell through the liquid-metal inlet by means of vacuum filling. During vacuum filling, the spacers can also prevent the outer PDMS chamber from collapse, which ensures the successful filling of LM. A photograph of the prepared LIB with the LM-based seal is shown in Fig. 2C. The process for patterning the glass beads is shown in fig. S11. As shown in Fig. 2D, glass beads were patterned on the PDMS sheet and separated from each other. The cross-sectional image shows that part of the glass beads was embedded into the PDMS sheet, which helps generate strong bonding (Fig. 2E). The separation between glass beads ensures the stretchability of the PDMS sheets during the stretching operation of the sealed LIB (Fig. 2, F and G). A stress-strain curve of the sealed LIB was measured and compared with that of a control LIB without the LM-based seal (fig. S12). Two stress-strain curves (fig. S13) almost overlap, and the calculated Young's modulus of both the LIB with and the LIB without the LM-based seal is about 0.83 MPa , which is reasonable considering an effectively zero Young's modulus of the LM.

The hermetic performance of the LM-based seal was characterized by monitoring the mass change of the LIB filled with a water-based electrolyte. The inner cell of the LIB was filled with

an electrolyte through the electrolyte inlet. After filling the inner cell, the LIB was placed onto an analytical balance, which was inside a glove box that was filled with argon, to monitor the mass change. As shown in Fig. 2H, the mass of the LIB with the LM-based seal (Fig. 2H, brown and blue curves) did not change during 24-hour measurement under both the original state and 20% strain. In comparison, the control LIB without the LM-based seal (fig. S12) exhibited rapid mass loss (Fig. 2H, black and red curves), indicating outward permeation of water vapor through PDMS sheets. The enlarged surface area of the control LIB under 20% strain increased outward permeation of water vapor, resulting in a larger mass change than that of the LIB with no stretching.

Performance of the stretchable LIBs with the LM-based seals

The electrical performance of the stretchable LIBs with and without the LM-based seal was first characterized under no deformation. The room-temperature-cycle lives of the two LIBs with and without the LM-based seal are shown in Fig. 3A. The one with the LM-based seal exhibited a reversible capacity retention of $\sim 90\%$ after 140 cycles and $\sim 72.5\%$ after 500 cycles. The capacity decrease for the unstretched LIB is primarily due to the in-

evitable side reactions during the operations of LIBs rather than the gas permeation through the LM-based seal. In comparison, the control LIB without the LM-based seal (fig. S12) showed large capacity decay, with complete failure after 160 cycles owing to the outward permeation of the water vapor and inward permeation of air though the PDMS sheets (4, 31). The coulombic efficiency of the LIB with the LM-based seal was $\sim 98\%$. A comparison of the electrochemical impedance spectroscopy (EIS) of the two LIBs at the 100th cycle is shown in Fig. 3B; the impedance of the LIB with the LM-based seal was much lower than that of the LIB without the LM-based seal. Because of the lack of the LM-based seal, the impedance of the control LIB continuously increased during the operation owing to the gradual drying out of the electrolyte and deterioration of electrodes (Fig. 3C) (4, 32, 33), resulting in the failure of the LIB. As shown in Fig. 3D, the LIB with the LM-based seal also showed a slow decline of discharge capacity during the continuous 227 cycles in 28 days, and the detailed galvanostatic voltage profiles of the first nine cycles are shown in fig. S14. When the LIB was intermittently operated for only nine cycles in the same 28 days (Fig. 3D), however, the performance degradation was much smaller than that of the LIB with continuous

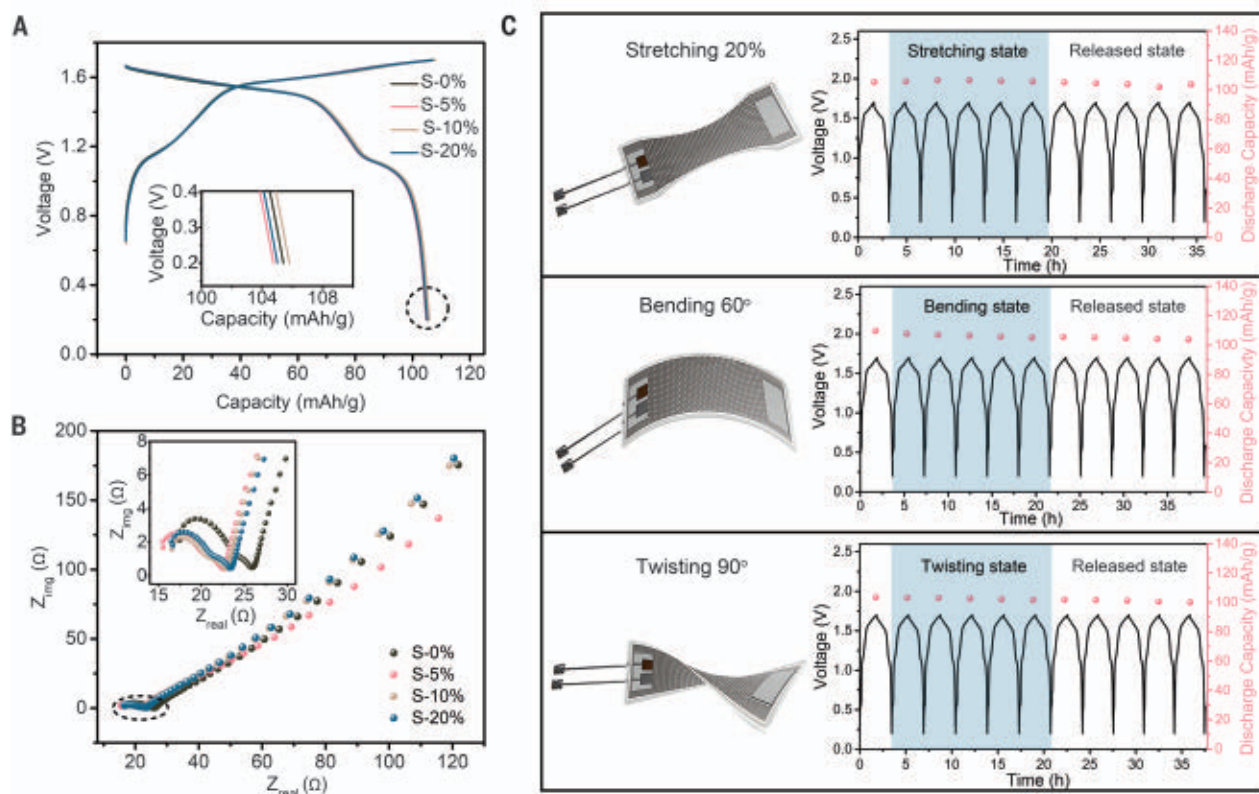


Fig. 4. Electrical performance of the stretchable LIBs with the LM-based seals under deformation. (A) Galvanostatic voltage profiles and (B) EIS of a LIB with the LM-based seal under 0, 5, 10, and 20% strain. The dashed shapes in (A) and (B) indicate the enlarged area shown in the respective insets. (Top inset) Detailed look at the ends of the galvanostatic discharge curves of the LIB

under 0, 5, 10, and 20% strain. (Bottom inset) Detailed look at the high frequency range of the EIS of the LIB. (C) The voltage profile (black curve) and discharge capacity (pink dots) of the LIB under continuous cyclic stretching (20%), bending (60°), and twisting (90°). (Insets) The schematics of corresponding deformations of the LIB.

operation. The capacity retention of the intermittently operated LIB after nine cycles in 28 days was nearly the same as that of the LIB that was continuously operated after nine cycles in ~1 day. The results indicate that the performance degradation of the LIB during the continuous cycling was mainly due to the inevitable side reactions, such as evolution of H_2 and O_2 from aqueous electrolytes and active materials dissolution (32, 34), rather than the permeation of gases through the seal.

The charge and discharge rate capabilities (Fig. 3E, black and blue dots) of the LIB with the LM-based seal were measured at various current densities. A stable specific capacity of ~100 mA-hour/g could be achieved at the current density of 0.6 mA/cm². Overall, it could achieve a high average specific capacity of ~90, 80, 70, and 50 mA-hour/g at 1.2, 1.8, 2.4, and 4.8 mA/cm², respectively. The decrease of the specific capacity with the increase of current density is ascribed to the electrode polarization at high currents. When the current density decreased back to 0.6 mA/cm², the capacity also recovered to ~100 mA-hour/g. The corresponding galvanostatic charge and discharge curves at different current densities are presented in fig. S15.

Under deformation, the electrical performance of the stretchable LIB with the LM-based seal was further characterized. The LIB was operated at the current density of 0.6 mA/cm² and in the potential window between 0.2 and 1.7 V. The corresponding galvanostatic charge-discharge curves of the LIB under the released state and stretched states with different strains are shown in Fig. 4A. A high reversible capacity of ~105.5 mA-hour/g was achieved for the LIB at the released state, and the capacity can be sustained at 104.8, 105.8, and 105.0 mA-hour/g under 5, 10, and 20% strain, respectively. The close overlapping of these curves indicates that this LIB can function well even under 20% strain. The EIS in Fig. 4B also shows the relatively good stability of the LIB during stretching. The tighter contact between the tabs and electrodes of the LIB under stretching states might decrease the contact impedances in the high-frequency range as shown in Fig. 4B, inset (33). Furthermore, different stretching states might result in random changes of the electrochemical environment in the inner cell, such as changes of the distance between two electrodes and the position of the residual bubbles (from the possible evolution of H_2 and O_2), which causes the random differences of the

diffusion impedances in the low-frequency range (Fig. 4B) (33). To further evaluate electrical performance of the LIB with the LM-based seal under continuously cyclic deformation, we performed cycling tests at 0.6 mA/cm² under a strain of 20%, a bending angle of 60°, and a twisting angle of 90° (Fig. 4C and fig. S16). The LIBs first operated one cycle under the released state; five cycles under stretching, bending, or twisting state; and then five cycles under the released state. The galvanostatic charge-discharge curves in Fig. 4C and the corresponding capacities remained almost the same, regardless of the deformation state of the LIB. With the use of arrays of glass beads as the spacers, the collapse of the PDMS shells within the LM encapsulation is avoided during the deformation operation of the LIBs, which enables the stable hermetic sealing of the LM-based seal. The demonstrated stability of the LIBs with the LM-based seal offers promising potential of using such devices as the power component in stretchable electronics (fig. S17).

LM-based seals for a stretchable phase-change-based heat transfer device

Besides LIBs, this LM-based hermetic seal can also be used for other stretchable systems. In

the supplementary materials, we further describe the application of this LM-based seal in a stretchable phase-change-based heat transfer device that can be used for the thermal management of stretchable electronics (fig. S18). Thermal management of stretchable electronics becomes increasingly important with the increase of the power used. Phase-change-based heat transfer devices have been widely used in modern electronics because of their superior thermal transport capability (35). The development of stretchable phase-change-based heat transfer devices, however, is limited owing to the lack of stretchable and hermetic seals. Both the inward permeation of noncondensable gas and the outward permeation of gasified working fluid will decrease the thermal conductivity of phase-change-based heat transfer devices. The prepared LM-based seal performed well against the permeation of ethanol (fig. S18D), which is the working fluid in the heat transfer device. The hermetic seal functions well even under heating during the stretching operation of the phase-change-based heat transfer device (fig. S18G), which showed an increased thermal conductivity of $\sim 309 \text{ W/(m K)}$ at 10% strain.

LM-based seals for wireless communication

Because LM is an electric conductor, it can block electromagnetic communication into and out of the seal. In the design of a LM-based seal that allows wireless communication, we included a glass window into the original design (fig. S21, A and B). In the design, the glass window is used to transmit electromagnetic wave and at the same time provide the hermetic sealing locally. The LM surrounding the glass window provides stretchability and hermetically seals the rest of the device. To characterize the wireless communication, stretchability, and gas permeability of the new design of the LM-based seal, we fabricated a wireless communication device with the modified LM-based seal (fig. S21, C and D).

As shown in a schematic (fig. S22A), when a working radio frequency identification (RFID) reader (RD906M, 906 MHz, Guangzhou Wangyuan Electronic Equipment Co.) is connected with a computer, it will send out radio signals. Without the presence of the RFID tag (CER1207, 860 to 960 MHz, Guangzhou Wangyuan Electronic Equipment Co.), no responding signals can be transmitted back to the reader, which results in only the lighting up of the red light-emitting diode (LED) on the reader and a blank screen of the computer (fig. S22, A, schematic, and B, the optical images captured during the experiment). With the presence of the wireless communication device fabricated (fig. S21D), there was communication between the RFID tag in the device and the outside reader. Both the red

LED and the green LED on the reader lighted up, and there were signals displayed on the computer (fig. S22, C, schematic, and D, the optical images captured during the experiment; and movie S1). The experimental results in fig. S22E show that there was communication between the RFID tag inside the device and the outside reader even when we turned over the device (movie S2). Moreover, the wireless communication device with the modified LM-based seal could continuously communicate with the reader even under 20% strain (fig. S22F and movie S3). We also filled the inner cell of the device with deionized water containing $\sim 2.8 \text{ wt } \%$ red dye (Wilton Industries, IL) through the copper tube and found that the filled device could still communicate with the outside reader even under 20% strain (fig. S22G and movie S4).

The hermetic performance of the modified LM-based seal was also characterized. After filling the inner cell with a water-based electrolyte, the same one used in LIBs, the mass of the wireless communication devices with and without the modified LM-based seal was monitored through an analytical balance inside a glove box that was filled with dry argon. As shown in fig. S22H, the mass of the device with the modified LM-based seal (fig. S22H, brown and blue curves) did not change under both the original state and 20% strain state during 24-hour measurement, which is similar to the performance of the LIBs with the LM-based seal without the glass window and indicates good hermetic sealing of the modified LM-based seal. In comparison, the control device without the modified LM-based seal exhibited rapid mass loss (fig. S22H, black and red curves), which is also similar to the rapid mass loss in the LIBs without the LM-based seals.

With the integration of spacers, this work demonstrates a stretchable LM-based seal that has low permeability for blocking the transport of gases and vapors such as oxygen, water, and ethanol. In addition, LMs have metallic, thermal, chemical, and electrical properties, which may be further harnessed for additional functionality in such a barrier material that encases electronic devices. Considering the demonstrated barrier properties, this work provides a promising route for creating soft and stretchable devices with stable long-term operation.

REFERENCES AND NOTES

1. Y. Jiang *et al.*, *Science* **375**, 1411–1417 (2022).
2. J. T. Reeder *et al.*, *Science* **377**, 109–115 (2022).
3. S. Wang *et al.*, *Nature* **555**, 83–88 (2018).
4. D. G. Mackanic, M. Kao, Z. Bao, *Adv. Energy Mater.* **10**, 2001424 (2020).
5. D. G. Mackanic, T.-H. Chang, Z. Huang, Y. Cui, Z. Bao, *Chem. Soc. Rev.* **49**, 4466–4495 (2020).
6. P. Le Floch *et al.*, *ACS Appl. Mater. Interfaces* **9**, 25542–25552 (2017).

7. P. Le Floch, S. Meixuanzi, J. Tang, J. Liu, Z. Suo, *ACS Appl. Mater. Interfaces* **10**, 27333–27343 (2018).
8. M. D. Dickey, *Adv. Mater.* **29**, 1606425 (2017).
9. T. Daeneke *et al.*, *Chem. Soc. Rev.* **47**, 4073–4111 (2018).
10. A. Zavabeti *et al.*, *Science* **358**, 332–335 (2017).
11. Y. Ding *et al.*, *Adv. Mater.* **32**, e2002577 (2020).
12. E. J. Markvicka, M. D. Bartlett, X. Huang, C. Majidi, *Nat. Mater.* **17**, 618–624 (2018).
13. S. Liu, D. S. Shah, R. Kramer-Bottiglio, *Nat. Mater.* **20**, 851–858 (2021).
14. H. Wang *et al.*, *Adv. Mater.* **33**, e2103104 (2021).
15. C. Wang *et al.*, *Sci. Adv.* **7**, eabe3767 (2021).
16. Y. Lin *et al.*, *Lab Chip* **17**, 3043–3050 (2017).
17. T. Merkel, V. Bondar, K. Nagai, B. D. Freeman, I. Pinnau, *J. Polym. Sci., B, Polym. Phys.* **38**, 415–434 (2000).
18. C. Wang *et al.*, *Science* **377**, 517–523 (2022).
19. D. Jung *et al.*, *Science* **373**, 1022–1026 (2021).
20. Z. Yan *et al.*, *Science* **375**, 852–859 (2022).
21. H. J. Kim, B. Chen, Z. Suo, R. C. Hayward, *Science* **367**, 773–776 (2020).
22. X. Xiao *et al.*, *Sci. Adv.* **7**, eabl3742 (2021).
23. Z. Zhang *et al.*, *Nature* **603**, 624–630 (2022).
24. J. R. Sempionatto *et al.*, *Nat. Biomed. Eng.* **5**, 737–748 (2021).
25. M. Mariello, K. Kim, K. Wu, S. P. Lacour, Y. Leterrier, *Adv. Mater.* **34**, e2201129 (2022).
26. M. Gu *et al.*, *Sci. Adv.* **5**, eaaw1879 (2019).
27. K. Liu *et al.*, *Joule* **2**, 1857–1865 (2018).
28. D. G. Mackanic *et al.*, *Nat. Commun.* **10**, 5384 (2019).
29. G.-M. Weng *et al.*, *Energy Storage Mater.* **24**, 557–564 (2020).
30. N. Ochirkhuyag *et al.*, *ACS Appl. Mater. Interfaces* **14**, 48123–48132 (2022).
31. J.-Y. Luo, W.-J. Cui, P. He, Y.-Y. Xia, *Nat. Chem.* **2**, 760–765 (2010).
32. H. Kim *et al.*, *Chem. Rev.* **114**, 11788–11827 (2014).
33. N. Meddings *et al.*, *J. Power Sources* **480**, 228742 (2020).
34. L. Suo *et al.*, *Science* **350**, 938–943 (2015).
35. H. Tang *et al.*, *Appl. Energy* **223**, 383–400 (2018).

ACKNOWLEDGMENTS

We thank Q. Kang, P. Li, X. Huang, X. Yan, and J. Gu for the help with the instruments used in preparing and characterizing LIBs. We thank W. Cheng for the help with the modeling of the spacers. **Funding:** This work was supported by the Innovation Program of Shanghai Municipal Education Commission (grant 2019-01-07-00-02-E00069), the National Natural Science Foundation of China (51973109 and 51873105), the Zhi-Yuan Endowed fund from Shanghai Jiao Tong University, and Shanghai Jiao Tong University Overseas Study Grants. M.D.D. is grateful for the support from the National Science Foundation (ASSIST, EEC-1160483, and CMMI- 2032415). W.J. acknowledges the support from MOTIE (Ministry of Trade, Industry and Energy) in Korea, under the Fostering Global Talents for Innovative Growth Program (P0008746) supervised by the Korea Institute for Advancement of Technology (KIAT). **Author contributions:** Q.S., J.W., W.S., M.D.D., and T.D. conceived and planned the study. Q.S., M.J., R.W., K.S., M.H.V., W.J., F.K., R.K., and F.Z. performed fabrication, testing, and characterizations. J.W., W.S., M.D.D., and T.D. supervised the study. All authors discussed and analyzed the results and contributed to the writing of the paper. **Competing interests:** The authors declare that they have no competing interests. **Data and materials availability:** All data are available in the main text or the supplementary materials. **License information:** Copyright © 2023 the authors; some rights reserved; exclusive licensee American Association for the Advancement of Science. No claim to original US government works. <https://www.science.org/about/science-licenses-journal-article-reuse>

SUPPLEMENTARY MATERIALS

science.org/doi/10.1126/science.ade7341

Materials and Methods
Supplementary Text
Figs. S1 to S22
References (36, 37)
Movies S1 to S4

Submitted 8 September 2022; accepted 5 January 2023
10.1126/science.ade7341

ORGANIC CHEMISTRY

Asymmetric counteranion-directed photoredox catalysis

Sayantani Das^{1†}, Chendan Zhu^{1†}, Derya Demirbas¹, Eckhard Bill^{2‡},
Chandra Kanta De^{1*}, Benjamin List^{1*}

Photoredox catalysis enables distinctive and broadly applicable chemical reactions, but controlling their selectivity has proven to be difficult. The pursuit of enantioselectivity is a particularly daunting challenge, arguably because of the high energy of the activated radical (ion) intermediates, and previous approaches have invariably required pairing of the photoredox catalytic cycle with an additional activation mode for asymmetric induction. A potential solution for photoredox reactions proceeding via radical ions would be catalytic pairing with enantiopure counterions. However, although attempts toward this approach have been described, high selectivity has not yet been accomplished. Here we report a potentially general solution to radical cation-based asymmetric photoredox catalysis. We describe organic salts, featuring confined imidodiphosphorimidate counteranions that catalyze highly enantioselective [2+2]-cross cycloadditions of styrenes.

Photoredox catalysis is an emerging field in chemistry, enabling the design and development of diverse transformations that often complement the traditional tool kit of chemical synthesis (1). Typically, in a photoredox transformation, light is absorbed by the photocatalyst, which then triggers a single electron transfer (SET) event, leading to the formation of highly reactive radical ions. For example, in an oxidative mode, SET delivers the corresponding substrate radical cation. In contrast, in a reductive mode, a radical anion is initially generated through

SET from the catalyst to the substrate. Both pathways have led to the design of a large diversity of different and often broadly useful transformations (2–5). Consequently, the development of asymmetric photoredox catalysis (6) has become a topic of high current relevance. However, because general enantioselective methods toward the control of radical ions per se have not been available, previous approaches to asymmetric photoredox catalysis invariably required a second activation mode and catalytic cycle to enable the stereoselective bond forming event (Fig. 1A). Examples include enamine (7) and iminium ion catalysis (8), carbene catalysis (9), Brønsted acid catalysis (10–12), transition metal catalysis (13–16), and Lewis acid catalysis (17–21), which all benefit from previously established methods of asymmetric induction. While these dual catalysis approaches have led to useful trans-

formations with excellent enantioselectivity, the requirement of a second catalytic cycle, even in those cases when only a single catalyst is used, creates certain limitations regarding substrate functionalization and, more importantly, reaction diversity in general. Approaches not in need of such a second catalytic cycle could potentially offer a more general solution to asymmetric photoredox catalysis and enable enantioselective versions of a multitude of broadly useful methods for chemical synthesis.

One particularly promising and elegant recent approach uses (modified) enzymes (22), which by virtue of their well-defined active sites can preorganize highly reactive intermediates to engage in stereoselective transformations. An alternative strategy involves the use of enantiopure counterions paired with an achiral, charged photocatalyst. Recently, attempts toward this approach in radical cation-based Diels-Alder reactions (23) and in anti-Markovnikov hydroetherifications (24) have been reported. However, the employed chiral binol-based phosphates did not provide high enantioselectivity. We hypothesized that to advance this asymmetric counteranion-directed catalysis (ACDC) (25) approach to photoredox catalysis toward greater selectivity and generality, two features of the enantiopure counteranion would be required. First, its basicity should not be too high, to avoid deprotonation of the typically highly acidic radical cation intermediates, which could lead to nonproductive radical pathways. The second important anion feature we expected to be required would be a confined active site, capable of controlling the selectivity in reactions of only weakly coordinating radical cations. Indeed, we were hopeful that our recently introduced imidodiphosphorimidate (IDPi) (26) anions, which have enabled control over other challenging

¹Max-Planck-Institut für Kohlenforschung, D-45470 Mülheim an der Ruhr, Germany. ²Max-Planck-Institut für Chemische Energiekonversion, D-45470 Mülheim an der Ruhr, Germany. *Corresponding author. Email: list@kofo.mpg.de (B.L.); de@kofo.mpg.de (C.K.D.)

†These authors contributed equally to this work.

‡Deceased.

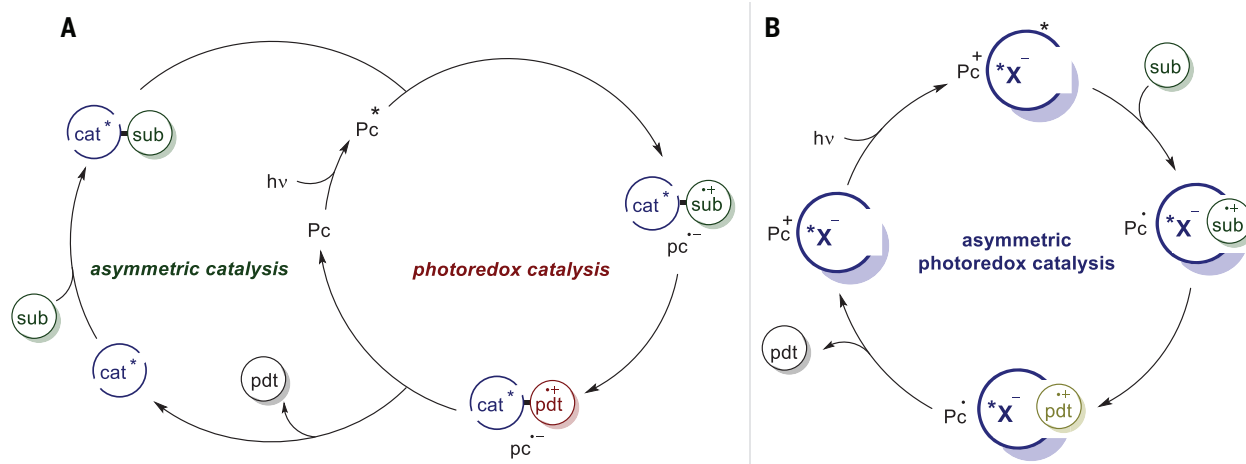


Fig. 1. General catalytic cycles for enantioselective photoredox catalysis. (A) Previous approaches have been based on two catalytic cycles, a photoredox cycle and an asymmetric catalysis cycle. (B) The approach suggested in this work. sub, substrate; cat, catalyst; pdt, product; pc, photocatalyst; X, enantiopure anion; hv, photon energy.

and previously inaccessible cations, such as aliphatic oxocarbenium ions (27) and even purely hydrocarbon-based carbocations (28), could offer a solution in this context. Such an ACDC approach to photoredox catalysis, by only requiring a single catalytic cycle, could offer great potential generality (Fig. 1B). A minimal and sufficient requirement of this strategy would be just the formation and involvement in the stereoselectivity-determining step of a radical cation intermediate.

At the onset of our study, we decided to explore the photoredox catalytic intermolecular [2+2] cycloaddition reaction between *trans*-anethol and styrene. Despite pioneering contributions on enantioselective photocatalytic [2+2] cycloadditions (29, 30), this challenging and potentially useful reaction has not previously been accomplished enantioselectively. We began by exchanging the counteranion of the commercially available pyrylium tetrafluoroborate photoredox catalyst **4g** with a series of enantiopure anions, derived from acids covering a broad pK_a range (where K_a is the acid dissociation constant) (Fig. 2). A brief investigation of reaction conditions revealed the requirement of naphthalene as an electron relay cocatalyst (see table S1 for details) (31). As expected, the conjugate base of a chiral phosphoric acid (CPA; **a**) and an imidodiphosphoric acid (IDP; **b**) were too basic to impart any reactivity. Similar results were observed when using the anion of an iminoimidodiphosphoric acid (IIDP; **c**) and a chiral disulfonimide

(DSI; **d**). In sharp contrast, the anion of our highly acidic and confined imidodiphosphorimidate (IDPi; **e**), catalyst **4e**, enabled superior catalytic performance. More importantly, high enantioselectivity was already observed with this pyrylium-IDPi salt. Notably, the anion of the even more acidic phosphoramidimide (PADi; **f**) afforded the product in only moderate yield and poor enantioselectivity. While 58% consumption of substrate **1a** was observed, only 16% yield of product **3a** was obtained, with poor enantioselectivity, presumably owing to a lack of confinement. The parent tetrafluoroborate catalyst **4g** gave a moderate conversion of substrate **1a** but provided only traces of the product. Upon a brief screening of catalysts and reaction conditions (see table S1 for details), we selected catalyst **4e** and a 1:1 solvent mixture of dichloromethane and 2-methyltetrahydrofuran at -100°C for 1 day and found that cycloaddition product **3a** can be obtained in excellent yield and with excellent enantioselectivity [95.5:4.5 enantiomeric ratio (er)].

A broad range of styrenes with different electronic properties and substituents at different ring positions were evaluated in the reaction with *trans*-anethol derivatives, and the cyclobutane products were obtained with good to excellent yields and enantioselectivities (Fig. 3). Moreover, all products were obtained as single diastereomer, as judged from inspecting crude nuclear magnetic resonance (NMR) spectra. Styrenes with electron-withdrawing

substituents gave products **3b** to **3f** in good yields and with good to excellent enantioselectivities. Similarly, styrenes featuring electron-donating substituents, apparently independent of their steric properties, provided products **3g** to **3j** in excellent enantioselectivities. Disubstituted arene-based styrenes were also found to be suitable reaction partners and furnished the desired products (**3k** and **3l**) with excellent enantioselectivity. Notably, the reaction is compatible with alcohol, silyl ether, aldehyde, ester, and even terminal olefin functionality, leading to products **3m** to **3q** in good yield and with excellent enantioselectivities. We also investigated two other anethol derivatives providing benzyl ether **3r** and free phenol **3s** with excellent enantioselectivity. For additional substrates, see fig. S1.

As one would expect for a reaction proceeding via radical cation-IDPi anion pair, we found almost identical enantioselectivities when we used a variety of photocatalysts that feature an identical IDPi counteranion (Fig. 4). For example, three different photoredox catalysts that are known to be excited with blue light were evaluated (**4e**, **5e**, and **6e**). All led to full consumption of olefin **1a**. However, whereas our standard catalyst **4e** and the frequently used *N*-Ph acridinium organophotoredox catalyst **5e** led to the product in 90 and 56% yields, respectively, and with identical enantioselectivities, popular iridium catalyst **6e** did not provide the desired product. Recently, several different organophotoredox catalysts

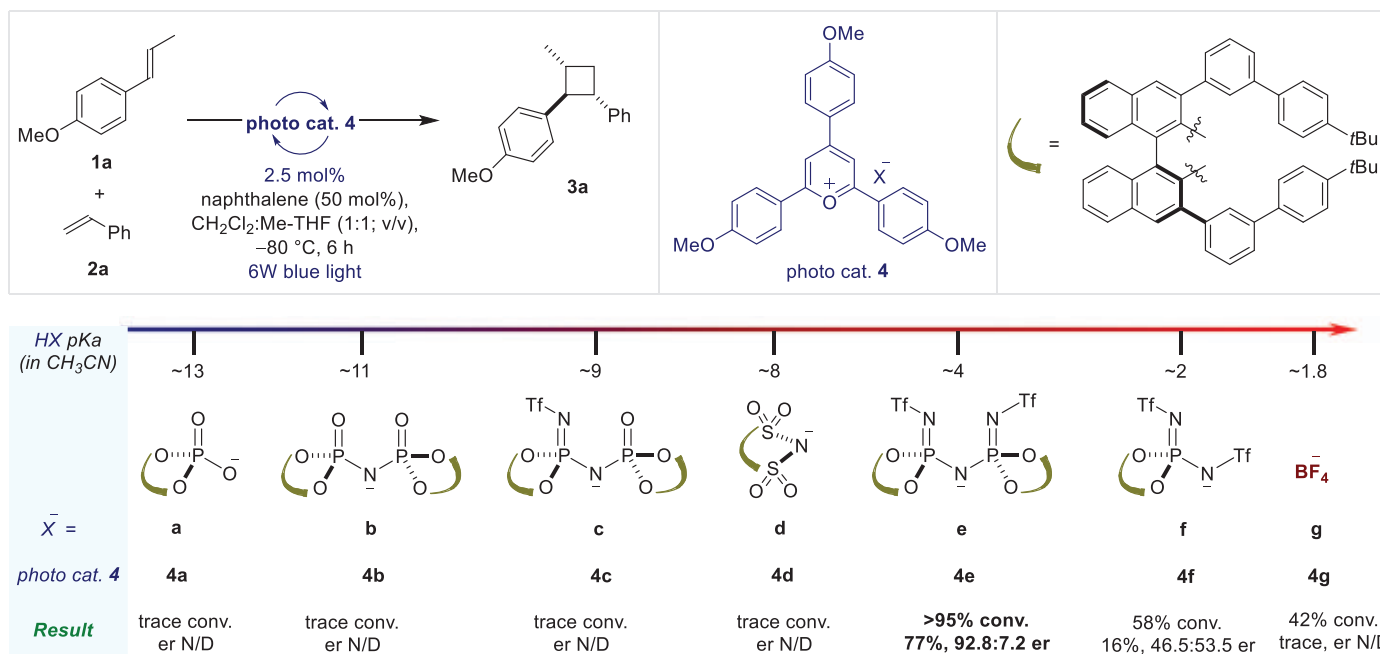


Fig. 2. Investigation of different counteranions in the pyrylium photoredox catalytic intermolecular [2+2] cycloaddition reaction between *trans*-anethol and styrene. Yields were determined by proton NMR spectroscopy using benzyl methyl ether as an internal standard. The enantiomeric ratio was determined by high-performance liquid chromatography (HPLC). MeO, methoxy; Ph, phenyl; Me-THF, methyltetrahydrofuran; *t*Bu, *tert*-butyl; HX, Brønsted acid; conv., conversion; Tf, triflyl; N/D, not determined.

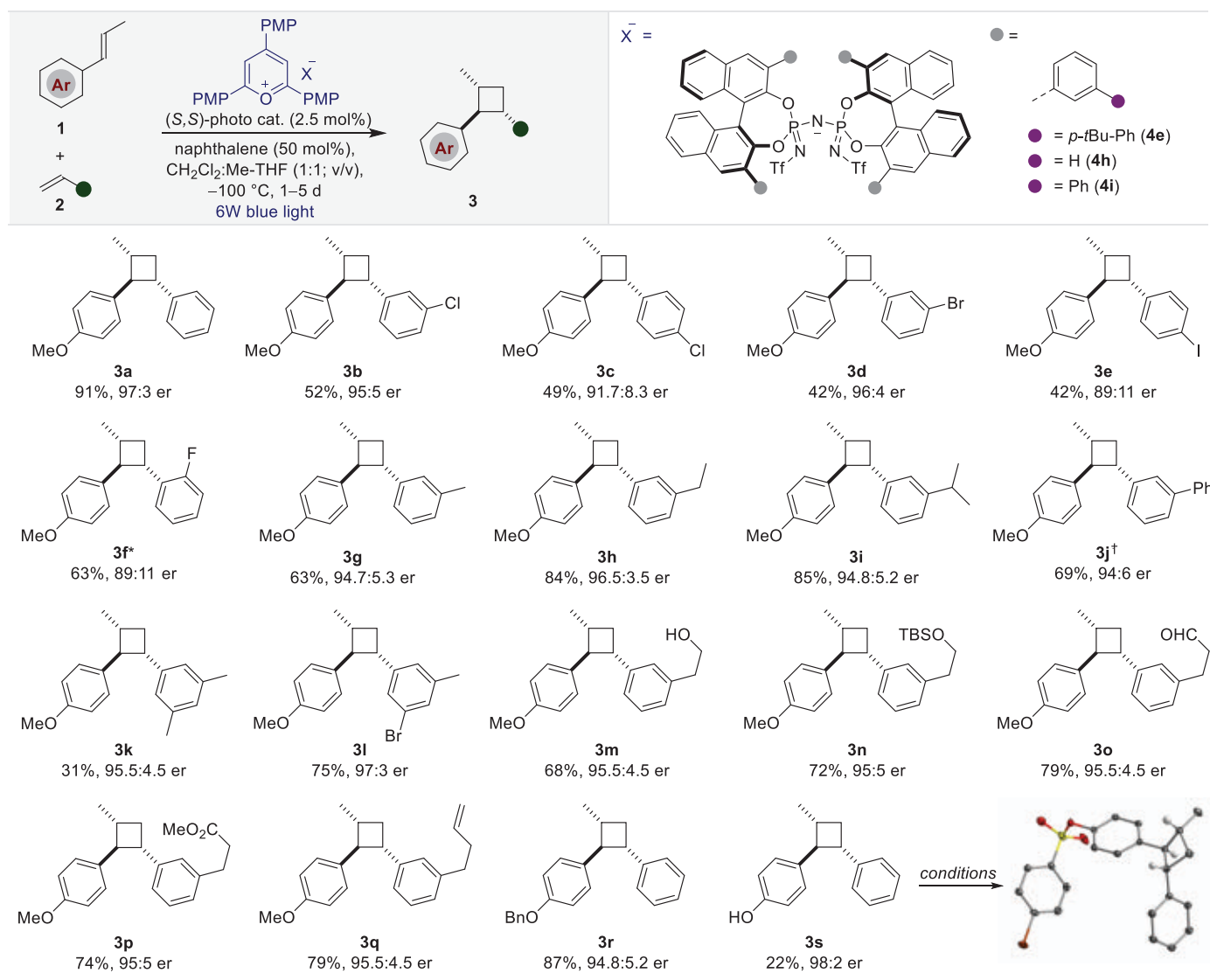


Fig. 3. Scope of the intermolecular [2+2] cycloaddition reactions. Reactions were performed at 0.1 mmol scale. Enantiomeric ratio was determined by HPLC (see supplementary materials for details). The asterisk symbol indicates use of catalyst **4h**. The single-dagger symbol indicates use of catalyst **4i**. PMP, *p*-methoxyphenyl; *p*-*t*Bu-Ph, *p*-*tert*-butyl-phenyl; TBSO, *tert*-butyldimethylsilyloxy; OHC, aldehyde functional group.

that can be excited with green light were disclosed (32, 33), and we became interested in exploring these cationic species paired with our IDPi counteranion. Indeed, upon green-light irradiation, photoredox catalysts **7e** and **8e** furnished the product in 92 and 19% yield, respectively, and with the same enantioselectivity. Finally, a ruthenium-based photoredox catalyst, **9e**, irradiated with white light furnished product **3a** in <5% yield and once again with a similar er (97.3:2.7). The small changes of enantioselectivity may arise from the heat generated by the different light sources. The obtained results clearly support our ion-pairing design and suggest generality of asymmetric counteranion-directed photoredox catalysis (ACPC).

The availability of these enantiopure photocatalysts by means of simple salt metathesis

enabled an evaluation of their chemical stability and photophysical properties. At first, to establish the stability of catalyst **4e**, our model reaction between *trans*-anethol and styrene was carried out under optimized conditions, and the reaction mixture was analyzed by NMR spectroscopy after ~60% conversion. Both fluorine-19 (^{19}F) NMR (Fig. 5A) and phosphorous-31 (^{31}P) NMR (Fig. 5B) spectra confirmed that essentially no decomposition took place. We further compared catalysts **4g** and **4e** by ultraviolet-visible (UV-vis) absorption and fluorescence spectroscopy. As expected, both catalysts have very similar spectra in the visible range, with absorption maximum 1 ($\lambda_{\text{max}1}$) at 425 nm and $\lambda_{\text{max}2}$ at 456 nm (Fig. 5E, solid lines). Similarly, upon excitation at 425 nm, similar fluorescence spectra with

λ_{max} at 535 nm were measured for both catalysts (Fig. 5E, dashed lines). Our spectroscopic investigations thus confirm the stability of the pyrylium photocatalyst. Furthermore, to identify which reagent engages in the initial oxidative SET with the excited-state catalyst, steady-state fluorescence (34, 35) quenching experiments with the individual reaction components were conducted. We measured the steady-state fluorescence decay for both catalysts **4g** and **4e**, respectively, using 425 nm pulsed excitation in the presence of starting material **1a** or **2a**, respectively. As expected from the redox potential of catalyst **4g** [+1.84 V versus saturated calomel electrode (SCE)], anethol (**1a**; +1.14 V versus SCE) showed a strong and concentration-dependent fluorescence decay (Fig. 5C). A very similar behavior was observed with catalyst

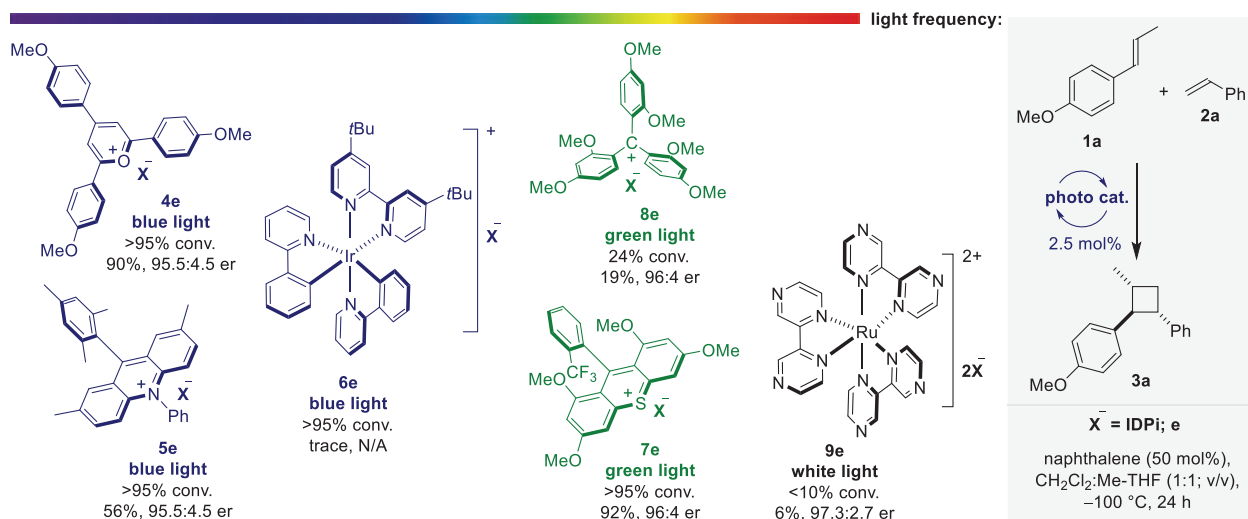


Fig. 4. Evaluation of different photocatalysts with IDPi counteranion under different light wavelengths.

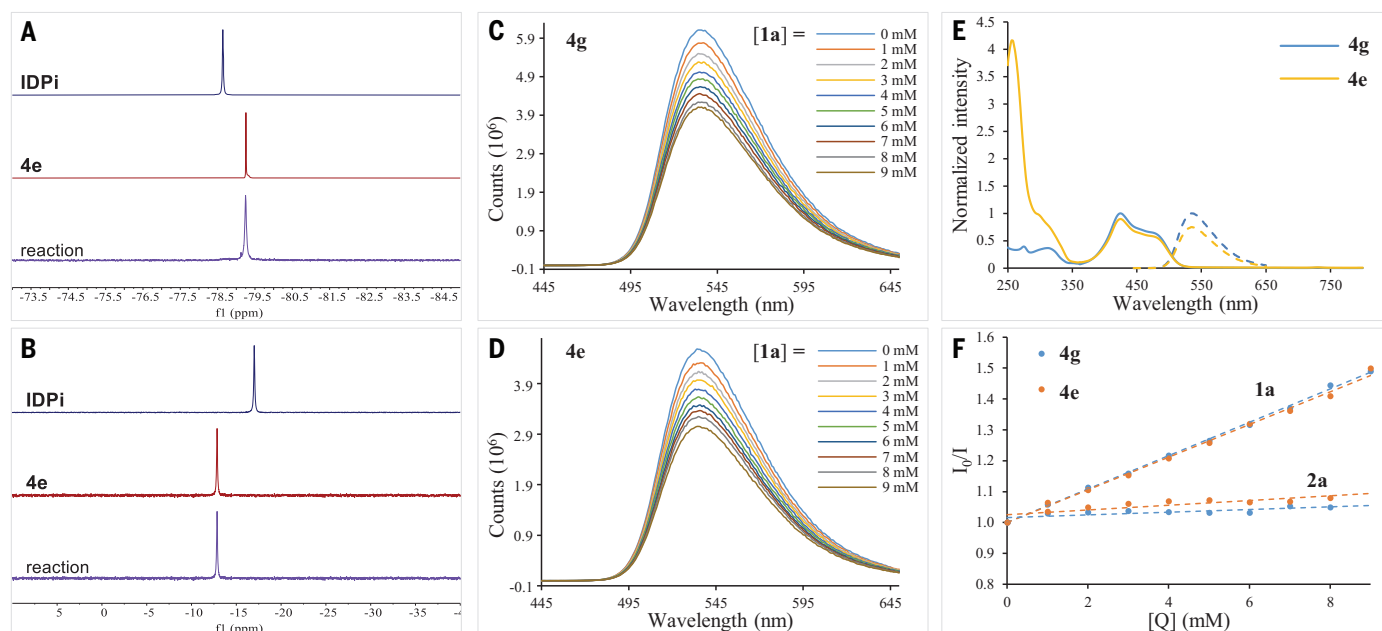


Fig. 5. Spectroscopic investigations. (A) ^{19}F NMR stacks. (B) ^{31}P NMR stacks. (C) Fluorescence quenching of catalyst **4g** with anethol (**1a**). (D) Fluorescence quenching of catalyst **4e** with anethol (**1a**). (E) UV-vis and fluorescence spectra of catalysts **4e** and **4g**. (F) Stern-Volmer plot of the fluorescence quenching of catalysts **4g** (blue) and for **4e** (orange) by substrates **1a** and **2a**. ppm, parts per million.

4e (Fig. 5D). In sharp contrast, neither catalyst **4g** nor catalyst **4e** showed any significant fluorescence decay with styrene **2a** (+1.97 V versus SCE). The similar fluorescence quenching of catalysts **4g** (blue) and **4e** (orange) by substrate **1a** is further presented in Stern-Volmer plots (I_0/I versus concentration of **1a**) (Fig. 5F).

Our results are consistent with the previously established catalytic cycle of the intermolecular [2+2] cycloadditions under photoredox catalysis or single-electron Lewis acid conditions (36–39). Accordingly, photocatalyst **4e** is first converted into its excited state **4e*** upon blue-light irradiation (Fig. 6A). Excited catalyst **4e***

then accepts an electron from anethol (**1a**), producing the corresponding radical cation **1a^{•+}** and rendering the photocatalyst a neutral radical species **A**. Intermediate **1a^{•+}** engages in subsequent and presumably stepwise C–C bond forming events, furnishing radical cation intermediate **3a^{•+}** (40). We speculate that the first of these two steps is enantio-determining and the second step is diastereo-determining, creating the bond between the two benzylic positions in a thermodynamically and kinetically preferred trans-relationship. A single electron reduction of this intermediate will then give rise to product **3a**.

There are several possibilities for how this last SET step proceeds. Plausible pathways include: (i) a propagation mechanism in which substrate **1a** serves as an electron donor toward radical cation intermediate **3a^{•+}**, delivering reactive species **1a^{•+}** along with product **3a**; (ii) electron transfer from **A** to product radical cation **3a^{•+}**, to provide product **3a** while simultaneously regenerating photocatalyst **4e**; (iii) oxidation of catalyst radical **A** by an electron relay catalyst (naphthalene, for example), the reduction product of which would subsequently reduce radical cation **3a^{•+}**, regenerating the electron relay catalyst while furnishing

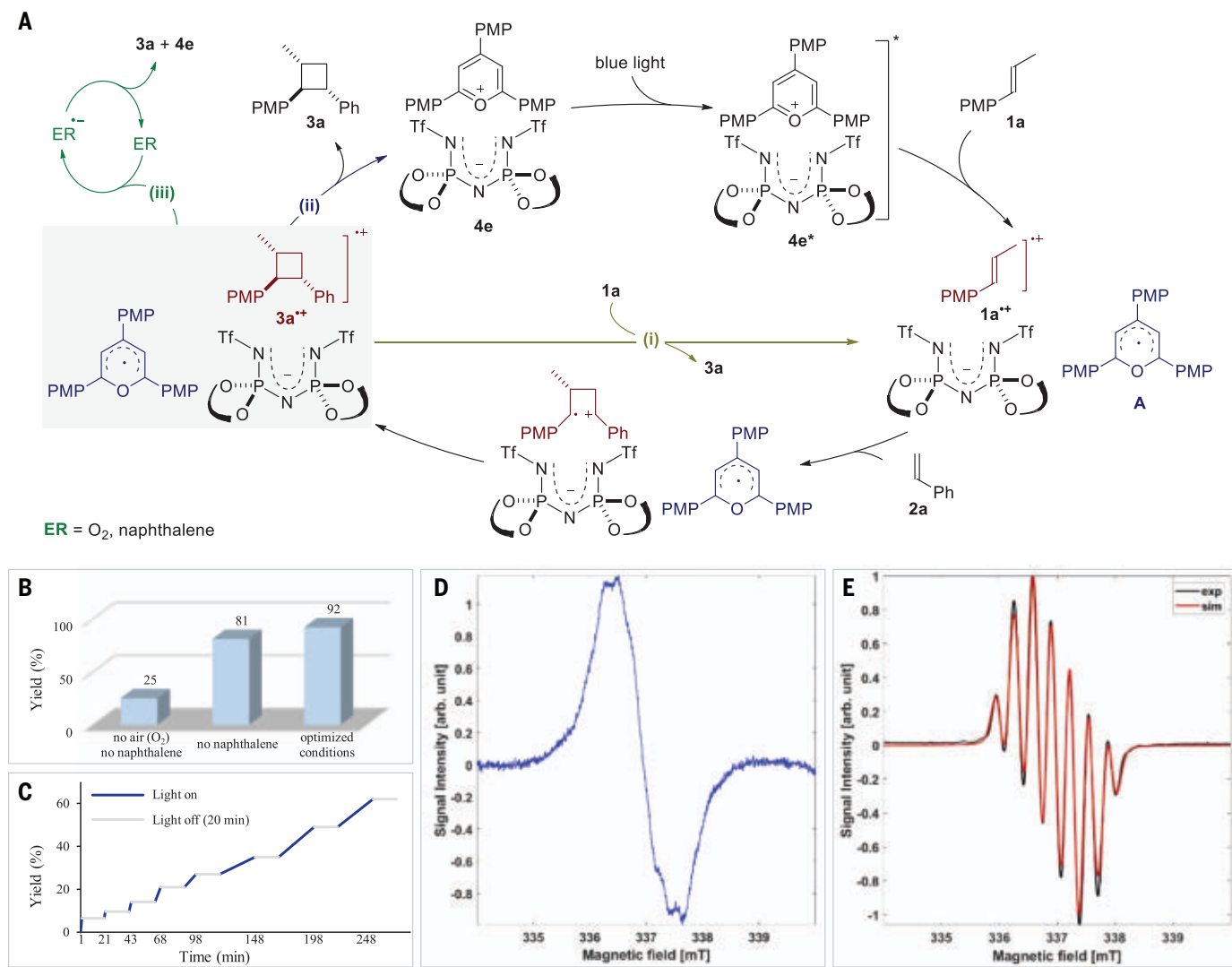


Fig. 6. Mechanistic investigations. (A) Proposed catalytic cycle. (B) Results with or without electron relay (ER) catalysts naphthalene or oxygen. (C) Light on-off cycles. (D) EPR measurements of the reaction using catalyst **4e** at -83°C and (E) EPR measurements of the reaction mixture using photocatalyst **5e** at -30°C under continuous photoexcitation with blue light. arb. unit, arbitrary units; exp, experimental; sim, simulated.

product **3a**. In this scenario, the role of the electron relay catalyst is to overcome the kinetic obstacle of step (ii), which requires the reaction of two highly reactive intermediates, each present in only small concentrations.

To gain further insight into the catalytic cycle, electron paramagnetic resonance (EPR) experiments were performed. First, the individual components of the reaction (solvent, reactants **1a** and **1b**, naphthalene, photocatalyst **4e**) in 1:1 dichloromethane:tetrahydrofuran were irradiated under steady-state conditions separately with blue light at -83°C in the spectrometer. As expected, no EPR signal was detected under either one of these conditions (see fig. S4 for details). However, a distinct EPR signal was observed when we investigated the entire reaction mixture (Fig. 6D). While radical cation **1a**^{••} (**4l**) could not be detected under these conditions, we hypothesize

that the observed signal is due to the formation of catalyst radical **A**, consistent with a previously reported system (35). An isotropic and fast-motional doublet radical electron spin coupling was observed in the continuous wave X-band EPR spectrum of radical **A** with $g = 2.003$. Additionally, to further support our hypothesis, *N*-Ph acridinium photocatalyst **5e** was used in the EPR measurements. As expected, EPR spectra of *N*-Ph acridinium photocatalyst with 10-mW power and with a modulation amplitude of 0.2 G shows seven hyperfine splitting lines (Fig. 6E). The hyperfine coupling is presumably due to the *N*-Ph moiety of the catalyst, which is in agreement with the EasySpin simulated spectra with $a_1(1\text{H})$, $a_2(1\text{H})$, $a_3(1\text{H})$ ($n = 2, 2, 1$) nuclei at $g = 2.0034$, $A = (0.2751, 0.3826, 0.5909)$, and Lorentzian width (0.2503, 0.0419). These experiments are consistent with the proposed SET from sub-

strate **1a** to the excited state of the photocatalyst. Furthermore, because continuous light irradiation is needed to achieve full consumption of starting material **1a**, propagation pathway (i) cannot be the primary pathway to complete the catalytic cycle. This assumption is further supported by light on-off cycles (Fig. 6C). In the dark, no conversion was observed, and progress of the reaction resumed in presence of light. Additionally, a time-dependent continuous EPR signal intensity decay in the dark was observed when the reaction mixture was first irradiated with blue light at -83°C in the EPR spectrometer for a few minutes, after which the light was switched off (see fig. S4 for details). To support the role of the electron relay catalyst, control experiments were performed and summarized in Fig. 6B. In the absence of an ER catalyst (oxygen or naphthalene), an almost threefold rate deceleration was observed.

Asymmetric counteranion-directed photoredox catalysis (ACPC) offers a broadly useful and general approach to photoredox catalysis proceeding via all types of radical cations. Wider application of the principles described here can be anticipated.

REFERENCES AND NOTES

- N. A. Romero, D. A. Nicewicz, *Chem. Rev.* **116**, 10075–10166 (2016).
- T. P. Yoon, M. A. Ischay, J. Du, *Nat. Chem.* **2**, 527–532 (2010).
- C. K. Prier, D. A. Rankic, D. W. C. MacMillan, *Chem. Rev.* **113**, 5322–5363 (2013).
- D. M. Schultz, T. P. Yoon, *Science* **343**, 1239176 (2014).
- R. Brimiouille, D. Lenhart, M. M. Maturi, T. Bach, *Angew. Chem. Int. Ed.* **54**, 3872–3890 (2015).
- E. Meggers, *Chem. Commun.* **51**, 3290–3301 (2015).
- D. A. Nicewicz, D. W. C. MacMillan, *Science* **322**, 77–80 (2008).
- J. J. Murphy, D. Bastida, S. Paria, M. Fagnoni, P. Melchiorre, *Nature* **532**, 218–222 (2016).
- D. A. DiRocco, T. Rovis, *J. Am. Chem. Soc.* **134**, 8094–8097 (2012).
- L. J. Rono, H. G. Yayla, D. Y. Wang, M. F. Armstrong, R. R. Knowles, *J. Am. Chem. Soc.* **135**, 17735–17738 (2013).
- E. M. Sherbrook et al., *Nat. Commun.* **12**, 5735 (2021).
- R. S. J. Proctor, H. J. Davis, R. J. Phipps, *Science* **360**, 419–422 (2018).
- H. Huo et al., *Nature* **515**, 100–103 (2014).
- L. Huan, X. Shu, W. Zu, D. Zhong, H. Huo, *Nat. Commun.* **12**, 3536 (2021).
- P. Zheng et al., *Nat. Commun.* **12**, 1646 (2021).
- J. Li et al., *Nat. Commun.* **9**, 2445 (2018).
- M. P. Sibi, J. Ji, J. H. Wu, S. Gürtler, N. A. Porter, *J. Am. Chem. Soc.* **118**, 9200–9201 (1996).
- J. Du, K. L. Skubi, D. M. Schultz, T. P. Yoon, *Science* **344**, 392–396 (2014).
- H. Guo, E. Herdtweck, T. Bach, *Angew. Chem. Int. Ed.* **49**, 7782–7785 (2010).
- R. Brimiouille, T. Bach, *Science* **342**, 840–843 (2013).
- X. Huang et al., *J. Am. Chem. Soc.* **139**, 9120–9123 (2017).
- M. A. Emmanuel, N. R. Greenberg, D. G. Oblinsky, T. K. Hystrer, *Nature* **540**, 414–417 (2016).
- P. D. Morse, T. M. Nguyen, C. L. Cruz, D. A. Nicewicz, *Tetrahedron* **74**, 3266–3272 (2018).
- Z. Yang, H. Li, S. Li, M.-T. Zhang, S. Luo, *Org. Chem. Front.* **4**, 1037–1041 (2017).
- S. Mayer, B. List, *Angew. Chem. Int. Ed.* **45**, 4193–4195 (2006).
- L. Schreyer, R. Properzi, B. List, *Angew. Chem. Int. Ed.* **58**, 12761–12777 (2019).
- S. Lee, P. S. J. Kaib, B. List, *J. Am. Chem. Soc.* **139**, 2156–2159 (2017).
- R. Properzi et al., *Nat. Chem.* **12**, 1174–1179 (2020).
- R. Alonso, T. Bach, *Angew. Chem. Int. Ed.* **53**, 4368–4371 (2014).
- D. I. Schuster, G. Lem, N. A. Kaprinidis, *Chem. Rev.* **93**, 3–22 (1993).
- M. Riene, D. A. Nicewicz, *Chem. Sci.* **4**, 2625–2629 (2013).
- K. Tanaka, M. Kishimoto, M. Sukekawa, Y. Hoshino, K. Honda, *Tetrahedron Lett.* **59**, 3361–3364 (2018).
- L. Wang et al., *Nat. Commun.* **13**, 3621 (2022).
- V. Kottisch, Q. Michaudel, B. P. Fors, *J. Am. Chem. Soc.* **138**, 15535–15538 (2016).
- Q. Michaudel et al., *J. Am. Chem. Soc.* **139**, 15530–15538 (2017).
- J. H. Shin, E. Y. Seong, H. J. Mun, Y. J. Jang, E. J. Kang, *Org. Lett.* **20**, 5872–5876 (2018).
- Y. Yu, Y. Fu, F. Zhong, *Green Chem.* **20**, 1743–1747 (2018).
- K. Tanaka et al., *Org. Lett.* **22**, 5207–5211 (2020).
- R. Li et al., *ACS Catal.* **7**, 3097–3101 (2017).
- Y. Okada, K. Chiba, *Chem. Rev.* **118**, 4592–4630 (2018).
- P. S. Lakkaraju, D. Zhou, H. D. Roth, *Chem. Commun.* **1996**, 2605–2606 (1996).

ACKNOWLEDGMENTS

We are grateful to M. Leutzsch for assistance with NMR spectroscopy, M. Meyer and H. Tüysüz for assistance with UV-vis and fluorescence spectroscopy, and H. Zhou for assistance with determining the absolute configuration by circular dichroism spectrometry. We acknowledge the excellent support of the late Eckhard Bill, a renowned and leading expert in the field of

EPR spectroscopy, who will always be remembered for his outstanding contributions to science. **Funding:** Generous support from the Max Planck Society, the Deutsche Forschungsgemeinschaft Cluster of Excellence Ruhr Explores Solvation (RESOLV), and the European Research Council [Early Stage Organocatalysis (ESO)] to B.L. **Author contributions:** Conceptualization: B.L. and C.K.D. Methodology: S.D., C.Z., and C.K.D. Investigation: S.D., C.Z., and C.K.D. Project administration: C.K.D. and B.L. Supervision: B.L. Electron paramagnetic resonance: D.D. and E.B. Writing – original draft: S.D. Writing – review & editing: S.D., C.Z., C.K.D., and B.L. **Competing interests:** A patent W02017037141 (A1) filed by the Max-Planck-Institut für Kohlenforschung and B.L. covers the IDPi catalyst class and its applications in asymmetric synthesis. The authors declare no other competing interests. **Data and materials availability:** All data and synthetic details used in the analysis are available in the supplementary materials. **License information:**

Copyright © 2023 the authors, some rights reserved; exclusive licensee American Association for the Advancement of Science. No claim to original US government works. <https://www.science.org/about/science-licenses-journal-article-reuse>

SUPPLEMENTARY MATERIALS

science.org/doi/10.1126/science.ade8190
Materials and Methods
Supplementary Text
Figs. S1 to S5
Tables S1 to S3
References (42–57)

Submitted 9 September 2022; resubmitted 25 November 2022
Accepted 4 January 2023
10.1126/science.ade8190

BATTERIES

A room temperature rechargeable Li₂O-based lithium-air battery enabled by a solid electrolyte

Alireza Kondori¹, Mohammadreza Esmaeilirad¹, Ahmad Mosen Harzandi¹, Rachid Amine², Mahmoud Tamadoni Saray³, Lei Yu⁴, Tongchao Liu⁵, Jianguo Wen⁴, Nannan Shan^{2,6}, Hsien-Hau Wang², Anh T. Ngo^{2,6}, Paul C. Redfern², Christopher S. Johnson⁵, Khalil Amine^{5,7,8}, Reza Shahbazian-Yassar³, Larry A. Curtiss^{2,*}, Mohammad Asadi^{1,*}

A lithium-air battery based on lithium oxide (Li₂O) formation can theoretically deliver an energy density that is comparable to that of gasoline. Lithium oxide formation involves a four-electron reaction that is more difficult to achieve than the one- and two-electron reaction processes that result in lithium superoxide (LiO₂) and lithium peroxide (Li₂O₂), respectively. By using a composite polymer electrolyte based on Li₁₀GeP₂S₁₂ nanoparticles embedded in a modified polyethylene oxide polymer matrix, we found that Li₂O is the main product in a room temperature solid-state lithium-air battery. The battery is rechargeable for 1000 cycles with a low polarization gap and can operate at high rates. The four-electron reaction is enabled by a mixed ion–electron-conducting discharge product and its interface with air.

There is growing interest in developing chemistries to replace currently available energy storage systems that mainly work based on intercalations (*I–3*). One area of study has been Li–O₂ batteries based on the formation of lithium peroxide (Li₂O₂), the result of a two-electron reaction between Li⁺ and O₂, or disproportionation of lithium superoxide (LiO₂), the result of a one-electron reaction (*4, 5*). A Li–O₂ battery cell based on the lithium oxide (Li₂O) formation and decomposition could in theory deliver a higher energy density because it is based on a four-electron reaction either through a direct elec-

tron transfer [Fig. 1, pathway (I)] or indirectly through disproportionation [Fig. 1, pathway (II)].

Li₂O is more difficult to achieve compared with its counterparts LiO₂ and Li₂O₂ because it involves breaking an O₂ bond during discharge and remaking an O₂ bond during charge. There have been several studies of Li-ion batteries based on reversible Li₂O formation from other lithium oxides (e.g., peroxide or superoxide) or a nitrate molten salt (*6–8*). Recently, a lithium nitrate/potassium nitrate (LiNO₃/KNO₃) eutectic molten salt has been used as the electrolyte in a Li–O₂ battery to reversibly form and decompose crystalline Li₂O in a four-electron transfer redox (*E*^o = 2.9 V versus Li/Li⁺) at elevated temperatures (*7, 9*). An alternative approach to achieving the four-electron Li₂O reaction in a Li–O₂ battery is to use a cell based only on gas and solid phases to promote fast reaction kinetics by avoiding problems with interfacial resistance and O₂ solubility (*10*). This could enable Li₂O formation as in pathway (I) (Fig. 1) if there is a sufficient supply of Li cations and electrons. A critical aspect would be the initial formation of a LiO₂/Li₂O₂ phase, both components of which can be ionically and electronically conductive (*11–15*), and having an air

¹Department of Chemical and Biological Engineering, Illinois Institute of Technology, Chicago, IL 60616, USA. ²Materials Science Division, Argonne National Laboratory, Lemont, IL 60439, USA. ³Department of Mechanical and Industrial Engineering, University of Illinois at Chicago, Chicago, IL 60607, USA. ⁴Center for Nanoscale Materials, Argonne National Laboratory, Lemont, IL 60439, USA. ⁵Chemical Sciences and Engineering Division, Argonne National Laboratory, Lemont, IL 60439, USA. ⁶Department of Chemical Engineering, University of Illinois at Chicago, Chicago, IL 60607, USA. ⁷Material Science and Engineering, Stanford University, Stanford, CA 94305, USA. ⁸Institute for Research&Medical Consultations (IRMC), Imam Abdulrahman Bin Faisal University (IAU), Dammam, Saudi Arabia.

*Corresponding author. Email: curtiss@anl.gov (L.A.C.); m.asadi@iit.edu (M.A.)

interface as a source of O_2 . This system could then provide the needed mixed electron/ionic conduction properties for electrochemical formation of Li_2O , resulting in an overall four-electron reaction as in pathway (I), as well as avoiding electrolyte instabilities (16, 17). Such an approach to attaining a four-electron reaction for a $Li-O_2$ battery requires the development of a stable, solid-state electrolyte with good ionic conductivity that interfaces well with the cathode.

Although there has been much research on the development of solid-state electrolytes (SSEs) for Li-ion batteries (18–22), there has been much less work done for $Li-O_2$ batteries. Thus far, the SSEs used for $Li-O_2$ have been based on metal phosphates, show fairly low reversibility and cyclability, and have Li_2O_2 as the main product (23–29).

The SSE used in this work was synthesized using a silane-coupling agent, mPEO-TMS {3-[methoxy(polyethyleneoxy)₆₋₉ propyl]trimethoxysilane}, to chemically bond with $Li_{10}GeP_2S_{12}$ (LGPS) nanoparticles in a PEO-LiTFSI matrix (supplementary materials, section S1). The LGPS nanoparticles are highly conductive, Li-rich ionic conductors (30, 31). In addition, we used mPEO-TMS because of (i) its similar molecular structure compared with PEO, which avoids any phase separation between them; (ii) its higher Li^+ transference number (t_{Li^+}) in a certain molecular weight range compared with that of PEO (32, 33); and (iii) its $-OCH_3$ termination, which improves the electrochemical stability window and the Li anode stability of the synthesized SSE (34). In this composite polymer electrolyte (CPE), the LGPS nanoparticles with an average crystallite size of 17 ± 6 nm (supplementary materials, section S2.1) are connected to the mPEO-TMS chains by strong chemical bonding of S atoms in Li_2S groups in LGPS to the Si in mPEO-TMS, which protects the LGPS from potential decomposition at the Li metal anode and the active cathode interfaces (supplementary materials, fig. S1 and section S1.2).

This bonding is known to occur due to the similarity between O–H and S–Li bonds (35). To confirm this, we performed x-ray photoelectron spectroscopy experiments on the CPE (Fig. 2, A and B, and supplementary materials, fig. S4 and section S2.2). The peaks at 162.0 and 103.1 eV in the S 2*p* and Si 2*p* spectra (Fig. 2, A and B) correspond to the presence of the Si–S bond, which strongly proves the interaction between Si atoms in mPEO-TMS and S atoms in LGPS. The C 1*s*, O 1*s*, and S 2*p* spectra also confirm the presence of PEO, mPEO-TMS, LGPS, and LiTFSI.

To analyze the structural morphology and chemical composition of the electrolyte, we performed scanning electron microscopy (SEM), as shown in Fig. 2C (supplementary materials, section S2.3). The SEM image of the SSE shown in Fig. 2C reveals a porous poly-

mer matrix with an average pore size of ~ 500 nm (inset in Fig. 2C). The elemental composition analysis using energy-dispersive x-ray spectroscopy also shows the uniform dispersion of the elements in the CPE (supplementary materials, fig. S5 and section S2.3).

We investigated the electronic properties of the CPE, first by measuring ionic conductivity at room temperature using electrochemical impedance spectroscopy (supplementary materials, section S3) (36–38). The Nyquist plots fitted with the circuit shown in the inset of Fig. 1D indicate an ionic conductivity of 0.52 mS/cm at room temperature for the SSE (thickness of 138 μ m), which is 10 times higher than that of the SSE without LGPS (i.e., PEO/mPEO-TMS/LiTFSI: 0.06 mS/cm; supplementary materials, fig. S6 and section S3). Moreover, the synthesized CPE exhibits ~ 15 times higher ionic conductivity compared with polymer electrolytes such as PEO with ionic conductivity of ~ 0.035 mS/cm at room temperature (39).

We measured the electrochemical stability of the SSE, which is a key factor to determining its practical application in Li batteries (supplementary materials, section S4). As shown in Fig. 1E, the CPE exhibits a large electrochemical redox stability window of 5.27 V. The high electrochemical stability of the CPE can be correlated to presence of $-OCH_3$ side chains in the mPEO-TMS, which form a stable interface with the Li metal anode (34).

Furthermore, we measured the Li transference number (t_{Li^+}) of the SSE with and without LGPS (supplementary materials, section S5) (40). The results shown in Fig. 1F indicate a t_{Li^+} of 0.73 for the CPE that is ~ 2 times higher than that of the SSE without LGPS (t_{Li^+} of 0.36; fig. S7). We attribute the improved t_{Li^+} of the CPE to improved Li transport pathways, enabled by characteristic features of both the polymer and ceramic electrolytes and their interphase. This will provide three potential Li transport pathways (41, 42), including those through (i) the bulk polymer matrix of PEO and mPEO-TMS, (ii) the bulk ceramic part (LGPS), and (iii) the newly formed interphase between LGPS and the mPEO-TMS. Moreover, using the silane-coupling agent ($Si-OCH_3$) group available in the mPEO-TMS, the LGPS nanoparticles are incorporated in the PEO matrix. This is known to eliminate the phase boundary between ethylene oxide-repeating units and the LGPS while reducing the grain boundary resistance between LGPS nanoparticles (42).

Performance analysis of the Li-air battery

The electrochemical performance of the CPE was examined in a custom-designed Li-air battery cell composed of a Li chip as the anode, the CPE as the SSE, and a cathode made up of trimolybdenum phosphide (Mo_3P) nanoparticles (43, 44) loaded on a hydrophobic gas diffusion layer in an air-like atmosphere composed of 78% N_2 , 21% O_2 , $\sim 45\%$ relative humidity, and 500 ppm of CO_2 (supplementary materials, section S6.1). The capacity-limited cycling experiments were performed at room temperature under applied discharge and charge constant current densities of 1 A/g (0.1 mA/cm^2) and a capacity of 1 Ah/g measured based on the cathode material loading (0.1 mg/cm^2). For an example of a high cathode loading, see the supplementary materials, section S6.4.

Figure 3A shows the operation of the solid-state Li-air battery cell over 1000 cycles with charge and discharge potentials of 2.95 and 2.90 V compared with Li/Li^+ at the end of the first cycle, respectively. The charge and discharge voltage profiles of the solid-state Li-air battery cell over different cycles, i.e., 1, 200, 400, 600, 800, and 1000, are shown in Fig. 3B. The variations in coulombic efficiency (in red), energy efficiency (in green), and the polarization gap (in blue) of the solid-state Li-air battery cell are shown in Fig. 3C. Our measurements over the continuous cycling of the battery cell indicate a coulombic efficiency of 100% over 1000 cycles, with a polarization gap that increased from 50 mV at the first cycle to ~ 430 mV at the 1000th cycle. The energy efficiency of the first cycle was 92.7%, and it gradually dropped to 87.7% after 1000 cycles.

We also examined the rate capability of the developed battery cell at different rates including 2, 3, and 5 A/g (0.5 mA/cm^2) rates at a capacity of 0.5 mAh/cm^2 (supplementary materials, section S6.2). The results indicate that the solid-state Li-air battery can operate at faster rates; however, the polarization gap at the end of the first cycle became somewhat larger (fig. S8). Deep discharge capacity experiments also showed some losses at the higher rates (fig. S9).

Characterization of products

To characterize the chemistry of the cell and to identify discharge products in our developed solid-state Li-air battery cell, we first performed in situ Raman spectroscopy experiments (supplementary materials, section S7). Figure 4A

Fig. 1. Li_2O formation pathways.

Shown are two reaction pathways to the formation of Li_2O based on the reaction of O_2 , Li^+ , and e^- .

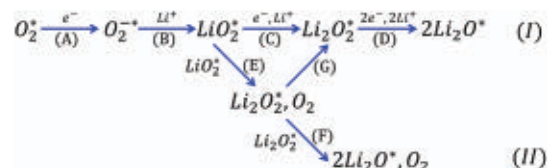
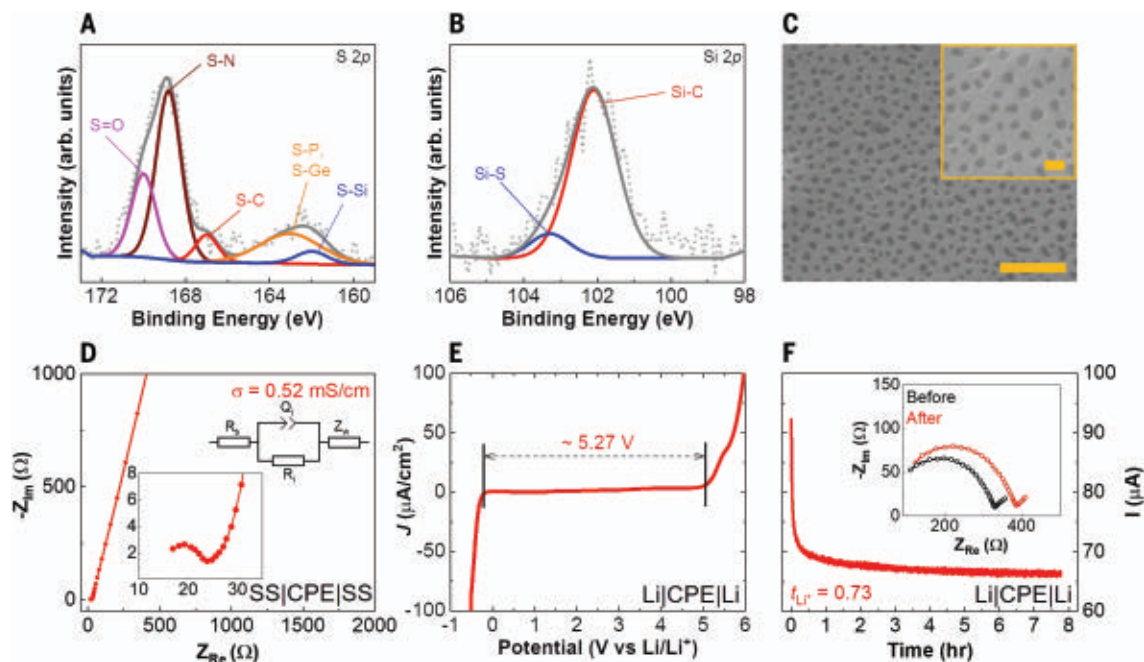


Fig. 2. Physicochemical and electrochemical characterization of the CPE. (A) S 2p and (B) Si 2p x-ray photoelectron spectroscopy of the CPE. (C) Low-magnification SEM image of the CPE (scale bar, 5 μm). The top right inset shows a high magnification of the SEM image, indicating an average pore size of 500 nm (scale bar, 1 μm). (D) Nyquist plot of the CPE indicating an ionic conductivity of ~ 0.52 mS/cm. The circuit used to fit the Nyquist plot of the CPE is shown in the inset of Fig. 1D. (E and F) Electrochemical redox stability of the CPE determined by a linear sweep voltammetry (LSV) experiment (E) and DC/AC analysis to measure the t_{Li^+} of the CPE (F). The inset in this figure shows the electrochemical impedance spectroscopy spectra of the cell before and after applying a DC bias of 30 mV for ~ 8 hours.



experiment (E) and DC/AC analysis to measure the t_{Li^+} of the CPE (F). The inset in this figure shows the electrochemical impedance spectroscopy spectra of the cell before and after applying a DC bias of 30 mV for ~ 8 hours.

shows the Raman spectra obtained at different time intervals (every 7.5 min or ~ 125 mAh/g) during the first discharge process (current density of 1 A/g, room temperature) compared with the pristine cathode. As shown in Fig. 4A, after the first 7.5 min of the discharge process, three new peaks appeared that are relevant to the formation of LiO_2 (at ~ 1125 cm^{-1}), Li_2O_2 (at ~ 788 cm^{-1}), and Li_2O (at ~ 528 cm^{-1}) (5, 44, 45). This indicates that all of these species (LiO_2 , Li_2O_2 , and Li_2O) formed during the discharge process. To understand the interplay between the Li species that formed during discharge, we measured and compared the relative Raman peak intensities. The Li_2O peak intensity constantly increased over 1 hour of the discharge process (Fig. 4B). By contrast, the Li_2O_2 and LiO_2 peak intensities gradually increased during the initial time intervals, followed by a constant plateau during the rest of the discharge process. Raman spectroscopy results did not show any peaks associated with lithium hydroxide (LiOH) or lithium carbonate (Li_2CO_3) formation at the first discharge cycle. The in situ Raman spectroscopy experiments during the charge process also revealed that the Li_2O Raman peak disappeared after 1 hour of the charge process, whereas LiO_2 and Li_2O_2 Raman peaks disappeared after approximately half of the charge capacity (30 to 45 min) (supplementary materials, fig. S14 and section S7).

To gain more insight into the $\text{LiO}_2/\text{Li}_2\text{O}_2$ part of the discharge product, we performed a series of Raman spectroscopy experiments for the aged, discharged cathode under ultra-high-

purity Ar and a vacuum environment (supplementary materials, section S7) to determine whether the LiO_2 would disproportionate (46). The Raman spectra of the aged samples (fig. S15) revealed that the signature Raman peak intensities associated with the LiO_2 (at 1125 and 1510 cm^{-1}) decreased with time, whereas the Raman peak intensity for Li_2O_2 increased under both Ar atmosphere and vacuum. These results confirm that disproportionation of LiO_2 to Li_2O_2 is favorable, with a slower disproportionation reaction under an Ar atmosphere. Moreover, after 5 days under the vacuum, the Raman spectrum of the discharged cathode indicated that the peak intensities associated with Li_2O_2 (788 cm^{-1}) increased, whereas none of the peaks relevant to the presence of LiO_2 (at 1125 and 1510 cm^{-1}) could be observed. This suggests that the LiO_2 and Li_2O_2 are on the outer surface of the discharge product, because the LiO_2 peak disappeared (and Li_2O_2 increased) with time and was dependent on whether the discharge product was in an Ar or a vacuum environment (46).

To further quantify the products formed during the discharge process, we performed titration coupled with ultraviolet-visible (UV-Vis) spectroscopy experiments as a function of discharge time (supplementary materials, section S8) (6, 9, 46, 47). The titration results (Fig. 4C) indicated that an average electron to oxygen ratio (e^-/O_2) of 3.96 was transferred during the discharge process, suggesting that the discharge product is predominantly composed of Li_2O by an approximately four-

electron transfer electrochemical reaction. These results suggest that the slight deviation from the theoretical e^-/O_2 ratio of 4.0 was due to the formation of small amounts of Li_2O_2 and LiO_2 , as shown by the in situ Raman spectroscopy experiments shown in Fig. 4B. In addition, our results indicate that the total Li_2O formed over 30 min of the discharge process at a current density of 1 A/g was ~ 0.82 μmol (0.025 and 0.031 μmol for LiO_2 and Li_2O_2), which increased to ~ 1.77 μmol Li_2O over 60 min. The amount of LiO_2 and Li_2O_2 formed after 60 min of discharge process was ~ 0.023 and 0.032 μmol , respectively, much lower (two orders of magnitude) than that of Li_2O . Furthermore, these results indicate that the amount LiO_2 and Li_2O_2 remained almost unchanged over the last 30 min, whereas Li_2O predominantly increased during the discharge process, which is consistent with the in situ Raman spectroscopy experiments (Fig. 4, A and B).

The measured e^-/O_2 ratio obtained in our titration experiments was confirmed by performing ex situ and in situ differential electrochemical mass spectroscopy (DEMS) during the discharge and charge processes, respectively (supplementary materials, sections S9 and S10) (5, 44, 45). As shown in the inset of Fig. 4C, our ex situ DEMS experiment found an e^-/O_2 ratio of 3.97 over the discharge process, which is consistent with our titration experiments, confirming the formation of Li_2O as the discharge product in a nearly four-electron transfer reaction. The in situ DEMS experiment

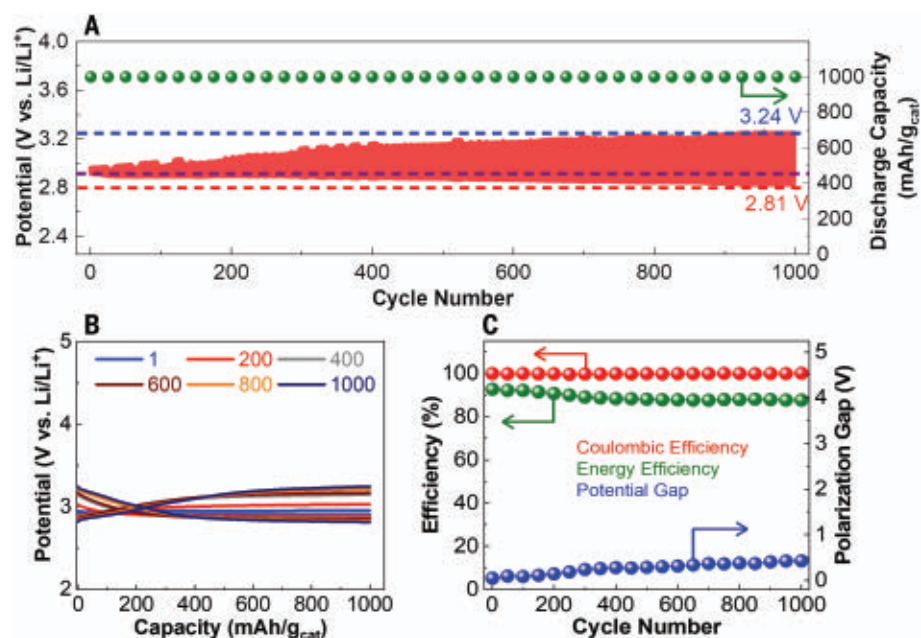


Fig. 3. Solid-state Li-air battery cell performance at a constant current density of 1 A/g and a limited capacity of 1 Ah/g. (A) Galvanostatic cycling over 1000 cycles. **(B)** Discharge/charge profiles at different cycles. **(C)** Coulombic efficiency (red dots), energy efficiency (green dots), and polarization gap at the end of cycle (blue dots) over 1000 cycles.

of the charge process (Fig. 3D) at a constant current density of 2.5 A/g and a capacity of 1 Ah/g showed an average e^-/O_2 of 3.94, which is quite close to that of the discharge process, meaning that the discharge product of the solid-state Li-air battery cell was reversibly decomposed. No change was observed in the CO_2 and H_2O signals of the DEMS, confirming the absence of species such as LiOH and Li_2CO_3 during the discharge process.

XRD experiments were performed to study the type and morphology of the discharge products in the solid-state Li-air battery cell and their reversibility with cycling (Fig. 4E and supplementary materials, section S11). Comparing the diffraction pattern of the discharged cathode at the first cycle with the pristine cathode showed two major peaks at 33.8° and 56.4° that were attributed to the (111) and (022) reflections of Li_2O crystals (9). No peaks were observed for either Li_2O_2 or LiO_2 , which could be for one of two reasons: (i) there was only a small amount of deposited Li_2O_2 and LiO_2 as found by the UV-Vis experiments or (ii) that the deposited species were amorphous rather than crystalline. No characteristic peak related to that of Li_2CO_3 and LiOH was found in the diffraction patterns of the discharged cathodes. After the charge process of the first cycle, no characteristic peaks of Li_2O were observed, meaning that the Li_2O discharge product was fully removed by oxidation. This trend was similar in higher cycle numbers, e.g., 100 and 200.

We also compared the electrochemistry of the developed SSE with that of the liquid

electrolyte in the Li-air battery cell using our previously developed liquid electrolyte with a Mo_3P -based cathode under identical experimental conditions (supplementary materials, section S12) (44). Characterization results for the discharged and charged cathodes of the liquid electrolyte Li-air battery cell indicated the reversible formation and decomposition of film-like Li_2O_2 (fig. S22). These results confirm that in the case of liquid electrolyte, the chemistry of the cell is mainly governed by the formation of Li_2O_2 in a two-electron reaction process, as opposed to a SSE battery, which favors nearly four-electron reaction chemistry by reversible formation and decomposition of Li_2O as the main product.

Elucidating the mechanism

The discharge mechanism in this solid-state Li-air battery has been deduced mainly on the basis of experimental results. The growth of the discharge products, including the major product, Li_2O , occurs in the space from incomplete contact between the cathode and CPE. Our AFM studies indicate that the cathode has roughness sufficient for space to exist (supplementary materials, fig. S23 and section S13). The cathode has pores ~ 40 nm in diameter for air flow (supplementary materials, figs. S24 and S25 and section S14). Additional experimental evidence used to deduce a growth mechanism is given in Fig. 5. This includes SEM images of the pristine cathode (Fig. 5A and fig. S24) and the discharged cathode (Fig. 5B and fig. S25, A and B) showing discharge product at

the bottom of the “valleys” of the cathode structure. Also given in Fig. 5, C to F, are Raman mappings of different components of the discharged cathode (supplementary materials, section S15). These include Raman imaging of Mo_3P (Fig. 5D), Li_2O (Fig. 5E), and Li_2O_2 (Fig. 4F). It can be seen from Fig. 5, E and F, that the Li_2O and Li_2O_2 are located in the valleys and on the sides of the valleys. There was no LiO_2 in the Raman mapping because the cathode had been aged, which is consistent with our studies showing no LiO_2 in Raman after aging (supplementary materials, section S7). The Raman mapping of a nonaged sample is also shown in fig. S26. In addition, transmission electron microscopy (TEM) images of the discharge product indicate that some Mo_3P nanoparticles have an amorphous film 10 to 20 nm thick (Fig. 5, G and H), presumably the $\text{LiO}_2/\text{Li}_2\text{O}_2/\text{Li}_2\text{O}$ observed by the Raman mapping. In addition, there were large particles that were amorphous with some crystalline parts. Additional Raman spectroscopy and TEM results are given in figs. S26 and S32.

On the basis of the trends from acid-base titration coupled with UV-Vis experiments (fig. S20), all three products grew initially and then the amount of Li_2O_2 and LiO_2 reached a steady state after ~ 15 min (for a 60-min discharge). This is consistent with the in situ Raman peak intensities shown in Fig. 4B. The titration results indicate that LiO_2 and Li_2O_2 were each $\sim 1\%$ of the total discharge product by weight after 1 hour. The aging experiment (supplementary materials, section S7) discussed previously is evidence that the LiO_2 is on the surface of the discharge product, with the Li_2O_2 being in close proximity based on its Raman peak intensity increase with loss of LiO_2 on aging.

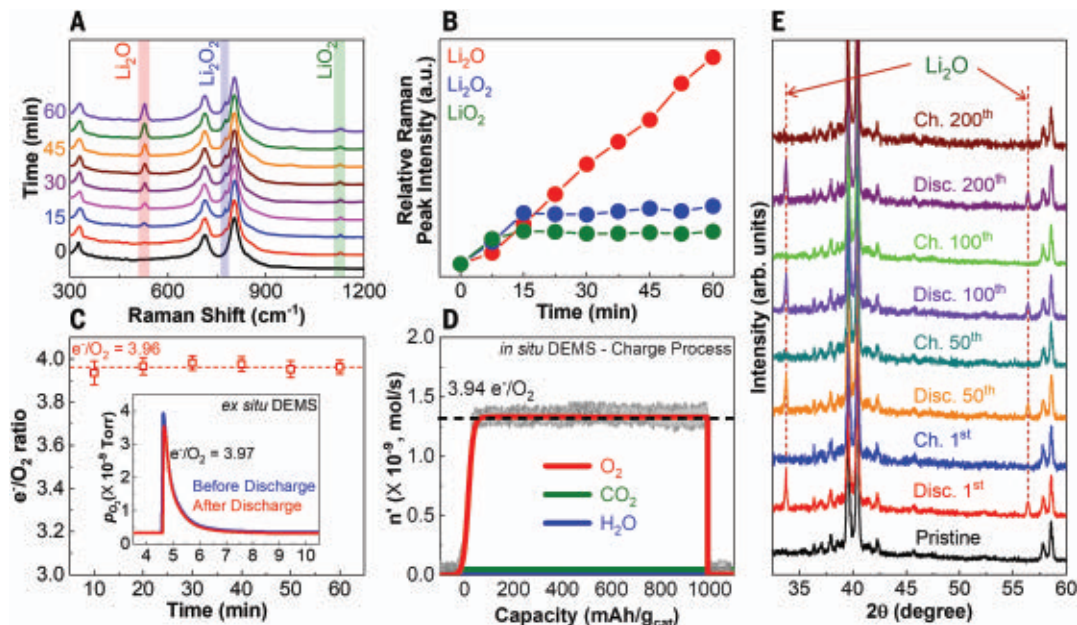
The predominance of the four-electron Li_2O reaction in this solid-state Li-air cell depends on the ionic and electronic conducting properties of the discharge product combined with the source of electrons (Mo_3P cathode), source of Li cations (CPE/Li anode), and abundance of O_2 (air). Moreover, with regard to the conducting properties of the discharge product, studies have shown that LiO_2 and Li_2O_2 can have good conductivity properties. Computational and experimental studies of LiO_2 have shown that it is electronically conducting (11, 48), whereas computational studies have shown that amorphous Li_2O_2 has enhanced ionic conductivity (12) and that the surface of Li_2O_2 can have good electronic conductivity (13). It has also been shown in computational studies that amorphous Li_2O can be a fast ionic conductor (49). In addition, there may be nonstoichiometric Li_xO_y regions in the discharge product, because the reactions at the interfaces between stoichiometric compounds (LiO_2 , Li_2O_2 , and Li_2O) will not necessarily be the ideal ones shown by reaction I in Fig. 1.

Fig. 4. Discharge product analysis.

(A) In situ Raman spectroscopy experiments at different time intervals (capacity of ~125 mAh/g) during the discharge process at a current density of 1 A/g, indicating the evolution of peaks relevant to LiO_2 , Li_2O_2 , and Li_2O .

(B) Relative Raman peak intensities as the function of time during the discharge process. (C) Calculated e^-/O_2 ratios using titration experiments at different time intervals, indicating an average e^-/O_2 of 3.96 during the discharge process at a current density of 1 A/g and a capacity of 1 Ah/g. The inset shows ex situ DEMS results for the discharge process indicating an e^-/O_2 ratio of 3.97 (in agreement with titration experiments) attributed to the formation of Li_2O during the discharge process.

(D) In situ DEMS experiment for the charge process indicates an average e^-/O_2 of 3.94 at a constant current density of 5 A/g and a capacity of 1 Ah/g. (E) Thin-film diffraction patterns of the discharged/charged cathodes at different cycle numbers, i.e., 1, 50, 100, and 200, compared with the pristine cathode sample.



This is illustrated by the more detailed reaction I in Fig. 5J and could introduce more possibilities for ionic and electronic conductivity.

There are two growth stages of the discharge product, as illustrated in Fig. 5I: a pre-steady state and a steady state. After $\text{LiO}_2/\text{Li}_2\text{O}_2$ growth is initiated at a three-phase junction involving O_2 from air, Li^+ from the CPE, and the Mo_3P cathode as an electrocatalyst, the $\text{LiO}_2/\text{Li}_2\text{O}_2$ will continue to grow. We performed density functional (DFT) calculations showing that O_2 has a binding on a LiO_2 surface (supplementary materials, section S16.2), which will enable steps A and B in reaction I (Fig. 1). The subsequent reaction of LiO_2 to Li_2O_2 occurs by the addition of a second electron and Li cation to LiO_2 (reaction I, Fig. 1, step C) or possibly by disproportionation of LiO_2 (reaction II, Fig. 1, step E). During the pre-steady-state phase (Fig. 5I), in addition to LiO_2 and Li_2O_2 growth, there will also be Li_2O formation from the last two electron/cation additions in reaction I (Fig. 1, step D). On the basis of the Raman peak intensities as a function of time (Fig. 4B), after ~15 min, the LiO_2 and Li_2O_2 reach a steady state and the Li_2O continues to grow due to excess Li cations. It has been speculated that disproportionation of Li_2O_2 (reaction II, Fig. 1, step F) may be a mechanism for the formation of Li_2O from Li_2O_2 (9). We do not believe that Li_2O_2 disproportionation occurs in a room temperature solid-state cell because the reaction is very endergonic, as shown by DFT calculations (supplementary materials, section S16). Thus, because LiO_2 is on the discharge product surface,

it can regenerate while being a source for formation of Li_2O_2 , which likewise can be a source for the formation of Li_2O (reaction II, Fig. 1, step D).

It is hypothesized that this set of sequential reactions will be forced to Li_2O by the abundance of O_2 at the gas-solid interface, excess Li cations due to the ionic conductivity of the CPE, and electronic conductivity of the cathode combined with the mixed electron-ion conductor nature of the amorphous phase of the discharge product, which we call a sequential reaction interphase. Figure 5J illustrates the sequential reactions occurring in this amorphous phase on a Mo_3P nanoparticle. This could also occur in the bottoms of the valley (supplementary materials, fig. S33 and section S18.1). There is experimental evidence that supports this postulated sequential reaction mechanism in our solid-state Li-air battery. First, when the battery was run under the same conditions except for a liquid electrolyte, the reaction only proceeded to Li_2O_2 , as already discussed. This is probably because of the availability of O_2 at the liquid-solid interface compared with the reactions in the amorphous phase, where no oxygen is present. Second, an Li- O_2 battery performed poorly with only PEO as a solid-state electrolyte (50), probably because the ionic conductivity of PEO at room temperature is much lower (39). Third, we have performed several restart experiments in which the cell was run for 30 min and then allowed to age for 5 days in a vacuum to allow LiO_2 to disproportionate to Li_2O_2 . In such cases, in which there is no Raman evidence for

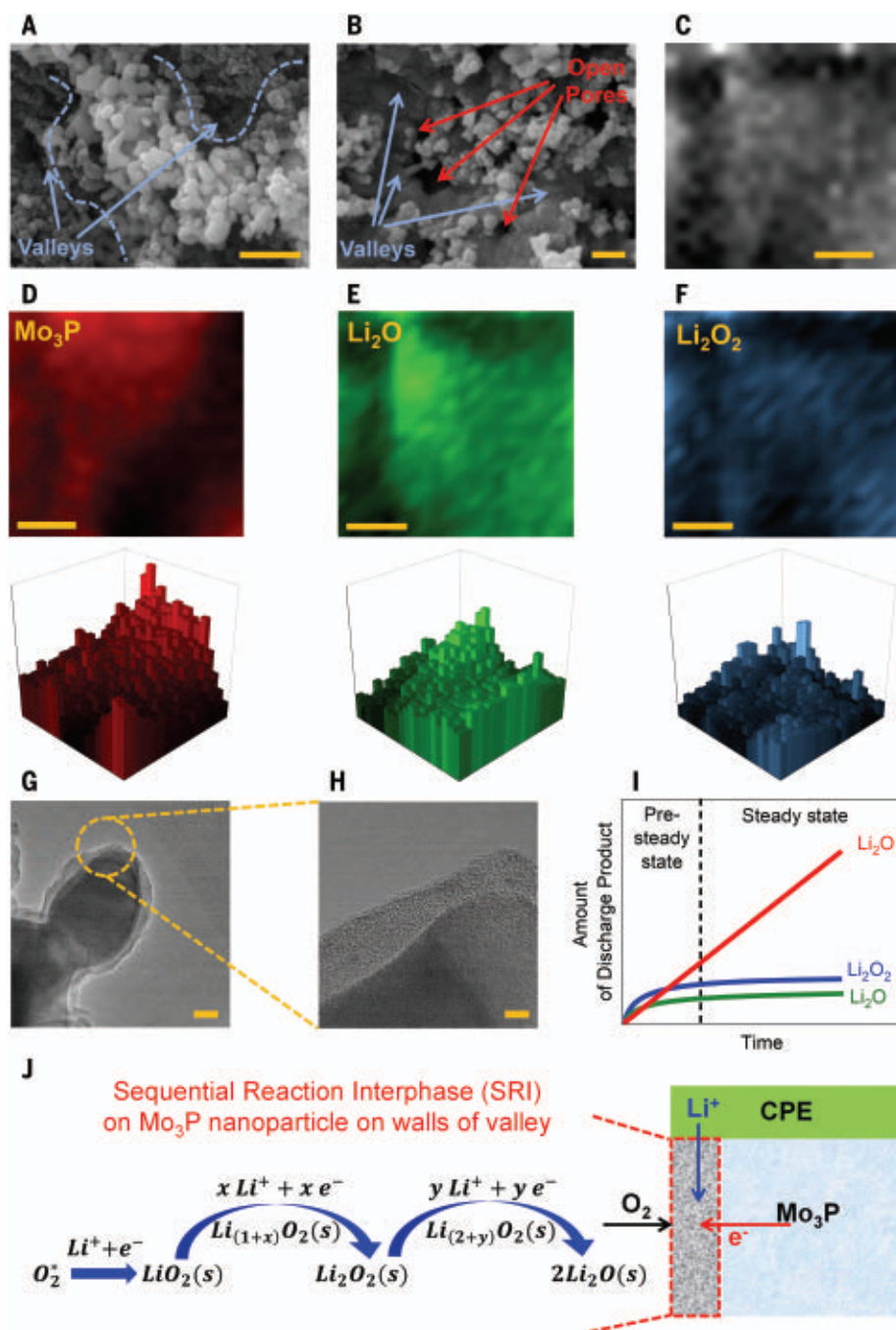
LiO_2 , the battery still operates both for charge and discharge, although at a slightly higher or lower voltage, respectively (supplementary materials, fig. S34 and section S18.2). This is probably because of loss of some electronic conductivity from disproportionation of LiO_2 . Finally, we also note that conversion of Li_2O_2 to Li_2O in liquid cells without O_2 has been shown to be possible under the right environments (6, 8).

During charge, the in situ Raman peak intensities for the different products (supplementary materials, fig. S14 and section S7) reveal that a somewhat different mechanism is present, because there was no steady-state period for $\text{LiO}_2/\text{Li}_2\text{O}_2$ decomposition as there was for formation during discharge. Instead, the intensities indicate that the three products decomposed at different rates, with LiO_2 and Li_2O_2 intensities disappearing after 30 to 45 min. The decomposition likely occurs in the reverse steps of the sequential reaction in the initial stage of the charge reaction (supplementary materials, fig. S35 and section S18.3) because O_2 is detected in DEMS throughout the charge (Fig. 4D), but with nonstoichiometric components contributing to the charge mechanism after the LiO_2 and Li_2O_2 components have largely disappeared (supplementary materials, fig. S35 and section S18.3).

Our results demonstrate that an SSE in a Li-air battery can enable a room temperature, reversible, four-electron Li_2O reaction for 1000 cycles with a low polarization gap at a high rate that operates in air. We also investigated the potential of this solid-state Li-air battery

Fig. 5. Discharge reaction mechanism.

(A) SEM image of a pristine cathode (scale bar, 500 nm); dashed blue lines show valleys. (B) SEM image of a discharged cathode (scale bar, 200 nm); blue arrows show the discharge products deposited in the valleys and red arrows show pores for air flow. (C) Raman microscope optical image [scale bars in (C) to (F), 1 μm] of the zone where the Raman maps shown in (D) to (F) were collected. (D) Two- and three-dimensional spatially resolved Raman mapping results of Mo_3P on the cathode surface. (E) Li_2O on the cathode surface. (F) Li_2O_2 on the cathode surface. (G and H) TEM images of the Mo_3P nanoparticle from the discharged cathode (scale bar, 20 nm) covered by the discharge product, which is an amorphous film ~10 to 20 nm thick [scale bars in (G) and (H), 5 nm]. (I) Diagram of discharge products as a function of time based on Raman spectra intensities. (J) Detailed reaction mechanism I (Fig. 1) for an SRI on a Mo_3P nanoparticle surface.



by performing deep discharge-charge experiments (supplementary materials, section S6.3). The results shown in fig. S9 indicate that this solid-state Li-air battery cell can work up to a capacity of ~10.4 mAh/cm², resulting in a specific energy of ~685 Wh/kg_{cell}. In addition, the cell has a volumetric energy density of ~614 Wh/L_{cell} because it operates well in air with no deleterious effects (supplementary materials, section S6.3). Thus, Li-air battery architectures based on SSEs can be constructed that are conducive to a four-electron Li_2O reaction and provide a real opportunity to obtain a projected specific energy of >1 kWh/kg (volumetric

energy density of 1000 Wh/L), which is beyond what is possible from Li-ion technology.

REFERENCES AND NOTES

- Z. Peng, S.A. Freunberger, Y. Chen, P.G. Bruce, *Science* **337**, 563–566 (2012).
- Y.-C. Lu et al., *Energy Environ. Sci.* **6**, 750–768 (2013).
- Y. Li, J. Lu, *ACS Energy Lett.* **2**, 1370–1377 (2017).
- W.-J. Kwak et al., *Chem. Rev.* **120**, 6626–6683 (2020).
- J. Lu et al., *Nature* **529**, 377–382 (2016).
- Y. Qiao, K. Jiang, H. Deng, H. Zhou, *Nat. Catal.* **2**, 1035–1044 (2019).
- V. Giordani et al., *Nat. Chem.* **11**, 1133–1138 (2019).
- Z. Zhu et al., *Nat. Energy* **1**, 16111 (2016).
- C. Xia, C. Y. Kwok, L. F. Nazar, *Science* **361**, 777–781 (2018).
- C. Zhao et al., *Angew. Chem.* **133**, 5885–5890 (2021).
- N. R. Mathiesen, S. Yang, J. M. García-Lastra, T. Vegge, D. J. Siegel, *Chem. Mater.* **31**, 9156–9167 (2019).
- F. Tian, M. D. Radin, D. J. Siegel, *Chem. Mater.* **26**, 2952–2959 (2014).
- M. D. Radin, J. F. Rodriguez, F. Tian, D. J. Siegel, *J. Am. Chem. Soc.* **134**, 1093–1103 (2012).
- R. Gao et al., *Nano Energy* **41**, 535–542 (2017).
- S. Li, J. Liu, B. Liu, *Chem. Mater.* **29**, 2202–2210 (2017).
- S. A. Freunberger et al., *J. Am. Chem. Soc.* **133**, 8040–8047 (2011).
- N. Mahne et al., *Nat. Energy* **2**, 17036 (2017).
- W. Liu et al., *Nat. Energy* **2**, 17035 (2017).
- J. Wan et al., *Nat. Nanotechnol.* **14**, 705–711 (2019).
- Y. Zhu et al., *Adv. Energy Mater.* **4**, 1300647 (2014).
- Y. Wang et al., *Nat. Mater.* **14**, 1026–1031 (2015).
- Z. Du et al., *J. Electrochem. Soc.* **168**, 050549 (2021).
- B. Kumar et al., *J. Electrochem. Soc.* **157**, A50 (2010).
- S. Wang et al., *J. Mater. Chem. A Mater. Energy Sustain.* **6**, 21248–21254 (2018).

25. Y. Liu *et al.*, *ACS Appl. Mater. Interfaces* **7**, 17307–17310 (2015).
 26. Y. Wang, H. Zhou, *Energy Environ. Sci.* **4**, 1704–1707 (2011).
 27. H. Kitaura, H. Zhou, *Energy Environ. Sci.* **5**, 9077–9084 (2012).
 28. X. Zhu, T. Zhao, P. Tan, Z. Wei, M. Wu, *Nano Energy* **26**, 565–576 (2016).
 29. S. Hasegawa *et al.*, *J. Power Sources* **189**, 371–377 (2009).
 30. N. Kamaya *et al.*, *Nat. Mater.* **10**, 682–686 (2011).
 31. Y. Mo, S. P. Ong, G. Ceder, *Chem. Mater.* **24**, 15–17 (2012).
 32. C. Zhang *et al.*, *Nat. Mater.* **8**, 580–584 (2009).
 33. Z. Gadjourova, Y. G. Andreev, D. P. Tunstall, P. G. Bruce, *Nature* **412**, 520–523 (2001).
 34. X. Yang *et al.*, *Energy Environ. Sci.* **13**, 1318–1325 (2020).
 35. T.-Z. Hou *et al.*, *Angew. Chem. Int. Ed.* **56**, 8178–8182 (2017).
 36. X. Z. Yuan, C. Song, H. Wang, J. Zhang, *Electrochemical Impedance Spectroscopy in PEM Fuel Cells: Fundamentals and Applications* (Springer, 2010).
 37. X. C. Chen *et al.*, *ACS Energy Lett.* **4**, 1080–1085 (2019).
 38. M. J. Palmer *et al.*, *Energy Storage Mater.* **26**, 242–249 (2020).
 39. N. H. A. M. Hashim, R. H. Y. Subban, *AIP Conf. Proc.* **2031**, 020021 (2018).
 40. P. G. Bruce, J. Evans, C. A. Vincent, *Solid State Ion.* **28–30**, 918–922 (1988).
 41. J. Ou, G. Li, Z. Chen, *J. Electrochem. Soc.* **166**, A1785–A1792 (2019).
 42. K. Pan *et al.*, *Adv. Mater.* **32**, e2000399 (2020).
 43. A. Kondori *et al.*, *Adv. Energy Mater.* **9**, 1900516 (2019).
 44. A. Kondori *et al.*, *Adv. Mater.* **32**, e2004028 (2020).
 45. M. Asadi *et al.*, *Nature* **555**, 502–506 (2018).
 46. D. Zhai *et al.*, *Nano Lett.* **15**, 1041–1046 (2015).
 47. H. H. Wang *et al.*, *J. Phys. Chem. C* **121**, 9657–9661 (2017).
 48. S. T. Plunkett *et al.*, *ACS Appl. Energy Mater.* **3**, 12575–12583 (2020).
 49. J. S. Lowe, D. J. Siegel, *ACS Appl. Mater. Interfaces* **12**, 46015–46026 (2020).
 50. J. Hassoun, F. Croce, M. Armand, B. Scrosati, *Angew. Chem. Int. Ed.* **50**, 2999–3002 (2011).
- ACKNOWLEDGMENTS**
- Funding:** M.A., R.A., K.A., T.L., A.N., C.J., and H.W. were supported by the US Department of Energy under contract DE-AC02-06CH11357 from the Vehicle Technologies Office, Office of Energy Efficiency and Renewable Energy. M.A. efforts were also partially supported by the Illinois Institute of Technology Armour College of Engineering, Wanger Institute for Sustainable Energy Research (WISER) seed fund (262029 221E 2300). N.S., P.R., and L.C. were supported by the Joint Center for Energy Storage Research (JCESR), an Energy Innovation Hub funded by the Office of Science, Basic Energy Sciences. R.S.Y. was supported by NSF grant DMR-1809439. Characterization Work by A.K., A.M.H., and M.E. was performed at the Keck-II facility of Northwestern University's NUANCE Center, which has received funding from the SHyNE Resource [National Science Foundation (NSF) grant ECCS-1542205]; the MRSEC program (NSF grant DMR-1720139) at the Materials Research Center; the International Institute for Nanotechnology (IIN); the Keck Foundation; and the State of Illinois through the IIN. Work by J.W. and Y.L. was performed at the Center for Nanoscale Materials, a US Department of Energy (DOE) Office of Science User Facility supported by the US DOE Office of Basic Energy Sciences under contract DE-AC02-06CH11357.
- Author contributions:** M.A. and A.K. conceived the idea. A.K., A.M.H., and M.E. synthesized the battery cell components, the cathode, and the SSE. A.K., A.M.H., and M.E. performed the battery cell run experiments. A.K. and M.E. performed the XRD, x-ray photoelectron spectroscopy, Raman spectroscopy, UV-Vis spectroscopy, DEMS, and electrochemical experiments. M.A. supervised the experimental efforts in design, synthesis, characterization, and electrochemical testing and analyses. C.J. helped with experimental design and analyses. M.T.S. and R.S.Y. performed SEM and energy-dispersive x-ray spectroscopy analyses of the cathode and the SSE. R.A., L.Y., T.L., J.W., H.W., and K.A. performed TEM and AFM experiments. N.S., P.R., and A.N. performed DFT calculations. L.C. helped with deducing the reaction mechanism based on the experimental observations and DFT calculations. All authors contributed to writing the manuscript.
- Competing interests:** M.A., A.K., and M.E. have filed a provisional patent application for the work described herein. The remaining authors declare no competing financial interests.
- Data and materials availability:** All data are available in the main manuscript or the supplementary materials.
- License information:** Copyright © 2023 the authors, some rights reserved; exclusive licensee American Association for the Advancement of Science. No claim to original US government works. <https://www.science.org/about/science-licenses-journal-article-reuse>
- SUPPLEMENTARY MATERIALS**
- science.org/doi/10.1126/science.abq1347
- Sections S1 to S18
Figs. S1 to S35
Tables S1 to S4
References (51–75)
- Submitted 21 March 2022; accepted 23 November 2022
10.1126/science.abq1347



Viral RNA Extraction from Nasal and Throat Swab Samples

Employing a novel dual frit extraction design, the Chromatrap Homogenizer Spin Column reduces lysate viscosity and captures insoluble debris by centrifugation. This easy-to-use spin column offers a fast

and efficient “one-stop” alternative to using traditional syringe and needle homogenization techniques. The homogenized lysate sample is then ready for RNA extraction. Employed as a single-use consumable, the Chromatrap Homogenizer Spin Column eliminates the possibility of sample cross-contamination. Fully compatible with all manual RNA extraction kits, the Chromatrap Homogenizer Spin Column provides an ideal sample preparation solution for RNA miniprep and midiprep.

Chromatrap

For info: +44-(0)-1978-661144

www.chromatrap.com/homogeniser-spin-column

Customer-Defined Knock-In Cell Lines

Via a patented FAST-HDR plasmid vector system, AMS Biotechnology (AMSBIO) can dramatically speed vector construction and reduce the time required to successfully isolate modified clones following transfection. Using modular plasmid backbones, in which key components are readily swappable, AMSBIO can rapidly implement customer-defined knock-in combinations. Fail-proof directional cloning of homology arms into the vector takes less than a day. Levering the power of CRISPR/Cas9 and homology-directed repair, the FAST-HDR plasmid vector system enables isolation of pure, successfully modified clones within just 2 weeks of transfection. The efficiency of this process allows us to deliver a stable cell line with as many as three knock-ins in as few as 30 days. Using the FAST-HDR plasmid vector system, AMSBIO can deliver a cell pool even more quickly. For a wide range of applications including drug screening, differentiation studies, and inducible expression studies, the specialists at AMSBIO can collaborate with you to develop an optimized, custom cell line to stably express your gene of interest.

AMS Biotechnology

For info: +1-617-945-5033

www.amsbio.com/custom-cell-line-development

RNA Library Prep Kit

The SEQuoia Express Stranded RNA Library Prep Kit from Bio-Rad offers a cost-effective and automation-friendly solution to the current challenges in library generation. The three-tube kit uses a novel reverse transcriptase alongside a ligation-free adaptor addition chemistry to yield a reproducible, quantitative RNA-Seq library in 3 hours. The kit enables researchers to construct robust libraries that capture mRNA and long noncoding RNA (>200 bp) transcripts for differential gene expression analysis and novel transcript discovery. Bio-Rad provides a complementary and customized bioinformatics solution to streamline the full next-generation sequencing (NGS) workflow, from library preparation to data analysis.

Bio-Rad Laboratories

For info: +1-800-424-6723

bio-rad.com/SEQuoiaExpress

Automated System for FISH, ISH, IHC

NanoVIP 100 and 300 are diverse, fully automated barcoded systems for fluorescence in situ hybridization (FISH), in situ hybridization (ISH), miRNA ISH, and IHC. Its reliable automation combined with eXACT temperature modules, predefined protocols, and liquid level sensors for accurate liquid handling ensures robust and reproducible results. The All-in-One system can run 10 (NanoVIP® 100) and 30 (NanoVIP® 300) different protocols simultaneously. This instrument can simplify a complex 33-step manual FISH protocol and reduce it to three simple steps: load, click, and view completed slides. With quality engineered hardware, unparalleled software capabilities, and multifunctional yet compatible, the NanoVIP 100 and 300 remain an ideal choice for clinical laboratories.

BioGenex

For info: +1-800-421-4149

<https://biogenex.com/nanovip-100>

NGS library/Sample Prep Technology

Miro Canvas from Miroculus is a compact, digital microfluidic platform which enables automation of complex NGS library prep and hybridization protocols with only minutes of hands-on time. The system utilizes an open cartridge to minimize reagent usage and accommodate multiple sample preparation protocols, including protocols for long-read sequencing technologies, target enrichment, and on-demand processing of samples. Called the Miro Cartridge, it incorporates microfluidic channels that sit in a layer above an open electrowetting plane, where the movement of droplets is controlled digitally by the electrodes the cartridge sits upon. An electrode board contains four thermal zones and four magnetic zones, including one dual magnetic-thermal zone. Processes such as nucleotide extraction, PCR, and magnetic bead cleanups can be performed. Miroculus NGS library preparation kits include fully optimized workflows from whole genome to targeted panels using well-validated protocols and reagents from established manufacturers.

Miroculus

For info: +1-415-770-8089

<https://miroculus.com/miro-canvas>

Microvolume Spectrophotometer

The Spex NanoSNAP provides high-performance measurements of nucleic acids and proteins in a snap. It is dedicated to life sciences applications but also provides additional methods for self-defined protocols such as spectrum scanning, multiwavelength, quantitation, and concentration. This spectrophotometer assesses the purity of DNA, RNA, proteins, and any other type of assay for samples available in small quantities within seconds, using as little as 1 µL of sample with no dilution required. It is versatile, with full wavelength coverage from 190 nm to 1,000 nm. It combines high performance with ease of use thanks to its nano hydrophobic-coated sample window, LED viewing light, and the cushioning design of the detection arm. Reports are saved on the internal memory and can be easily transferred to USB. The integrated 7-inch color touch screen displays an intuitive graphic interface that makes navigation between the different measurement modes easy to learn and quick to use.

Spex

For info: +1-855-438-7739

spexsampleprep.com

Electronically submit your new product description or product literature information! Go to www.science.org/about/new-products-section for more information.

Newly offered instrumentation, apparatus, and laboratory materials of interest to researchers in all disciplines in academic, industrial, and governmental organizations are featured in this space. Emphasis is given to purpose, chief characteristics, and availability of products and materials. Endorsement by *Science* or AAAS of any products or materials mentioned is not implied. Additional information may be obtained from the manufacturer or supplier.



**Shenzhen Institute of
Advanced Technology**
Chinese Academy of Sciences



Established in partnership between the Chinese Academy of Sciences and the Shenzhen Municipal Government, the Shenzhen Institute of Advanced Technology (SIAT) is a newly-created university with an objective to become the world's preeminent institute for emerging science and engineering programs. SIAT is equipped with state-of-art teaching and research facilities and is dedicated to cultivating international, visionary, and interdisciplinary talents while delivering research support to pursue innovation-driven development.

SIAT is located in Shenzhen, also known as the "Silicon Valley of China," a modern, clean, and green city, well-known for its stunning architecture, vibrant economy, and its status as a leading global technology hub. SIAT is seeking applications for faculty positions of all ranks in the following academic programs: Computer Science and Engineering, Bioinformatics, Robotics, Life Sciences, Material Science and Engineering, Biomedical Engineering, Pharmaceutical Sciences, Synthetic Biology, Neurosciences, etc. SIAT seeks individuals with a strong record of scholarship who possess the ability to develop and lead high-quality teaching and research programs. SIAT offers a comprehensive benefits package and is committed to faculty success throughout the academic career trajectory, providing support for ambitious and world-class research projects and innovative, interactive teaching methods.

Further information:

<https://www.siat-sz.edu.cn/>



ICYS Research Fellow at ICYS, NIMS, Japan

The International Center for Young Scientists (ICYS) of the National Institute for Materials Science (NIMS) invites applications for ICYS Research Fellow positions. ICYS will offer you the freedom to conduct independent and self-directed research in various areas of materials science with full access to NIMS advanced research facilities.

The common language at ICYS is English. Clerical and technical support in English will be given by the ICYS staff. A research grant of 2 million yen per year will be provided to each Research Fellow. Also, advantage is given when applying to NIMS permanent researcher position (about 50% of the applicants are accepted).

The annual salary is over 6 million yen*, which is the top class in Japan. The initial contract term is 3 years, renewed up to 5 years based on annual evaluation**.

All applicants must have obtained a PhD degree within the last 10 years. Applicants should submit an **application form** including a research proposal during the ICYS term, **CV**, a **list of DOI of journal publications**, **PDF files of three significant publications**, and **PhD Certificate** to the ICYS Recruitment Desk by **March 30, 2023 JST**. The format for the application documents can be downloaded from our website. The selection will be made on the basis of originality and quality of the research proposal as well as the research achievements. Please visit our website for more details.

*Approximately 23% of annual salary will be deducted as social insurance premium, residence tax and income tax.

**If the applicant is already in NIMS as a non-permanent researcher (Post doc et al.), the max contract term depends on work experience at NIMS.

ICYS Recruitment Desk
National Institute for Materials Science
www.nims.go.jp/icys/recruitment/



香港城市大學
City University of Hong Kong

#54

World
University

#4

World's top 50
Universities
under age 50

#1

World's Most
International Universities



Global Scholar Recruitment Campaign

City University of Hong Kong (CityU) is one of the world's leading universities, known for innovation, creativity and research. We are now seeking exceptional scholars to join us as Assistant Professors/Associate Professors/Professors/Chair Professors (on substantiation-track) in all academic fields with special focuses on **One Health, Digital Society, Smart City, Matter, Brain**, and related interdisciplinary areas. Research fields of particular interest include, but not limited to:



- biomedical science and engineering
- veterinary science
- computer science and data science
- neuroscience and neural engineering
- bio-statistics and AI-healthcare
- smart/semi-conductor manufacturing
- AI/robotics/autonomous systems
- aerospace and microelectronics engineering
- energy generation and storage
- digital business and innovation management
- fintech and business analytics
- computational social sciences
- digital humanities
- digital and new media
- law and technology
- private law
- healthy, smart and sustainable cities

Successful candidates should have a demonstrated ability to build a world-class research programme related to CityU's strategic research areas, plus a commitment to education and student mentorship. Candidates must possess a doctorate in their respective field by the time of appointment.

Outstanding faculty joining the University will be considered for nomination of the **Global STEM Professorship Scheme** sponsored by the Government of the Hong Kong Special Administrative Region, and may be provided with subsidy for their research teams and for setting up laboratories.

Please visit Colleges, Schools and Departments in CityU at
<https://www.cityu.edu.hk/academic/colleges-schools-and-departments>



City University of Hong Kong is an equal opportunity employer. We are committed to the principle of diversity. Personal data provided by applicants will be used for recruitment and other employment-related purposes.

Worldwide recognition ranking #54 (QS 2023), and #4 among top 50 universities under age 50 (QS 2021); #1 in the World's Most International Universities (THE 2020); #1 in Automation & Control/Electrical & Electronic Engineering/Materials Science & Engineering/Metallurgical Engineering/Nanoscience & Nanotechnology and #3 in Telecommunication Engineering in Hong Kong (GRAS 2022); and #41 Business School in the World and #4 in Asia (UT Dallas 2017 to 2021)



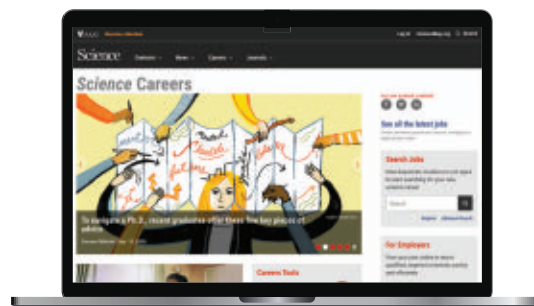
Science Careers helps you advance your career. Learn how !

- Register for a free online account on **ScienceCareers.org**.
- Search hundreds of job postings and find your perfect job.
- Sign up to receive e-mail alerts about job postings that match your criteria.
- Upload your resume into our database and connect with employers.
- Watch one of our many webinars on different career topics such as job searching, networking, and more.
- Download our career booklets, including Career Basics, Careers Beyond the Bench, and Developing Your Skills.
- Complete an interactive, personalized career plan at "my IDP."
- Visit our Employer Profiles to learn more about prospective employers.
- Read relevant career advice articles from our library of thousands.

Visit **ScienceCareers.org**
today — all resources are free

ScienceCareers

FROM THE JOURNAL SCIENCE  AAAS



SCIENCECAREERS.ORG

Who's the top employer for 2022?

Science Careers' annual survey reveals the top companies in biotech & pharma voted on by *Science* readers.

Read the article at sciencecareers.org/topemployers



INDIANA UNIVERSITY
BLOOMINGTON

TENURED OR TENURE TRACK FACULTY POSITION IN VIROLOGY INDIANA UNIVERSITY BLOOMINGTON

As part of a major, multi-year initiative to expand specific research areas across the IU Bloomington campus, the Departments of Biology and Molecular and Cellular Biochemistry invite applications at the Associate or Full Professor level in the area of **Virology**; established Assistant Professors will also be considered. We are particularly interested in scientists investigating the biology and pathogenesis of human viruses, emphasizing emerging and re-emerging viruses including (but not limited to) SARS coronavirus, influenza virus, norovirus, and HIV. Scientists with expertise in the immunology, molecular epidemiology, or molecular biology of these viruses are also encouraged to apply. Start dates of **Fall 2023** or **Fall 2024** are possible.

The hire will complement and broaden the highly collaborative IU community of internationally recognized virologists. The community includes fifteen well-funded laboratories in the Departments of Biology, Molecular and Cellular Biology, Chemistry, and Bioengineering. Scientific strengths include structural virology, virus-host interaction, virus assembly, VLP platform technologies, antiviral and vaccine development, and development of cutting-edge analytical methods for examining viruses. Several virology-oriented labs have strong interactions with industry to translate academic research into real world applications. IU virology laboratories are supported by outstanding research resources, including state-of-the-art facilities for genomics and bioinformatics, light and electron microscopy, flow cytometry, protein analysis, biophysical instrumentation, and crystallography.

Applicants must hold a Ph.D. in relevant fields, with a strong record of research accomplishments and external funding. Successful candidates will be expected to maintain a vigorous externally funded research program, and to participate in teaching at the undergraduate and graduate levels. To apply, please submit a cover letter, CV, research statement (past, present, and future; up to three pages), teaching statement (up to two pages), a 1-2 page statement on fostering diversity, equity, and inclusion in and out of the classroom, and the names and contact information for three or more references via <https://indiana.peopleadmin.com/postings/16365>. Applications will start to be evaluated on **February 15, 2023**, but the position will remain open until filled. Please address inquiries concerning the search to Jennifer Tarter at 812-856-3984 or jenjones@indiana.edu.

**IT'S NOT
JUST A JOB.
IT'S A CALLING.**



Find your next job at ScienceCareers.org

Whether you're looking to get ahead, get into, or just plain get advice about careers in science, there's no better or more trusted authority. Get the scoop, stay in the loop with *Science Careers*.

ScienceCareers

FROM THE JOURNAL SCIENCE AAAS

By Barbara A. Wanchisen and Heidi A. Schweingruber

Losing, and finding, a home

During one of our breakfasts several years ago, Barb revealed what felt like a dirty secret: “I don’t feel comfortable at academic research conferences anymore.” We both felt that way, but were nonetheless shocked to have it out on the table. When we were academics—Heidi as a postdoc and a short stint as a research professor, Barb through tenure and beyond—small research conferences were our intellectual home. They were where we presented our data, learned about the newest discoveries in our fields, and explored new directions for our work. We met people with shared interests who might become lifelong colleagues and friends. But with our transition to the nonprofit policy world, we lost that home.

After leaving academia, we continued to attend many of the conferences that had formerly been places of such personal and intellectual invigoration. Surely, we thought, we would still find reward in connecting with former colleagues, learning about others’ research, and sharing updates on our own endeavors.

But the feeling of being outsiders quickly emerged, and only grew over time. It was often difficult to find relevant sessions to attend. Few if any people suggested going for a drink, having a meal, or even attending a lecture together. The mere mention of nonacademic work often brought blank stares and an almost palpable lack of interest. Some even asked, “Didn’t you get tenure?” mystified that we had left academia.

Admitting to each other that we had both struggled with painful feelings of rejection was deeply cathartic. We realized that during our time in academia we had internalized expectations about academic success that are emphasized at conferences—namely, advancing one’s own research program. In our new work, this goal was not meaningful. We needed to find a new intellectual home.

Slowly, we developed a network of friends and colleagues who, like us, were expatriates from the academic world. We met scientists who were involved in public policy, attended meetings with them, and became involved in joint projects. In time, our networks expanded to include people in government, nonprofits, foundations, professional organizations, and advocacy groups.

This collection of like-minded colleagues became the new professional home we were looking for, where we celebrate each other’s wins and commiserate over difficult losses. We share our frustration about the difficulty of building con-



“Moving away from communities that used to be a central part of our identity was bittersweet.”

nections between researchers and policymakers and celebrate together when our work behind the scenes leads to new legislation or opens up new areas of research.

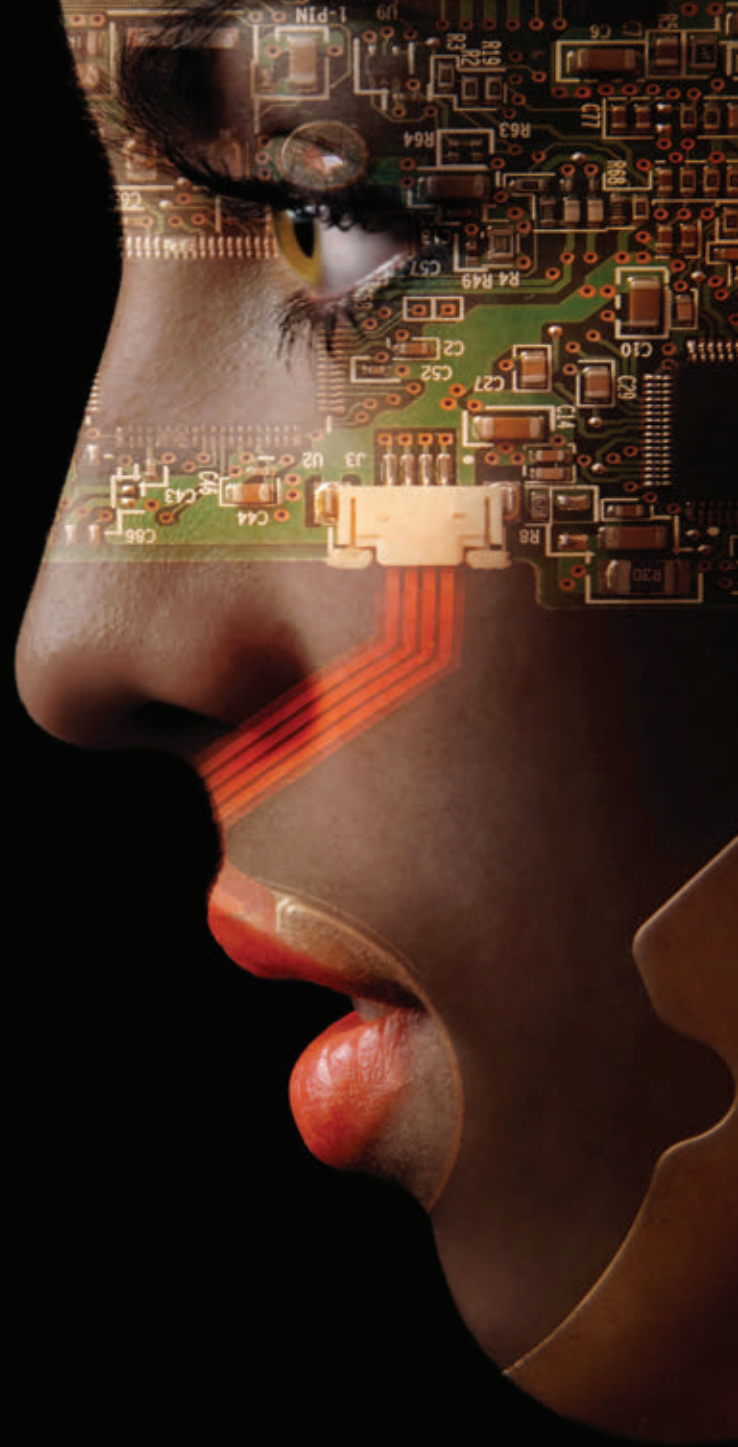
The two of us have also found new conferences that focus on policy and the application of research to social problems—topics seldom covered in typical academic research conferences. And we still attend larger academic conferences. We look for—and sometimes give—talks on topics such as applying science to public policy and interdisciplinary discussions about research that could affect national concerns. Encountering colleagues who are focused solely on research can be uncomfortable, but we have learned to embrace what these larger conferences can offer.

At the same time, we have virtually abandoned the small, highly focused research conferences that were once a mainstay of our academic lives. Moving away from communities that used to be a central part of our identity was bittersweet, but we no longer felt at home there.

Going from one professional world to the next is a process, and the emotions are mixed and messy, but the rewards have been worth it. And some day, a move to a new phase of our careers might mean we have to again rethink our definitions of “success” and “home.” But now we know that’s OK. ■

Barbara A. Wanchisen is senior adviser for behavioral sciences and Heidi A. Schweingruber is director of the Board on Science Education at the National Academies of Sciences, Engineering, and Medicine (NASEM). We thank Steven Breckler, Deborah Olster, and Amber Story for helpful comments on an early draft. The views in this essay are those of the authors and do not reflect those of NASEM.


Share Your Robotics Research with the World.




Shaping the future of robotics with high impact research!

As a multidisciplinary online-only journal, *Science Robotics* publishes original, peer-reviewed, research articles that advance the field of robotics. The journal provides a central forum for communication of new ideas, general principles, and original developments in research and applications of robotics for all environments.

Submit your research today. Learn more at: **science.org/journal/scirobotics**

 Twitter: @SciRobotics

 Facebook: @ScienceRobotics

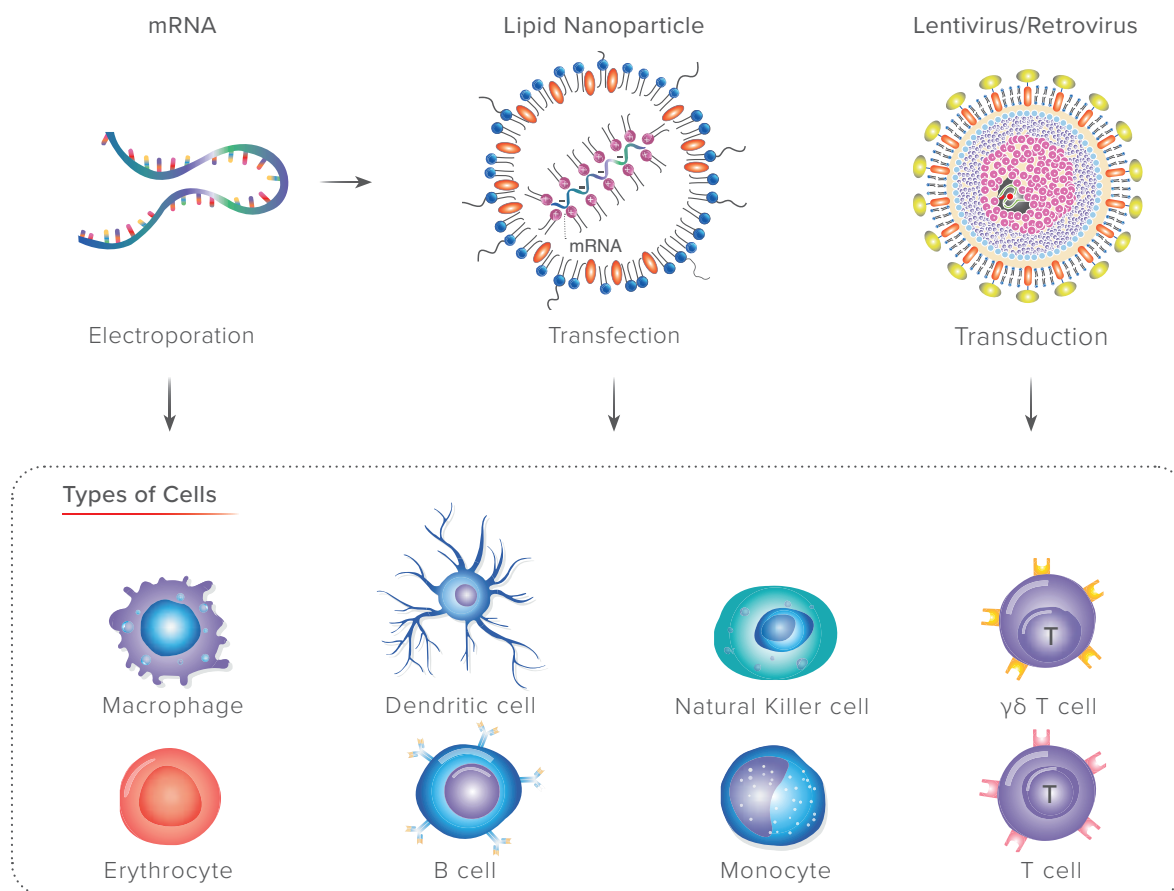
Science Robotics

 AAAS

Cell Therapy Research & Development CRO

Innovative Solutions for Customizing Immune Cells

Gene Delivery Methods



ProMab Biotechnologies provides many products and services to aid cell therapy research. As the world's first established CAR-T CRO, we bring over 6 years of experience developing lentiviral vectors for integrating novel genes and chimeric antigen receptors into a variety of cell types. Now, we look towards transient methods and expanded our offerings for mRNA transfection and lipid nanoparticle gene delivery. Leverage our platform for your cell therapy research with tailor-made products and service offerings.

Cell Therapy Research Services

- Lentivirus Production: GMP/Non-GMP
- mRNA Production & Lipid Nanoparticle Encapsulation
- CAR-T/NK Cell Generation
- CAR-T/NK Animal Models
- Immune Cell Engineering
- CRISPR Gene Knock-Outs

All products are for research use only

Discover more | www.promab.com



2600 Hilltop Dr, Building B, Suite C320, Richmond, CA 94806
1.866.339.0871 | info@promab.com

